Politecnico di Milano
Department of Aerospace Engineering
Doctoral Programme In Aerospace Engineering

Advanced Control Laws for Variable-Speed Wind Turbines and Supporting Enabling Technologies

Doctoral Dissertation of:
Carlo E.D. Riboldi
M.738537

Supervisor:
Prof. Carlo L. Bottasso

Tutor:
Prof. Giuseppe Sala

The Chair of the Doctoral Program:
Prof. Sergio Ricci

Year 2012 – XXIV Doctoral Cycle

Acknowledgements

This work has been fueled by the interest of many research and industrial subjects, whose contribution in providing useful advices and cross-checking tools to make this work more valuable is gratefully acknowledged.

They are the Department of Mechanical and Mechatronics Engineering of the Kangwon National University, Chooncheon, South Korea, and in particular Professor Yoonsu Nam and his many students; the Department of Electronic Systems Automation & Control of the University of Aalborg, Denmark, and in particular Professors Rafael Wisniewski, Mohsen Soltani and Mikael Svenstrup; the firms LeitWind S.p.A., Italy and Clipper Windpower, California.

The credit for a great many good ideas presented in this thesis goes to the supervisor, Professor Carlo Luigi Bottasso. A large contribution to the research activities reported herein came also from his collaborator Alessandro Croce, PhD. They fulfilled their essential roles according to the best tradition of university teaching.

Many master's thesis students contributed to this work, helping in the completion of several time-consuming analyses and processes.

A strong support came from my friends and fellow PhD students, and from all those colleagues who in the last years often shared their time, knowledge and enthusiasm, and – unfortunately for them – also their office, with the author.

Finally, I wish to thank my family and all my longtime friends: without their constant encouragement, this endeavor would never have come to a conclusion.

"All in all, not bad, not bad at all."
Reagan

Contents

List of Figures

Chapter 1

Introduction

Even if at a first glance wind turbines look rather simple among the power plants available today – those based on oil or gas combustion or on nuclear source –, the nature of the power source which they rely on – the wind – makes their operation a complex problem, which can be effectively dealt with by the extensive use of control systems. As the wind is an ever changing source of power, the first and most obvious control goal will be that of producing a power output sufficiently regular in time, to allow the plugging of the wind turbine to the existing electrical grids without hampering their stability.

Moreover, the usual power of nowadays turbines, of the order of the megawatts (MW), is obtained from plants where the diameter of the rotor and the height of the tower often exceed 80 meters. That size, combined with the use of light materials and smart designing technologies, aimed at saving some of the material cost in the assembly of many parts of the plant, exposes them to relevant loads and deformations. As a consequence, in order to prolongate the life of the plant, thus better distributing its initial cost, great attention must be paid to the control and dampening of loads, which represent other primary goals of existing controllers.

Despite the efforts necessary to design and operate these plants, much work has been done in the last twenty years to explore and develop wind turbines with various architectures and different sizes, which have now become reality. Such an effort, fueled by substantial governmental funding in several countries and by the generally positive mood of the public opinion with respect to this source of electrical power, has actually produced an array of different models, each of them typically aimed at a specific application.

As an instance, there exist various vertical-axis or limited size horizontal-axis wind turbines, typically designed to supply power to a local grid, and customized for isolated power utilities. On the other end, the aforementioned larger multi-MW size horizontal-axis wind turbines, often placed relatively

close to each other in on-shore or off-shore farms, are conceived and designed to supply regional or nationwide grids, just like more classical large power plants based on other sources. Turbines of this latter kind, typically two or three-bladed, have reached a good level of diffusion and standardization in the last two decades, also benefitting from a long period of experimentation, beginning coincidentally with the first modern studies on wind power back in the 1970s and 1980s.

The present work focuses on many control aspects related to this kind of turbines. A more in-depth, still rather simplified description of a typical horizontal-axis wind turbine will be provided next, followed by a review of many control strategies proposed more or less recently, with their different aims. Finally, the main topics treated in the present work will be presented at the end of the chapter.

1.1 Description of a Horizontal-Axis Wind Turbine

A wind turbine is basically a plant able to extract power from the wind and to transform it into electrical power. A schematic description of a horizontal-axis wind turbine with its main components is presented in Fig. 1.1.

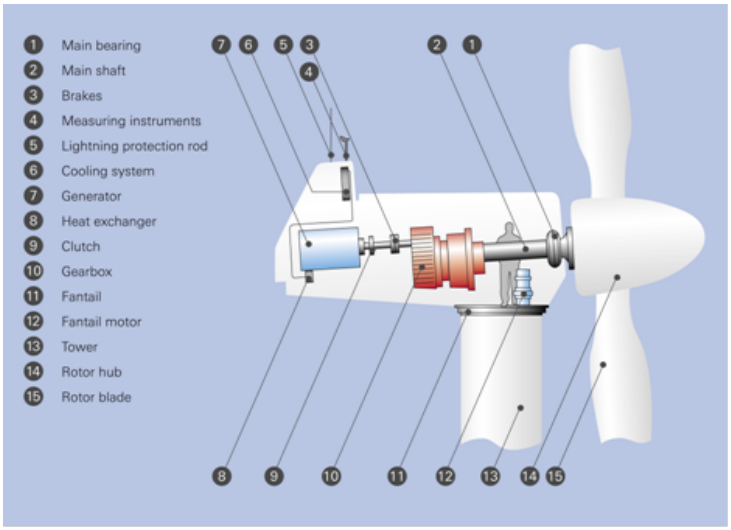

Figure 1.1: Sketch of an upwind wind turbine with two shafts, illustrating the position of the main components (source: climatetechwiki.org).

The most prominent part is the rotor assembly, made up by the blades, usually three on larger wind turbines for a matter of efficiency [1], and con-

nected to the hub. The materials which the blades are made of are usually glass fiber and carbon fiber. The total weight of a typical 40 m blade made for a 2–3 MW turbine can be of the order of 7–9 tons depending on the selected materials and internal structure. The hub is perhaps the strongest structural part of the turbine, weighing in excess of 20 tons and usually made of steel.

The hub is connected by means of a bearing to the fixed structural part of the nacelle, which also encloses the electrical generator. In most cases, the rotor is connected to the generator (or generators) by means of two shafts coupled by a drive-train, which has the function of raising the rotational speed and lowering the mechanical torque coming from the main rotor, to cope with the characteristics of the electrical part. On larger turbines this gear has often to manage a huge and unsteady mechanical power input. As a consequence, it is a critical part of the design. For this reason, on some turbines a different kind of electrical generator is installed, able to deal with large torque values and low rotational speeds, typically of the order of the rotational speed of the rotor, thus making the drive-train unnecessary. These latter turbines are called direct-drive turbines.

Typical regime values for the rotational speed of the rotor on 2–3 MW plants are of the order of 14–17 rpm, and decreasing with the size of the rotor to avoid excessive peripheral speeds. For such turbines, the gear ratio of the installed drive-trains varies with the specifications of the electrical generator, and may be of the order of 50–100.

The nacelle and rotor assembly is mounted on top of the tower, usually made of steel and based on a reinforced concrete foundation in the case of on-shore plants, and on concrete-metallic floating or non-floating bases in the case of off-shore turbines.

Given the large size and slender shape of the components and their relatively low mass, besides the rigid rotation of the rotor and shaft (or shafts for non-direct-drive models), the motion of the turbine is usually dominated by relevant deformations, interesting in particular the tower, blades and shaft (or shafts). Moreover, as the forcing effect of the wind is usually spatially non-uniform and unsteady, the resulting overall motion can be rather complicated. To limit the non-uniformity of the incoming flow due to the effect of the tower wake, the turbine is designed to work aligned with the incoming wind flow in an upwind configuration, meaning that the wind reaches the rotor before reaching the tower. This configuration has in principle the shortcoming of being unstable, as the tower head assembly tends to be twisted by the action of the aerodynamic forces around the tower axis, actually towards a stable downwind condition. To cure this stability issue, some blocking mechanical devices are mounted on the bearing connecting the tower head

assembly to the tower, keeping it oriented towards the desired direction. Today, smaller and bulkier turbines can be found still intended to work in a downwind configuration, but in this work only upwind turbines will be considered.

As stated above, the primary task of the wind turbine is to extract power from an air stream. The power associated to the flow can be expressed with the usual equation [1]

$$P_w = \frac{1}{2}\rho A U_w^3 \tag{1.1}$$

where ρ is the density of air, and A is the considered section of the flow normal to the average wind speed vector. The modulus of the latter is U_w. Considering a turbine with a rotor area of A_r, it is possible to define the extracted power as

$$P_{el_e} = \frac{1}{2}\rho A_r U_w^3 C_{P_e} \tag{1.2}$$

where the C_{P_e} factor, namely the power coefficient of the turbine, behaves in a characteristic way for a given turbine, and can be expressed basically as a function of the tip-speed ratio $\lambda = \frac{\Omega R}{U_w}$ and of the collective pitch of the blades β. This coefficient expresses the efficiency of a specific turbine with a rotor radius R to extract power from a wind flow with speed U_w, given a certain operating condition with rotor speed Ω and pitch β. It can be shown that for theoretical reasons this efficiency is limited by a superior bound of about 59% [1]. Usually, top C_{P_e} values for existing turbines can come rather close to that limit, being about 45–50% [2].

A generic bottom-level control aims at keeping the machine at an optimal value of efficiency, thus maximizing the power extracted from the wind flow while accounting for some constraints. Nowadays, all multi-MW size turbines are actively controlled by means of two scalar control inputs: collective blade pitch, meaning that all the blades receive the same input from the control system, and generator torque.

The rated wind speed U_w^{rated} is the minimum wind speed for which the turbine can work steadily at the rated power output $P_{el_e}^{rated}$. Below that wind speed the machine is typically kept close to its maximum efficiency $C_{P_e,sup}$, itself a function of a certain pitch $\beta_{C_{P_e,sup}}$ and of a given $\lambda_{C_{P_e,sup}}$ [3]. Over that wind speed, a constraint is imposed by the electrical part of the generator, by the drive-train and by the flexible and most loaded parts of the machine. For this constraint, it is necessary to scale down the power extracted with respect to the power made available by the wind flow (which grows with the third power of the wind speed), in order to avoid excessive loads or rotational speeds. This constraint is usually managed by lowering the efficiency C_{P_e} as the wind speed, and hence the input power P_w, is increasing, in order to keep

the same power output P_{el_e} for several values of the wind speed. Scaling down the efficiency term is typically obtained by raising the collective pitch [3].

On the other hand, as just pointed out, under the rated wind speed it makes sense to keep the machine at its maximum efficiency [3]. As the latter comes for a given value of pitch, for wind speeds under the rated this control is basically left unchanged. Moreover, the maximum efficiency is reached for a precise value of λ, which must be maintained for decreasing wind speeds. This in turn means that the rotational speed must be lowered linearly with the wind speed. Moreover, as the aerodynamic torque for a given pitch of the blades is roughly proportional to the wind speed U_w^2, to achieve equilibrium the generator torque must be scaled down with the wind speed too [3].

There exist two extreme wind speeds, limiting the envelope of possible working wind speeds. The cut-in wind speed U_w^{cut-in} is the minimum wind speed at which the turbine is activated, and is such that under it the efficiency is deemed too low, also due to friction and dispersion effects. The cut-out wind speed $U_w^{cut-out}$ is the top operating wind speed, over which the loads resulting from a sudden increase in the wind or failures of the control system may cause damage to the rotating components or to the most exposed structural parts of the machine.

The machine is said to work in region II when the wind speed is between cut-in and rated, while region III extends from rated to cut-out. For larger turbines, it is common to find a third operating region, basically a sub-part of region II extending from a given wind speed under the rated up to the rated, and called region II$^{\frac{1}{2}}$. In that region the turbine operates at rated rotational speed but under rated power. A more in-depth analysis of the peculiarities of the operating regions will be presented in chapter 2.

1.2 Control Systems for Horizontal Axis Wind Turbines

As stated right at the beginning of this chapter, wind turbines rely heavily on automatic control systems. Since an interest on wind power systems first appeared in the 1970s, the controllability issues related to the operation of such plants have been a constantly active research topic [4].

The lowest-order control issue, namely power tracking, was first dealt with by implementing single-input single-output (SISO) controllers able to change collective pitch to keep the correct rotational speed of the rotor, following a proportional-integral (PI) regulation logic. In order to avoid a worsening effect on loads of some structural parts of the plant, basically the shaft and

tower, whose deformations can be severely affected by a periodic oscillation of the collective pitch, attention was paid to avoid control actions at the natural frequencies of those parts. The resulting controller was typically made up by an active part, aimed at power tracking, and a passive part devoted to avoid excessive structural loading [5–10]. The use of pitch was considered for the design of the control law in region III [10, 11], while torque-based controllers were investigated for use in region II, where moreover little attention was paid to the monitoring of loads [3] mainly because of the lower control authority of the pitch input which is usually limited by a lower physical limit in that region [12].

As soon as it was realized that the effects of the aerodynamic loads due to the wind or induced by the action of controls had a non-negligible effect on the machine durability and reliability, greater attention began to be paid to the design of multiple-input multiple-output control laws, able to actively target some loads besides tracking the desired power output. In a first stage, only multiple decoupled SISO loops were considered and designed separately, each aimed at a particular target. This design approach usually accounted for a pretty low number of target loads, and often resulted in complex overall control algorithms able to account for the potential coupling effects of the various control loops [13, 14].

In order to effectively target loads deriving from the spatial non-uniformity of the incoming wind field, the use of cyclic pitch was explored, aimed at the reduction of bending loads mainly on the shaft bearings and at the root of the blades.

The appearance at the end of the 1990s of some high-order wind turbine simulators like `Bladed` [15], `FAST` [16], `SymDyn` [17] and `Cp-Lambda` [18, 19] allowed both an easier testing of more complex control laws and the synthesis of reduced models, very useful for the design of integrated MIMO controllers. Many design algorithms like LQR and H_∞ had been available since long before. They allow an integrated design of the controller in a linear framework, accounting for all the modeled couplings between all different states and controls [20–22]. Moreover, the design can be managed with straightforward operations, provided there exists a suitable linear or linearized model of the system to be controlled.

Linear models accounting for several structural states can be obtained from some of the aforementioned simulation codes [15–17], or can be set up analytically and completed with data obtained from *ad hoc* simulations [23]. The availability of high-order linearized models has made possible some experimentations with individual pitch control designed in time-domain. It has been shown how its use can be helpful in lowering the flapwise bending moments at the roots of the blades, using a coupled MIMO integrated design

considering the flapwise deflections of the blades as structural states besides the fore-aft deflection of the tower and the usual rotational speed [24–31]. Further proofing of the concept came from field testing [32, 33]. Moreover, several applications with LQR and periodically varying gains have been explored [26, 31, 34].

A simpler and smart use of individual pitch control, based on the use of the Coleman's transformation, has been investigated besides more complex integrated time-domain design techniques, working in conjunction with other control laws for trimming purposes [35–38].

Even very basic models of a wind turbine, for instance accounting only for the dynamics of the rotor, should consider a non-linear behavior with respect to the wind speed and controls, and thus with respect to the operative condition of the plant. For this reason, when dealing with MIMO control design strategies, some form of scheduling or switching between gains calculated at several linearization points is typically necessary even for simple design models. The scheduling parameter is usually selected as the wind speed itself. This approach is now common practice, but should be used with caution, as some stability issues may intervene in the case of fast variations of the scheduling parameter. For this reason, some form of filtering should be implemented when using wind sensors or observers for the measurement of wind to feed to the controller for scheduling purposes [23, 39–41], when the scheduling logic is based on interpolation between pre-calculated gains. An alternative can be that of switching between pre-stored gains without interpolation. This has been tested with a focus to application in region III [42], or in association with simpler non-LQR control design techniques [43].

A more sophisticated control design approach useful for MIMO systems, in the middle between gain scheduled linearly-designed controllers and non-linear design techniques, is linear parameter varying control (LPV). This control design algorithm is useful for non-linear systems whose non-linearity can be modeled as a dependence of the coefficients of the matrices of a linear representation of the system with respect to a given parameter. For such systems it is possible to synthesize a controller based on a cost-function optimization with linear matrix inequality constraints. The latter can be used to specify stability requirements as well as for the balancing between control authority and admitted state variability, like with the design of the LQR. The theoretical advantage of these controllers with respect to other gain-scheduled MIMO controllers lies in the guaranteed stability for any admitted value of the parameter or of its time rate.

This form of control has been applied only recently in the field of wind energy, first with a control objective limited to power tracking and damping of shaft loads [30, 44, 45]. More complex works have shown the advantages

of using multiple cost functions and considering operative regions II and III separately [46]. The basic critical issue of this design method comes from the choice of the parametrization variable, which becomes very relevant especially when dealing with larger state arrays.

More sophisticated MIMO feed-back control laws, based on neural networks, fuzzy control or sliding mode control have been tested on wind turbines [47–49]. Because of their complex design procedure, such controllers have been designed on relatively low-order systems, typically accounting for only one control input at a time, resulting in pitch-only or torque-only control laws.

A general issue when using higher-order systems for control design is the applicability of the resulting control laws in real environment. When accounting for structural states able to describe the deformation of the blades or tower it is necessary to envisage realistic ways to accurately measure these quantities in reality. Such methods are usually based on observers, which can be synthesized with time domain algorithms, typically based on the Kalman theory. For the fore-aft motion of the tower a similar observer, based on accelerometric and curvature sensors, has been tested successfully in closed loop with an LQR-based controller accounting for that structural state besides others [18, 31].

In parallel with the attention given to observers of structural states, some effort has been devoted to the characterization of the wind by a limited set of states, and to the measurement of such quantities by means of suitable wind state observers. The possibility to observe the horizontal wind speed by means of Kalman-based algorithms making use of the measured rotational speed of the rotor and its dynamic behavior, described by a first order differential equation in the rotational speed, was demonstrated in several works, where the observed quantity was used also for supervisory or gain scheduling tasks [23, 28, 50, 51]. Moreover, the definition of the dependence of the state equations involving the structural states and the rotational speed on some wind states, like the hub-height wind speed or the vertical shear, has been explored and explicitated also by linear relationships in some control synthesis tools [16, 17], where basically these wind states are considered as disturbances. The critical issue when dealing with a more complex characterization of the wind, typically making use of multiple wind states, lies in the estimation of such states, which has been found very tricky especially in turbulent conditions [52].

However, the ability to quantitatively account for the effects of some wind states on the structural states has made theoretically possible to prepare control laws suitable to reduce these generally negative effects. Some work has been done on feed-forward controllers based on the idea of counteracting the

wind disturbances by using a direct measurement of the wind, and the same matrix defining the sensibility of the turbine states with respect to the wind states to design a control gain (basically by some inversion process). These methods show good results when tried on simple simulators and without accounting for the dynamics of actuators in the design phase. Moreover, it is important that the measurement of wind – by common anemometers or observers of some kind – provide the control system with a knowledge of the instantaneous wind. All the control laws designed to make use of this wind information are basically feed-back laws [53, 54].

More recent advances in sensor technology have made possible the measurement of the incoming wind, i.e. of the wind at some distance ahead of the turbine. The LiDAR technology (Light Detection And Ranging), based on the reflection of light beams to measure the local speed of the wind, already allows to know the value of some relevant components of the wind speed vector in given positions, upwind with respect to the rotor [55].

A very simple use of the LiDAR information was based once more on simple feed-forward control techniques, making use of pre-calculated control actions scheduled with respect to the wind speed. The effect of different wind preview windows was investigated, and it was found that for a given turbine an optimal value could be used to get satisfying results for any wind speed [56–58]. A reduction on fore-aft bending and on the rotational speed error was observed. Further studies involving a similar control scheme and the use of individual pitch control to cope with measured non-uniformity of the flow scanned by the LiDAR were recently conducted [59, 60]. It was also shown how the effect of an error on the wind measurement could heavily impact the performance of the controller, causing an increase in loads instead of the desired alleviation especially in a turbulent flow [52].

Some preliminary work on reference-augmented predictive controllers or extensions of the LQR framework to make possible the use of an anticipate knowledge of the wind was carried out at a theoretical level before data about new measuring technologies were available [61, 62].

The anticipated knowledge of the wind has made possible the implementation of model predictive controllers (MPC), which make direct use of the predicted wind to calculate a control time history over a given prediction window. The control history is usually calculated as the solution of an optimization problem, which must be computed online, and which can be constrained by constraints able to account for instance for the limited actuation speed of the actuators. All these control laws involve a system propagation step, where the response of the system to the measured incoming wind and to the tentative input is evaluated. This propagation can involve a linear or non-linear model of the system, resulting in linear or non-linear MPC

algorithms.

Studies considering an MPC making use of a linearized model based on an extended set of turbine states and defined for several wind speeds and interpolated online have been conducted showing good results in deterministic wind conditions in region III, lowering tower loads and variations of the rotational speed of the rotor by applying a suitable collective pitch control [63].

A comprehensive study has been carried out for both regions II and III with a linear MPC, in deterministic and in turbulent wind conditions. Making use of accurate and complex measures – yet still realistic – of the incoming wind, the advantage on tower, shaft and blade loads was significant for deterministic gusts in region III, while less visible in turbulent wind fields or in region II. Also the necessity for a form of filtering of the wind history provided by the LiDAR was highlighted [64].

Of course, a less complex use of model predictive control laws can be based on measurements of the actual wind, obtained in the usual way through observation or direct measurement from anemometers, i.e not obtained from a LiDAR sensor. Placing some hypotheses on the future behavior of the wind given its instantaneous value, it is possible to apply the MPC algorithms, based on either a linear or non-linear model of the system, to get a control history to feed to the actuators. Some studies of this kind have shown mixed results especially in terms of blade load alleviation [18, 65].

1.3 Contributions of the Present Work and Outline

The present work is focused on two macro-areas of research: the first is related to the synthesis and testing of control laws aimed both at power tracking and alleviation of specific loads which may be of great relevance for some structural parts of the machine; the second is related to those technologies which make possible the application of such laws.

1.3.1 Research Approach

As witnessed by the cited literature – itself providing only a partial picture of what has been done – many control problems related to the operation of wind turbines have been faced at least from a theoretical viewpoint. However, many control laws have been tested typically on relatively low-order simulation tools, often without accounting for the dynamics of actuators, and usually only not systematically, i.e. with a focus on a particular operating region or on some wind condition.

Fueled by the interest of many collaborating industrial subjects, the results presented in this work reflect the great care which has been paid to the creation of realistic and applicable algorithms for control and supervision. For this reason, all the proposed algorithms have been evaluated both in deterministic and turbulent wind conditions, and without restricting the analysis to a particular operating region or another.

Moreover, a main basis of the present work has been to complete the assessment of the performance of all the considered control systems on a detailed simulator, able to describe the dynamics of the wind turbine in a very realistic way. The simulator used for all the trials presented herein is `Cp-Lambda`, a code developed internally by the Department of Aerospace Engineering of the Politecnico di Milano (DIA-PoliMi). This software, well described in [19], is a multi-body code, allowing not only a sophisticated description of the topology of a real horizontal-axis wind turbine including all the relevant rigid dynamics and those of actuators, but also making possible a very detailed finite-element based modeling of many kind of beams and deformable structures, like the blades, shaft, tower and its foundations. Moreover, it implements an array of algorithms for aerodynamic computations of growing complexity and specifically made for rotors. Additional models allow to account for inflow, tower shadow and tower dam effects. The simulator copes correctly with spatially non-uniform, three-dimensional wind fields [66], and is able to manage both deterministic and non-deterministic incoming winds. The gust (EOG) and turbulence models proposed by IEC have been used extensively in this work to test the capabilities of all control systems.

This simulator has been successfully used in collaborations with several industrial subjects and research centers not only to evaluate the performance of control systems, but also in the optimization of the design and in the exploration of the operating envelope of many horizontal-axis wind turbines. The code has been validated with respect to models assembled in well-known commercial working environments, like `Bladed` and `Adams`, the results showing the total reliability and accuracy of the code in reproducing not only the integral performance (represented for instance by the $C_{P_e} - \lambda$ curves), but also the time histories of all considered loads and of the displacements on the flexible parts, like the tower, blades and shaft (or shafts).

The use of this simulation code to analyze the results of the application of the proposed control laws and observers makes possible to apply a good level of confidence to the results. Moreover, it exacerbated some problems related to the use of individual pitch control systems in a realistic environment, in particular in turbulent wind conditions, when the use of a high-order dynamic model is pivotal to correctly reproduce the loads and deformations of the

turbine. This in turn led to the use of additional care in the design of control systems able to successfully cope with such realistic operating conditions.

The control and observation routines designed to work in association with this code have been developed and assembled in `C++` or mixed `Fortran 90/C++`. To improve the interfaceability of the resulting libraries with other existing simulation environments, as well as with real time hardwares, the usual `Bladed` control interface has been adopted. A tree of sub-libraries has been implemented, complying with the idea of modular design, and in turn allowing an enhanced industrial expendability of the control and observation software, whose parts can be distributed separately.

To guarantee a direct applicability of the code without the need for further programming effort, the designed control code implements also a supervisory system, able to deal with emergency situations, actuator or sensor failures, or to start and stop the machine based on the wind speed. All these effects, as well as the noise on the accelerometers and strain gauges when working with observation routines have always been accounted for in the present analysis.

1.3.2 Considered Turbines

Thanks to a number of collaborations of the Department of Aerospace Engineering with research groups of other Universities and with some industrial subjects, it was possible to make use of the data of some existing turbines. Moreover, as these subjects made available their simulation models, assembled in some of the commercial simulation environments suitable for model characterization and testing in an advanced design phase, it was possible to both build up the `Cp-Lambda` model of these turbines and validate the so-obtained model using results obtained from other commercial codes.

In this presentation three turbines have been considered. All share a similar global architecture, being horizontal-axis, upwind, on-shore, three-bladed, multi-Megawatt size wind turbines. All allow an individual blade pitch control and torque control.

One is a 3.0 MW machine designed by the Kangwon National University [67]. It features a rotor diameter in excess of 93 m, a tower height of about 77 m, a drive-train with a reduction ratio of about 90. This machine is certified as IEC class A, and its operating wind speed envelope goes from 3 to 25 m/sec, with a region $II\frac{1}{2}$ extending from 9 m/sec to the rated wind speed of 11.5 m/sec. The standard operating rotor speed in region III is 15 rpm. This machine has been used for the obtainment of the greatest part of the results presented herein (see chapters 2, 3, 6).

A second turbine is the classical model LTW62 by the Italian manufacturer LeitWind S.p.A. [68]. This is a direct drive machine, with a rotor

diameter in excess of 62 m, a tower height in excess of 58 m. The machine does not show a transition region. Its working envelope extends from 3 up to 25 m/sec. The rotor speed in region III is in excess of 25 rpm. A model of this plant has been used in chapter 5.

A third turbine is the Liberty C 96 model by the US manufacturer Clipper Windpower [69]. This produces a power output of 2.5 MW, with a rotor radius of about 96 m and a tower height of about 78 m. It features roughly the same wind speed envelope as the 3.0 MW machine, with somewhat different internal boundaries between the operating regions. This machine is certified as IEC class A. A model of this turbine has been used to obtain the results presented in chapter 4.

The use of different turbines is bound to the interest of the collaborating subjects in particular topics treated in the present research. Many cross-plant checks of the proposed algorithms have been performed internally, in particular when dealing with the substantial research presented in chapter 4, thus validating the proposed technologies by multiple testing on different turbines. For the sake of clarity, only results for a single turbine are presented in each chapter.

1.3.3 Treated Topics and Presentation Outline

Given the widespread use of PI control systems in industry, a considerable effort has been devoted in a first stage of the present work to quantify the advantages or disadvantages given in terms of performance on power tracking and load alleviation by LQ regulators with respect to those well known industrial systems. The results of that analysis, carried out both in IEC deterministic and turbulent wind conditions, show that the two controllers are almost equivalent from the viewpoint of the performance on mean power and power quality, while the performance on some loads is in favor of the LQR MIMO approach.

The problem of model mismatch between the reduced model used for control and the much more sophisticated multi-body code is successfully solved here by the smart addition of an integral control to the normal linearized system. It is worth notice the fact that, as shown in the next chapter, similar problems rarely show up when working in a simplified simulation environment: this highlights once more the necessity for a simulation tool to be as much realistic as possible.

As usual, the use of MIMO controllers makes the implementation of some observers a necessity. Simple Kalman-based observers of the structural states of the machine necessary for the adoption of the proposed LQ control systems are described. Moreover, as the use of observers usually brings in the need

for more sensors, which in turn makes more likely a loss of operability of a full-state feedback control systems because of sensor faults, some alternative sub-optimal LQ output-feedback algorithms have been studied. In real environment, this makes possible to prolongate the operative time of the machine even in presence of sensor faults, without renouncing to the advantages of the integrated and straightforward design typical of the LQR approach, which are indicated for a complex system like the wind turbine.

These analyses basically related the trimming problem are presented in chapter 2. It has been conducted with data of a real turbine, and fueled by many industrial subjects interested in the design, which has already found some real environment applications.

As highlighted in the previous paragraph, control systems able to account for the anticipated knowledge of the wind, which can be provided by LiDAR sensors, are being actively investigated by many research groups. In the present work a throughout comparison between two proposed predictive controllers is carried out. One controller is a classical receding horizon controller, while the second is an extension of the LQR design able to manage an exogenous input term, namely the predicted wind. It will be shown in chapter 3 how these laws can yield very similar and good results both in deterministic and turbulent wind conditions. These results further remark the usefulness of an LQR design, which by using a computationally not relevant add-on to cope with the LiDAR measurement can reach levels of performance which compare well with those of a much more computationally-heavy controller, like the receding horizon. A possible implementation of a LiDAR simulator will be shown, able to perform the same filtering action of the real thing, which is so important to get good results especially in turbulent wind fields.

Up to now, the control laws considered in the present work have been based only on collective pitch and electrical torque as inputs. As today individual pitch control is achievable on almost every large wind turbine, the large-scale use of control laws involving different pitch inputs for each blade can easily become reality. On the other hand, switching from a straightforward and well known design of the collective pitch component of the controller to a more complicated one, which in addition may be potentially less reliable and more requiring from the viewpoint of the usage of actuators, is a move not favoured by industry. In chapter 4 a smart way to deal with this constraint is presented, in the shape of a multi-layer control architecture where different and independently designed controllers operate, each toward a specific aim. Similar controllers based more or less on the same idea – modularity – have been presented in the past [35–37]: in that case the trimmer operated besides a controller targeting selected shaft loads. Here more con-

trol layers based on the use of cyclic pitch input are implemented in order to target some load components more effectively, considering in particular the distinction between deterministic and non-deterministic components. Results in IEC turbulent conditions show that some advantage can be obtained with respect to existing individual pitch control laws when targeting shaft loads. Moreover, in an alternative decentralized control configuration, a very significant performance on blade loads can be obtained, considering also here realistic turbulent wind conditions.

In the last two chapters an extensive work in the field of structural and wind observation is presented. In chapter 5 a Kalman-based approach is analyzed, starting from preliminary observations of some relevant structural states to infer the characteristics of the wind causing their variations in time. An exogenous reduced model of the turbine dynamics is used to express the effect of the considered wind states on the structural states. The resulting architecture is made up of multiple Kalman observers operating in sequence. Good observation results are obtained from the structural observers and under some conditions for a set of wind states. In chapter 6 a very effective and more robust mechanism of observation of the misalignment between the rotor axis and the incoming flow is presented. Unlike the previous approach, this observation scheme is based on a model obtained through an identification procedure from the very high-fidelity multi-body simulator. The robustness of this observer is demonstrated also in IEC turbulent wind fields.

In the last chapter 7 some critical conclusions will be presented along with some planned future activities.

1.4 Technical Note

This work is extensively based on the datasheets of real turbines provided by the aforementioned collaborating subjects. Many of these data are covered by industrial secrecy. For this reason, in this introduction and in the following chapters only a very basic description of the considered turbines is provided. Moreover, some results pertaining to critical quantities are presented in irreversible non-dimensional form.

The cited code `Bladed` is a licensed product of GL Garrad Hassan; `Adams` is a trademark and licensed software of MSC.Software Corporation; `Matlab` is a licensed product of The MathWorks, Inc.. The software `CVXGEN` is distributed under academic license by its programmers, while `FAST`, `SymDyn` and `TurbSim` are freeware codes distributed by the National Renewable Energy Laboratory (NREL). `Cp-Lambda` is a licensed product of the Department of Aerospace Engineering of the Politecnico di Milano.

Chapter 2

Collective Control for Trimming Purposes

2.1 Introduction

Wind turbines are usually designed to provide a specific power output for a given wind speed. To effectively track the desired power output corresponding to the speed of the incoming flow the implementation of an active control system is arguably the easiest way to proceed. There are several ways to synthesize a control law able to keep the output power close to the desired set point, based on different approaches (see chapter 1). Besides the existing differences, all the simplest controllers aimed at that goal make use of the collective pitch of the blades and of the generator torque as inputs, even if these are not necessarily actuated simultaneously: the span of operating wind speeds is usually divided into regions, and the use of multiple control laws, each specifically designed to give optimal performance only in one region, is rather common and often involves the use of only pitch or torque.

The use of collective pitch and torque, while well suited for trimming purposes, is not limited to the tracking of the desired power set point. Several laws have been proposed aimed at multiple control goals besides that of power tracking, based on an appropriate use of these control inputs (see chapter 1).

In this chapter a general description of the trimming problem is provided for the case of horizontal-axis wind turbines. Next a family of model-based multiple-state, multiple-input trimming control laws is presented thoroughly, showing the differences with respect to more widespread non-model-based design approaches. Exploiting the integrated MIMO design approach, based on the LQR design algorithm, it will be shown how besides the trimming action – basically the control of power output – these controllers are also

able to account for other controlled variables, providing some advantage in particular on fore-aft loads with respect to more common SISO trimmers. Moreover, these novel control laws are rather simple and robust, making possible their extensive use in the next chapters as baseline controllers operating in conjunction with more sophisticated control laws aimed at other goals, or used to keep the turbine controlled while performing tests of various observers under many different wind conditions. In the last paragraph of this chapter some results assessing the performance of the proposed MIMO trimmers will be provided. They will not show extreme differences between all the considered trimmers, the main advantages provided by a comprehensive MIMO approach being basically bound to the ease of design, which will be highlighted in the paragraphs devoted to the description of the LQR control design technique.

2.2 Regulation Strategies for Trimming Control

The main design goal for any baseline controller to be put on a wind turbine is usually the tracking of a given power setting [70]. As the power of the incoming wind stream tube goes with the third power of the instantaneous wind speed averaged over its cross section, when the wind speed changes the associated power changes too. The machine is usually rated at a given wind speed, meaning that it is designed to give the nominal power output $P_{el_e}^{rated}$ for a minimum wind speed, averaged over the rotor, equal to U_m^{rated}. Under that wind speed ($U_m < U_m^{rated}$) the power in the wind flow, weighed by the efficiency of the machine, is lower than the nominal power $P_{el_e}^{rated}$. On the other hand, for $U_m > U_m^{rated}$ the power in the flow is such that, even if weighed by the efficiency of the machine, it is greater than $P_{el_e}^{rated}$: in this second condition the turbine will be set in order to extract only a part of the power associated with the flow. A minimum wind speed U_m^{cut-in} can be defined as the wind speed under which the power that can be extracted from the flow is too low to counteract internal friction and dispersion phenomena. On the other hand, the maximum wind speed $U_m^{cut-out}$ is the wind speed over which the turbine could be subject to excessive stresses on some structural or electrical parts, especially in case of failure of the control system. The so called operative regions II and III extend from U_m^{cut-in} to U_m^{rated} and from U_m^{rated} up to $U_m^{cut-out}$ respectively.

On modern multi-MW size horizontal-axis wind turbines the array of inputs considered in the core control law used to keep the machine at an

equilibrium point in terms of the rotational speed Ω for a given wind speed U_m is made up by the generator torque T_{el_e} and the collective blade pitch β_e, where the index "e" stands for "effective" and is meant to distinguish these variables from the commanded input variables prescribed by the control system (subscript "c" in the following) but not yet filtered by the dynamics of the actuators.

The pitch value is inversely proportional to the aerodynamic force exerted by the wind flow on each blade in the direction normal to the rotor axis. As a consequence, the torque that will be extracted from the air flow will be a decreasing function of pitch, all things being equal.

In region II the power set point of the machine is under the $P_{el_e}^{rated}$ value. In this region the aim of a trimming control law is usually that of maximimizing power capture. To do that, it is common practice to leave the pitch input to a fixed value, typically that for which $P_{el_e}^{rated}$ is obtained. The aerodynamic torque is an increasing function of the wind speed for a given pitch. Given a certain wind and pitch, the demanded generator torque will be set in order to equal the aerodynamic torque and keep the turbine trimmed, i.e. in equilibrium. As the torque output of the generator is usually an increasing function of its rotational speed, the higher is the considered U_m in region II, the higher will be the set point of the rotational speed Ω, in order to generate a torque value to cope with the aerodynamic torque exerted at that wind speed. As both set points for Ω and for the generator torque increase with U_m in region II, the power output set point, bound to the product of these two factors, will increase with U_m too in that region.

In region III the machine will be regulated to the same power output for any U_m. This means that the set points for Ω and torque will usually be fixed to a given value for all wind speeds in region III. If the value of the generator torque is fixed, in order to keep the machine at the same Ω for increasing values of U_m it is necessary to scale down the value of the aerodynamic torque: this is typically achieved by increasing pitch.

For machines featuring only regions II and III the diagrams showing the regulation curves for power P_{el_e}, Ω and the control inputs as functions of U_m have the typical shape presented in Fig. 2.1.

On several larger wind turbines there exists another operating region, commonly defined as region $II^{\frac{1}{2}}$, which extends from a wind speed $U_m^{II^{\frac{1}{2}}}$ up to U_m^{rated}. For this range of wind speeds the machine is kept at the rotational speed Ω^{rated} defined for the wind speed U_m^{rated} (and for all wind speeds in region III), but with torque values which are lower than that defined for the rated wind speed. As in this region the set point for torque is lower than the rated value, the set point for pitch is prescribed in order to keep the

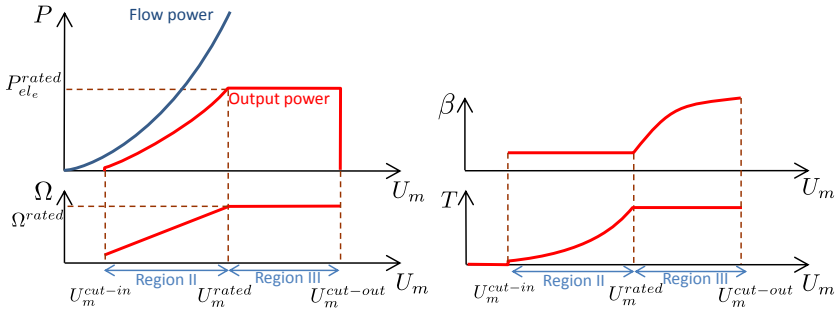

Figure 2.1: Sketch of possible set point curves for a wind turbine not featuring a transition region. All quantities expressed as functions of the wind speed. Top-left: power; bottom-left: rotor rotational speed; top-right: collective pitch; bottom-right: torque.

rotational speed at a constant value, and unlike in region II, in region II$\frac{1}{2}$ it varies with U_m.

The necessity for this region arises in most cases from noise limitations. As aerodynamics-borne noise on rotors is proportional to the peripheral speed of the lifting surfaces, which for a given rotational speed is obviously higher for larger rotors, on rather large turbines the value of the top Ω set point needs to be constrained to avoid excessive noise emission. By implementing generators able to provide different values of torque for a given value of the rotational speed, it is possible to manage this constraint without renouncing to a $P_{el_e}^{rated}$ higher than what is obtained from the product of $\Omega_{II\frac{1}{2}} T_{el}{}_{e,II\frac{1}{2}}$, that is the power associated with the rotational speed and torque defined for the lower end of region II$\frac{1}{2}$. Fig. 2.2 shows typical regulation curves for a machine featuring a region II$\frac{1}{2}$.

All these considerations can be reviewed on the characteristic $C_{P_e} - \lambda$ diagram, where the value of the power coefficient $C_{P_e} = \frac{P_{el_e}}{\frac{1}{2}\rho\pi R^2 U_m^3}$ is plotted as a function of $\lambda = \frac{\Omega R}{U_m}$ and the curves are parametrized for different collective pitch angles β_e. In these expressions R is the rotor radius, while ρ represents air density.

When the turbine operates in region II the goal is to extract the maximum power from the wind flow: that is achievable working on the supremum of the $C_{P_e} - \lambda$ diagram, at a value of $C_{P_e} = C_{P_e,sup}$. This of course corresponds to a combination of given values of β_e and λ, defined as $\beta_{e,C_{P_e,sup}}$ and $\lambda_{C_{P_e,sup}}$.

Considering a turbine without a region II$\frac{1}{2}$, the machine is usually kept at $C_{P_e,sup}$ for a range of wind speeds U_m such that $U_m^{cut-in} < U_m \leq U_m^{rated}$. As λ is kept fixed to the value $\lambda_{C_{P_e,sup}}$, the rotational speed Ω will be linearly increased with U_m in this region. As the wind speed U_m approaches the

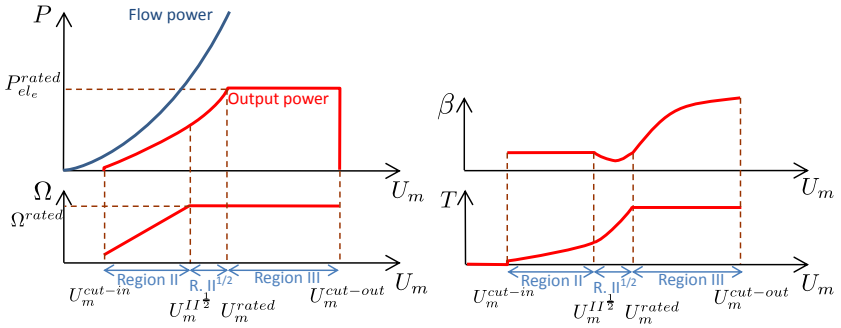

Figure 2.2: Sketch of possible set point curves for a wind turbine featuring a transition region $II\frac{1}{2}$. All quantities expressed as functions of the wind speed. Top-left: power. Bottom-left: rotor rotational speed. Top-right: collective pitch. Bottom-right: torque.

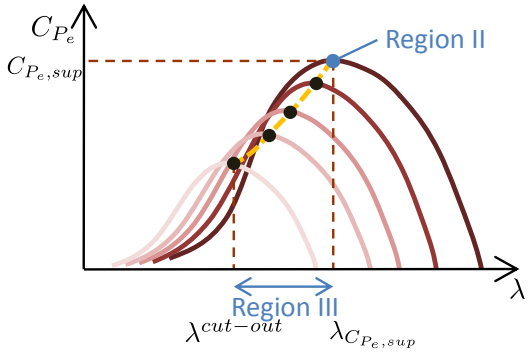

Figure 2.3: Sketch of a typical C_{P_e} regulation curve on the $C_{P_e} - \lambda$ diagram for a turbine working in regions II and III, without a transition region. Yellow dashed line: regulation curve.

rated value U_m^{rated} with fixed $C_{P_e} = C_{P_e,sup}$, the power output P_{el_e} comes closer to $P_{el_e}^{rated}$. For rated wind speed U_m^{rated} the power output $P_{el_e} = P_{el_e}^{rated}$ with $C_{P_e} = C_{P_e,sup}$. If U_m is further increased, leading into region III, the operating C_{P_e} will be decreased to a lower value to keep the power output to the same rated value $P_{el_e}^{rated}$. This is obtained by keeping $\Omega = \Omega^{rated}$, and this results in values of λ which will be progressively lower than $\lambda_{C_{P_e,sup}}$ as U_m is increased. In order to keep the desired equilibrium C_{P_e} for any given λ in region III (that is, for any U_m in region III) a suitable pitch β_e, for every given λ will be selected, usually increasing with decreasing values of λ. A sketch of a typical regulation strategy for a turbine with operating regions II and III is presented in Fig. 2.3 on a hypothetical $C_{P_e} - \lambda$ diagram.

For a turbine featuring an operating region $II\frac{1}{2}$, for a range of wind speeds

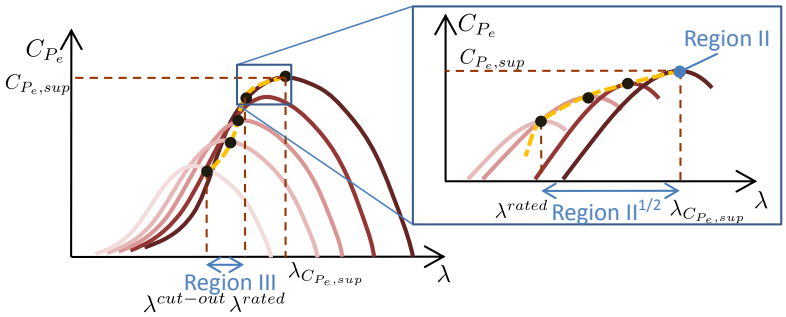

Figure 2.4: Sketch of a typical C_{P_e} regulation curve on the $C_{P_e} - \lambda$ diagram for a turbine featuring a transition region. Yellow dashed line: regulation curve.

$U_m^{II\frac{1}{2}} < U_m \leq U_m^{rated}$ the machine is kept at constant $\Omega = \Omega^{rated}$, and thus at values of λ which will decrease with the wind speed. As for these turbines the generator torque can be regulated to different set points for the same Ω, and as the imposed change in λ does not come along with the necessity to scale down the power extracted from the wind flow (as it was the case when switching directly from region II to region III), it is possible to keep the machine to the highest value of C_{P_e} achievable for any given λ in region II$\frac{1}{2}$. Given the particular shape of the $C_{P_e} - \lambda$ curves, this means that the value of β_e may also decrease with the wind speed U_m. An example of the resulting regulation curve is presented in Fig. 2.4: for those λ corresponding to region II$\frac{1}{2}$ the machine is kept trimmed at values of C_{P_e} belonging to the envelope of the maxima of C_{P_e}, visible on the $C_{P_e} - \lambda$ diagram.

2.3 Trimming Control Laws

As previously stated, the trimming controller keeps the machine trimmed around a given Ω set point, depending on the value of the incoming wind, by means of appropriate pitch and torque settings [70]. The measure of the incoming wind is necessary to select the reference for the rotational speed Ω, which is the actual controlled variable. This may be obtained from simple and widespread cup or ultrasound anemometers, suitably placed on or ahead of the machine. As shown in [23,50,71] and described in later chapters (5, 6), an estimation of some characteristic states of the wind can be carried out also based on suitable observers.

It should be noted that the goal of the trimmer is that of keeping the machine close to a given power set point. Typically, the power output is measured as the product of the rotational speed of the generator multiplied

by the generator torque, hence the necessity to control the rotational speed of the rotating part of the turbine in order to control the power output. This rotational speed may be defined as that of the rotor (or low speed shaft) or that of the generator (or high speed shaft). The two shafts are usually connected by a drive-train incorporating a gearbox with a fixed gear ratio, so that the knowledge of one rotational speed implies the knowledge of the other. On some machines, equipped with particular permanent-magnets generators, the electrical part rotates at low rotational speeds and produces high values of torque: for these machines, where the rotor and the generator are connected without a gearbox (direct drive configuration), the rotor rotational speed is only one and univocally defined.

Many rather widespread trimmers account for the operative regions of the machine applying different control laws for each of them. Usually, the basic idea behind these controllers is that of trimming only by means of the generator torque in region II and of collective pitch in region III. In transition region $\mathrm{II}^{\frac{1}{2}}$ both controls are used for power regulation: in this region with most controllers the Ω reference is changed between two extreme values corresponding to the set points defined for the lower wind speed $U_m^{II^{\frac{1}{2}}}$ and for U_m^{rated}, according to the value of the wind speed [3]. Sometimes, besides the normal operating regions II, $\mathrm{II}^{\frac{1}{2}}$ and III, there exists a region below cut-in wind speed where the controller which manages the start-up of the turbine regulates torque most like in region $\mathrm{II}^{\frac{1}{2}}$, changing the reference for Ω between zero and the minimum design value envisaged for operations in region II. Being used for start-up, this branch of the control scheme – when present – is not part of the core control algorithm applied in normal power production conditions.

The main advantage of this formulation is the simple tuning of the gain parameters, as the control law implemented in each of the considered regions can be a very simple PI controller, basically designed on a SISO system, as only one control is used at a time and the controlled variable is only one. More sophisticated controllers of the same kind make use of gains scheduled as functions of U_m.

The most obvious shortcoming is the resulting global architecture of the controller, which paradoxically is not so straightforward, as multiple control laws have to be implemented aimed at the same control goal. Moreover, some roughness of the time histories of the demanded control can be expected when the turbine is operating in real environment (and so with ever changing wind) close to those wind speeds for which a switch between two control laws is scheduled (usually close to $U_m^{II^{\frac{1}{2}}}$ and U_m^{rated}). To avoid excessive loads resulting from a coarse control action in proximity of those wind speeds,

it is necessary to envisage a switching or blending logic between the controllers designed for each region. The same is true at the end of the start-up manoeuvre, when changing the regulation logic between start-up and power production in lower region II. This in turn makes the overall design even more complex [43].

In the following chapters two such controllers are considered as references for the performance assessment of other control laws. They are similar to one another, and both have been designed to provide a control capability in region $II^{\frac{1}{2}}$.

In the first, tailored to control a 3.0 MW three-bladed turbine featuring a region $II^{\frac{1}{2}}$ (see chapter 1), the pitch control is kept constant for wind speeds below $U_m^{II^{\frac{1}{2}}}$, while for wind speeds in region $II^{\frac{1}{2}}$ and III it is regulated using a PI control law based on the feedback of Ω. The torque control is calculated differently depending on the rotational speed of the rotor. The control system activates the machine at the rotational speed Ω^{cut-in}. As usual in region $II^{\frac{1}{2}}$ and III the turbine is kept at a constant value of rotational speed, Ω^{rated}. A further Ω^{limit} is defined in this control architecture as the mean value $\Omega^{limit} = \frac{1}{2}(\Omega^{cut-in} + \Omega^{rated})$. Now, in the region defined as $\Omega^{cut-in} \leq \Omega \leq \Omega^{limit}$ the torque control is obtained from a simple PI controller based on the feedback of the difference (error) between the rotor speed and a reference value set to Ω^{cut-in}. Moreover, the obtained torque value is limited between a null value and the characteristic torque value for the considered rotational speed of the generator. In the complimentary region defined as $\Omega^{limit} < \Omega \leq \Omega^{rated}$ the torque control is computed once more based on the error of the rotational speed, this time calculated with respect to Ω^{rated}. The torque control is then limited between the characteristic value of the generator for the considered Ω and the rated value.

The scheme just described is presented synthetically in Fig. 2.5.

The second controller was designed for a 2.5 MW turbine, featuring a region $II^{\frac{1}{2}}$ (see chapter 1). In this control architecture, as in the previous one, the pitch input is kept fixed when the turbine operates under the rated wind speed U_m^{rated}, and it is regulated by a PID based on the feedback of the error between Ω and Ω^{rated}. The torque control is calculated for any condition evaluating an analytical function of Ω and of the pitch input. This controller is actually in use on real turbines.

A different approach to the design of the trimmer, implemented as described in [23] and further developed in this work, is based on a MIMO approach and on the LQR theory for the synthesis of the control law [41]. Differently from the previous one, this kind of approach causes the need for a suitable reduced model to be used to actually synthesize the control law.

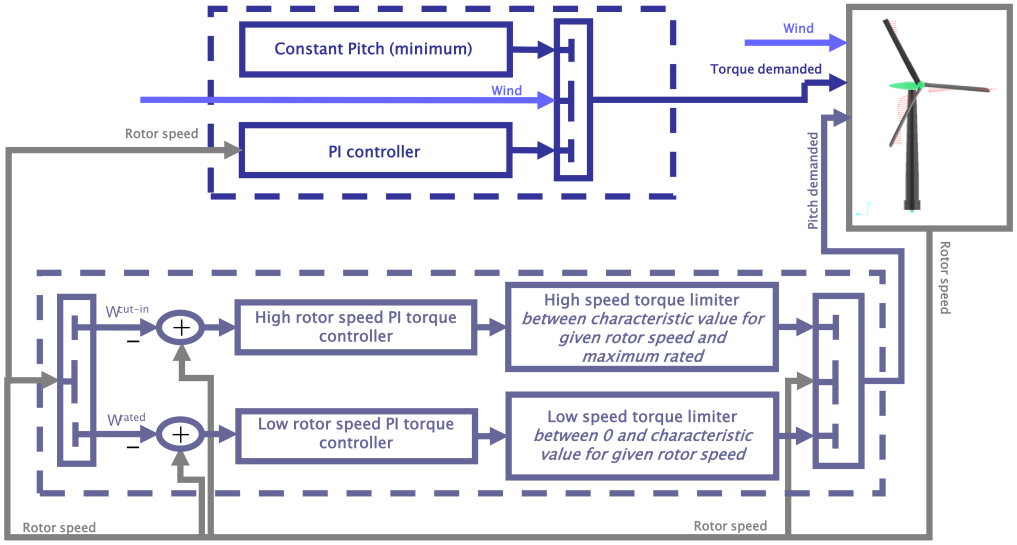

Figure 2.5: Industrial PI-based control scheme for the regulation of the rotational speed for a 3.0 MW turbine featuring a transition region.

Taking full advantage of the LQR control architecture, it is possible to consider a set of states (not only Ω) and dynamic equations able to describe in greater detail the behavior of the machine. The considered equations are that expressing the dynamic equilibrium of the rotor, written in terms of Ω, an equation for the fore-aft dynamics of the tower and more equations for the dynamics of the generator and pitch actuators, all included in the reduced model.

The extremely straightforward LQR-based control scheme is presented in Fig. 2.6.

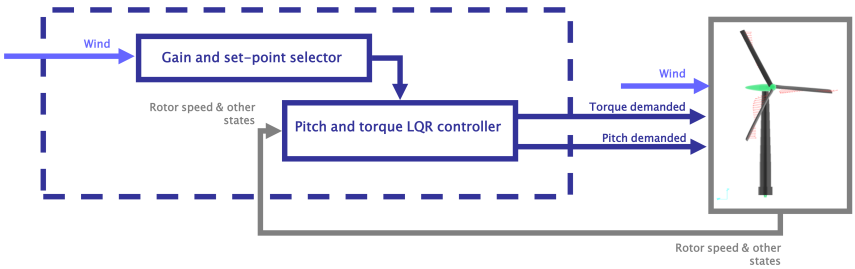

Figure 2.6: Proposed LQR control scheme.

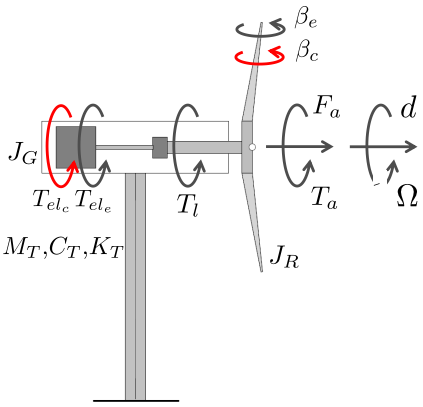

Figure 2.7: Scheme of the reduced model considered for the synthesis of the LQR control law.

2.3.1 Full-State Feedback LQR Controller

Consider the simplified scheme in Fig. 2.7, where the variables considered in the reduced model are graphically described. The considered set of states is composed by the fore-aft displacement of the tower head, d, and its time derivative $\dot{d}$; the rotor rotational speed Ω measured on the low speed shaft (as stated above, there is always a linear kinematic relationship between this and the rotational speed of the high speed shaft); the measured pitch angle β_e, which is the same for all three blades, and its time derivative $\dot{\beta}_e$; finally, the measured generator torque T_{el_e}.

The array of the inputs is made up by the demanded collective pitch β_c and electrical torque T_{el_c}.

The aerodynamic loads considered in the reduced model are only due to the rotor-flow interaction (no aerodynamics of the tower or nacelle), and the corresponding global action measured at the hub is given by the aerodynamic force F_a and torque T_a. The rotor-shaft assembly has a rotational inertia J_R, while that of the generator is J_G. The loss of torque due to effects of mechanical friction is modeled by the torque load term T_l.

Finally, let M_T, C_T and K_T be the mass, damping and stiffness respectively for a second order system modeling the fore-aft dynamics of the tower head, based on a modal description of the tower dynamics truncated at the first mode.

Based only on these actors, it is possible to write the following system of

equations for the reduced model:

$$(J_R + J_G)\dot{\Omega} + T_l(\Omega) + T_{el_e} - T_a(\Omega, \beta_e, U_w - \dot{d}, U_m) = 0 \tag{2.1}$$

$$M_T\ddot{d} + C_T\dot{d} + K_T d - F_a(\Omega, \beta_e, U_w - \dot{d}, U_m) = 0 \tag{2.2}$$

$$\ddot{\beta}_e + 2\xi\omega\dot{\beta}_e + \omega^2(\beta_e - \beta_c) = 0 \tag{2.3}$$

$$\dot{T}_{el_e} + \frac{1}{\tau}(T_{el_e} - T_{el_c}) = 0. \tag{2.4}$$

The first is a second order equation for the rotational dynamics of the rotor. The second is the aforementioned tower fore-aft dynamic equation. The last two are implemented to model the dynamics of the actuators: a second order equation for the pitch actuator and a first order equation for the generator (torque actuator). The actuators usually feature very different filtering behaviors, as the pitch actuators are generally slow, with a characteristic frequency of 1–1.5 Hz for turbines with a rotor diameter of 90 m, while the torque actuator usually reacts with time constants of the order of the hundredths of a second.

Notice that the aerodynamic loads T_a and F_a in Eq. (2.1) and (2.2) depend on several terms: the rotational speed Ω, the measured pitch β_e, the wind speed U_m, defined as the axial speed averaged over the rotor and over a suitably large time frame (the meaning of this definition will be clarified shortly) and the relative speed between the incoming flow and the tower head $(U_w - \dot{d})$. The wind speed can be defined as $U_w = U_m + U_t$, meaning that the rotor-averaged instantaneous axial wind can be defined as the sum of a time-averaged value U_m and a zero-mean oscillatory term U_t, representing the turbulent fluctuation. Following a filtering action on the value of the measured U_w, the value of U_m is found, while the fluctuating part U_t is eliminated.

The reason for the choice of this set of variables to express the dependence of the aerodynamic force and moment from the incoming wind field can be clarified recurring to the widely used definition for the aerodynamic torque and force exerted on the rotor, involving the non-dimensional force and torque coefficients C_{F_e} and C_{P_e}, where R is the radius of the rotor:

$$T_a = \frac{1}{2}\rho\pi R^3 \frac{C_{P_e}(\lambda, \beta_e, U_m)}{\lambda}(U_w - \dot{d})^2 \tag{2.5}$$

$$F_a = \frac{1}{2}\rho\pi R^2 C_{F_e}(\lambda, \beta_e, U_m)(U_w - \dot{d})^2. \tag{2.6}$$

The aerodynamic thrust force and aerodynamic torque are both related to the square of the actual wind speed seen by the rotor, which is the difference $(U_w - \dot{d})$. Also the tip speed ratio λ can be defined as a function of the relative

wind speed, as $\lambda = \Omega R/(U_w - \dot{d})$. The non-dimensional coefficients can be expressed as functions of only β_e and λ, provided the rotor is rigid. To take into account the deformability of the rotor and its effect on the relationship between C_{F_e} and λ, and between C_{P_e} and λ, it is useful to explicitly account for the average wind speed U_m. Typically, when the wind speed increases the blades get deformed and bent downwind. As a result, the global rotor area is changed, resulting in a change of the aforementioned relationships between the coefficients and the usual λ and β_e. Of course, this level of complexity is justified for larger rotor areas and for slender, deformable blades. For small rotors and smaller deformations, it is not necessary to account for these effects.

It is clear that equations (2.1) and (2.2) are nonlinear in the forcing terms, as they depend on $\dot{d}$ and Ω. This nonlinear reduced model can be easily linearized for a given equilibrium condition, defined by a given state and input set point corresponding to an assigned value of the wind speed U_m. In analytical terms, a trim condition is defined by a reference $\{\boldsymbol{x}^*, \boldsymbol{u}^*, U_m^*\}$, the turbulent fluctuation having been set to zero, $U_t = 0$. Under the latter hypothesis, the nonlinear system (2.1–2.4) can be rewritten in the form

$$\dot{\boldsymbol{x}} = \boldsymbol{f}(\boldsymbol{x}, \boldsymbol{u}, U_m), \tag{2.7}$$

where the state array is defined as $\boldsymbol{x} = (d, \dot{d}, \Omega, \beta_e, \dot{\beta}_e, T_{el_e})^T$ and the input array $\boldsymbol{u} = (\beta_c, T_{el_c})$. This can be linearized to give a form like

$$\Delta\dot{\boldsymbol{x}} = \boldsymbol{A}(\boldsymbol{x}^*, \boldsymbol{u}^*, U_m^*)\Delta\boldsymbol{x} + \boldsymbol{B}(\boldsymbol{x}^*, \boldsymbol{u}^*, U_m^*)\Delta\boldsymbol{u}, \tag{2.8}$$

where $\Delta\boldsymbol{x} = \boldsymbol{x} - \boldsymbol{x}^*$ and $\Delta\boldsymbol{u} = \boldsymbol{u} - \boldsymbol{u}^*$.

Notice that in practice the linearization can be completed following a differentiation of the system (2.1–2.4), but to find the actual values of the coefficients of the $\boldsymbol{A}$ and $\boldsymbol{B}$ matrices it is necessary to know the derivatives $\frac{\partial C_{T_e}}{\partial \boldsymbol{x}}$, $\frac{\partial C_{T_e}}{\partial \boldsymbol{u}}$, where the torque coefficient C_{T_e} is by definition $C_{T_e} = \frac{C_{P_e}}{\lambda}$, and similar derivatives for C_{F_e}. Provided the characteristics C_{P_e} (and hence C_{T_e}) and C_{F_e} are available as punctual functions of λ and β_e for the considered machine, from experiments, theory or from simulations in a virtual environment, these derivatives can be calculated numerically. This is the procedure followed in this work, where the characteristic coefficients are known punctually on a dense matrix of λ and β_e, from simulations performed with `Cp-Lambda`.

It is important to realize that the linearization is performed for a given value of U_m. Obviously, the values of the coefficients of the linearized system must be evaluated for several U_m covering the span between U_{cut-in} and $U_{cut-off}$. As a result, for each trim point selected for the design of the controller, the linearized system can be written as

$$\Delta\dot{\boldsymbol{x}} = \boldsymbol{A}(U_m)\Delta\boldsymbol{x} + \boldsymbol{B}(U_m)\Delta\boldsymbol{u}, \tag{2.9}$$

where $\Delta\boldsymbol{x} = \boldsymbol{x} - \boldsymbol{x}^*(U_m)$ and $\Delta\boldsymbol{u} = \boldsymbol{u} - \boldsymbol{u}^*(U_m)$.

The theory of LQR is based on the minimization of the cost function

$$J = \frac{1}{2}\int_0^\infty \left(\Delta\boldsymbol{x}^T\boldsymbol{Q}\Delta\boldsymbol{x} + \Delta\boldsymbol{u}^T\boldsymbol{R}\Delta\boldsymbol{u}\right)\,\mathrm{d}t \tag{2.10}$$

over an infinite time horizon, imposing the dynamics of the linearized system as a constraint. With this cost function and this shape of the linearized system, the optimal control solution can be obtained in closed form for a given U_m as

$$\Delta\boldsymbol{u} = -\boldsymbol{R}^{-1}\boldsymbol{B}^T\boldsymbol{P}\Delta\boldsymbol{x}, \tag{2.11}$$

where $\boldsymbol{P}$ solves the algebraic Riccati equation

$$\boldsymbol{P}\boldsymbol{A} + \boldsymbol{A}^T\boldsymbol{P} - \boldsymbol{P}\bar{\boldsymbol{R}}\boldsymbol{P} + \boldsymbol{Q} = 0, \tag{2.12}$$

and $\bar{\boldsymbol{R}} = \boldsymbol{B}\boldsymbol{R}^{-1}\boldsymbol{B}^T$.

In real environment, the gain matrix $\boldsymbol{K} = \boldsymbol{R}^{-1}\boldsymbol{B}^T\boldsymbol{P}$ and the reference state and input arrays $\boldsymbol{x}^*$ and $\boldsymbol{u}^*$ are stored and available for a number of U_m^* between cut-in and cut-out. As previously explained, the actual value of U_m is obtained online from the U_w signal coming from the anemometer on top of the machine (or from a similar sensor or observer), filtered to exclude the turbulent component U_t. Usually in this work a moving average filter is used, with a time window of 30 sec. Based on the instantaneous value of U_m, it is possible to linearly interpolate between the closest available stored values of both the gains and the references [23]. Following this procedure, at every control instant it is possible to find the control input as

$$\boldsymbol{u} = -\boldsymbol{K}(U_m)(\boldsymbol{x} - \boldsymbol{x}^*(U_m)) + \boldsymbol{u}^*(U_m). \tag{2.13}$$

Notice that following this control approach switching from a control law to another when passing from an operating region to another is totally unnecessary.

Moreover, by an appropriate use of the weights $\boldsymbol{Q}$ and $\boldsymbol{R}$, which can be tuned as functions of the wind speed U_m ($\boldsymbol{Q}(U_m)$ and $\boldsymbol{R}(U_m)$), it is possible to customize the behavior of the controller with respect to the operating speed. This feature can be used for instance to limit the pitch input β_c when working at low wind speeds, where in turbulent wind a pitch history prescribed by the controller may be not actuated, because of pitch range constraints. On the other hand, at higher wind speeds (region III) the torque input T_{el_c} may be limited by means of a higher weight on that control input to avoid excessive oscillations on power output.

As already stated above, notice that thanks to the LQR approach, which is an extremely advantageous control solution for MIMO systems, besides

the obvious weight on Ω, necessary as a mean to control power output, it is also possible to impose weights on the fore-aft motion of the tower, usually resulting in a lower tower-base fore-aft bending moment. Obviously, this advantage comes at the cost of the necessity for more sensors. In particular, as the displacement of the tower cannot be measured directly, a way of observing it must be envisaged. To this end it is possible to deploy a Kalman-based observer, based on one accelerometric and one strain measurement (see chapter 5 for a detailed description of a possible observer of this kind). The sensors required for these measurements are not difficult to implement, and are often present at least on larger machines. Nonetheless, a greater number of sensors implies an increased probability of sensor failures, which must be dealt with to guarantee the robustness of the trimmer in real environment. A way to do that is described in a following paragraph.

Finally, by taking into account also the dynamics of the actuators, the control solution is calculated with a knowledge of their characteristic delay, resulting in a more prompt behavior of the actual control β_e and T_{el_e}. Notice that, as long as only collective pitch is used, a single pitch actuator can be accounted for in the design, instead of three.

2.3.2 Full-State Feedback LQR Controller with Integral State

The reduced model, even if sophisticated and able to account for a number of dynamics, is an approximation of the real thing. Moreover, the characteristic coefficients C_{F_e} and C_{T_e} are usually measured or estimated from suitable models, and then affected by errors. One of the visible results of such an error shows up in the definition of the linearization conditions. The trim condition $\{\boldsymbol{x}^*, \boldsymbol{u}^*, U_m^*\}$, chosen as a reference for the machine on the basis of an approximated model, may be not an equilibrium condition on the real machine, because of the errors brought in by the characteristic coefficients C_{P_e} and C_{F_e} used to define the trim point in the design phase. As a result, a control law trying to keep the machine at that trim point may not succeed in perfectly trimming the machine at the correct pitch, torque and rotational speed even for a constant value of $U_w = U_m^*$.

The problem may be worsened by a not smart tuning of the weights.

The most apparent result of this control problem, which is basically due to a model mismatch between reality and the reduced model or a part of it (as explained above, the values of force and torque coefficients included in the reduced model may be affected by errors), is usually an incorrect average power output. This is due to the fact that both states and controls are not

kept to the desired set point.

To address this problem an elegant solution was envisaged and tested with good results. This is based on the adoption of a new state, defined as $\int \Omega \, \mathrm{d}t$, and used to augment the state array, which can be redefined as $\boldsymbol{x}_{aug} = (d, \dot{d}, \Omega, \beta_e, \dot{\beta}_e, T_{el_e}, \int \Omega \, \mathrm{d}t)^T$. Operating directly on the linearized system, the new linearized state equation can be written as

$$\Delta \dot{\boldsymbol{x}}_{aug} = \boldsymbol{A}_{aug}(\boldsymbol{x}^*, \boldsymbol{u}^*, U_m^*)\Delta \boldsymbol{x}_{aug} + \boldsymbol{B}_{aug}(\boldsymbol{x}^*, \boldsymbol{u}^*, U_m^*)\Delta \boldsymbol{u}, \tag{2.14}$$

where

$$\boldsymbol{A}_{aug}(\boldsymbol{x}^*, \boldsymbol{u}^*, U_m^*) = \begin{bmatrix} & & & & & & \\ & & & & & & \\ & & & & & & \\ & \boldsymbol{A}(\boldsymbol{x}^*, \boldsymbol{u}^*, U_m^*) & & & & & \\ & & & & & & \\ & & & & & & \\ \begin{bmatrix} 0 & 0 & 1 & 0 & 0 & 0 \end{bmatrix} & & & & & & 0 \end{bmatrix}$$

and

$$\boldsymbol{B}_{aug}(\boldsymbol{x}^*, \boldsymbol{u}^*, U_m^*) = \begin{bmatrix} \boldsymbol{B}(\boldsymbol{x}^*, \boldsymbol{u}^*, U_m^*) \\ \begin{bmatrix} 0 & 0 \end{bmatrix} \end{bmatrix}.$$

It is important to notice that there is no need to calculate any new coefficients with respect to the previous writings of the state equation, based on the original set of states. Also, from the viewpoint of implementation the only new feature is the presence of the integral state, which must be calculated and updated at every control time step. This can be done accounting for a time window of the order of the tens of seconds (30 sec has been used throughout this work) and evaluating the integral over a finite buffer of measures of Ω, using a suitable numerical method, like for instance the trapezoidal rule.

The equations of the linearized system based on the augmented state array can be used to set up an optimal control problem like that previously described for the matrices not accounting for the integral state on Ω, following the LQR approach, obtaining a gain matrix for any considered wind speed.

The results of this implementation are compared in the paragraph at the end of this chapter to the results of the basic LQR control described above.

2.3.3 Output Feedback LQR

In all previous considerations the availability of measurements of all the states required for control was implicitly hypothesized (full-state feedback). In order to make a controller able to manage the breakdown of some sensors it is

possible to implement a hierarchy of control laws able to control the machine to the best of its possibilities based on the array of available measures. Without renouncing to an integrated design technique, very useful when working with MIMO systems, it is possible to forget about some of the dynamics of the system, rewriting a reduced model without some of the equations, redesigning the gain matrix on a system with less dynamic equations.

A more elegant approach is constituted by the implementation of an output feedback controller [72]. For the LQR approach it is easy to switch from a full-state feedback to an output feedback, the difference being only the definition of a suitable rectangular matrix $\boldsymbol{C}$ such that $\boldsymbol{y} - \boldsymbol{y}^*(U_m) = \boldsymbol{C}(\boldsymbol{x} - \boldsymbol{x}^*(U_m))$. Obviously, the matrix will select only those states which are available out of the array $\boldsymbol{x}$ in any given fault scenario.

The optimal output-feedback gain matrix $\hat{\boldsymbol{K}}$, such that

$$\Delta\boldsymbol{u} = -\hat{\boldsymbol{K}}(U_m)\Delta\boldsymbol{y}, \tag{2.15}$$

comes from the solution of the optimization problem based on the cost function

$$\begin{aligned} J &= \frac{1}{2}\int_0^\infty \left(\Delta\boldsymbol{x}^T\boldsymbol{Q}\Delta\boldsymbol{x} + \Delta\boldsymbol{u}^T\boldsymbol{R}\Delta\boldsymbol{u}\right)\,\mathrm{d}t \\ &= \frac{1}{2}\int_0^\infty \left(\Delta\boldsymbol{x}^T\boldsymbol{Q}\Delta\boldsymbol{x} + \Delta\boldsymbol{y}^T\boldsymbol{C}^T\hat{\boldsymbol{K}}^T\boldsymbol{R}\hat{\boldsymbol{K}}\boldsymbol{C}\Delta\boldsymbol{y}\right)\,\mathrm{d}t \\ &= \frac{1}{2}\int_0^\infty \left(\Delta\boldsymbol{x}^T\boldsymbol{W}(\hat{\boldsymbol{K}})\Delta\boldsymbol{x}\right)\,\mathrm{d}t. \end{aligned} \tag{2.16}$$

A typical fault situation where this control law may be of great use is constituted by a fault in the sensors needed for the observation of the tower motion. In that scenario, the matrix $\boldsymbol{C}$ will select the states different from d and $\dot{d}$ out of the array $\boldsymbol{x}$, thus taking the shape

$$\boldsymbol{C} = \begin{bmatrix} 0 & 0 & 1 & 0 & 0 & 0 \\ 0 & 0 & 0 & 1 & 0 & 0 \\ 0 & 0 & 0 & 0 & 1 & 0 \\ 0 & 0 & 0 & 0 & 0 & 1 \end{bmatrix}$$

so that given the state array $\boldsymbol{x} = (d, \dot{d}, \Omega, \beta_e, \dot{\beta}_e, T_{el_e})^T$ previously defined, the resulting output would be $\boldsymbol{y} = (\Omega, \beta_e, \dot{\beta}_e, T_{el_e})^T$.

Unlike the full-state feedback problem, this optimization, subject to the linearized system dynamics, does not yield a closed form solution. A rather straightforward iterative method to find the optimal $\Delta\boldsymbol{u}$ has been found in [73] and applied (the procedure for the synthesis of the gains is summarized in appendix B).

A shortcoming of this approach is the absence of a solution for the linearized system based on the augmented state array accounting for the integral of Ω. This is due to some rank requests on the characteristic matrices of the system, imposed by the iterative method, which are not satisfied by $\boldsymbol{A}_{aug}$ and $\boldsymbol{B}_{aug}$.

The results which can be expected from this controller on the loads are obviously less good than those obtained in a full-state feedback scenario [31]. Moreover, lacking the integral state on Ω, this system may be rather inaccurate in maintaining the machine close to the trimmed condition.

2.4 Results

The purpose of this paragraph is to show a comparison between three trimming control laws. The first is a typical industrial PI control law, described previously in this chapter. The second is the full-state feedback LQR presented above. The third is the LQR accounting for the integral of Ω. Several simulations were carried out on the `Cp-Lambda` model of the 3.0 MW three-bladed horizontal-axis wind turbine.

In order to assess the performance of these controllers, a deterministic wind condition was considered first. The selected time history of the wind was that of an EOG-1-year gust as specified by the normative IEC [74]. A set of simulations was performed on the `Cp-Lambda` model of the turbine at three reference wind speeds U_m of 7, 15 and 21 m/sec. In a gusty wind condition what is expected from the trimmer is to keep the oscillation of the rotational speed as limited as possible, by fastly reacting to the marked gradient of the wind speed. The action of the trimmer should also restore the machine to the correct reference speed shortly after the gust is over. A correctly tuned trimmer will react by means of an as-fast-as-possible increase in pitch and torque while the wind is increasing, and with a fast reduction after the wind peak has been left behind.

In Fig. 2.8 the time histories of the rotational speed Ω obtained with the considered trimmers are reported for a gust at reference speed 15 m/sec. It is noteworthy that the PID and the LQR with augmented state are almost undistinguishable, while a problem in maintaining the reference value of Ω in the constant wind condition experienced before the gust is noticeable with the standard LQR. This highlights the importance of the integral component of the state array, which corrects this problem.

Fig. 2.9 shows the behavior of the control inputs β_e and T_{el_e} for the EOG-1-year at 15 m/sec. A greater load on the pitch actuator is associated to the use of the augmented LQR.

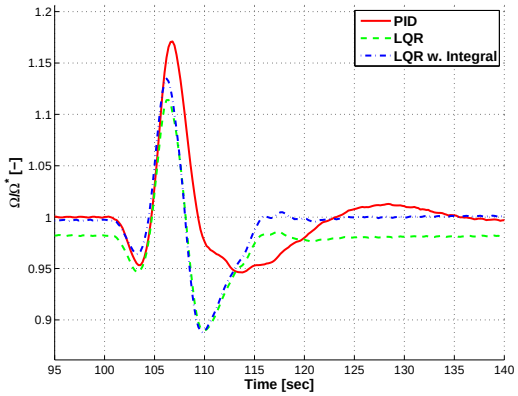

Figure 2.8: Normalized time history of the rotor rotational speed Ω corresponding to an IEC gust of 15 m/sec. Performance comparison between a PI, an LQR and an LQR with an augmented state array.

To this extent, the performance of the PI and augmented LQR look very close to each other.

In Fig. 2.10 the performance of the controllers in terms of mean rotor rotational speed and standard deviation is presented for turbulent wind conditions: each point on these plots is obtained from a simulation lasting 600 sec, performed in turbulent wind of category A [66, 74]. Here it is clear how the LQR with the augmented state array works well both in terms of keeping the machine trimmed to the correct set point Ω^* and of damping the oscillations which would result in an increase in standard deviation of the rotational speed, and thus of power output. This is true except for very low wind speeds.

Keeping the turbine closer to the set point for Ω helps getting the expected value of power output. In terms of power quality the two LQR control systems show very similar performance (Fig. 2.11), while that of the PI is somewhat worse.

The advantage of an integrated control approach like the LQR is clearly visible on those states which are not taken into account in the PI design, focused only on the tracking of the rotational speed Ω. On Fig. 2.12 the performance of the three trimmers on the damage equivalent load (DEL) calculated from the fore-aft moment at the tower base is presented for many simulations in turbulent wind conditions. DELs have been computed by using rainflow analysis as

$$M_{\mathrm{DEL}} = \Big(\sum_i \Delta M_i^m N_i / N_{\mathrm{tot}} \Big)^{1/m}, \tag{2.17}$$

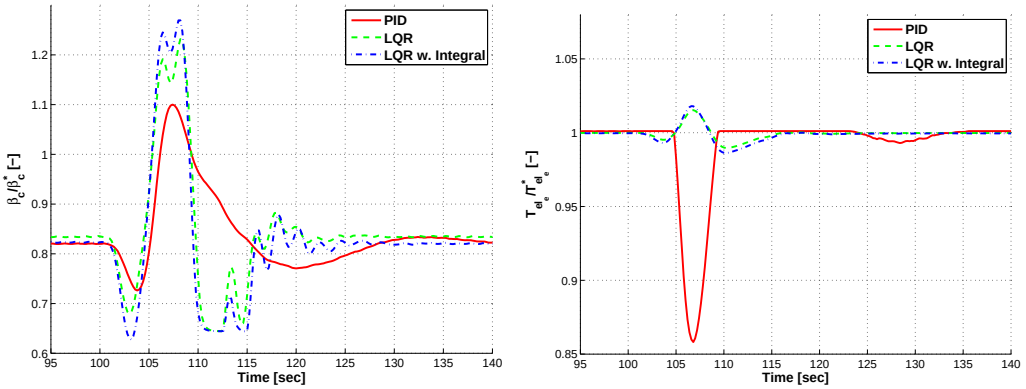

(a) (b)

Figure 2.9: Normalized time histories of pitch β_e (left) and torque T_{ele} (right) controls corresponding to an IEC gust of 15 m/sec. Performance comparison between a PI, an LQR and an LQR with an augmented state array.

ΔM_i being the ith cycle amplitude, N_i the number of cycles at the ith amplitude, and N_{tot} the total number of cycles. For the S-N fatigue slope of the material, labeled m in the previous equation, the value $m = 3.5$ was used for evaluating the tower loads since this is a typical value for steel structures. Notice that while the two LQRs are rather similar, their performance is clearly better than that obtained with the PI.

2.5 Conclusions

The aim of the comparison presented in this chapter was to show the practical equivalence of an industrial PI controller and an LQR with respect to turbine power tracking. To complete such a comparison, it was possible to make use of a typical industrial design based on a PI regulation logic and a basically SISO design approach in region II and III and a smart form of blending in region II$\frac{1}{2}$. On the other hand, the presented LQR has been designed on a set of dynamic equations describing the fore-aft motion of the tower head, the motion of the rotating assembly of the turbine, and the dynamic behavior of the actuators. The reduced model was formulated analytically, and completed with coefficients coming from *ad hoc* simulations performed in `Cp-Lambda`. Also the linearization was performed analytically, and a gain matrix was obtained for many reference conditions between the cut-in and cut-out wind speeds, thus embracing all the operating regions without distinction in the control design technique. In order to make possible the use of

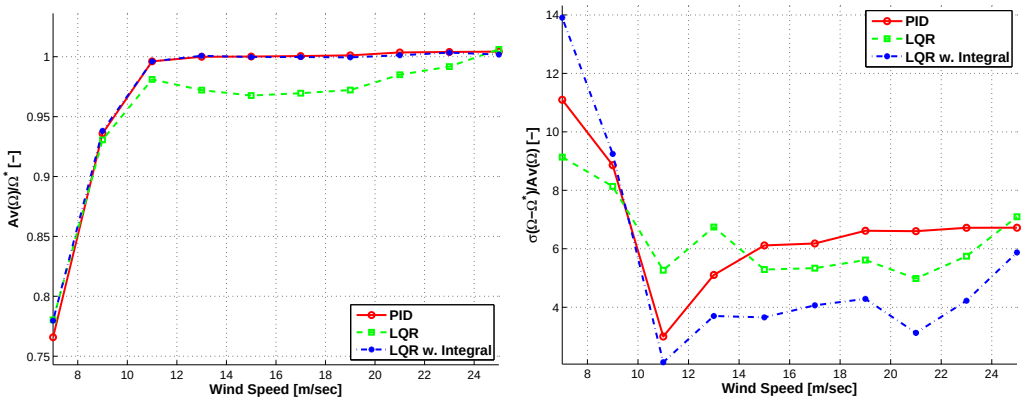

(a) (b)

Figure 2.10: Normalized average $\mathrm{Av}(\Omega)$ (left) and standard deviation $\sigma(\Omega - \Omega^*)$ (right) of the rotational speed Ω for 600 sec IEC turbulence A simulations performed at different reference wind speeds. Performance comparison between a PI, an LQR and an LQR with an augmented state array.

the LQR law it was necessary to implement an observer for the motion of the tower head. Such observer was not described here, but will be thoroughly presented in chapter 5.

The first comparisons on a 3.0 MW turbine, made in deterministic gust conditions, were used for some very easy tuning of the LQR, and allowed to emphasize a problem with the steady-state trimming ability of the LQR. It was soon realized that it was due to the mismatch between the reduced model and the very detailed `Cp-Lambda` simulator, representing a high-fidelity model of the real turbine. This issue was successfully addressed using an augmented linearized system, with the addition of the integral of the rotational speed.

Results obtained in IEC turbulent conditions revealed the good abilities of the PI and LQR with augmented state to correctly follow the reference. A scheduling based on a linear interpolation between several pre-calculated gains was implemented when working with the LQR controller, in order to deal with the ever changing wind speed average typical of a turbulent wind field. A full range of analyses performed all over the spectrum of operating wind speeds has not highlighted any problem of stability, and moreover the ability of the LQR trimmer to reduce the oscillations of the rotational speed and to lower the fore-aft damage equivalent load have been verified.

An output-feedback alternative design algorithm, which does not need the knowledge of the motion of the tower head, has been envisaged, allowing to deal with potential faults of the sensors without renouncing to the basic LQR framework.

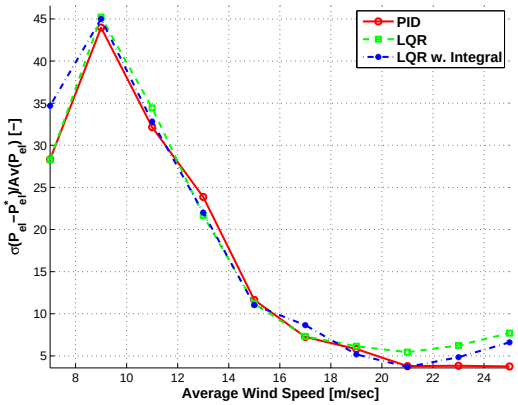

Figure 2.11: Normalized standard deviation of the power output, $\sigma(P_{el_e})$ (power quality index) for 600 sec IEC turbulence A simulations at different mean wind speeds. Performance comparison between a PI, an LQR and an LQR with an augmented state array.

The practical results obtained from trials in a high fidelity simulation environment show that it is possible to get trimming results from the LQR with augmented state which are as good as those of a PI industrial controller, or even somewhat better on those parameters which are not accounted for in the design of the PI. As a consequence, these controller can be considered equivalent from the viewpoint of the performance on power tracking.

Based also on the presented results, it is possible to conclude that the LQR design approach provides some adavantages and disadvantages with respect to other existing control algorithms. Among the advantages given by the LQR design framework:

- depending on the choice of the reduced model, it allows a comprehensive design of a MIMO control law aimed at several control goals, for instance power tracking and control of the fore-aft loads;
- for the specific case of a wind turbine, it does not require any *a priori* distinction between working regions, even for a plant featuring a region $\text{II}\frac{1}{2}$;
- differently from non-model-based design approaches, a satisfactory tuning of the weights can be achieved by means of some physical considerations, for instance choosing to attribute more importance to the power tracking task with respect to the dampening of tower-base loads;
- in the case of large, horizontal-axis wind turbines, it has been shown in this chapter that the use of the gain scheduling technique can be suc-

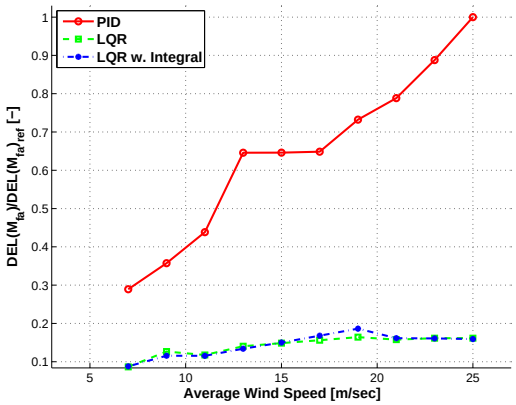

Figure 2.12: Normalized damage equivalent load (DEL) of the fore-aft bending moment at tower base, for 600 sec IEC turbulence A simulations at different mean wind speeds. Performance comparison between a PI, an LQR and an LQR with an augmented state array.

cessfully used to deal with the non-linearities of the controlled system, without incurring in any form of instability all over the spectrum of operational wind speeds, even considering rather requiring and realistic IEC turbulent conditions.

These advantages highlight a certain ease of design which is typical of the LQR approach with respect to other approaches.

The main disadvantages of the proposed LQR approach can be summarized as follows:

- the potentialities of the integrated MIMO approach can be unfolded only provided there exist a suitable reduced model of the turbine; in the analyzed case it has been shown that the choice of the reduced model may bring in some criticity in presence of any mismatch between the reduced model and a very sophisticated simulation tool; this can be addressed by using an additional integral state;

- the ability of the LQR approach to treat a larger array of states can be fully exploited by providing the controller with the necessary measurements: this makes it in principle more sensible to sensor faults; as previously shown, this issue can be cured by preparing a hierarchy of output-feedback controllers to be managed appropriately by a supervisory system, on the base of the detected sensor faults;

- the scheduling strategy selected in this work is based on some knowledge of the wind, which must be provided by means of a suitable sensor

or observer; much work has been devoted to the analysis of observers for the horizontal wind speed, which can be synthesized rather easily as shown in [23,28,50,51], and may be used to augment the wind measurement coming from the anemometer, which is always present on larger turbines, but is often affected by non-negligible inaccuracies (mainly due to the rotor wake and the interaction with the boundary layer of the nacelle); moreover, the necessity for the knowledge of the wind is typical for various control schemes, not only for the LQR.

It should be pointed out that, even if presented here for the specific case of the LQR, these advantages and disatvantages can be referred to a more general model-based control design approach. Actually, as clarified in the conclusions (see chapter 7), the choice of the LQR with respect to other model-based controllers of comparable complexity is bound to the high level of efficiency and automatability typical of the linear-quadratic regulator. This feature can be exploited in the assembly of optimization tools for the integrated aero-servo-elastic design of wind turbines [75].

2.6 Closing Notes

In the research activities described in this work all the kinds of trimmer presented above have been used. As demonstrated above, their performance is quite similar under many analysis criteria. Whenever possible, the original LQR with augmented state has been used. In certain analyses, often because of particular requests from collaborating subjects, the PIs proposed by the pertinent industries have been used instead. All these choices are thoroughly reported whenever necessary. However, to the scope of the analyses described in the following chapters the choice of the trimmer has not a great relevance, nor in any case does it hamper the generality of the results.

Chapter 3

LiDAR-Based Predictive Control

3.1 Introduction

In the previous chapter (2) some controllers have been proposed based on some different algorithms, but all basically aimed at the effective tracking of the correct power output. All these controllers operate on the basic feedback principle: the control inputs at a given instant are calculated from the values assumed by a set of variables at the same time or before it, i.e. in the past. The aim of the current chapter is to describe some control techniques based on the knowledge of the time history of one or a set of variables in a prediction window extending from the actual instant up to a certain time in the future, and to show examples of their performance when applied to wind turbines. In particular, the control schemes that will be described in this chapter will benefit from some measurements of the incoming wind field at some distances in front of the rotor. The availability of this kind of signal in real environment is coming every day closer to reality, as new LiDAR (Light Detection And Ranging) systems are becoming a reliable, light and affordable technology. These sensors can be mounted onboard the machine (for instance in the nacelle), and by illuminating the water or powder particles transported by the wind flow by means of suitable light beams, and by catching their reflections, they are able to provide a detailed spatial description of the wind velocity field almost simultaneously at several distances of the order of tens of meters ahead of the turbine.

There are various control schemes able to exploit the knowledge of the incoming wind. Two of them are considered in the following. One is an elegant extension of the concept of scheduled LQR, accounting for an ex-

ogenous input (i.e. the wind) besides the usual control and input variables (see chapter 2). This control scheme will be referred to as non-homogeneous LQR [62, 76]. A second approach is what is called receding horizon control (RHC). Unlike that of the first one, the implementation of this latter control law is not totally original, as it has been based on some preassembled routines which have not been developed in this research work. Moreover, the idea is far from new, even if it has been considered for wind power only recently [18, 64].

In the present work a particular stress was given to the simulation of the technological features of the LiDAR sensor, which in real environment performs a strong filtering action on the wind measurement, a depurating effect which is particularly important in turbulent wind conditions [77]. The LiDAR modelled in this way has been tested first in conjunction with a linear receding horizon control (RHC) in both deterministic and turbulent wind conditions, finding good results in terms of oscillations of the rotational speed of the rotor and of the fore-aft bending moment with respect to a non-predictive controller. The resulting performance of this controller has been used as a reference to compare to what can be obtained with the proposed non-homogeneous LQR approach, that despite a somewhat lower performance brings the great advantage of a straightforward implementation and easier tuning.

It should be noted at this level that both the non-homogeneous LQR and RHC controllers are actually two expressions of an integrated MIMO states-space optimal control design approach, and from the theoretical viewpoint they differ basically in the extension of the prediction window: for the receding horizon control it is finite, while for the non-homogeneous LQR it extends from the actual instant to infinity. As it is widely known, the receding horizon control problem does not yield a closed form solution, causing the need for an online optimizer to find the optimal control solution at a given control instant. On the other hand, the non-homogeneous LQR is obtained from a closed form solution, allowing an offline computation of the optimal gains, which can be suitably treated online with a wind speed-based scheduling logic. So, the non-homogeneous LQR can be seen as a computationally advantageous sub-case of the RHC, where the length of the prediction window has been extended up to an infinite value.

The main aim of this chapter is to show how the simpler non-homogeneous LQR controller be able to give results that are not too far from what is obtained with a more sophisticated and computationally heavy RHC.

3.2 Measurement of the Incoming Wind

As previously stated, the application of predictive control laws to wind turbines benefits from the knowledge of the wind ahead of the turbine. This can be provided by LiDAR sensors. A detailed description of the underlying measuring mechanism of this sensor is beyond the scope of this work [56]. Nonetheless, some working characteristics dictated by the technology implemented in the sensor assembly are relevant for at least two reasons: first, the wind measured by the LiDAR sensor results from a volumetric average of the speed of the air particles over a given volume, whose general shape and size are determined by the characteristics of the sensor; second, the time taken by the sensor to collect all the samples over the scanned volume is far from infinitesimal, and should be taken into account to perform a realistic exploration of the limits of a LiDAR-based predictive control.

Because of the impact that the characteristics of a LiDAR sensor can have on the performance of a controller able to make use of an anticipated knowledge of the wind [59,60,78,79], it is important to correctly simulate the behavior of the sensor, transposing its working algorithm into the simulation environment, thus actually setting up a LiDAR simulator. This is the main topic of this paragraph.

The present analysis is based on a hypothetical LiDAR sensor whose characteristics have been taken from the existing literature [80]. They represent a realistic sample of the features of the current technology. However, the developed LiDAR simulator implements a simulation methodology and thus it is not necessarily bound to a specific LiDAR technology or to a particular existing sensor.

3.2.1 LiDAR Simulator

To generate the wind signal to be used by the controller on a given time span ahead of the turbine in the way a LiDAR sensor would provide it, a given LiDAR architecture has been hypothesized, namely that of a wave pulse LiDAR. A typical example of this piece of machinery may be placed in the nacelle [80]. The emitter produces a straight beam with very low dispersion. The emitter is moved in such a way to describe a certain pattern with the emitted beam (Fig. 3.1). When a beam is emitted in a given direction, a number of measures along its trajectory is collected at different distances from the source. The time required for a complete excursion of the emitter along the prescribed pattern depends basically on three factors: the complexity of the pattern, which may be cross-shaped, circular, multi-lobated, etc., resulting in a longer travelling time of the emitter; the number of samples

collected along the beam for every stop over the considered pattern; finally, the number of such stops. For existing LiDAR hardwares the collection of a full array of samples all over the pattern may take about 0.5–3 sec. The number of focus distances along a beam can be typically 5–10, while the number of stops over the pattern can be 10–30. The maximum distance between the source and the measurement point furthest away from the turbine can be of the order of 1.5 rotor diameters even for large multi-MW turbines [80].

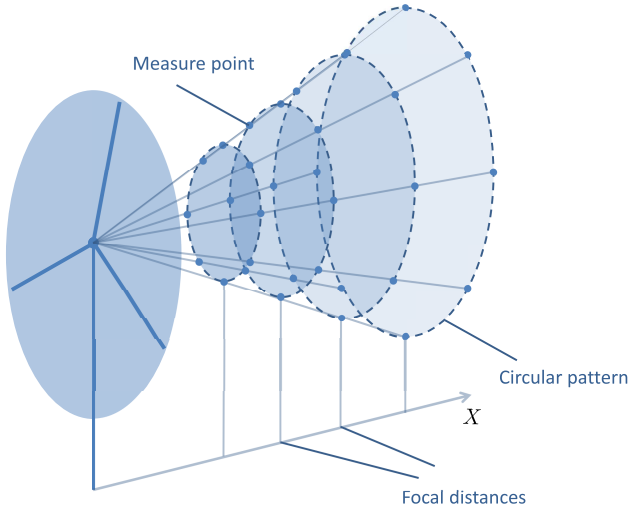

Figure 3.1: Schematic representation of a LiDAR sensor, featuring a circular pattern, 4 focal distances and 8 stops over the prescribed pattern.

The real sensor takes its measurements at given distances along the beam for each stop along the prescribed pattern, that is in some geometrical positions in space defined with respect to the position of the emitter, which is usually rather close to the hub.

To account for the inaccuracies which are typical of any LiDAR sensor in capturing the value of the wind speed in a given point in space, it is possible to define the wind speed measured by the LiDAR simulator as an average of the values of the wind speed measured at several points along the beam, weighed by a suitable weighing function [81–83]. The latter can be based on the usual Lorentz profile, as

$$w(x, x_s) = \frac{e^{-4ln_2(\frac{x-x_s}{W})^2}}{\int_{-\infty}^{\infty} e^{-4ln_2(\frac{x-x_s}{W})^2} dx} = \frac{2ln_2 e^{-4ln_2(\frac{x-x_s}{W})^2}}{W\sqrt{ln_2(\pi)}}, \tag{3.1}$$

where x_s is the designated focus distance ahead of the rotor, and the parameter W defines the span of the weighing function. It is common practice

to define W as an increasing function $W = W(x_s)$, meaning that the span of the function will be larger as the distance from the source is increased: this is made to account for the decrease in the accuracy of the measurements when getting farther from the source of the beam.

It must be pointed out that this form of inaccuracy has – somewhat paradoxically – a good effect on the performance of the predictive controllers designed to cope with a so obtained knowledge of the incoming wind. Because of this effect, modelled in the LiDAR simulator by means of a weighed (Eq. (3.1)) average of many (100) measurements along the beam for each considered focal distance, the LiDAR performs an intrinsic filtering action. This may be not good when the objective of the sensor was that of getting a sophisticated local description of the incoming wind, to be dealt with by individual pitch controllers, but on the contrary it is exactly what is needed for the control aim of a collective pitch and torque controller. Particularly in turbulent wind, the ability of the LiDAR to naturally capture the lower part of the frequency spectrum of the wind is very useful, as the slowly varying components of the wind field are the only ones whose effect on the tower fore-aft loads and the rotor speed can be compensated with a collective pitch and torque trimming controller [58, 77]. Moreover, in case an individual pitch control potentially able to alleviate the loads deriving from a nonuniform incoming wind field was of interest, then the limit on the bandwidth of the pitch actuators would make difficult an effective use of a very detailed spatial information, updated with a high temporal frequency – such a description may be probably more useful in conjunction with flap-controlled blades.

In order to get a synthetic measure for a given focal distance the wind speed values collected over the pattern at that distance are averaged, resulting in a single wind speed for each focal distance ahead of the sensor. With this operation, the measures defined over the 2–D domain constituted by the trajectory described by the beam on a plane at a given focal distance are collapsed to a single measure, representative of that focal distance.

What is needed to apply the predictive part of the proposed control laws is a knowledge of the wind at some time instants ahead of the turbine. In order to pass from a collection of measures over a geometrical domain to a set defined over a time grid ahead of the turbine it is necessary to provide the simulator the knowledge of some time average of the wind. Usually, the value of the time average $\bar{U}_m$ of the horizontal wind is set to remain constant during a simulation. Moreover, the problem of the dynamics of the incoming flow is addressed by invoking the Taylor's frozen turbulence hypothesis, stating that the spatial wind profile measured in a given position x_0 ahead of the rotor at a given time instant t_0 will be the same measured at time $t_0 + \Delta t$ in $x_0 - \bar{U}_m \Delta t$ [58], closer to the rotor.

Finally, the time histories referring to each focal point are averaged, completing the volumetric averaging operation typical of the LiDAR sensor. The result is a single value of predicted wind for each time instant, i.e. a time history of the incoming wind.

To remark the importance of this preliminary detailed work on the LiDAR sensor, it can be reported that trials performed with a simpler LiDAR simulator, basically measuring only the wind speed in the direction of the axis of the rotor and without the filtering effect of the Lorentz weighing functions (Eq. (3.1)), have provided bad results when these measurements have been used in closed loop with the proposed predictive control laws [84].

In the present analysis, focused on the 3.0 MW turbine (see chapter 1), the selected pattern has a circular shape. The resulting conical surface over which the measures are picked up has an aperture angle such that the area included in the circular pattern at the maximum distance from the emitter be the same as that of the rotor. The maximum focal distance is 1.5 diameters ahead of the hub. The number of focal distances has been fixed at 5, equally spaced between the maximum and the hub (of course, the hub itself is not considered as a focus point). The number of stops over the circular trajectory has been fixed at 12. As a consequence, an array of 5 measurements will be picked up every 15 deg of a LiDAR revolution. To simulate the LiDAR spatial inaccuracy, for every stop along the circular trajectory and at every focal distance, the LiDAR simulator provides a speed value based on measures read at 100 points along a 30 m portion of the beam, centered at the focal distance, using the weighing function (3.1) to average them. The speed values collected at a given focus distance over the circular trajectory are used to get an average value representative of the wind profile over a 2–D domain at that distance. Starting from these measures, defined on a geometrical domain, the knowledge of the time histories of the wind measured at a given focal distance is obtained using the frozen turbulence hypothesis and an assumption of constant average wind speed during all the simulation. From the resulting array of time histories, one for each focal point, a single time history of the volumetric average is obtained by a further average. An example of the resulting signal is presented in Fig. 3.2 for a category A turbulent wind field with a mean wind speed of 15 m/sec.

From Fig. 3.2 the filtering effect typical of the LiDAR can be partially noticed visively when passing from one of the time histories characteristic of the a given focal point to the global volumetric average. A more visible evidence of the filtering effect of the LiDAR sensor can be given for the same time history of the wind considered in Fig. 3.2 by showing the coherence between the time history of the signal coming from the LiDAR and that of

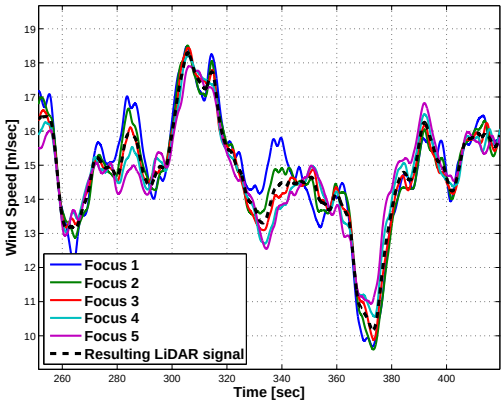

Figure 3.2: Example of LiDAR signal obtained from a 15 m/sec IEC turbulence A wind. Reported are the time histories corresponding to the 5 considered focal distances, each obtained from an average between the measures taken at 12 stops over a circular pattern. The resulting predicted speed is obtained from the average of the values of the other 5 curves.

the horizontal wind speed at hub. The coherence can be calculated from

$$\gamma^2 = \frac{|P_{xy}(f)|}{P_{xx}(f)P_{yy}(f)}, \tag{3.2}$$

where the terms P_{xx} and P_{yy} are the power spectral densities of the LiDAR signal and of the real wind, while P_{xy} is the cross power spectral density [77]. The spectral densities are expressed as functions of the frequency f. The coherence parameter, which may vary between 0 and 1, provides an expression of the relationship between the frequency contents of the two signals.

The coherence diagram for the considered case is shown in Fig. 3.3. It confirms that there is a good accordance between the frequency contents of the LiDAR signal and of the real wind for low frequencies, while the LiDAR operates a filtering action on the real wind for higher frequencies, resulting in a lower coherence for increased frequencies.

Up to now, no hypothesis on the update frequency of the measurement has been made, and the measurements from the simulator can be collected at an arbitrary time pace (as in Fig. 3.2). Actually, the characteristic update time has been left as a free design parameter in a preliminary stage of the work, to better understand its impact on the performance of the predictive controllers in closed loop. For reasons which will be better clarified in the following paragraphs, an update time of 3 sec was selected for the assessment of the performance of the two proposed predictive controllers. This value is in accordance with the typical aforementioned real speed limits of this sensor.

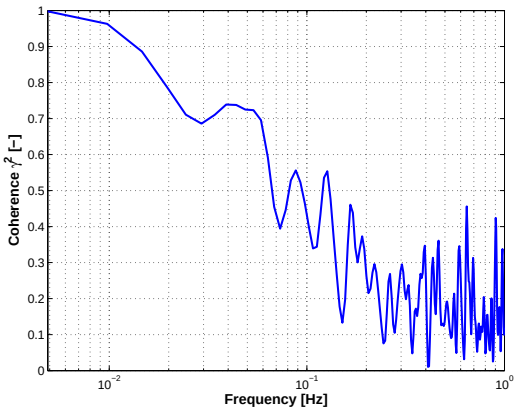

Figure 3.3: Coherence diagram for a 600 sec time history of IEC category A turbulent wind, obtained from the histories of the real hub-height wind and from the time history provided by the LiDAR.

To simulate the effect of a low – realistic – update frequency, the final time history resulting from the volumetric average is kept fixed at a constant value for the considered update time. More details about the application of this simulation algorithm will be provided for both the predictive controllers considered in this chapter.

This LiDAR simulator has been used for all the simulations whose results are presented in this chapter, even if its use is of primary importance only in turbulent wind, for the reasons described above and basically bound to its intrinsic filtering ability.

3.3 Non-Homogeneous LQR Control

This paragraph is based on the description of the LQR trimmer made in chapter 2. Recall the set of nonlinear equations of the reduced model of the wind turbine, as in system (2.1–2.4). The considered equations are those of the fore-aft tower motion, that of the rotational dynamics of the rotor (rotor balance), those of the pitch and torque actuators. Given a trim condition specified by an array as $\{\boldsymbol{x}^*, \boldsymbol{u}^*, U_m^*\}$, where $\boldsymbol{x}^*$ and $\boldsymbol{u}^*$ are respectively the states and controls at the trim point of wind speed U_m^*, it is possible to linearize the system (2.1–2.4) around that trim condition:

$$\Delta\dot{\boldsymbol{x}} = \boldsymbol{A}(\boldsymbol{x}^*, \boldsymbol{u}^*, U_m^*)\Delta\boldsymbol{x} + \boldsymbol{B}(\boldsymbol{x}^*, \boldsymbol{u}^*, U_m^*)\Delta\boldsymbol{u} + \boldsymbol{G}(\boldsymbol{x}^*, \boldsymbol{u}^*, U_m^*)\Delta\boldsymbol{w}, \quad (3.3)$$

where, as usual, $\Delta\boldsymbol{x} = \boldsymbol{x} - \boldsymbol{x}^*$, $\Delta\boldsymbol{u} = \boldsymbol{u} - \boldsymbol{u}^*$, and $\Delta\boldsymbol{w} = \boldsymbol{w} - \boldsymbol{w}^* = \{U_w - U_m^*\}$ is defined as an exogenous input, where U_m in real practice (i.e.

in turbulent wind conditions) can be thought of like a slowly varying moving average of the measured wind speed U_w. In principle, it would be possible to consider a more comprehensive list of wind states in $\Delta\boldsymbol{w}$, able to better describe the incoming wind field. For now, only the hub height wind speed has been considered, basically for two reasons. The first, as we are implementing a collective pitch and torque controller it would not be smart to consider some wind states able to describe a nonuniform incoming wind field, whose effects show up typically in the form of oscillatory loads for instance on the blades, and can be successfully dealt with only by making use of cyclic or individual pitch control. The second reason is bound to the characteristics of the selected model-based control approach, for which it is sufficiently easy to find out the coefficients of the matrix $\boldsymbol{G}$ appearing in Eq. (3.3) if the exogenous input $\Delta\boldsymbol{w}$ is based on the aforementioned U_m alone. On the other hand, dealing with an increasing number of wind states would make the definition of the $\boldsymbol{G}$ matrix less straightforward. About this issue, recall that the reduced model considered for control design has been written in analytical form and completed with coefficients obtained from *ad hoc* simulations carried out on the `Cp-Lambda` model of the considered turbine, as explained in chapter 2. The new required coefficients can be obtained from the punctual knowledge of the $C_{P_e} - \lambda$ and $C_{F_e} - \lambda$ curves, basically by finding through numerical differentiation the values of $\frac{\partial C_{P_e}}{\partial U_m}$ and $\frac{\partial C_{F_e}}{\partial U_m}$. This procedure extends that presented in chapter 2 for the usual feedback LQR controller.

Given the state equation (3.3), it is possible to set up an optimal control problem, based on the usual infinite horizon cost function

$$J = \frac{1}{2}\int_0^\infty (\Delta\boldsymbol{x}^{\boldsymbol{T}}\boldsymbol{Q}\Delta\boldsymbol{x} + \Delta\bar{\boldsymbol{u}}^{\boldsymbol{T}}\boldsymbol{R}\Delta\bar{\boldsymbol{u}})\,\mathrm{d}t, \tag{3.4}$$

whose minimum has to be found under the constraint of the system dynamics $\Delta\dot{\boldsymbol{x}} = \boldsymbol{A}\Delta\boldsymbol{x} + \boldsymbol{B}\Delta\bar{\boldsymbol{u}} + \boldsymbol{G}\Delta\boldsymbol{w}$. The solution of the control problem will be a $\Delta\bar{\boldsymbol{u}}(t)$ minimizing the cost function over an infinite horizon. For a state equation without the exogenous term the solution can be driven in closed form from the Riccati equation associated to the control problem. In presence of that term, the solving procedure (presented in the next subsection) is based on the usual Lagrange multipliers, and under the hypothesis of steady state solution with $t \to \infty$ it produces the optimal control input in the following closed form:

$$\Delta\bar{\boldsymbol{u}}(t) = -\boldsymbol{R}^{-1}\boldsymbol{B}^T\boldsymbol{P}\Delta\boldsymbol{x}(t) - \boldsymbol{R}^{-1}\boldsymbol{B}^T\int_t^\infty e^{-\bar{\boldsymbol{A}}^T(t-\tau)}\boldsymbol{P}\boldsymbol{G}\Delta\boldsymbol{w}(\tau)\,\mathrm{d}\tau, \tag{3.5}$$

where $\bar{\boldsymbol{A}} = \boldsymbol{A} - \boldsymbol{B}\boldsymbol{R}^{-1}\boldsymbol{B}^T\boldsymbol{P}$ and $\boldsymbol{P}$ solves the usual algebraic Riccati

equation. The solution (3.5) is made up of two components:

$$\Delta\bar{\boldsymbol{u}}(t) = \Delta\boldsymbol{u}(t) + \Delta\boldsymbol{u}_{nh}(t) \tag{3.6}$$

where the first term

$$\Delta\boldsymbol{u}(t) = -\boldsymbol{R}^{-1}\boldsymbol{B}^T\boldsymbol{P}\Delta\boldsymbol{x}(t) \tag{3.7}$$

is the solution that can be found without having the exogenous input in the constraining state equation of the system. The second term

$$\Delta\boldsymbol{u}_{nh}(t) = -\boldsymbol{R}^{-1}\boldsymbol{B}^T\int_t^\infty e^{-\bar{\boldsymbol{A}}^T(t-\tau)}\boldsymbol{P}\boldsymbol{G}\Delta\boldsymbol{w}(\tau)\,\mathrm{d}\tau \tag{3.8}$$

is bound to the values assumed by the wind state $\Delta\boldsymbol{w}$ over an infinite prediction window, and hence is the predictive part of the control law.

The following paragraph, devoted to the theoretical explanation of the origin of the closed form solution, is self-contained and can be skipped virtually without hampering the comprehension of the rest of the chapter.

3.3.1 Formulation of the Non-Homogeneous LQR

A sufficiently general demonstration for Eq. 3.5 is presented here, and has been elaborated from [76] and references therein. The procedure to get to the control solution in a closed form can be developed in a very general case, with the cost function of the optimization defined over a finite horizon extending from the initial instant, supposed to be $t = 0$, up to a final time T:

$$J = \frac{1}{T}\int_0^T \Delta\boldsymbol{x}^T\boldsymbol{Q}\Delta\boldsymbol{x} + \Delta\boldsymbol{u}^T\boldsymbol{R}\Delta\boldsymbol{u}\mathrm{d}t. \tag{3.9}$$

The cost function is augmented by adding the dynamic equation of the linearized system, weighed by the unknown Lagrange multipliers. To show the solving procedure, based on the use of a transition matrix, for a general case let the state array $\Delta\boldsymbol{x}$ be made up by two subparts, $\Delta\boldsymbol{x}_1$ and $\Delta\boldsymbol{x}_2$,

$$\Delta\boldsymbol{x} = \left\{ \begin{array}{c} \Delta\boldsymbol{x}_1 \\ \Delta\boldsymbol{x}_2 \end{array} \right\}. \tag{3.10}$$

where only the final value of the first is subject to some constraints at final time T.

The constraint on the state $\Delta\boldsymbol{x}_1$ at final time T can be expressed as:

$$\boldsymbol{\Psi}(\Delta\boldsymbol{x}(T)) = \boldsymbol{\psi}(T)\Delta\boldsymbol{x}(T) - \boldsymbol{\psi}_0 = \boldsymbol{0}, \tag{3.11}$$

where

$$\boldsymbol{\psi}(T) = \begin{bmatrix} \boldsymbol{\psi}_1(T) & \mathbf{0} \\ \mathbf{0} & \mathbf{0} \end{bmatrix} \tag{3.12}$$

and

$$\boldsymbol{\psi}_0 = \begin{bmatrix} \boldsymbol{\psi}_0^1 \\ \mathbf{0} \end{bmatrix}. \tag{3.13}$$

The values of the states contained in $\Delta\boldsymbol{x}_2$ are weighed at final time T, so that

$$\boldsymbol{\phi}(\Delta\boldsymbol{x}(T)) = \frac{1}{2}\Delta\boldsymbol{x}^T(T)\boldsymbol{P}\Delta\boldsymbol{x}(T), \tag{3.14}$$

where the weight matrix $\boldsymbol{P}$ is

$$\boldsymbol{P} = \begin{bmatrix} \mathbf{0} & \mathbf{0} \\ \mathbf{0} & \boldsymbol{P_2} \end{bmatrix}. \tag{3.15}$$

The constraints on the final values (3.11) are added to the original cost function J, already enriched by the constraint at time T, and now further augmented by adding another suitable set of Lagrange multipliers, $\boldsymbol{\nu}(t)$:

$$\bar{J} = \{\boldsymbol{\phi}(\Delta\boldsymbol{x}(T)) + \boldsymbol{\nu}(t)\boldsymbol{\Psi}(\Delta\boldsymbol{x}(T)) + J\}. \tag{3.16}$$

In order to get an expression of the optimal control solution it is necessary to set the first-order variation of the cost function to zero. Given the arbitrariety of the variations $\delta\Delta\boldsymbol{x}$, $\delta\Delta\boldsymbol{x}(T)$ and $\delta\Delta\boldsymbol{u}$ it is possible to obtain the system:

$$\Delta\dot{\boldsymbol{x}} = \boldsymbol{A}\Delta\boldsymbol{x} + \boldsymbol{B}\boldsymbol{R}^{-1}\boldsymbol{B}^T\Delta\boldsymbol{\lambda} + \boldsymbol{G}\Delta\boldsymbol{w} \tag{3.17}$$

$$\dot{\boldsymbol{\lambda}} = \boldsymbol{Q}\Delta\boldsymbol{x} - \boldsymbol{A}^T\boldsymbol{\lambda} \tag{3.18}$$

$$\Delta\boldsymbol{u}^* = \boldsymbol{R}^{-1}\boldsymbol{B}^T\boldsymbol{\lambda} \tag{3.19}$$

$$\boldsymbol{\lambda}(T) = -\frac{\partial\boldsymbol{\phi}^T}{\partial\Delta\boldsymbol{x}}|_{t=T} - \boldsymbol{\psi}^T\boldsymbol{\nu}|_{t=T} \tag{3.20}$$

$$\boldsymbol{\lambda}(T) = -\boldsymbol{P}\Delta\boldsymbol{x}(T) - \boldsymbol{\psi}^T(T)\boldsymbol{\nu}(T) \tag{3.21}$$

$$\Delta\boldsymbol{x}(0) = \Delta\boldsymbol{x}_0 \tag{3.22}$$

$$\Delta\boldsymbol{w}(T) < \infty. \tag{3.23}$$

Hypothesize now that the array of the multipliers $\boldsymbol{\lambda}(t)$ could be described by the following expression:

$$\boldsymbol{\lambda}(t) = -[\boldsymbol{P}(t)\Delta\boldsymbol{x}(t) + \boldsymbol{Z}(t)\boldsymbol{\nu}(t)]. \tag{3.24}$$

By differentiating the latter equation,

$$\dot{\boldsymbol{\lambda}}(t) = -[\dot{\boldsymbol{P}}\Delta\boldsymbol{x} + \boldsymbol{P}\Delta\dot{\boldsymbol{x}} + \dot{\boldsymbol{Z}}\boldsymbol{\nu} + \boldsymbol{Z}\dot{\boldsymbol{\nu}}], \tag{3.25}$$

where the dependence of the various components of the right-hand-side term on the time t has been omitted.

By substituting the expressions for $\Delta\dot{\boldsymbol{x}}$ given by Eq. (3.17) and for $\boldsymbol{\lambda}$ given by (3.24) into Eq. (3.25), a first expression for $\dot{\boldsymbol{\lambda}}(t)$ can be obtained. A second expression for the same quantity comes by substituting the definition of $\boldsymbol{\lambda}(t)$ from (3.24) into (3.18). Exploiting these two expressions of the same quantity, the following equation can be written:

$$\begin{aligned}(-\dot{\boldsymbol{P}} - \boldsymbol{P}\boldsymbol{A} + \boldsymbol{P}\boldsymbol{B}\boldsymbol{R}^{-1}\boldsymbol{B}^T\boldsymbol{P} - \boldsymbol{Q} - \boldsymbol{A}^T\boldsymbol{P})\Delta\boldsymbol{x} + \\ (\boldsymbol{P}\boldsymbol{B}\boldsymbol{R}^{-1}\boldsymbol{B}^T\boldsymbol{Z} - \dot{\boldsymbol{Z}} - \boldsymbol{A}^T\boldsymbol{Z})\boldsymbol{\nu} + \boldsymbol{Z}\dot{\boldsymbol{\nu}} - \boldsymbol{P}\boldsymbol{G}\Delta\boldsymbol{w} = \boldsymbol{0}.\end{aligned} \tag{3.26}$$

Eq. (3.26) is satisfied for

$$-\dot{\boldsymbol{P}} = \boldsymbol{P}\boldsymbol{A} + \boldsymbol{A}^T\boldsymbol{P} - \boldsymbol{P}\boldsymbol{B}\boldsymbol{R}^{-1}\boldsymbol{P}\boldsymbol{B} + \boldsymbol{Q} \tag{3.27}$$

and

$$\dot{\boldsymbol{Z}}\boldsymbol{\nu} + \boldsymbol{Z}\dot{\boldsymbol{\nu}} = -[\boldsymbol{A} - \boldsymbol{B}\boldsymbol{R}^{-1}\boldsymbol{B}^T\boldsymbol{P}]^T\boldsymbol{Z}\boldsymbol{\nu} - \boldsymbol{P}\boldsymbol{G}\Delta\boldsymbol{w}. \tag{3.28}$$

By defining $\boldsymbol{s} = \boldsymbol{Z}\boldsymbol{\nu}$, Eq. (3.28) can be written as

$$\dot{\boldsymbol{s}} = -[\boldsymbol{A} - \boldsymbol{B}\boldsymbol{R}^{-1}\boldsymbol{B}^T\boldsymbol{P}]^T\dot{\boldsymbol{s}} - \boldsymbol{P}\boldsymbol{G}\Delta\boldsymbol{w}. \tag{3.29}$$

Eq. (3.19) can be written as:

$$\Delta\boldsymbol{u}^* = -\boldsymbol{R}^{-1}\boldsymbol{B}^T\boldsymbol{P}\Delta\boldsymbol{x} - \boldsymbol{R}^{-1}\boldsymbol{B}^T\boldsymbol{s} \tag{3.30}$$

where matrix $\boldsymbol{P}$ is the solution of the usual Riccati equation without the exogenous input (3.27) while $\boldsymbol{s}$ solves Eq. (3.29), in the case of a constraint on $\boldsymbol{P}$ at final time T as $\boldsymbol{P}(T) = \boldsymbol{P}$ and $\boldsymbol{s} = \boldsymbol{s}(T)$. It should be noticed that the value $\boldsymbol{s}$ is unknown, but, having been defined as the product of the finite quantities $\boldsymbol{Z}(T)$ and $\boldsymbol{\nu}(T)$, it is finite.

Now, by driving T to infinity, $T \to \infty$, the following definition can be written:

$$\tilde{J} = \lim_{T\to\infty} \bar{J}. \tag{3.31}$$

Notice that in steady-state conditions Eq. (3.27) is an algebraic Riccati equation, while Eq. (3.29) becomes $\dot{\boldsymbol{s}}(\infty) = \boldsymbol{s}$. The method of the transition matrix can be used to solve these equations. Let matrix $\boldsymbol{\Phi}$ be such that $\boldsymbol{\Phi}^{\boldsymbol{s}}(t,\tau) = e^{-\bar{\boldsymbol{A}}^T(t-\tau)}$, where $\bar{\boldsymbol{A}} = \boldsymbol{A} - \boldsymbol{B}\boldsymbol{R}^{-1}\boldsymbol{B}^T\boldsymbol{P}$. The resulting solution for $\boldsymbol{s}$ is

$$\boldsymbol{s} = \boldsymbol{\Phi}^{\boldsymbol{s}}(t,\infty)\boldsymbol{s}_\infty - \int_\infty^t \boldsymbol{\Phi}^{\boldsymbol{s}}(t,\tau)\boldsymbol{P}\boldsymbol{G}\boldsymbol{w}(\tau)d\tau. \tag{3.32}$$

Matrix $\bar{\boldsymbol{A}}$ represents the dynamic matrix of the controlled system, which is stable by definition as the control gain comes from the solution of an LQR problem. Moreover, as previously pointed out, the value of $\boldsymbol{s}_\infty$ is finite by definition. For these reasons, Eq. (3.32) takes the shape

$$\boldsymbol{s} = \int_t^\infty \boldsymbol{\Phi}^{\boldsymbol{s}}(t,\tau)\boldsymbol{P}\boldsymbol{G}\Delta\boldsymbol{w}(\tau)d\tau = \int_t^\infty e^{-\bar{\boldsymbol{A}}^T(t-\tau)}\boldsymbol{P}\boldsymbol{G}\Delta\boldsymbol{w}(\tau)d\tau. \tag{3.33}$$

By substituting Eq. (3.33) into Eq. (3.30) the optimal control solution can be obtained as:

$$\Delta\boldsymbol{u}^* = -\boldsymbol{R}^{-1}\boldsymbol{B}^T\boldsymbol{P}\Delta\boldsymbol{x} - \boldsymbol{R}^{-1}\boldsymbol{B}^T\int_t^\infty e^{-\bar{\boldsymbol{A}}^T(t-\tau)}\boldsymbol{P}\boldsymbol{G}\Delta\boldsymbol{w}(\tau)d\tau. \tag{3.34}$$

3.3.2 Adaptation of the Non-Homogeneous LQR to the Control Problem in Real Environment

In order to apply the considered control law, the knowledge of $\Delta\boldsymbol{w}(t)$ over an infinite window would be required in theory.

To manage the integral on an infinite prediction window it is possible to hypothesize that the disturbance to the wind be constant. In that case the variable $\Delta\boldsymbol{w}$ can be extracted from the integral, and the remaining function can be integrated without approximation, yielding

$$\Delta\boldsymbol{u}_{nh} = -\boldsymbol{R}^{-1}\boldsymbol{B}^T\bar{\boldsymbol{A}}^{-T}\boldsymbol{P}\boldsymbol{G}(\boldsymbol{w} - \boldsymbol{w}^*). \tag{3.35}$$

This shows that, under that hypothesis, the gain of the predictive control component can be calculated and stored offline as a function of the system and weight matrices.

Now, it is clear that in real practice the hypothesis of constant wind over an infinite time span cannot be met, as any LiDAR sensor will only be able to provide a prediction over a finite span, and moreover the wind is obviously not constant. A smart way to deal with that hypothesis in real environment is that of making use of a piecewise constant time history for the exogenous input [84], i.e. the wind measured by the LiDAR. From the viewpoint of the LiDAR simulation, getting from the LiDAR measurements of $U_w(t)$ collected by the simulator at an arbitrarily high frequency to a piecewise constant input is a task which can be accomplished rather easily by averaging the wind measurements available from the LiDAR over a time span T_C, with $T_C \leq T_P$, where T_P is the time extension of the LiDAR prediction window and can be calculated under the hypothesis of constant U_m during a simulation as the ratio between the distance of the focal point farthest away from the sensor and U_m (see Fig. 3.4).

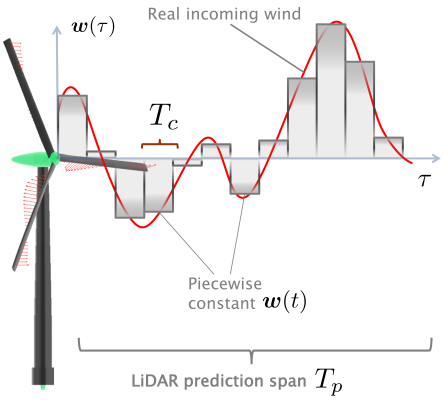

Figure 3.4: Schematic representation of the incoming wind as realistically obtained from a LiDAR sensor, accounting for a slow updating frequency. Graphical definition of T_P and T_C.

Notice that the two parameters T_C and T_P are not parameters of the control system, but they are characteristic of the LiDAR simulator. On the other hand, as it is important to provide to the non-homogeneous LQR control law a constant wind input, as required by theory, these characteristics of the LiDAR may have an impact on the performance of the controller, as they may define the update frequency of the LiDAR meausurement, i.e. of the exogenous input of the controller. To limit this potential effect and to keep the tuning of the controller independent from the tuning of the LiDAR as much as possible, a further time parameter can be introduced, the actual prediction window of the control system T_A, which has been considered as a tunable parameter with the constraint $T_A \leq T_C$. This prediction window of the controller, extending forward in time from the current instant, is used to actually evaluate the value of the incoming wind Δw to feed to the controller. By definition, $\Delta w = U_w - U_m^*$. In this expression the value of U_w is calculated in practice as the average of the signal coming from the LiDAR, made up of steps of length T_C each, over the prediction window of length T_A. The second term in the definition, he reference value U_m^*, is obtained from a slowly-varying time average of the wind measured by the usual anemometer put on top of the machine. In practice, the averaging of the signal coming from the anemometer is obtained by filtering it with a moving average filter with a characteristic time of 30 sec.

It should be noted here that the extension of the LiDAR averaging window T_C is actually not totally unconstrained, as it is related to the update frequency of the LiDAR sensor. As previously shown in this chapter, the

collection of a complete array of spatial measurements by the LiDAR usually takes a time lapse of the order of a few seconds. This in turn does not allow to hypothesize an averaging time T_C inferior to that characteristic update time of the LiDAR. Moreover, given a value of T_C, the use of a control prediction window T_A larger than T_C is not correct from the theoretical viewpoint, as in that case the signal of the incoming wind would never be constant over the control prediction window T_A except in constant wind, because more than one wind step of length T_C would always be present in the considered prediction window of length T_A. For this reason, as previously stated, the characteristic time T_A of the prediction window of the control system is constrained to be inferior to the length of the LiDAR step, $T_A \leq T_C$.

To suitably tune the two time parameters T_C and T_A, characteristic of the LiDAR and of the controller respectively, a parametric study has been performed [84] to explore the quality of the solution for different values of both the prediction window T_A and the wind step length T_C (the latter being bound to the LiDAR update frequency). Several simulations have been carried out on the model of the 3.0 MW turbine (see chapter 1) in deterministic IEC gusty wind conditions, at reference speeds of 3 to 25 m/sec every 2 m/sec and for each choice of T_C from 0.5 to 5 sec and for T_A from 0.5 sec up to T_C. The performance of the same controller based on each couple of T_C and T_A has been evaluated in terms of maximum peak-to-peak oscillation of the fore-aft bending moment and rotor rotational speed. The best compromise turned out to be $T_A = 1$ sec and $T_C = 3$ sec, the latter being fully compatible with the updating frequency of a real LiDAR sensor. These results may be not general and bound, among other influencing factors, to some characteristics of the turbine. On the other hand, the relatively short size of the prediction window T_C of the controller highlights the fact that for a typical 3.0 MW sized turbine it is not important to know what the time history of the wind will be many seconds (or meters) ahead of the turbine, but only what the incoming wind will behave like a few seconds ahead.

3.4 Receding Horizon Control

As stated in the introduction to this chapter, a receding horizon control has been considered besides the usual trimmer to assess the quality of the performance of the non-homogeneous LQR. The receding horizon control (RHC) algorithm implemented here, briefly described in the following, is used rather more commonly than the non-homogeneous LQR, so the reader may be more familiar with this predictive architecture, which is not original at all.

Even if more straightforward than the non-homogeneous LQR from the viewpoint of theory, the RHC control is usually more complex from the viewpoint of the implementation (i.e. programming) and tuning of the parameters.

The basic idea behind the RHC control is that of solving a cost function optimization problem on a finite time window instead of considering an infinite window as for the non-homogeneous LQR. The new cost function may be defined as

$$J = \frac{1}{2}\int_0^{T_f} (\Delta \boldsymbol{x}^{\boldsymbol{T}} \boldsymbol{Q} \Delta \boldsymbol{x} + \Delta \bar{\boldsymbol{u}}^{\boldsymbol{T}} \boldsymbol{R} \Delta \bar{\boldsymbol{u}})\, \mathrm{d}t + \frac{1}{2}\Delta \boldsymbol{x}^{\boldsymbol{T}}(T_f)\boldsymbol{Q}_f \Delta \boldsymbol{x}(T_f), \quad (3.36)$$

and its minimization is subject to the system dynamics (3.3). An advantage of this formulation is the possibility to naturally put inequality constraints in the optimization problem, in the form $\boldsymbol{D}\Delta\boldsymbol{x} + \boldsymbol{E}\Delta\boldsymbol{u} \leq \boldsymbol{0}$, which may be helpful to account for control time-rate limitations, e.g. pitch rate, directly in the optimization problem. The obvious disadvantage is that there is no closed form solution to the optimization problem.

In order to apply existing numerical solving schemes it is necessary to switch to a discretized formulation, based on both a discretized cost function and state equation. Consider a discretization of the prediction window T_f by N steps, such that $t_k = t, t + \Delta t_k, \ldots, T_f$ and $\Delta t_k = \frac{T_f}{N}$. The discretized cost function can be written as

$$\hat{J} = \frac{1}{2}\sum_{k=1}^{N} (\Delta \boldsymbol{x}_k^T \boldsymbol{Q} \Delta \boldsymbol{x}_k + \Delta \boldsymbol{u}_k^T \boldsymbol{R} \Delta \boldsymbol{u}_k) + \frac{1}{2}\Delta \boldsymbol{x}_N^T \boldsymbol{Q}_f \Delta \boldsymbol{x}_N, \quad (3.37)$$

which has to be minimized subject to the dynamics of the system in discrete form

$$\Delta \boldsymbol{x}_{k+1} = \boldsymbol{A}_k \Delta \boldsymbol{x}_k + \boldsymbol{B}_k \Delta \boldsymbol{u}_k. \quad (3.38)$$

Any linear inequality constraints may be imposed for each time step in the prediction window as $\boldsymbol{D}\Delta\boldsymbol{x}_k + \boldsymbol{E}\Delta\boldsymbol{u}_k \leq \boldsymbol{0}$.

There exist many very efficient solving algorithms for a so structured minimization problem. In this work the metacode `CVXGEN` was selected [85]. Using a web interface it is possible to define and upload the optimization problem of interest, using a very simple Matlab-like language. The `CVXGEN` routines then return an implementation of a solver for that specific problem in `C` language, based on direct transcription of the optimization problem and quadratic programming. The solver routine is easily integrable in the control framework developed in this work, written in `C/C++`. Besides the enormous advantage of the ease of use, the code produced by `CVXGEN` is rather fast,

and does not impose an unbearable toll in terms of computational time with respect to the main control and supervisory routines. It also assures the use of the same number of operations for the computations involved in the numerical optimization, this way making possible a potential use in real-time and for real-environment control applications. The relatively short execution time is partially obtained through the large-scale use of static variables. A shortcoming of this programming approach is a rather small flexibility of the code with respect to a change in the size of the problem, not only in terms of the size of the state and input arrays, but also of the number of time steps considered for the discretization of the prediction window.

Notice that the necessity to keep down the computational cost of the optimization, given a certain set of machine and wind states and inputs, imposes a limit to the number of time steps to be considered in the prediction window. In other words, the number of time instants in the prediction window at which the control solution will be calculated should not exceed a reasonably low number. Actually, in `CVXGEN` the total number of variables in the optimization problem, bound to the size of the system and to the number of time steps in the prediction window used to define the control solution, is limited to a maximum. This general limit on the number of time steps in the prediction window must be considered together with the limit on the time span between different subsequent time steps in the window, which in turn is bound to the necessity to integrate the dynamics of the system from the actual condition all over the prediction window without incurring in problems of numerical stability. Of course, the upper limit of the time step used for the discretization of the prediction window is bound to both the characteristic time of the considered dynamic equations, and to the numerical method implemented to manage the integration. A practical consequence of the combined effect of these constraints is the necessity to keep the prediction window of the RHC controller to a rather limited value, of the order of the seconds. However, based on the same considerations presented about the time length of the prediction window used with the non-homogeneous LQR, the use of a longer window is not useful for the considered control purposes, and so the aforementioned constraints do not hamper the performance of the RHC and the goodness of the results.

Also for this control algorithm a parametric study has been carried out to find out the optimal value of the length of the prediction window. A fixed number of 10 time steps has been assumed, being such to keep the computational cost of the optimization to an acceptable value. Several lengths of the prediction window have been considered between 0.1 and 10 sec [84]. The same IEC gusty wind simulations considered for the non-homogeneous LQR were performed also here (recall the pertinent paragraph). Moreover,

as with that controller, a wind history made up of a piecewise constant was considered, with a time length T_C of the step of 3 sec, which was selected as the best for the case of the non-homogeneous LQR, and which complies with the limits on the update frequency of a real LiDAR sensor. Nonetheless, it should be noted that, differently from the non-homogeneous LQR case, in the RHC case it is not necessary to hypothesize a steady wind input over the prediction window: as a consequence, it is not necessary to consider a length of the prediction window inferior to the length of each wind step, that is shorter than 3 sec in the considered case. Actually, what turned out from the parametric analysis was that an RHC prediction window of 1 sec gives the best results for the considered controller and turbine, considering as usual the peak-to-peak of the fore-aft bending moment at the tower base and of the rotor rotational speed as performance parameters.

As previously highlighted, the design of the RHC allows taking into account some limits on the control input in the form of inequality constraints. These constraints have been used to avoid an excessively fast motion of the pitch actuators, which in reality are limited by a maximum value of the pitch-rate.

From the viewpoint of implementation, the RHC calculations are called at every control step, which on the considered turbine cycles at 50 Hz, so that an optimal control history over the prediction window is calculated at each step. Only the first value of the optimal control history found by the optimizer is actually used and commanded to the actuators, after having been limited in terms of rate and value as prescribed by the limits of the actuators. The variability of the model matrices with respect to the wind is accounted for by an appropriate matrix scheduling with respect to the predicted wind at each time step in the prediction window.

In this research activity the model used to design the non-homogeneous LQR is the same used to run the RHC routines, thus making the comparison between the two controllers more meaningful. The discretization of the dynamic equation of the system has been made the simplest way, with an explicit Euler method. Using a prediction window of 1 sec and 10 discretization steps gives an integration step of 0.1 sec, which is low enough to guarantee a correct propagation of the system over the prediction window. This is due to the relatively slow dynamics of the machine states considered in the design, in particular the tower fore-aft displacement and rotor rotational speed. For safety, the results of the integration of the considered wind-scheduled linearized system obtained with the explicit Euler method have been verified in a separate environment (and not in closed loop) with respect to those obtained with an explicit fourth-order Runge-Kutta method in both deterministic and turbulent conditions, finding discrepancies with

the selected time step only with some wind conditions and after 500 sec of integration. This means that problems of numerical stability may arise with the selected lower-order method only with prediction windows of the order of 500 sec, a value of no interest in real practice.

3.5 Results

As stated previously in this chapter, the basic idea behind the design of the non-homogeneous LQR is that of finding a way to augment the basic LQR controller by accounting for a measurement of the incoming wind, i.e. of an incoming disturbance. The advantage given by this control algorithm lies in the chance to precalculate the gain matrices, thus making the implementation very easy. On the contrary, the RHC control is much more computationally heavy, but it can be seen as a more comprehensive and accurate way to treat the predicted incoming wind.

In this section, results obtained from the LQR without predictive part (the same described in chapter 2), from the non-homogeneous LQR and from the RHC are all compared. In particular, all the implementations account for the integral state on Ω. Both IEC gusts and turbulent fields have been considered [66,74]. Several simulations were carried out on the `Cp-Lambda` model of the 3.0 MW turbine, which features a transition region (see chapter 1).

As previously reported, the prediction span for the non-homogeneous LQR is $T_C = 3$ sec, which is the time length of the wind step, while the control span is $T_A = 1$ sec. As explained above, they have been selected as optimal, yet realistic values on the basis of a parametric analysis involving simulations on the full array of wind speeds and several different values for T_C and T_A. The weight matrices of the non-homogeneous LQR have been manually scheduled with respect to the wind in the control design phase, so as to try to improve the local performance over all the operating regions of the turbine. The gain matrices and the references, stored for 12 wind speeds from 3 up to 25 m/sec, are interpolated as functions of a slowly varying wind speed signal, obtained as a moving average of the anemometric signal with a characteristic time of 30 sec. The same signal is used to evaluate the difference $\Delta \boldsymbol{w}$ to feed to the predictive part of the controller.

For the RHC, the prediction window is 1 sec long, and 10 discretization steps are considered. The weight matrices are also here scheduled in wind. The actual model and weight matrices are interpolated as functions of the wind over the prediction window: as the wind is known at every point in the prediction window, the matrices can be obtained from interpolation of the stored values for each considered point. Like for the non-homogeneous LQR,

the LiDAR update frequency is such to provide a measured signal made of subsequent steps each lasting 3 sec. The slowly varying average of the wind, necessary for the calculation of $\Delta \boldsymbol{w}$ at each point over the prediction window, is obtained from a 10 sec moving average of the average of the predicted wind measured over the prediction window.

3.5.1 Deterministic Gusts

The considered array of reference speeds used for simulations in IEC gusty wind extends from 5 to 23 m/sec every 2 m/sec. The characteristics of the LiDAR sensor are those presented above (basically, circular scanning pattern, 5 focal distances, 12 stations over a pattern).

Before showing a synthetic view of the results, in Fig. 3.5 are presented the normalized time histories of the rotational speed of the rotor and of the fore-aft bending moment at the base of the tower for a reference speed of 21 m/sec. As it can be clearly noticed, the reduction in the peak-to-peak values due to the presence of a predictive control component is rather substantial. The two predictive formulations give similar results, the RHC doing somewhat better than the non-homogeneous LQR on both performance indices.

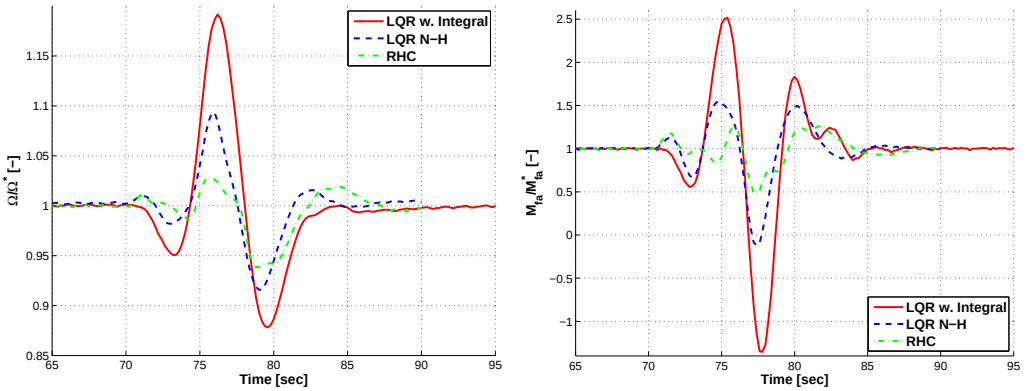

(a) (b)

Figure 3.5: Normalized time histories of the rotational speed (left) and fore-aft bending moment (right) for an IEC gust with reference speed of 21 m/sec. Comparison between the effects of a non-predictive LQR, a non homogeneous LQR and an RHC.

In Fig. 3.6 the corresponding behavior of the control inputs is presented. The faster reaction of the RHC control is perfectly visible on the pitch input. This in turn makes the use of the torque input less critical for this control. On the contrary, being less fast on the actuation of an appropriated pitch

command, the non-homogeneous LQR makes a larger use of the torque control. The effect of multiple wind steps can be clearly noticed on this time history.

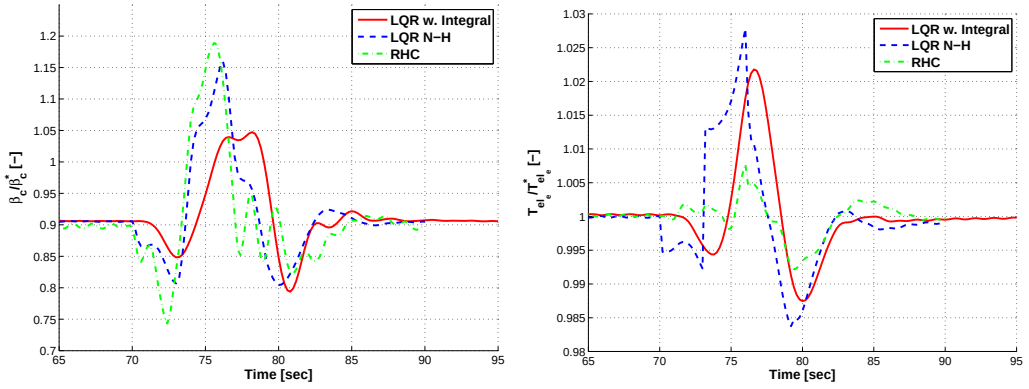

(a) (b)

Figure 3.6: Normalized time histories of the collective pitch (left) and torque (right) controls for an IEC gust with reference speed of 21 m/sec. Comparison between the effects of a non-predictive LQR, a non homogeneous LQR and a RHC.

In Fig. 3.7 it is reported the behavior of the peak-to-peak difference for both the rotational speed Ω and the fore-aft bending moment, for all considered reference speeds. All results are normalized with respect to the value obtained in a constant wind with the same wind speed. The results of the two predictive algorithms are very similar for both the considered quantities in region II, up to 9 m/sec for this turbine. They are almost undistinguishable in region II$\frac{1}{2}$, up to 11 m/sec. In region III the RHC controller behaves globally better than the non-homogeneous LQR in particular on the fore-aft load, but the improvement given by the latter controller with respect to the LQR lacking the predictive component is remarkable.

3.5.2 Turbulence

The tuning of the parameters carried out in deterministic wind conditions has provided a set of good results in gusty wind. On that base, and because simulations in turbulent conditions take a longer execution time with respect to those performed in deterministic wind, thus making the tuning phase potentially very time-consuming, the same set of tuning parameters has been used for simulations in IEC category A turbulence.

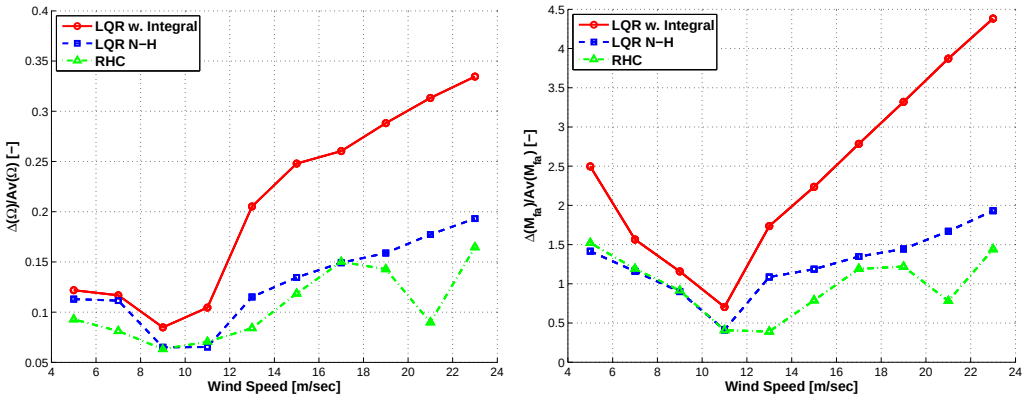

(a) (b)

Figure 3.7: Normalized peak-to-peak variations of the rotational speed (left) and fore-aft bending moment (right) for simulations in IEC gust wind conditions. Performance comparison between the effects of a non-predictive LQR, a non homogeneous LQR and a RHC.

Also here the array of considered reference wind speeds extends from 5 to 23 m/sec, covering the three operating regions of the 3.0 MW machine.

In Fig. 3.8 the performance of the LQR, the non-homogeneous LQR and the RHC is presented in terms of the standard deviation of the power output, calculated on 600 sec simulations and normalized with respect to the reference value for the considered wind speed, and of the damage equivalent load (DEL, see chapter 2), obtained from a rainflow analysis of the time histories of the fore-aft bending moment at the root of the tower for any considered wind speed, also here normalized by the pertinent reference value.

It can be observed that the standard deviation of power, obviously larger in region II where torque is used much more than collective pitch to control the turbine, is not too different for all controllers, the predictive controllers providing a similar performance if compared to the non-predictive controller. However, given the relatively lower values of this index for higher wind speeds, even in presence of little differences in the dimensional values, the percent changes can be expected to be not negligible. The peak of negative performance of the RHC controller for 9 m/sec is also noteworthy: it can be explained with an inappropriate weighting with regard to the rotational speed or control torque, both involved in the definition of power. Of course, the considered wind speed (9 m/sec) is critical, marking the lower end of the transition region, featuring a continuos switching between a condition where the phisical limit on pitch has a limiting effect on the pitch input, and one where this limit is less likely to intervene.

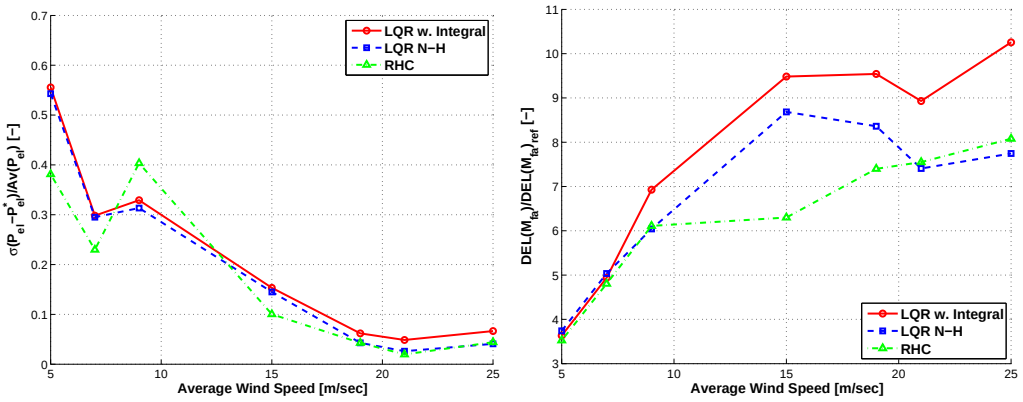

(a) (b)

Figure 3.8: Normalized power standard deviation (left) and tower-base fore-aft bending moment DEL (right) for simulations in IEC category A turbulent wind conditions. Performance comparison between the effects of a non-predictive LQR, a non homogeneous LQR and a RHC.

The results on the fore-aft moment are very encouraging especially in region III, where a visible difference between the behaviors of the predictive controllers and of the classical LQR controller can be noticed. Moreover, as could be expected, the more sophisticated RHC is able to get better results than the non-homogeneous LQR, which nonetheless assures a substantial reduction in the considered load index. For lower reference wind speeds, the effect of both predictive controllers is almost the same, and the improvement with respect to the non-predictive law is less remarkable.

3.5.3 Comparison of the Computational Cost

In order to quantify the computational cost of the proposed formulations, a customized testing environment was set up, separated from the simulator and from the supervisory system. The core routines of both controllers were isolated from the rest of the control code, and executed 10^5 times each to enhance the relative accuracy of the measurements. The initial and final times of the loop were recorded. For both control algorithms, only the operations from the definition of the array of measurements up to the evaluation of the control input have been considered. They involve basically two steps. In the first step the interpolation of the pertinent matrices, i.e. the gains for the non-homogeneous LQR and the system matrices, over the prediction window for the RHC is completed. Next, for the non-homogeneous LQR controller the gain matrix-state array product is executed, while for the RHC

the optimization problem is solved.

The testing program was run on a machine equipped with an `Intel Core™ 2 Duo E6550` 2.33 GHz processor and with 2 GB RAM. The process was executed under `Windows Vista™ Business` and passively monitored in order to make sure that there was no RAM saturation. The test was executed 60 times and the results averaged to avoid interference in the measurements due potentially uncontrolled underlying processes. Based on the recorded times, it was found that the average ratio between the execution time of the RHC and that of the non-homogeneous LQR is $\bar{R} = \frac{1}{60}\sum_{i=1}^{60} R_i = \frac{1}{60}\sum_{i=1}^{60}(\frac{T_{RHC}}{T_{LQR}})_i = 865.43$, where T_{RHC} is the time necessary to repeat the calculations implemented in the core routines of the RHC for 10^5 times, and T_{LQR} is a similar quantity defined for the non-homogeneous LQR. The relative standard deviation is $\frac{\sigma_R}{\bar{R}} = 4.43\%$, a rather small value, showing that the measured ratio R_i is not affected by intense noise. This in turn highlights the fact that the computational cost of the RHC is higher than that of the non-homogeneous LQR, roughly by almost three orders of magnitude. Based on the results presented above, the RHC imposes an increase in terms of computational cost which is larger than the advantage it provides on tower loads and power quality if compared to the non-homogeneous LQR.

3.6 Conclusions

The aim of this chapter was to implement and compare two predictive controllers, able to expand the trimming capabilities of a more common non-predictive, model-based controller by accounting for the anticipate knowledge of the incoming wind speed, provided by a LiDAR sensor.

In order to realize such comparison it was first necessary to implement a LiDAR simulator, able to treat the existing realistic wind flow information used for normal simulations and to perform on it the filtering action that the LiDAR actually performs on the real wind, this way obtaining a realistic measurement of the predicted incoming wind. To this aim a realistic architecture was hypothesized and the simulator assembled and implemented online with the control routines.

The designs of the two considered predictive controllers share the basic theoretical setup, as both are based on the optimization of a quadratic cost function very similar to that of the normal feedback LQR controller. The presented RHC implements an online numerical optimization of that cost function over a given prediction window, while the non-homogeneous LQR is based on a pre-calculated set of gains, designed to account for the anticipated knowledge of the incoming wind as a complimentary exogenous input,

and obtained from an infinite-horizon optimization. In the case of the non-homogeneous LQR, it was shown how to smartly deal with the hypothesis of constant future disturbance and how to apply this control algorithm in real environment, when the incoming disturbance, i.e. the wind, is known over a finite prediction window.

The two controllers have been tested on the `Cp-Lambda` model of the 3.0 MW turbine, first in IEC extreme operating gust (EOG) winds, covering all the spectrum of operating wind speeds in the process. This phase was practically used also to tune the two control systems, finding greater difficulties in the tuning of the RHC than with the other predictive controller. The size of the selected prediction window guarantees good results in deterministic wind conditions, also accounting for the finite and rather low update frequency of the LiDAR measurement. It was shown how, thanks to a smart use of the control input, the advantage on the peak-to-peak variation of the rotational speed and fore-aft moment was clearly visible when using the predictive controllers, with respect to what is obtained from a non-predictive LQR control. Moreover, at this stage it could be realized that the effects of the two predictive controllers were not so different in regions $\mathrm{II}\frac{1}{2}$ and III, while for very low wind speeds the predictive controllers behave similarly to each other and to the non-predictive LQR trimmer. All this in spite of the fact that the non-homogeneous LQR is a fairly simpler controller with respect to the RHC.

The results in turbulent wind are basically aligned with those in deterministic conditions. However, little absolute advantage was obtained in particular on the power output quality, which is even worsened by the RHC for some wind speed in region $\mathrm{II}\frac{1}{2}$. The reason for that has been attributed to the weighing process, which is particularly tricky in this region of operations. The result on the fore-aft DEL is very encouraging for both predictive controllers, while of course in region II the improvement with respect to the results of the classical feedback LQR is not large, as usual in this region, basically because of the physical limits on the pitch input.

Chapter 4

Higher Harmonic Control for Load Reduction

4.1 Introduction

In recent years several research activities have been focused on individual blade pitch control as a mean for reducing loads on crucial structural components of modern wind turbines, as blades, drive-train, bearings and tower. The current literature describes a variety of architectures of the control system and of approaches used for the synthesis of control laws, frequently using individual, decentralized or cyclic blade pitch control. For example, references [35–37, 86] document the development of individual blade pitch control techniques based on the Coleman's transformation, later extended to higher harmonics in Ref. [87] (see also chapter A). Reference [88] reports a similar approach, where the load alleviating control on each blade is implemented based on a decentralized architecture, superimposed to a baseline collective controller used for trimming the machine around each given set point. A decoupled approach is presented also in Ref. [30, 89], where a pitch controller is used for reducing the 1P fluctuations of each blade root bending moment through a H_∞ approach. The effectiveness of a decentralized control architecture aimed at blade load reduction at frequencies that are multiple of rev has also been demonstrated in Ref. [90], while Ref. [54] has studied a multivariable approach aimed at the synthesis of a time-domain controller capable of both trimming the machine and simultaneously reducing fatigue loads.

The research work presented in this chapter explores the multi-layer control architecture depicted in Fig. 4.1.

The proposed approach is based on a multi-layer architecture, that is in-

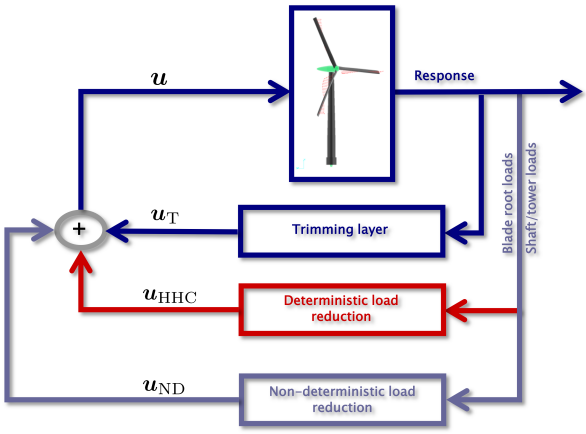

Figure 4.1: Multi-layer control architecture. Inner loop: centralized trimmer; middle loop: deterministic load reduction; outer loop: non-deterministic load reduction.

spired by the consideration that the control of wind turbines is in general a multi-objective optimization problem with (often contrasting) goals characterized by different underlying physical phenomena and space-time scales.

To better explain this issue, consider for instance the loads that arise on the blades when the machine is subject to a hypothetic constant wind, or when it works in turbulent wind conditions: in the first case the spectra of the load signals will feature neat peaks at multiples of the revolution frequency (1P,2P,...) and at the eigenfrequencies of the blades, with amplitudes which will decrease with increasing frequencies. In turbulence, the spectra of the same signals will be distributed continuously over a broad range of frequencies, with peaks at the multiples of rev and at the system eigenfrequencies, even if less marked than before. Generally speaking, in a scenario more like the first, dominated by deterministic loads and not by turbulence, a controller aimed at the reduction of blade loads would not need the same reactivity characteristics as in the second. On the other hand, the control activity and band necessary in a scenario dominated by turbulent loads like the second may not be needed when working with slower varying, more predictable loads typical of the first.

To effectively control the loads in both scenarios, in the present approach multiple control layers (multi-layer) are implemented, each aiming at a specific control target and cooperating with the other layers towards the obtainment of the various control goals; this way, the choice of the controller used on each layer can be optimized and tailored to the specific control goal of that layer, thereby improving performance and simplifying tuning. More

specifically, besides a basic trimming layer, a control loop aimed at the reduction of the loads caused by deterministically varying phenomena and one aimed at the abatement of stochastic oscillations are designed independently and implemented.

The following short paragraphs highlight the main goals and features of the three envisaged loops.

4.1.1 Inner Loop

The inner loop is responsible for the trimming of the machine, i.e. the regulation around a set point during power curve tracking, and for gust load alleviation. As thoroughly shown in chapter 2, this control layer can be implemented as a collective-pitch/torque controller, using a primarily constant pitch – variable torque control logic in region II, a primarily variable pitch – constant torque logic in region III, and some coupled strategy in the transition region between the two [41].

Typical inner loop controllers can be designed as PI, or LQR like that presented in chapter 2. The inner control loop is usually quite effective in the containment of loads caused by gusts characterized by a significant change of the wind speed over the entire rotor disk, where a rapid collective change in pitch setting is needed, possibly accompanied by a corresponding torque adjustment.

While a well designed and tuned collective-pitch and torque controller can show good performance with respect to rotor speed tracking and related tasks (as already demonstrated in chapter 2) and as witnessed by its widespread adoption in industry, such solution is not as effective in the reduction of the deterministic and non-deterministic load fluctuations that are responsible for the accumulation of fatigue damage to the structure, which require cyclic or individual blade pitch actuation.

4.1.2 Middle Loop

In the present control design, a middle loop (refer to Fig. 4.1) is responsible for the reduction of the deterministic loads; these are primarily caused by the blade weight and by the nonuniformity of the spatial distribution of the wind over the rotor disk. The latter effect is due to the vertical wind shear, possible lateral shear, tower shadow effect, and to the fact that the wind direction is in general not parallel to the rotor axis, because of the rotor uptilt and of the possible presence of lateral and vertical wind components (respectively due to operation in yawed conditions and to the terrain orography in proximity of the wind turbine). These loads have a limited bandwidth, with

their principal components located at the lower per rev harmonics: on blade loads, their effect causes peaks at the 1P, 2P, 3P, etc. and less markedly on lower blade natural frequencies; on shaft loads or yaw bearing loads, for three-bladed rotors the most prominent peaks will be at frequencies multiple of the 3P – the reason for that being bound to equilibrium considerations [91]. The harmonic amplitudes of such loads change with rather slow characteristic times, of the order of a rotor revolution for larger turbines, following changes in rotor RPM due to changes in the mean wind speed typical of real environment turbulent wind conditions.

In the multi-layer approach presented here, a higher harmonic control (HHC) law is used for the middle deterministic load layer. HHC is an optimal controller denoted by a quadratic cost function and formulated in the frequency domain, that uses a linear model to relate the harmonics of the inputs to those of the outputs (see references [92–95] and references therein). A full description of the theory and of the design procedure adopted here for the HHC control law will be presented in a following paragraph.

Moreover, two different implementations will be described:

a) When targeting blade loads, a decentralized controller operating the pitch of each single blade individually is used;

b) When targeting loads in the fixed reference frame (e.g. on the shaft bearing, yaw bearing, tower root, or when targeting the air gap in a direct drive machine, etc.), a centralized implementation that results in the coordinated control of the rotor blades is selected.

Since fatigue might be a design driver on some components of a machine and not on another, the choice of the centralized or decentralized implementation should reflect the specific characteristics of the target wind turbine. It may be reported that industrial subjects are usually more concerned about the fatigue loads on structural parts different from the blades, typically on the shaft. This is mainly due to the fact that envelope loads on the blades are typically found in load cases where the control system is not involved (like for instance in extreme turbulence with the turbine parked and at rest). As a consequence, greater importance is attributed by the customers to the centralized implementation. Nonetheless, both implementations will be described in the following, to provide a proof of the potential of the multi-layer control architecture by showing the good performance obtained considering two qualitatively different target loads.

4.1.3 Outer Loop

In principle, it would be possible to include in the HHC design a large number of harmonics, so as to make it effective in controlling also the quickly varying load components. However, this would make the problem of identifying the HHC input-output model much harder to solve. Hence, the HHC design used here accounts only for the slower harmonics dominating the deterministic response, while the control architecture includes also an additional outer control loop (see Fig. 4.1) targeting non-deterministic loads. These are defined as those loads which are caused by variations of the wind with fast temporal scales (fractions of a rotor revolution) and/or small spatial scales (small azimuthal angles, experienced by a blade in a fraction of a revolution), which are typical of wind turbulence.

As for the middle loop, the outer loop is implemented in two different ways, depending on which load is targeted:

a) In the decentralized case, a simple PD controller operates individually on each single blade, driven by estimates of the non-deterministic blade loads, computed as differences of the total measured loads and the lower harmonic ones feeding the middle control layer (see the cross-feed link connecting the inner and outer loops in Fig. 4.1 and see 4.2.2 for details);

b) In the centralized case, the simple but very effective Coleman's transform proportional-integral individual-blade-pitch (IPC) algorithm of Ref. [86] is used. Some details specific to the implementation of this control in our case are provided in section A.

In general, little can be said about the stability of a multi-loop architecture as the one used here. However, the individual blade pitch amplitudes commanded by the middle and outer loops are typically limited to rather small values for a number of reasons, as for example not to affect the regulation at the set point, to limit the actuator duty cycle, and to avoid excessive pitch differences among the blades that might lead to large loads in the case of extreme gusts. As such, these small individual pitch changes can be treated as disturbances, and the overall stability of the system will be determined to a large extent by the robustness to uncertainty of the underlying collective pitch controller, which is typically quite good.

4.2 Formulation of the Controller

In the following the multi-layer controller is mathematically formulated in a very general case, without restrictions on the number of blades B. As the number B is bound to the *a priori* characterization of the harmonic content of the loads in the rotating and nonrotating frames, the approach followed in this presentation makes it possible to apply the theory presented here to both two-bladed or three-bladed turbines, which are the most widespread turbine designs adopted by industry.

In the results section only results obtained applying the multi-layer controller to the model of an existing three-bladed turbine are reported. For a similar turbine, the theory presented here will be finalized with a value of $B = 3$.

Let the pitch-torque input vector to the wind turbine be

$$\boldsymbol{u} = \{\ldots, \beta_b, \ldots, T_{el_c}\}, \tag{4.1}$$

where β_b is the blade pitch input for the b-th blade, $b = (1, B)$, and T_{el_c} is the commanded generator torque. According to the control architecture of Fig. 4.1, input $\boldsymbol{u}$ is obtained as the sum of the contributions of the various control layers as

$$\boldsymbol{u} = \boldsymbol{u}_{\mathrm{T}} + \boldsymbol{u}_{\mathrm{HHC}} + \boldsymbol{u}_{\mathrm{ND}}, \tag{4.2}$$

where

$$\boldsymbol{u}_{\mathrm{T}} = \{\ldots, \beta_{b_{\mathrm{T}}}, \ldots, T_{\mathrm{T}}\} \tag{4.3}$$

is the pitch-torque input provided by the inner trimmer (subscript $(\cdot)_{\mathrm{T}}$ will be used in the following), where notice that $\beta_{1_{\mathrm{T}}} = \ldots = \beta_{B_{\mathrm{T}}}$ if the trimmer is a collective controller (as it usually is);

$$\boldsymbol{u}_{\mathrm{HHC}} = \{\ldots, \beta_{b_{\mathrm{HHC}}}, \ldots, 0\} \tag{4.4}$$

is the input provided by the middle layer devoted to the reduction of deterministic loads, which in the proposed architecture is implemented in the form of a higher harmonic controller (for this reason, subscript $\{\cdot\}_{\mathrm{HHC}}$ will be used for this layer); finally,

$$\boldsymbol{u}_{\mathrm{ND}} = \{\ldots, \beta_{b_{\mathrm{ND}}}, \ldots, 0\} \tag{4.5}$$

is the pitch input provided by the outer non-deterministic (subscript $(\cdot)_{\mathrm{ND}}$) load-reducing loop. Notice that, unless the inner loop (trimmer), the middle and outer loops are purely pitch controllers, giving a null torque input. When the middle and outer loops are implemented following a decentralized approach, so that the pitch contribution may not be coordinated

thus possibly resulting in a change in the collective pitch input, the trimmer implemented in the inner loop will react also by means of an appropriate torque input to keep the machine close to the set point for the rotor rotational speed. Of course, in that case the pitch control action requested by the middle and external layers shall not be intense compared to the pitch required by the inner trimming layer, in order to avoid an excessive drift from the trim condition.

4.2.1 Deterministic Loads: Formulation of the HHC Control Loop

As previously stated, the middle layer is implemented using the HHC approach (see Ref. [92] for details and background information). The algorithm, successfully applied in helicopter industry, consists of four main operations:

1) demodulation from the time to the frequency domain of inputs and outputs (respectively, blade pitch and target loads);

2) identification of a linear model relating harmonics of the inputs to those of the outputs;

3) calculation of the inputs by solving an optimal control problem;

4) remodulation of the computed optimal input harmonics, to obtain the time domain inputs.

For the practical application of this control law, 1) and 2) have to be completed before using the controller in closed loop. Actually, the model identification phase 2) takes place in order to find a relationship between the harmonic characteristics of the control inputs and of the target loads, and those harmonic characteristics are found by signal demodulation (step 1). Once a suitable model becomes available, 1), 3) and 4) can be performed online in closed loop, constituting the application of the HHC control law. Notice that 1) is common to both the offline model identification phase and the closed loop application of the HHC controller. Details about the implementation of all these steps are given in the next subsections.

Signal Demodulation

The signal demodulation problem is here formulated specifically accounting for the fact that wind turbines operate at variable rotor speed, hence in a condition of variable rotor rotational speed Ω. This fact, making the application of HHC to wind turbines different from its use in helicopter industry,

makes the use of an azimuth-based demodulation more suitable than one based on Ω.

At the rotor azimuthal position ψ_K, which can be defined as the azimuth angle of the blade for which $b = 1$, suppose to need to demodulate a signal $a(t)$ that is available in terms of measurements $\hat{a}(t_k)$, sampled at times $t_k = k\Delta t$ over the previous N_R rotor revolutions. The value of the azimuth ψ_K at which the demodulation is performed can be expressed as a function of a fraction $\Delta\psi$ of the round 2π, as $\psi_K = K\Delta\psi$.

Notice that from these definitions two different sampling rates can be defined, one in space (azimuth) and the other one in time:

- A slow azimuthal sampling $\Delta\psi$ corresponding to the frequency with which demodulation is performed (typically, four times per rev in this work, so that $\Delta\psi = \frac{\pi}{2}$), whose steps are indicated by capital index K. As previously pointed out, notice that, on account of the fact that the rotor rotational speed on a wind turbine varies in time, a spatial sampling based on the rotor azimuth is used instead of a temporal sampling.

- A fast time sampling Δt corresponding to the measurement rate of the sensors (typically, in the range of the tens of Hz), whose steps are labeled by index k.

Demodulation of the signal over a window of N_R revs is expressed as

$$\hat{a}(t_k) = \hat{a}(\psi(t_k)) \approx \boldsymbol{a}_K^T \boldsymbol{s}(\psi(t_k)), \quad \psi(t_k) \in [\psi_K - 2\pi N_R, \psi_K], \tag{4.6}$$

where

$$\boldsymbol{a}_K = \{a_K^0, \ldots, a_K^{i,s}, a_K^{i,c}, \ldots\}^T \tag{4.7}$$

is the unknown vector of harmonic amplitudes at the current demodulation step K, and

$$\boldsymbol{s}(\psi(t_k)) = \{1, \ldots, \sin(i\psi(t_k)), \cos(i\psi(t_k)), \ldots\}^T, i = (1, N_H), \tag{4.8}$$

is a vector of N_H harmonic bases. In principle, the size of the harmonic base N_H can be chosen arbitrarily, but an increase in the number of considered harmonics also increases the number of coefficients to be identified, and as a result the length and the complexity of the identification phase. Moreover, during closed-loop simulations a larger model is heavier to manipulate when making control calculations. Besides that, a control law based on a larger set of control/input variables, i.e. of harmonic amplitudes of pitch control and target loads, can be difficult to tune appropriately. A good choice

for the number of N_H may be suggested by some *a priori* considerations on the harmonic content of the considered signals. For instance, the spectra of blade loads will show prevalent peaks at multiples of the 1P, while those of shaft loads basically at multiples of the 3P.

Notice that the minimum swept angle that should be considered for the demodulation process is 2π, which is necessary to find the harmonic amplitude of signals oscillating at the 1P. Moreover, to correctly find the amplitude of the 1P oscillation when using samples collected over more than one rotor revolution, only multiples of 2π should be considered. For that reason, provided the 1P is a frequency of interest, as is usually the case for instance on blade loads, N_R should be an integer not inferior to 1.

The demodulation operation involves samples available at all time steps t_k covered during the last N_R revolutions. At the next demodulation step $K+1$, corresponding to an increase in rotor azimuth of the angle $\Delta\psi$, the new samples gathered over the latter $\Delta\psi$ rotation are added to the head of the demodulation window, while the oldest samples are discarded from its tail, to keep its azimuthal coverage of constant length. In other words, when moving from a demodulation azimuth ψ_K to the next $\psi_{K+1} = \psi_K + \Delta\psi$, the oldest set of data used for the demodulation at ψ_K are discarded in favor of the data collected between ψ_K and ψ_{K+1}. As a result the azimuth span over which the demodulation is performed remains always equal to $2N_R\pi$.

Fig. 4.2 illustrates through an example the definition of the azimuth spans considered for signal sampling and for HHC control application. Consider a signal measured on the blade for which $b = 1$. Given $N_R = 1$ and $\Delta\psi = \frac{\pi}{2}$, when the azimuth of that blade is such that $\psi = \psi_K$, then the demodulation is performed based on the data collected on the last 2π swept by the same blade. Then for the following $\Delta\psi$, from ψ_K up to ψ_{K+1}, the HHC pitch control based on the amplitudes found through demodulation at ψ_K is applied by the actuator of the considered blade.

Concerning the demodulation operation, the current estimate of the sine and cosine components of the i-th harmonic amplitude, labeled respectively $a_K^{i,s}$ and $a_K^{i,c}$, can be computed by projection as

$$\begin{aligned} a_K^{i,s} &= \frac{1}{\pi N_R} \int_{\psi_K - 2\pi N_R}^{\psi_K} \hat{a}(\psi) \sin(i\psi) \mathrm{d}\psi, \\ a_K^{i,c} &= \frac{1}{\pi N_R} \int_{\psi_K - 2\pi N_R}^{\psi_K} \hat{a}(\psi) \cos(i\psi) \mathrm{d}\psi, \end{aligned} \tag{4.9}$$

where the integrals, extended over the last N_R revolutions, can be easily evaluated using the classic trapezoidal rule.

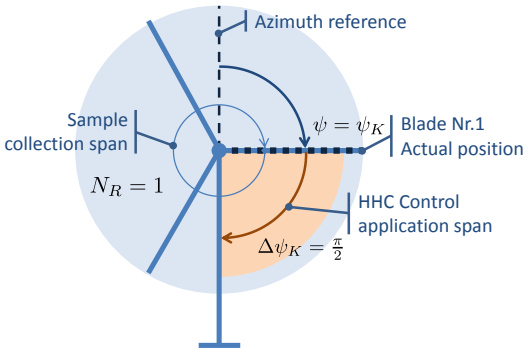

Figure 4.2: Graphical definition of the azimuth spans considered for signal sampling and for HHC control application. Example with $N_R = 1$ and $\Delta\psi = \frac{\pi}{2}$.

Model Identification

In order to identify a suitable linear model to be used for control calculations it is necessary to run an offline identification process. The idea pursued in the framework of HHC is that of finding a linear relationship between selected harmonic amplitudes of the pitch input and of the target load. The input-output model takes the form [92]

$$\boldsymbol{z}_K = \boldsymbol{T}(U)\boldsymbol{b}_K, \tag{4.10}$$

where the vector of output harmonics is

$$\boldsymbol{z}_K = \{\ldots, z_K^{i,s}, z_K^{i,c}, \ldots\}^T, \tag{4.11}$$

the vector of HHC input harmonics is

$$\boldsymbol{b}_{\mathrm{HHC}_K} = \{\ldots, \beta_K^{j,s}, \beta_K^{j,c}, \ldots\}^T, \tag{4.12}$$

and $\boldsymbol{b}_K = \{\boldsymbol{b}_{\mathrm{HHC}_K}^T 1\}^T$ its augmented form. Matrix

$$\boldsymbol{T}(U) = [\boldsymbol{\Theta}(U)\boldsymbol{z}_0(U)] \tag{4.13}$$

is the augmented transfer function, that includes the Jacobian $\boldsymbol{\Theta}(U)$ of the outputs with respect to the inputs, and the baseline output harmonics $\boldsymbol{z}_0(U)$, which account for the non-HHC related response of the machine. The notation highlights the fact that these quantities, in general, depend on the wind speed U, and hence Eq. (4.10) represents a linear parameter varying model.

As stated above, input-output models are identified offline. Since the model typically depends on the wind speed, separate identifications are conducted at a number of trim points of interest, that cover the entire operating range of wind speeds of the machine. At each trim point, denoted by the wind speed U_l, $l = (1, N_T)$, model (4.10) is identified by subjecting the plant to a suitable excitation, recording the response of the machine, demodulating inputs and outputs, and finally estimating $\boldsymbol{T}(U_l)$ using least-squares. More details about the identification simulations actually run are reported in the results paragraph.

Notice that the demodulation of the input is recommendable, because even if the input excitation is exactly known, it is filtered by pitch actuators whose dynamic response is usually rather slow. Moreover, the pitch excitation is superimposed to the trimmer control inputs, which are constantly adjusted to keep the machine well trimmed: this results in small and slow pitch movements, which nonetheless modify the actual pitch input with respect to the prescribed excitation. These issues can be easily dealt with by performing a demodulation also of the input signal.

Now consider an excitation phase lasting M rotor revolutions; over the K-th revolution, inputs and outputs are demodulated as previously explained using (4.9) with $\Delta\psi = 2\pi$, which yields estimates of the harmonic amplitudes of the two signals. The input and output harmonics of interest, i.e. those which enter into the definition of the input-output model (4.10), are gathered in vectors $\boldsymbol{z}_K$ and $\boldsymbol{b}_{\mathrm{HHC}_K}$, respectively, and stored in matrices as

$$\begin{aligned} \boldsymbol{Z} &= [\ldots \boldsymbol{z}_K \ldots], \\ \boldsymbol{B} &= [\ldots \boldsymbol{b}_K \ldots]. \end{aligned} \tag{4.14}$$

Minimization of the Frobenius norm $\|\boldsymbol{E}\| = \sqrt{\sum_{ij} E_{ij}^2}$ of the model error matrix $\boldsymbol{E} = \boldsymbol{Z} - \boldsymbol{T}(U_l)\boldsymbol{B}$, yields the least-squares estimate of the augmented transfer function at the current trim point:

$$\boldsymbol{T}(U_l) = \arg\min_{\boldsymbol{T}(U_l)} \frac{1}{2}\|\boldsymbol{E}\|^2 = \boldsymbol{Z}\boldsymbol{B}^T(\boldsymbol{B}\boldsymbol{B}^T)^{-1}. \tag{4.15}$$

Control Law

The HHC control action is obtained by minimizing the cost

$$J = \frac{1}{2}(\boldsymbol{z}_K^T \boldsymbol{Q} \boldsymbol{z}_K + \Delta\boldsymbol{b}_{\mathrm{HHC}_K}^T \boldsymbol{R} \Delta\boldsymbol{b}_{\mathrm{HHC}_K}), \tag{4.16}$$

subjected to the input-output model constraint (4.10). The symmetric weight matrices $\boldsymbol{Q}$ and $\boldsymbol{R}$ may be scheduled as functions of the mean wind,

i.e. $\boldsymbol{Q} = \boldsymbol{Q}(U)$ and $\boldsymbol{R} = \boldsymbol{R}(U)$. Vector $\Delta \boldsymbol{b}_{\mathrm{HHC}_K}$ represents the increment to the HHC control input in the frequency domain between step K and step $K+1$, i.e.

$$\boldsymbol{b}_{\mathrm{HHC}_{K+1}} = \boldsymbol{b}_{\mathrm{HHC}_K} + \alpha \Delta \boldsymbol{b}_{\mathrm{HHC}_K}, \tag{4.17}$$

$\alpha \in [0, 1]$ being a relaxation factor used for controlling stability and quickness of the controller [94].

Imposing the stationarity of the cost augmented by the constraints with respect to the input increment, leads to the optimal control policy:

$$\Delta \boldsymbol{b}_{\mathrm{HHC}_K} = -(\boldsymbol{\Theta}(U)^T \boldsymbol{Q} \boldsymbol{\Theta}(U) + \boldsymbol{R})^{-1} \boldsymbol{\Theta}(U)^T \boldsymbol{Q} \boldsymbol{z}_K, \tag{4.18}$$

which is driven by the demodulated loads at the current step, $\boldsymbol{z}_K$.

Wind scheduling is obtained by estimating the current mean wind U by using a moving average over a window of 10 sec of the instantaneous turbulent samples provided by an anemometer or a wind observer [23]. The wind scheduled input-output model is obtained by linear interpolation of the values stored at the trim points t and $t+1$, i.e.

$$\boldsymbol{\Theta}(U) = (1 - \xi)\boldsymbol{\Theta}(U_l) + \xi \boldsymbol{\Theta}(U_{l+1}), \tag{4.19}$$

where $\xi = (U - U_l)/(U_{l+1} - U_l)$, $\xi \in [0, 1]$.

The optimal HHC input (4.17) is held fixed until the next K step. At each one of the fast sampling time instants t_k at which the inner control loop operates, the HHC control input is modulated back in the time domain, added to the current input provided by the inner controller, and fed to the actuators.

It has been already mentioned that the choice of the HHC control update frequency, i.e. the azimuthal spacing of the K steps, is related to the choice of the harmonics in the HHC controller, and one should use faster updates in connection with an increasing number of harmonics targeted by the controller. In the examples shown later in this work, the highest harmonic never exceeded the 7P, and it was found that K steps could be spaced apart of a quarter of a revolution. In fact, faster updates did not lead to improvements in the quality of the results, since enough new measurements are necessary to generate changes in the estimates of the harmonic amplitudes.

4.2.2 Decentralized and Centralized Implementations

Decentralized Architecture

In the decentralized control architecture, depicted in Fig. 4.3, each blade operates independently from the other ones under the action of its own controller. This arrangement is suitable when the aim is the reduction of the

blade loads; notice that, since there is no coordination among the blades in this case, lower blade loads might not always imply similarly lowered loads in the fixed system (e.g., at the main or yaw bearings).

The HHC controllers are implemented as previously explained, using harmonics from 1P up to typically 3P both for inputs and outputs.

The external control loop is implemented as follows. Using the model definition (4.10), for a given wind speed U (which corresponds to a given input from the inner trimmer) and given control input $\boldsymbol{b}_{\mathrm{HHC}_K}$, the harmonic amplitudes that one should expect to be observing on the blade are

$$\boldsymbol{z}_{\mathrm{EXP}_K} = \boldsymbol{z}_0(U) + \boldsymbol{\Theta}(U)\boldsymbol{b}_{\mathrm{HHC}_K}. \tag{4.20}$$

This frequency domain load, modulated back in time using the vector of harmonic bases and evaluated at the current instant t_k, yields an expected load

$$z_{\mathrm{EXP}}(t_k) = \boldsymbol{z}^T_{\mathrm{EXP}_K}\boldsymbol{s}(\psi(t_k)). \tag{4.21}$$

In the absence of turbulence, and clearly in the absence of modeling errors as well, this quantity should match the load measured by the load sensors at the current time instant.

Hence, any difference with respect to the value provided by Eq. (4.21) can be interpreted as a fast disturbance generated by turbulence, which should induce a feedback in the blade pitch so as to try to reject it. The difference between the current sensor reading $\hat{z}(t_k)$, low-pass filtered so as to damp the effect of noise, and the expected value is computed as

$$\Delta z(t_k) = \hat{z}(t_k) - z_{\mathrm{EXP}}(t_k). \tag{4.22}$$

Based on this estimate of the load fluctuation, the pitch input of the non-deterministic layer is computed using a simple proportional-derivative control as

$$\beta_{\mathrm{ND}}(t_k) = -K_P\Delta z(t_k) - K_D\frac{\mathrm{d}\Delta z(t_k)}{\mathrm{d}t}. \tag{4.23}$$

This additional pitch input is combined with the ones provided by the inner and middle layers according to Eq. (4.2), and sent to the blade actuators.

Centralized Architecture

The centralized control architecture is depicted in Fig. 4.4. This architecture is suitable when the aim is the reduction of the loads in the fixed system (e.g., at the main or yaw bearings). In fact, in contrast to the previous

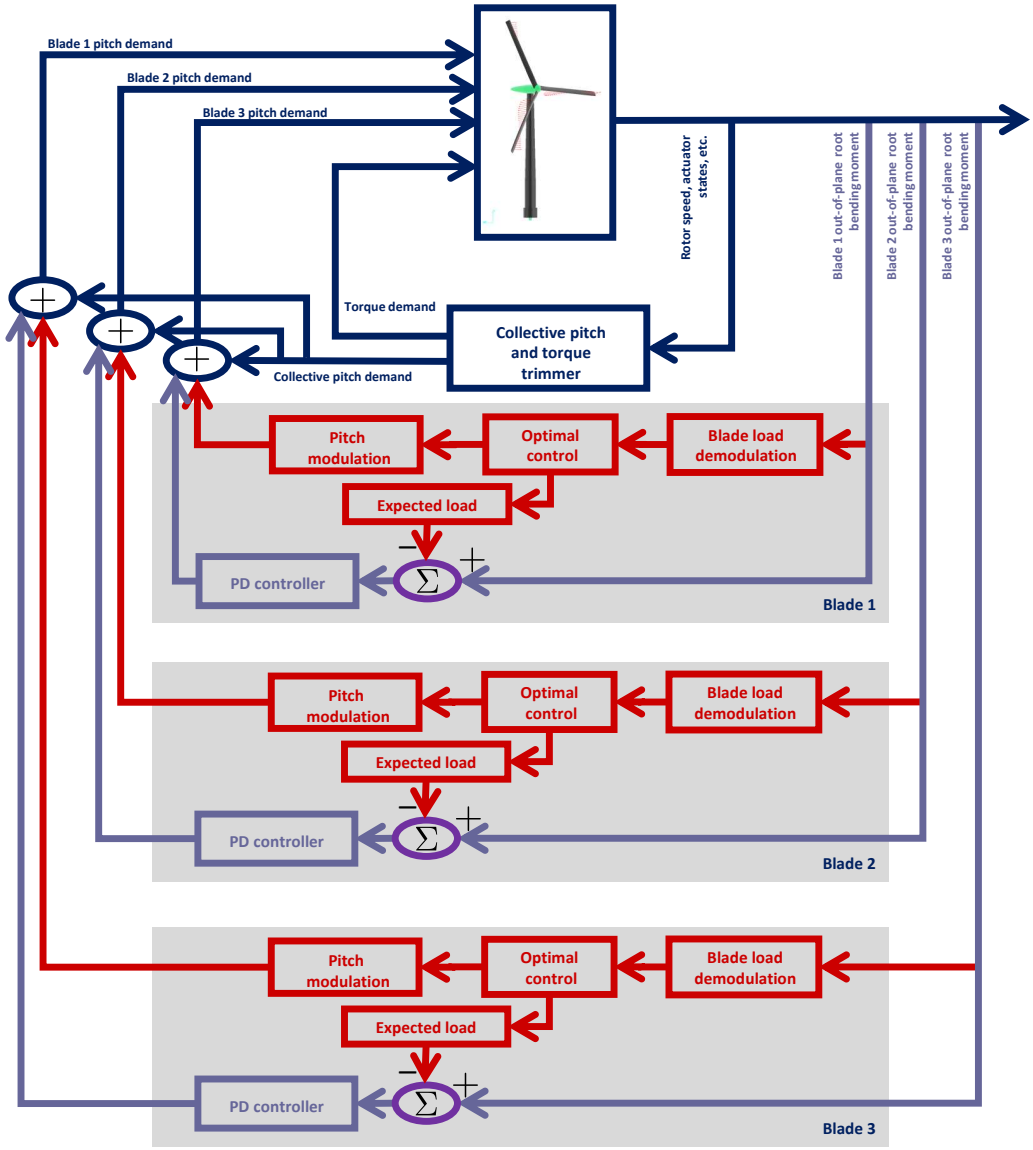

Figure 4.3: Decentralized control architecture.

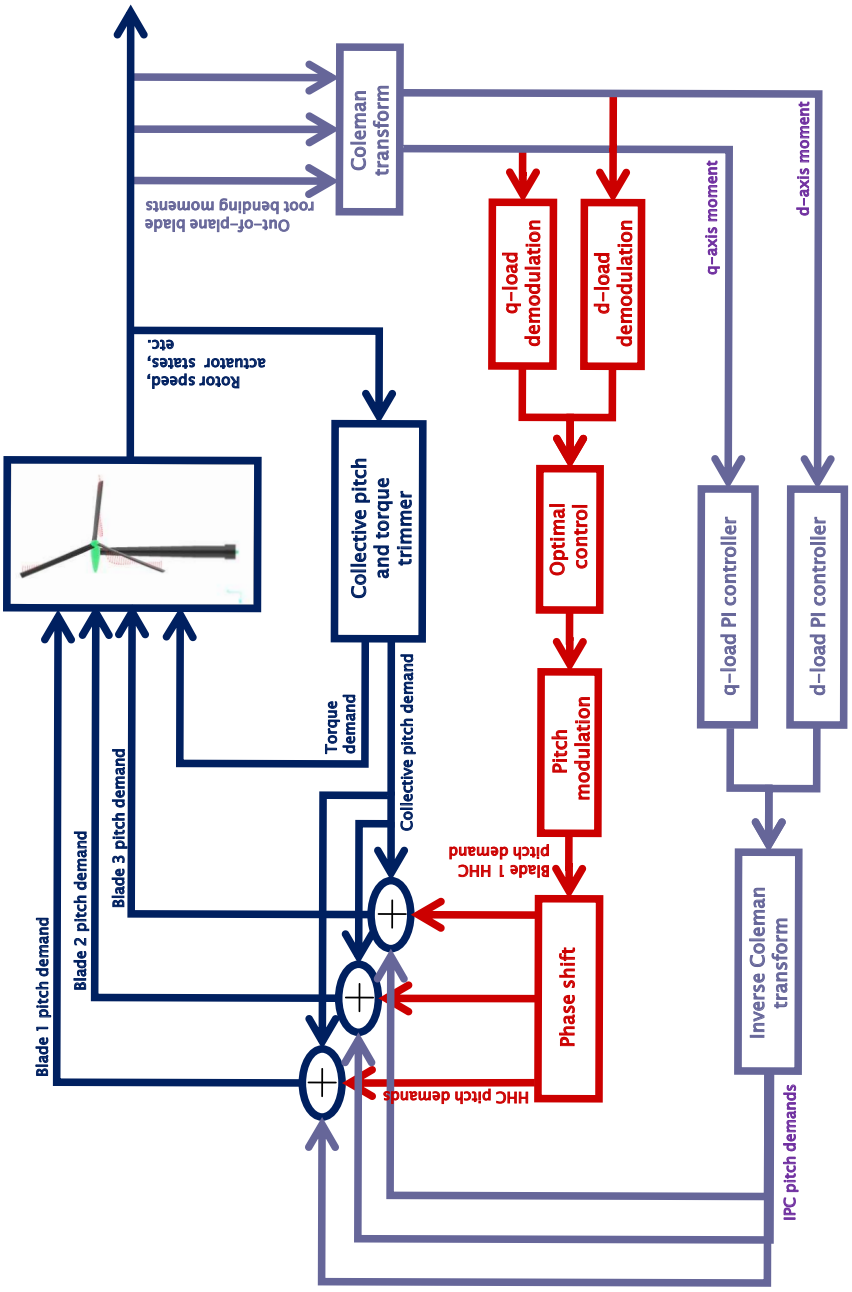

Figure 4.4: Centralized control architecture.

decentralized case, the action of the three blades must be coordinated to give a positive effect on one common target load.

A single centralized HHC controller is used for computing the pitch inputs of the master blade ($b = 1$), while the other blades are commanded using a cyclic pitch regulation logic. The HHC input vector (Eq. (4.12)) is represented by the blade pitch harmonics of the master blade. The master blade pitch input in the time domain is computed as

$$\beta_1(t_k) = \boldsymbol{\beta}_{1_K}^T \boldsymbol{s}(\psi_1(t_k)), \tag{4.24}$$

where the vector of master blade pitch amplitudes is

$$\boldsymbol{\beta}_{1_K} = \{\ldots, \beta_{1_K}^{j,s}, \beta_{1_K}^{j,c}, \ldots\}^T, \tag{4.25}$$

and

$$\boldsymbol{s}(\psi_1(t_k)) = \{1, \ldots, \sin(i\psi_1(t_k)), \cos(i\psi_1(t_k)), \ldots\}^T \tag{4.26}$$

is its harmonic base vector, with $i = (1, N_H)$. The time-domain pitch of the other blades is readily obtained as

$$\beta_b(t_k) = \boldsymbol{\beta}_{b_K}^T \boldsymbol{s}(\psi_b(t_k)), \tag{4.27}$$

where $\psi_b(t_k) = \psi_1(t_k) - 2\pi(b-1)/B$, $b = (2, B)$.

The HHC output vector (Eq. (4.11)) is represented by the harmonics of the moment components in the fixed system. If the machine is equipped with sensors that can measure the fixed system load components, then these quantities can be used directly; on the other hand, if the machine is equipped with sensors at the blade roots, then the fixed system components can be computed by using the Coleman's transformation [86], as shown in Fig. 4.4.

The choice of harmonics of inputs and outputs must be made considering the filtering characteristics of a rotor [91]. For example, the shaft bending moment will contain only harmonics at the multiple of the number of blades, iBP (for example 3P, 6P, etc. for a three bladed rotor), and are controlled by pitch inputs at $i(B-1)$P and $i(B+1)$P harmonics (for example, 2P and 4P blade pitch inputs control 3P loads).

The non-deterministic loop is implemented using the formulation presented in Ref. [86], where two independent single-input/single-output (SISO) proportional integral (PI) controllers are used for reducing the $(d-q)$ axis [86] loads, i.e. the fixed system yawing and nodding moment components. If $\hat{z}_d(t_k)$ and $\hat{z}_q(t_k)$ are the two load components measured on $(d-q)$ at time t_k, the fixed system PI pitch inputs are defined as

$$\begin{aligned} \beta_d(t_k) &= -K_P \hat{z}_d(t_k) - K_I \int_{t_k - T_I}^{t_k} \hat{z}_d(\tau)\, \mathrm{d}\tau, \\ \beta_q(t_k) &= -K_P \hat{z}_q(t_k) - K_I \int_{t_k - T_I}^{t_k} \hat{z}_q(\tau)\, \mathrm{d}\tau. \end{aligned} \tag{4.28}$$

The corresponding blade pitch inputs are computed using the partial inverse Coleman's transformation $\boldsymbol{C}(t_k)$ as

$$\left\{ \begin{array}{c} \beta_{\mathrm{ND}_1}(t_k) \\ \beta_{\mathrm{ND}_2}(t_k) \\ \beta_{\mathrm{ND}_3}(t_k) \end{array} \right\} = \boldsymbol{C}(t_k) \left\{ \begin{array}{c} \beta_d(t_k) \\ \beta_q(t_k) \end{array} \right\}, \tag{4.29}$$

where

$$\boldsymbol{C}(t_k) = \left[\begin{array}{cc} \cos\psi_1(t_k) & \sin\psi_1(t_k) \\ \cos\psi_2(t_k) & \sin\psi_2(t_k) \\ \cos\psi_3(t_k) & \sin\psi_3(t_k) \end{array} \right]. \tag{4.30}$$

These additional pitch inputs are combined with the ones provided by the inner and middle layers according to Eq. (4.2), and sent to the blade actuators.

4.3 Results

The example tests were conducted using a 2.5 MW class A wind turbine (see chapter 1). The inner loop uses a PID feedback term on the collective blade pitch driven by the rotor angular speed error, while the input torque is tabulated as a function of the current RPM and requested pitch. The pitch actuators in the plant simulation are modeled as second order systems, with a maximum pitch rate of 7 deg/sec. The machine is equipped with blade root strain gauges, which provide the readings for the load alleviating middle and outer loops at 20 Hz; when needed, loads in the fixed system are computed by use of the Coleman's transformation [35, 86].

As usual, all simulations were conducted using the software `Cp-Lambda`.

4.3.1 Quality Assessment of the Model Identification Phase

Input-output models were identified for both the centralized and decentralized implementations of the HHC controller. Pitch signals were obtained directly from the controller inputs sent to the actuators; this way, as stated above, the identified model automatically takes into account the pitch actuator dynamics. The identification process was based on simulations performed in non-turbulent wind conditions, with hub speeds between 5 and 23 m/sec every 2 m/sec. At each trim condition, the plant `Cp-Lambda` model was excited using a modulated pitch input featuring a prescribed harmonic content, for a duration of fifteen rotor revolutions. The pitch input was generated as

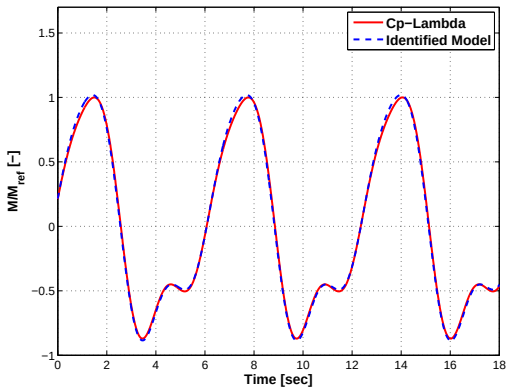

Figure 4.5: Comparison between plant and identified model outputs (blade out-of-plane bending moment) for a same excitation, for a trim point at 19 m/sec. Multi-body plant: solid line; identified model: dashed line.

a smooth signal with a different frequency content at each revolution, to improve the conditioning of the identification process. The response of the plant was used for identifying the input-output model, using the procedure described previously. For the centralized case, the nodding and yawing bending moments measured on the shaft are used. They are obtained by means of the Coleman's transformation starting from the lag and flap moments measured at the root of the blades. If direct measurements of the shaft moments were available, then the use of Coleman's transformation would not be necessary, as also stated in [86]. For the decentralized case, flap and lag moments at the root of the blades are used.

To verify the generality of the identification process, the plant `Cp-Lambda` and the identified models were excited with new pitch input time histories, having the same frequencies as those used for identification but with different amplitudes and phases. As an example relative to the decentralized implementation, Fig. 4.5 shows the normalized time histories of the out-of-plane blade root bending moment generated by the plant and by the identified model during this new excitation phase. The model shows an excellent fidelity to the plant, both in terms of amplitude and of phase. Results of similar quality were obtained at other trim points, and also for the centralized implementation.

A feature of the input-output models identified for the purpose of HHC control following the procedure specified above is the robustness with respect to a change in wind. If a model identified for a given average wind are verified using another wind value the result is not easily distinguishable from that presented in Fig. 4.5. This is true even for a couple of very different wind

speeds.

4.3.2 Centralized Implementation

Load Reduction in Deterministic Wind

In the centralized case, the target load is chosen as the bending moment at the low speed shaft cross section located at the interface with the rotor hub. In steady wind conditions, this load oscillates at the triple multiples of the rev frequency (i.e. 3P, 6P, etc.). As a consequence, the HHC model can be synthesized using the 3P and 6P harmonics of the outputs. These in turn can be controlled by means of cyclic pitch input oscillating at the 2P, 4P, 5P and 7P harmonics of the inputs. The reason for this choice of identified frequencies in the target loads and in the middle loop control input is bound to equilibrium and controllability considerations when passing from rotor loads, like bending moments at the root of the blades, to fixed frame loads, like the nodding and yawing bending moments on the shaft.

Moreover, even if it can be predicted that only the aforementioned frequencies should be present in the target load, and they should be controlled by means of some specific control input frequencies, in principle the model could be identified accounting for a full array of frequencies both in the input and in the output signals. This means that it is possible to excite the machine with an excitation pitch input featuring all the nP frequencies from 1P to 7P, and the same frequencies can be accounted for in the demodulation of the output. If the load behave as predicted by theory, than only the multiples of 3P will be present in the target load, and they will be controlled by 2P, 4P, 5P and 7P. Using this more general procedure it is possible to capture some coupling effects not predicted by theory, which holds precisely only in strictly periodic conditions (constant Ω) which are never met in real environment. These couplings are such that some effects of a control input moving at the 3P and 6P can be seen on the components of the target loads oscillating at the same frequencies. Of course, even in not strictly periodic conditions, these coupling effects are much less visible than what is predicted by theory for periodic conditions. As virtually no improvement in terms of load reduction can be appreciated using a model identified accounting for more frequencies than those suggested by theory, the use of more frequencies has been abandoned, thus reducing the difficulty of the weight tuning process. As a result, the control is applied by means of 2P and 4P in the input to target the load component at the 3P, and by means of the 5P and 7P to target the load component at the 6P.

As for the LQR control, diagonal weight matrices Q and R are used, and

as suggested above they can be tuned to be functions of the wind speed. The process of finding out weight values able to provide a good compromise between the increase in actuator duty cycles and the performance on loads may be very complicated when accounting for too many harmonics both in the input and output signals. This issue, typical of many control problems on MIMO systems, can be solved by manual tuning only if the number of considered states and controls remains limited. For larger problems, a weight optimization procedure can be set-up, but the needed calculation time is too high even for the relatively limited-size case specifically presented here.

After having identified models at a few trim points (specifically, every 2 m/sec starting from 5 up to 23 m/sec), as previously explained, simulations were carried out in constant-in-time winds, so as to perform a first assessment of the effectiveness of the proposed control architecture in the reduction of deterministic loads.

The HHC control law was updated four times per revolution ($\Delta\psi = \frac{\pi}{2}$), using the relaxation factor $\alpha = 0.1$.

Fig. 4.6 shows the time histories and spectra of the normalized resultant of the shaft bending moment, for a constant wind speed of 15 m/sec and an exponential shear layer coefficient of 0.2.

Three control systems are considered here: the collective PID trimmer, the same PID trimmer coupled to the SISO PI IPC controller of Bossanyi [86] (termed in the following B-IPC), and the proposed controller (trimmer with centralized HHC and external B-IPC loop) shown in Fig. 4.4. In this implementation wind-scheduled gains were considered for the B-IPC loop, to get an optimized performance with varying wind speed conditions.

The gain selection process, like the model selection for the HHC loop, is based on a linear interpolation between the closest stored data, and depends on the measured hub-height wind value averaged on the last 10 sec. The use of a filtered wind speed is not strictly necessary when working with deterministic wind fields, but is of great importance in turbulent wind conditions, to avoid excessive fluctuations of the gains and the resulting noise in the control input.

As can be noticed from the plot of the time histories, the B-IPC controller nicely reduces the load mean value (see the markers at the null frequency). From the spectra, the B-IPC is also rather capable of reducing the 3P load harmonics, but its effect is very limited or even slightly negative at the higher multiples of rev. On the contrary, the addition of the HHC loop, while still taking advantage of the good qualities of the B-IPC (in terms of reduction of the load mean value and 3P harmonic), effectively reduces also the higher harmonics of the target load.

Besides the performance recorded on the shaft, which is basically the

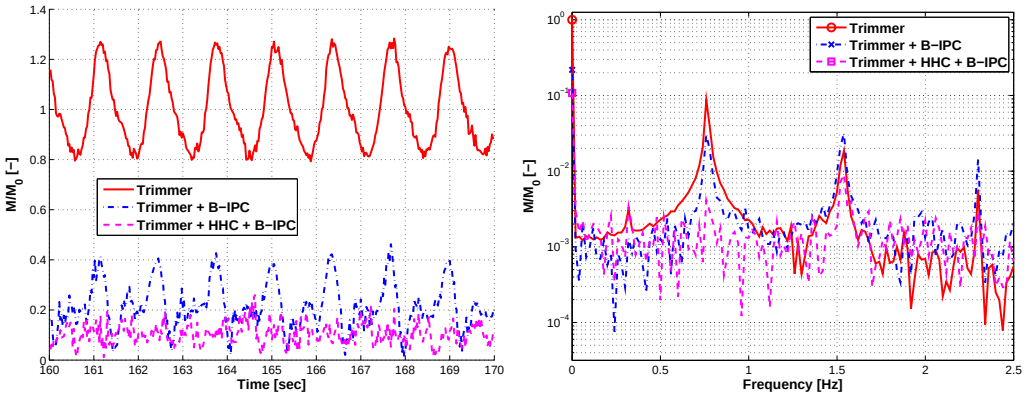

(a) (b)

Figure 4.6: Normalized time histories and spectra of the shaft bending moment resultant, obtained in constant 15 m/sec wind with 0.2 power law shear. Comparison between the effects of the trimmer, of the trimmer operating together with a B-IPC, and of the multi-layer control. Both time histories and spectra are normalized to the zero-frequency peak value obtained with the sole collective trimmer.

same for every mean wind in deterministic conditions, also the side-effects of this control are totally good on the blade out-of-plane moments (Fig. 4.7). Even if these are not directly targeted, a huge reduction of the 1P and 2P peak is achieved, at the cost of a slight increase in 3P, with the multi-layer controller. The constant value of this load is basically unaffected.

Also power output is left almost totally unchanged.

Load Reduction in Turbulent Wind

Next, simulations were conducted in turbulent wind conditions of category A intensity for a duration of 600 sec, for mean hub winds between 5 and 23 m/sec [66, 74]. To account for some of the slower effects caused by turbulent fluctuations, an estimate of the mean wind was computed using a moving average of the anemometer reading based on a time window of 10 sec. As for the deterministic case, the estimated mean wind speed was used for interpolating the models previously identified at the selected trim points.

A representation of the performance of the controllers is provided by the bar diagrams of Fig. 4.8. The figure refers to a mean hub wind speed of 21 m/sec, and reports the percent change in standard deviation (STD) and damage equivalent load (DEL) for the blade root and shaft bending moments, together with the percent change in STD and mean values of generated power.

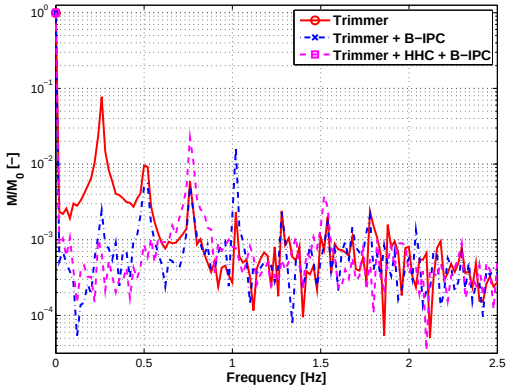

Figure 4.7: Normalized spectra of the Nr.1 blade out-of-plane bending moment in constant 15 m/sec wind with 0.2 power law shear. Comparison between the effects of the trimmer, of the trimmer operating together with a B-IPC, and of the multi-layer control. The spectra are normalized to the zero-frequency peak value obtained with the sole collective trimmer.

For the S-N fatigue slope of the material used for the DEL evaluation, the value $m = 3.5$ was used for the shaft loads and $m = 10$ for the blade loads, as these are typical values for steel and composite materials, respectively (see chapter 2).

The figure at left reports results obtained with the sole B-IPC controller, while that at right shows what happens with the proposed multi-layer controller; in both cases, comparisons are made with respect to the sole collective PID trimmer.

These plots show significant reductions slightly larger than 40% in both STD and DEL for the goal quantity, i.e. the shaft bending moment. The HHC layer brings some further improvement to the performance of the B-IPC controller, pushing the load reduction to slightly above 45%. In terms of blade loads, the new scheme and the B-IPC show very similar behavior. In all cases, the effects on power are quite small, with only a marginal rise in power STD, and this remains true for any mean wind speed in the full load region.

A more comprehensive view of the performance gain in terms of shaft load DEL is provided on Fig. 4.9.

For some wind speeds between the cut-in and cut-out speed values for the considered 2.5 MW machine, this plot shows a comparison between the percent reduction of the shaft bending moment DEL obtained with the B-IPC or with the multi-layer controller with B-IPC and HHC loops. In both cases, the percent reductions are evaluated with respect to the performance of the

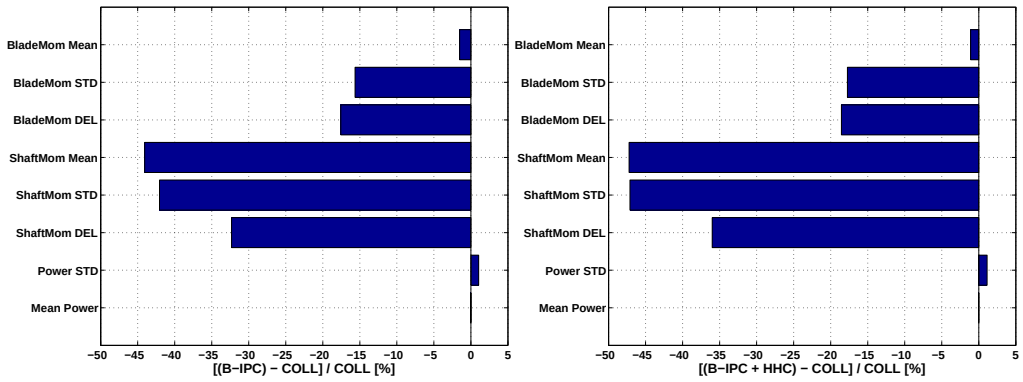

(a) B-IPC (b) B-IPC and HHC loops

Figure 4.8: Percent differences (wrt. collective PID trimmer) of some physical quantities for operation in IEC category A turbulent wind at 21 m/sec mean speed. Left: collective PID trimmer with B-IPC. Right: collective PID trimmer with centralized HHC and external B-IPC loops.

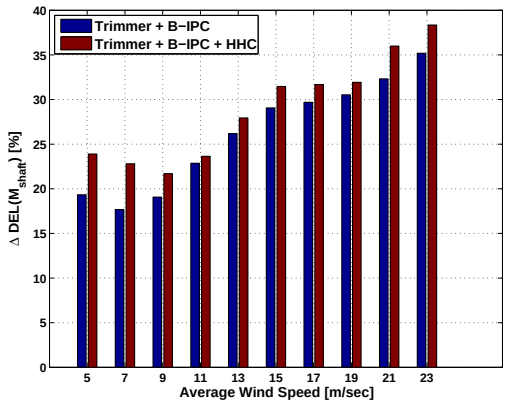

Figure 4.9: Percent performance gains (wrt. collective PID trimmer) on shaft bending moment DEL for operation in turbulent wind at several wind speeds between cut-in and cut-out, using collective PID trimmer with B-IPC (left columns) or PID trimmer with B-IPC and HHC loops (right columns). Positive gain values correspond to a load reduction with respect to the trimmer.

trimmer. The advantage given by the HHC loop is noticeable on this specific performance index for any considered wind speed, but the difference between B-IPC and multi-layer control is more visible in region II and in region III, close to the cut-out wind speed. It is noteworthy that even in region II, where the demanded pitch command is more often limited by a physical constraint of minimum pitch, it is still possible to get an improvement on performance with respect to the sole B-IPC by implementing an HHC loop.

Moreover, the B-IPC performs in an increasingly better way moving from lower towards higher wind speeds, while the improvement given by the HHC is larger close to the lowest and highest wind speeds, as previously pointed out. As the control gains of both controllers are scheduled in order to perform well at all wind speeds, the variable performance of these control laws should not be explained with a not appropriate tuning of the gains, but in particular for operations in region II to the physical minimum limit imposed to the movement of pitch. The varying performance shown by the HHC for different winds can be explained with a specific ability of this controller to thoroughly capture the behavior of the system in particular for some wind speeds (corresponding to some equilibrium configurations of pitch, torque and states of the machine), by accounting for the relevant harmonics in the target loads and for the effect given on them by the considered control inputs. In other words, the identified model used for the design of the HHC is very representative of the connection between the considered input and output harmonics in particular in region II and higher region III, thus allowing the HHC control to provide a sensible improvement with respect to the B-IPC.

Finally, on Fig. 4.10 it is presented a comparison of the percent difference of all the considered performance indices weighed on the Weibull distribution centered at 8.5 m/sec, recommended for the certification class this turbine. As before, on the left figure we show the results obtained comparing the B-IPC with the trimmer, while on the right one the comparison is between the trimmer and the multi-layer controller.

The advantage provided by the HHC loop is more visible on the performance indices related to the shaft bending moment, and in particular on the STD and DEL. Also worth mentioning is the very low difference in power output between the two considered control systems.

4.3.3 Decentralized Implementation

Load Reduction in Deterministic Wind

In the decentralized case, the target load of the HHC controller is chosen to be the total root bending moment of each blade. HHC models at different

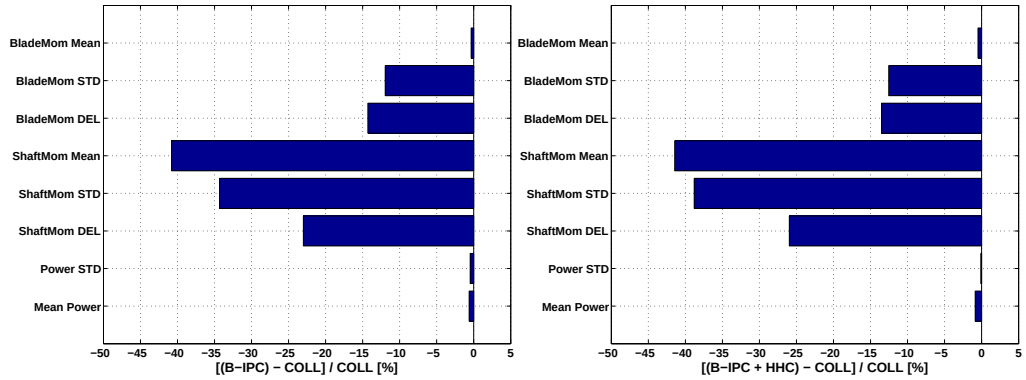

(a) B-IPC (b) B-IPC and HHC loops

Figure 4.10: Percent differences (wrt. collective PID trimmer) of some physical quantities for operation in turbulent wind, obtained from performances evaluated at several wind speeds between cut-in and cut-out, weighed on a Weibull distribution centered at 8.5 m/sec. Left: collective PID trimmer with B-IPC. Right: collective PID trimmer with centralized HHC and external B-IPC loops.

trim points in region III were synthesized using the 1P and 2P harmonics of both inputs and outputs.

For a constant-in-time wind speed of 15 m/sec and a shear layer exponent of 0.2, Fig. 4.11 shows the spectra of the normalized blade root bending moments.

The figure clearly shows that the HHC loop drastically reduces the first two load harmonics; the third harmonic, not having been included in the control goals, is essentially unmodified.

Load Reduction in Turbulent Wind

Tests were carried out also on the decentralized implementation, using the same turbulent conditions described for the centralized case.

Fig. 4.12 shows a bar diagram of the results for a mean hub wind of 21 m/sec, reporting percent changes in blade root and shaft bending moment STD and DEL, and STD and mean value of generated power. Here the comparison is between the collective PID trimmer and the proposed multilayer controller, featuring PID trimmer with decentralized HHC and external PD feedback loops, as shown in Fig. 4.3.

The results of Fig. 4.12 should be compared with those of the left part of Fig. 4.8. It appears that the proposed implementation gives some improve-

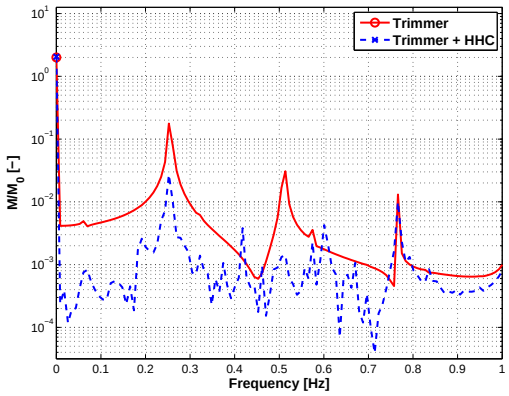

Figure 4.11: Normalized spectrum of the Nr.1 blade bending moment at root in constant 15 m/sec wind with 0.2 power law shear, for the PID trimmer operating alone or together with the HHC. The spectra are normalized to the zero-frequency peak value obtained with the sole collective trimmer.

ment on the blade loads when compared to the B-IPC. This can be explained by reasoning that, with the proposed approach, the control targets are indeed the blade loads, while in the B-IPC formulation the controller is designed so as to reduce the fixed system loads. While reduced fixed system loads imply reduced blade loads, it appears that larger reductions are possible when the controller is specifically optimized for targeting blade loads.

The same figure also shows that, since there is no coordination among the blades in the decentralized case, the fixed system loads are reduced to a lesser extent than in the centralized or B-IPC cases. This highlights once again the fact that, if one desires a reduction in the fixed system loads, then a centralized implementation should be used; on the other hand, if one seeks a reduction in the blade loads, then a decentralized implementation should be preferred.

Similar results on the blade moment DEL can be obtained all over the span between the cut-in and cut-out wind speeds (Fig. 4.13). Notice that the performance of the controller is better in region III, that is when wind speed is higher. This is because in this region the limit on the minimum pitch does not intervene, thus allowing the actuation of the pitch controls exactly as demanded by the control law.

Here again, the output power performance is virtually unaffected.

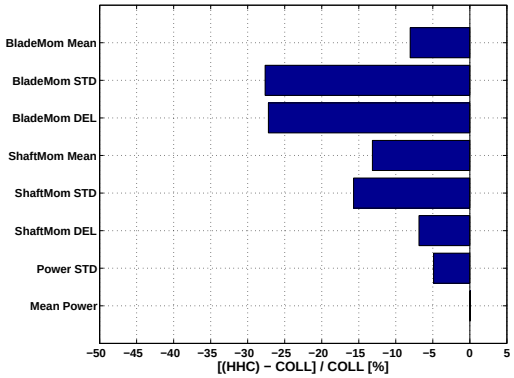

Figure 4.12: Percent differences (wrt. collective PID trimmer) of some physical quantities for operation in IEC category A turbulent wind at 21 m/sec mean speed, using collective PID trimmer with decentralized HHC and external PD loops.

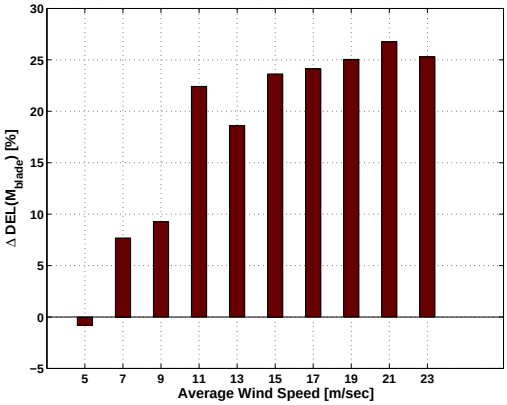

Figure 4.13: Percent performance gains (wrt. collective PID trimmer) on blade out-of-plane bending moment DEL for operation in IEC category A turbulent wind at several wind speeds between cut-in and cut-out, using collective PID trimmer with HHC and external proportional/derivative loops. Positive gain values correspond to a load reduction with respect to the trimmer.

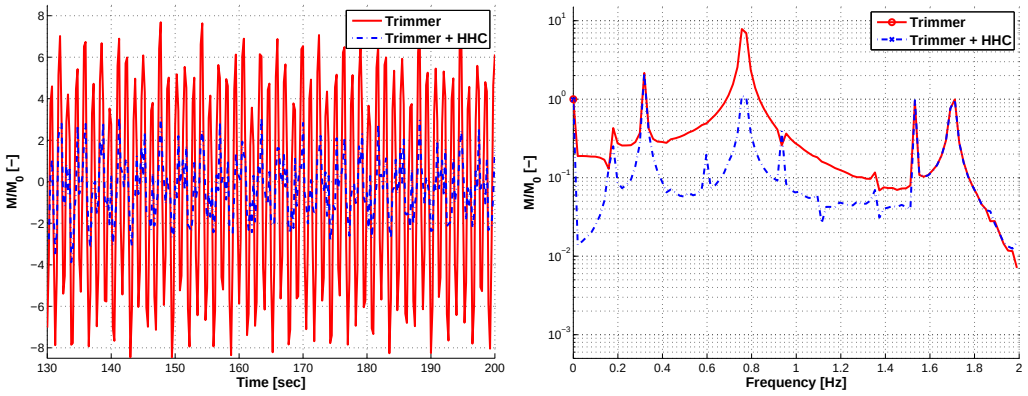

(a) (b)

Figure 4.14: Normalized time history (left) and spectra (right) of yaw moment resultant in constant wind at 15 m/sec, with power law shear 0.2, for the trimmer and the trimmer operating together with a centralized multi-layer controller. Both time histories and spectra are normalized to the zero-frequency peak value obtained with the sole collective trimmer.

4.3.4 Further Results

Up to now, the performance of the multi-layer architecture has been proved considering the total bending moment on a cross section of the shaft (centralized implementation) or the bending moments at blade root (decentralized implementation). As previously pointed out, the use of the decentralized implementation is very suitable for targeting blade-specific loads, while the centralized implementation can be used to reduce load on the shaft or on any non-rotating part of the machine, provided there exists a relationship between the target loads and pitch, thus making possible to identify a model between pitch inputs and the desired output.

One such case is constituted by the yaw moment measured on the interface between the nacelle and the tower. As it is the case for the shaft bending moments, the most relevant contributions to the oscillations come from the multiples of the 3P. Fig. 4.14 shows the time histories and spectra obtained from simulations with constant wind speed of 15 m/sec and standard shear. The PID trimmer and the PID trimmer with the superimposition of the middle HHC layer are considered. The HHC model is based only the 3P in the target load, and on the 2P and 4P in the control input. As it was the case with the shaft bending moment, also here it is possible to notice a reduction of the 3P of the target load.

4.4 Conclusions

In this chapter we have described a multi-layer architecture suitable for the control of wind turbines, which has often multiple objectives. The proposed approach uses distinct control layers to target different control goals, to reflect the multi-objective nature of the problem.

Three main goals have been identified here, and this has lead to a three-layer architecture. The first goal is the trimming around a set point and the load alleviation for gusts characterized by large spatial scales, for which purposes effective controllers can be designed using collective-pitch/torque inputs with a variety of methods. The second goal is the reduction of slowly varying deterministic loads, for which purpose the HHC approach developed by the rotorcraft community seems to be well suited. The third goal is the reduction of non-deterministic loads due to small scale spatial and temporal turbulent fluctuations in the wind, for which an individual blade controller with quick reaction times is needed.

It was shown that the present algorithm can be implemented in two markedly different ways: using a decentralized architecture when the aim is the reduction of the blade loads, or using a centralized architecture when the aim is the reduction of the loads in the fixed system. In both cases, the proposed procedures lead to a marked improvement of the performance obtained with the collective controller.

Many simulations in various deterministic and IEC turbulent test conditions were carried out on the `Cp-Lambda` model of a 2.5 MW turbine.

The more interesting results of the present investigation appear to be those obtained with the centralized implementation, especially since fatigue is usually one of the design drivers for components in the fixed system. In that case, the addition of the HHC loop is capable of broadening the band of affected loads with respect to the sole use of the B-IPC controller, which was used here as a benchmark for comparison. In deterministic winds, the HHC controller is capable of drastic reductions of the target harmonics, which are often completely wiped out. On the other hand, at high turbulence intensity levels the benefits of the HHC controller are less apparent, since loads are dominated by fast scales which are not captured by the HHC loop, and a good part of the load reductions with respect to the sole collective pitch case are due to the B-IPC non-deterministic loop. In between null and high turbulence, there is a continuous gradation of these effects, with excellent load reductions for the HHC at low turbulence, that progressively decrease, but never disappear completely, as the turbulence intensity increases.

Because of the fact that the middle and outer layers work basically adding a zero-mean contribution to the pitch input, in no case there is a significative

detrimental effect of the proposed centralized controllers on the power output.

More results obtained from the decentralized implementation show a good performance of this control architecture with respect to the reference when looking in particular at the effects on the blade loads, for the greatest part of the envelope of operating wind speeds.

In this case the power output is still not affected, as a result of the small contributions given by the intermediate and outer layers to the collective pitch input given by the inner trimming core.

In appendix A a different way to apply the individual pitch control based on the Coleman's transformation also accounting for higher harmonics in the target load will be described from a theoretical viewpoint. Some limited results in deterministic wind conditions will be shown.

Chapter 5

Cascading Kalman Observers of Structural Flexible and Wind States

5.1 Introduction

The aim of this chapter is to illustrate a Kalman-based formulation of observers of the structural flexible states used to model and characterize the motion of the tower and blades. Moreover, the formulation of an observer for the wind states based on the knowledge of the observed structural states will be described. As the wind observer operates based on the signals obtained from the observers of the structural part, in this scenario the observers operate as sequential stages in a cascading architecture.

As stated in the introduction (chapter 1), the motivation for the proposed observers is to provide estimates of these states to be used by advanced control laws. For example, knowledge of the tower fore-aft and side-side motions as well as of the blade flapping and lagging can be profitably used for designing sophisticated individual-blade control laws, so as to alleviate fatigue and gust-induced loads.

In the proposed architecture an assumed modal basis approach is used, and the flexible states reconstructed by the observers are represented by modal amplitudes and velocities of tower and blades. With estimates of these states made available by the proposed observers, one can synthesize model-based control laws which account for the aero-elastic response of such states. As an instance, the knowledge of the fore-aft displacement and velocity of the tower head is necessary to implement the LQR trimmer described in chapters 2, 3.

Furthermore, knowledge of the instantaneous over-the-rotor wind distribution can be exploited so as to explicitly account for this information in the pitch and torque control of a wind turbine. For example, knowledge of the current wind vertical and horizontal shear, as well of the vertical and lateral wind components can be profitably used for reducing oscillatory loads. Clearly, this information is of potential crucial efficacy in the design of control laws since it plays a central role in the determination of the aero-elastic response of the machine; however, the same information on the wind spatial distribution can not be obtained by the onboard anemometer, which can only provide mean hub-height wind values and is also disturbed by interactions with the rotor stream-tube and the nacelle, nor it can be easily obtained by other practical means. Although wind observers have been previously described in the literature [50], these provide only hub-height estimates, i.e. constant over-the-rotor wind values. While this information is useful and can be profitably used, for example for scheduling the control gains in terms of the wind speed, it does not account for important effects on the aero-elastic response of the wind turbine due to wind nonuniformity. The proposed wind observer tries to remove these limitations, by reconstructing a more complete picture of the instantaneous over-the-rotor wind distribution.

Another potential application not directly related to the measurement of the instantaneous wind components and to control, is that of better characterize the wind in the location chosen for a turbine. For instance, from prolonged observations it may be found that an average vertical wind component or a vertical shear of given intensity tend to show up in the incoming wind field. They might be given by the characteristic orography of the place where the plant has been placed, or by the effect of the wake of other turbines. This information may be of use to appropriately place a group of wind turbines.

In the proposed approach, estimates of all unknown states are obtained by a cascading series of Kalman filters. A first filter is responsible for the reconstruction of the tower states. A set of governing equations is obtained by expressing the accelerations sensed by accelerometers placed along the tower in terms of an assumed modal basis. At each time instant, the filter first predicts the tower flexible states by integrating forward in time the governing equations, and then corrects the predictions using the readings of a set of strain gauges, also placed along the tower length. This filtering approach accounts for the presence of noise in the measurements of both the accelerometers and the strain gauges. For reducing the need for tuning of the filter covariance matrices, an adaptive filtering approach is used, which reconstructs the noise statistics by keeping in memory a buffer of past values.

A second set of parallel filters operates in series to the tower filter, with

the goal of reconstructing the flexible blade states. For each blade, the accelerations sensed by accelerometers placed along the blade span are expressed in terms of the assumed modes of the blade, and of the accelerations transmitted by the tower; this last piece of information is at this stage known from the first filter. The filters predict the flexible blade states by integrating forward in time the resulting equations of motion, and then correcting the predictions based on readings provided by strain gauges.

The filters are formulated so as to be able to operate with an arbitrary number of sensors, under the constraint of observability of the reconstructed states. However, to keep the number of necessary sensors to a minimum, which is important for reasons of simplicity and applicability in real environment, the filters can operate with one accelerometer and one strain gauge for the tower and for each blade, which is a practical configuration already available on many instrumented wind turbines.

A wind state estimator is here formulated by considering that the flexible rotor of a wind turbine is a sophisticated "sensor" which spans the rotor disk and responds to the temporal and spatial variations of the wind blowing on it. By proper interpretation of the turbine response, one can infer the wind blowing on the rotor.

In this work, the spatial wind distribution is approximated using a simple model which accounts for mean hub wind, vertical and lateral shear, wind direction and vertical wind component. These unknown wind parameters are promoted to the role of dynamical states and are identified online using a third adaptive filter operating in series with the tower and blade ones. To this end, a wind turbine reduced model is used which accounts for the coupled dynamic equilibrium of drive-train, tower fore-aft and side-side motion, and elastic blade motion. At each instant of time, an adaptive extended Kalman filter estimates the wind states by enforcing in a stochastically optimal sense the satisfaction of the reduced model dynamic equilibrium equations. This is obtained by regarding the wind states as the sole unknowns of the model governing equations, whereas all control inputs and states are either available by readings of the onboard sensors or known through the estimates provided by the structural flexible state observers.

The proposed methodology is demonstrated as usual in the `Cp-Lambda` simulation environment. Extensive simulations in gusty and turbulent wind conditions demonstrate the ability of the proposed observers to identify with good accuracy both the flexible response of the machine and the spatial characteristics of the wind.

5.2 Formulation of the Observers

5.2.1 Notation

To derive the equations explaining the analytic base of the observers with mathematical rigour a suitable notation must be introduced.

A generic triad is indicated as $\mathcal{A} = \{\boldsymbol{a}_1, \boldsymbol{a}_2, \boldsymbol{a}_3\}$ and centered at point A, where $\boldsymbol{a}_i$, $i = 1, 2, 3$, are mutually orthogonal unit vectors.

The notation $(\cdot)^{\mathcal{A}}$ denotes components of a vector or tensor in triad $\mathcal{A}$. If $\boldsymbol{R}_{\mathcal{A}\to\mathcal{B}}$ is the rotation tensor which brings triad $\mathcal{A}$ into triad $\mathcal{B}$, then the components of a generic vector $\boldsymbol{v}$ in the two triads are related as $\boldsymbol{v}^{\mathcal{A}} = \boldsymbol{\alpha}\boldsymbol{v}^{\mathcal{B}}$, $\boldsymbol{v}^{\mathcal{B}} = \boldsymbol{\alpha}^T\boldsymbol{v}^{\mathcal{A}}$, where $\boldsymbol{\alpha}$ is the direction cosine matrix, $\boldsymbol{\alpha} = \boldsymbol{R}^{\mathcal{A}}_{\mathcal{A}\to\mathcal{B}} = \boldsymbol{R}^{\mathcal{B}}_{\mathcal{A}\to\mathcal{B}}$, $\boldsymbol{\alpha}^T\boldsymbol{\alpha} = \boldsymbol{I}$. Since the components of tensor $\boldsymbol{R}_{\mathcal{A}\to\mathcal{B}}$ are the same when measured in either $\mathcal{A}$ or $\mathcal{B}$, the use of the component superscript for rotation tensors is typically avoided, unless its components are measured in a triad other than $\mathcal{A}$ or $\mathcal{B}$.

The notation $\boldsymbol{v}_\times$ is used to indicate the skew-symmetric tensor associated with vector $\boldsymbol{v}$, and $(\cdot)^T$ as usual to indicate the transpose operation.

The symbol $\dot{(\cdot)} = \mathrm{d}\cdot/\mathrm{d}t$ indicates a derivative with respect to time t, while the symbol $(\cdot)' = \mathrm{d}\cdot/\mathrm{d}\xi$ indicates a derivative with respect to the curvilinear coordinate $\xi \in [0, L]$ measured along the beam reference line, L being the beam length.

The angular velocity of triad $\mathcal{B}$ with respect to triad $\mathcal{A}$ is noted $\boldsymbol{\omega}_{\mathcal{B}/\mathcal{A}}$, where $\dot{\boldsymbol{R}}_{\mathcal{A}\to\mathcal{B}} = \boldsymbol{\omega}_{\mathcal{B}/\mathcal{A}} \times \boldsymbol{R}_{\mathcal{A}\to\mathcal{B}}$. The curvature of triad $\mathcal{B}$ with respect to triad $\mathcal{A}$ is noted $\boldsymbol{c}_{\mathcal{B}/\mathcal{A}}$, where $\boldsymbol{R}'_{\mathcal{A}\to\mathcal{B}} = \boldsymbol{c}_{\mathcal{B}/\mathcal{A}} \times \boldsymbol{R}_{\mathcal{A}\to\mathcal{B}}$.

5.2.2 Observer of Structural Flexible States of a Wind Turbine

Tower State Observer

A tower state observer is here formulated by first expressing the accelerations sensed by accelerometers placed along the tower in terms of unknown modal states. The solution of the resulting equations of motion results in predicted modal states, which are then corrected based on the readings provided by strain gauges. This prediction-correction approach is implemented by a Kalman filter which accounts for noise in the measurements.

Consider the wind turbine tower depicted in Fig. 5.1. An accelerometer is placed on the tower at a location identified by the abscissa ξ_P measured along the tower axis. The undeformed tower configuration at that location along the span is described in terms of a local body-attached triad $\mathcal{P}_0$ centered

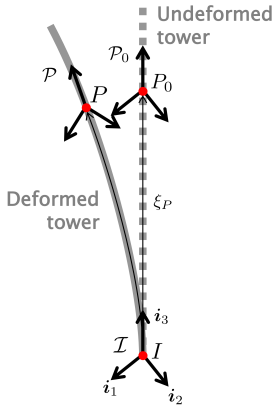

Figure 5.1: Reference frames for the tower observer.

at point P_0, while the deformed tower configuration is described by a body-attached triad $\mathcal{P}$ centered at point P. Furthermore, an inertial frame of reference is denoted by a triad of unit vectors $\mathcal{I}$ centered at point I.

The components of the acceleration in the body-attached frame, $\boldsymbol{a}^{\mathcal{P}}_{P/\mathcal{I}}$, are sensed by the accelerometer which yields a reading $\boldsymbol{a}_{\mathrm{acc}\,P}$ affected by noise $\boldsymbol{m}_{\mathrm{acc}}$[1]:

$$\boldsymbol{a}_{\mathrm{acc}\,P} = \boldsymbol{a}^{\mathcal{P}}_{P/\mathcal{I}} + \boldsymbol{m}_{\mathrm{acc}}. \tag{5.2}$$

The tower deformation is now modeled using N assumed mode shapes, whose components in $\mathcal{I}$ we assume to have been obtained by using some finite element software. This way, the inertial acceleration components at the accelerometer location can be computed as

$$\boldsymbol{a}^{\mathcal{I}}_{P/\mathcal{I}} = \sum_{i=1}^{N} \boldsymbol{\Phi}^{\mathcal{I}}_i(\xi_P)\dot{v}_i, \tag{5.3}$$

where $\boldsymbol{\Phi}^{\mathcal{I}}_i(\xi)$ are the components in $\mathcal{I}$ of the i-th tower displacement mode shape, q_i its associated unknown modal amplitude and $v_i = \dot{q}_i$ the unknown modal velocity.

[1]Notice that, when using an accelerometer located in the nacelle, the sensed acceleration components are

$$\boldsymbol{a}_{\mathrm{acc}\,P} = \boldsymbol{a}^{\mathcal{Y}}_{P/\mathcal{I}} + \boldsymbol{m}_{\mathrm{acc}}, \tag{5.1}$$

where $\mathcal{Y}$ is the nacelle-attached yawing triad, which are however readily transformed into the $\mathcal{P}$ triad as $\boldsymbol{a}^{\mathcal{P}}_{P/\mathcal{I}} = \boldsymbol{R}^{\mathcal{P}}_{\mathcal{P}\to\mathcal{Y}}\boldsymbol{a}^{\mathcal{Y}}_{P/\mathcal{I}}$, $\boldsymbol{R}_{\mathcal{P}\to\mathcal{Y}}$ being a planar rotation of yaw angle θ about the $\boldsymbol{t}_3$ axis (see description of reference frames in 5.2.2 and cf. Fig. 5.2).

On the other hand, the components of the acceleration vector in the inertial frame can also be written as

$$\boldsymbol{a}^{\mathcal{I}}_{P/\mathcal{I}} = \boldsymbol{R}_{\mathcal{I}\to\mathcal{P}}\boldsymbol{a}^{\mathcal{P}}_{P/\mathcal{I}}, \tag{5.4}$$

where the rotation tensor from triad $\mathcal{I}$ to triad $\mathcal{P}$ is

$$\boldsymbol{R}_{\mathcal{I}\to\mathcal{P}} = \boldsymbol{R}_{\mathcal{P}_0\to\mathcal{P}}\boldsymbol{R}_{\mathcal{I}\to\mathcal{P}_0}. \tag{5.5}$$

For a straight tower, as it is often the case, the rotation tensor from the inertial to the undeformed frame is $\boldsymbol{R}_{\mathcal{I}\to\mathcal{P}_0} = \boldsymbol{I}$. Furthermore, the relative rotation tensor which accounts for the tower deformation, given that mode shapes describe small motions about the reference configuration, can be expressed in the following linear form

$$\boldsymbol{R}^{\mathcal{I}}_{\mathcal{P}_0\to\mathcal{P}} = \boldsymbol{I} + \big(\sum_{i=1}^{N}\boldsymbol{\Theta}^{\mathcal{I}}_i(\xi_P)q_i\big)_\times, \tag{5.6}$$

where $\boldsymbol{\Theta}^{\mathcal{I}}_i(\xi)$ are the components in $\mathcal{I}$ of the i-th tower rotation mode shape. For shear undeformable beams, the rotational modes are simply the derivatives of the displacement modes with respect to the curvilinear abscissa ξ.

Using now (5.3) and (5.4), together with the given definitions of sensed acceleration and rotation tensors, we obtain the acceleration components at point P as

$$\sum_{i=1}^{N}\boldsymbol{\Phi}^{\mathcal{I}}_i(\xi_P)\dot{v}_i = \Big(\boldsymbol{I} + \big(\sum_{i=1}^{N}\boldsymbol{\Theta}^{\mathcal{I}}_i(\xi_P)q_i\big)_\times\Big)\boldsymbol{R}_{\mathcal{I}\to\mathcal{P}_0}(\boldsymbol{a}_{\mathrm{acc}\,P} - \boldsymbol{m}_{\mathrm{acc}}). \tag{5.7}$$

Consider now N_{acc} accelerometers located in the set of points S_{acc}, and define the $3N_{\mathrm{acc}}\times N$ matrix

$$\boldsymbol{A} = [\boldsymbol{\Phi}^{\mathcal{I}}_i(\xi_P)], \quad P\in S_{\mathrm{acc}}, \quad i = 1,\dots,N_{\mathrm{acc}}, \tag{5.8}$$

and the $3N_{\mathrm{acc}}\times 1$ vector $\boldsymbol{a} = \big\{\dots,\boldsymbol{a}^{\mathcal{I}^T}_{P/\mathcal{I}},\dots\big\}^T$ with $P\in S_{\mathrm{acc}}$, where the expression for $\boldsymbol{a}^{\mathcal{I}}_{P/\mathcal{I}}$ is given by the right hand side of (5.7). Defining the modal amplitude $\boldsymbol{q} = \{\dots,q_i,\dots\}^T$ and velocity $\boldsymbol{v} = \{\dots,v_i,\dots\}^T$ vectors, the modal equations of motion are obtained using least-squares on (5.7) as

$$\dot{\boldsymbol{q}} = \boldsymbol{v}, \tag{5.9a}$$

$$\dot{\boldsymbol{v}} = (\boldsymbol{A}^T\boldsymbol{A})^{-1}\boldsymbol{A}\boldsymbol{a}. \tag{5.9b}$$

Consider now a strain gauge placed at a location identified by the abscissa ξ_Q along the tower axis. The body-attached triads in the reference and deformed configurations are $\mathcal{Q}_0$ centered at Q_0 and $\mathcal{Q}$ centered at Q, respectively. The curvature components in $\mathcal{I}$ of the deformed beam at that location are

$$\boldsymbol{c}^{\mathcal{I}}_{\mathcal{Q}/\mathcal{I}} = \boldsymbol{c}^{\mathcal{I}}_{\mathcal{Q}_0/\mathcal{I}} + \boldsymbol{c}^{\mathcal{I}}_{\mathcal{Q}/\mathcal{Q}_0}, \tag{5.10}$$

where the curvature due to the tower deformation can be expressed as

$$\boldsymbol{c}^{\mathcal{I}}_{\mathcal{Q}/\mathcal{Q}_0} = \sum_{i=1}^{N} \boldsymbol{\Theta}_i'^{\mathcal{I}}(\xi_Q) q_i. \tag{5.11}$$

On the other hand, the same curvature components can be computed as

$$\boldsymbol{c}^{\mathcal{I}}_{\mathcal{Q}/\mathcal{Q}_0} = \boldsymbol{R}_{\mathcal{I}\to\mathcal{Q}} \boldsymbol{c}^{\mathcal{Q}}_{\mathcal{Q}/\mathcal{Q}_0}, \tag{5.12a}$$

$$= \Big(\boldsymbol{I} + \big(\sum_{i=1}^{N} \boldsymbol{\Theta}^{\mathcal{I}}_i(\xi_Q) q_i \big)_\times \Big) \boldsymbol{R}_{\mathcal{I}\to\mathcal{Q}_0} \boldsymbol{c}^{\mathcal{Q}}_{\mathcal{Q}/\mathcal{Q}_0}, \tag{5.12b}$$

so that the local body-attached curvature components are

$$\boldsymbol{c}^{\mathcal{Q}}_{\mathcal{Q}/\mathcal{Q}_0} = \boldsymbol{R}^T_{\mathcal{I}\to\mathcal{Q}_0} \Big(\boldsymbol{I} + \big(\sum_{i=1}^{N} \boldsymbol{\Theta}^{\mathcal{I}}_i(\xi_Q) q_i \big)_\times \Big)^{-1} \sum_{i=1}^{N} \boldsymbol{\Theta}_i'^{\mathcal{I}}(\xi_Q) q_i. \tag{5.13}$$

These components are sensed by the strain gauge which yields a reading $\boldsymbol{c}_{\mathrm{sg}\,Q}$ affected by noise $\boldsymbol{n}_{\mathrm{sg}}$, i.e.:

$$\boldsymbol{c}_{\mathrm{sg}\,Q} = \boldsymbol{c}^{\mathcal{Q}}_{\mathcal{Q}/\mathcal{Q}_0} + \boldsymbol{n}_{\mathrm{sg}}. \tag{5.14}$$

Considering N_{sg} strain gauges located in the set of points S_{sg}, we can define the $3N_{\mathrm{sg}} \times 1$ output vector

$$\boldsymbol{y} = \{\ldots, \boldsymbol{c}^{\mathcal{Q}^T}_{\mathcal{Q}/\mathcal{Q}_0}, \ldots\}^T, \quad Q \in S_{\mathrm{sg}}, \tag{5.15}$$

where the expression for $\boldsymbol{c}^{\mathcal{Q}}_{\mathcal{Q}/\mathcal{Q}_0}$ is given in (5.13), and measurement vector

$$\boldsymbol{z} = \{\ldots, \boldsymbol{c}^{T}_{\mathrm{sg}\,Q}, \ldots\}^T, \quad Q \in S_{\mathrm{sg}}. \tag{5.16}$$

The equations of motion (5.9) together with the output and measurement definitions (5.15,5.16) represent a set of states-space equations for the tower observer, which can be written in the following compact form

$$\dot{\boldsymbol{x}} = \boldsymbol{f}(\boldsymbol{x}, \boldsymbol{u}, \boldsymbol{m}), \tag{5.17a}$$

$$\boldsymbol{y} = \boldsymbol{h}(\boldsymbol{x}), \tag{5.17b}$$

$$\boldsymbol{z} = \boldsymbol{y} + \boldsymbol{n}, \tag{5.17c}$$

where the state vector is

$$\boldsymbol{x} = \{\boldsymbol{q}^T, \boldsymbol{v}^T\}^T, \tag{5.18}$$

while the input vector

$$\boldsymbol{u} = \{\ldots, \boldsymbol{a}^T_{\mathrm{acc}\,P}, \ldots\}^T, \tag{5.19}$$

with $P \in S_{\mathrm{acc}}$, the process noise vector $\boldsymbol{m} = \boldsymbol{m}_{\mathrm{acc}}$ (which here is in reality due to the accelerometer measurement noise), and the (strain gauge) measurement noise vector $\boldsymbol{n} = \boldsymbol{n}_{\mathrm{sg}}$.

State Estimation by Adaptive Kalman Filtering

The state estimation problem (5.17) can be solved with a number of filtering approaches. The Kalman filter is an optimal estimator for unconstrained linear systems with normally distributed process and measurement noise, while for nonlinear problem various methods have been proposed, including the extended Kalman filter, the unscented Kalman filter, the sigma point and particle filters [96]. In this work we use the extended Kalman filter, which amounts to an approximate generalization of the Kalman filter to nonlinear systems obtained by linearizing the system dynamics at each time step. Theoretical results on the stability and convergence of this approach are discussed in Ref. [97].

The equations of motion (5.17a) are integrated on each sampling interval $[t_k, t_{k+1}]$ to yield a state prediction $\bar{\boldsymbol{x}}_{k+1}$ together with its associated output vector $\bar{\boldsymbol{y}}_{k+1}$ from (5.17b). Next, at each sampling instant the state predictions are improved based on the innovations, i.e. the difference between the measurements $\boldsymbol{z}_{k+1}$ and the predicted outputs $\bar{\boldsymbol{y}}_{k+1}$, as

$$\hat{\boldsymbol{x}}_{k+1} = \bar{\boldsymbol{x}}_{k+1} + \boldsymbol{K}_{k+1}\left(\boldsymbol{z}_{k+1} - \bar{\boldsymbol{y}}_{k+1}\right), \tag{5.20}$$

where $\boldsymbol{K}_{k+1}$ is a time-varying gain matrix, which is propagated forward in time together with the state estimates based on the covariances of the estimation error, and of the process and measurement noise.

The latter two quantities are crucial parameters which govern the convergence behavior of the filter. To alleviate the need for careful tuning of these parameters, we use in this work an adaptive filtering method. The basic idea is in this case to reconstruct on-line during filtering the process and measurement noise statistics, keeping a buffer of past values to extract noise samples [98].

In our implementation, the measurement time histories are preprocessed using zero-phase digital filtering [99] before being passed to the Kalman filter, so as to remove the frequency components which are outside of the band of the adopted modal basis.

Rotor State Observer

A rotor state observer is formulated similarly to the tower state observer. First, for each blade, the accelerations sensed by accelerometers placed along the blade span are expressed in terms of unknown blade modal states. These accelerations also depend on the tower states, which are however known from the previously described computational procedure; therefore, the rotor state observers operate in series with the tower observer. The integration of the resulting equations of motion provide predictions of the blade modal states. Next, the predictions are corrected by using the readings provided by strain gauges placed along the blade span, using a Kalman filter.

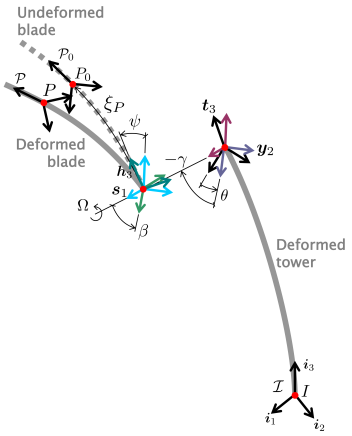

Figure 5.2: Reference frames for the blade observer.

Consider the wind turbine schematic configuration depicted in Fig. 5.2, where a single blade is shown for clarity. An accelerometer is placed on the blade at a location identified by the abscissa ξ_P measured along the blade axis. Similarly to the tower case, in order to express the acceleration at that location, it is necessary to describe the blade configuration with the help of a cascading series of frames of reference, which are described next. The known tower states are indicated with the notation $\hat{q}_{t_i}$ and $\hat{v}_{t_i}$, where the subscript $(\cdot)_t$ is used now to indicate tower quantities and the subscript $(\cdot)_b$ for blade related ones.

1. At the tip of the tower, a tower-attached triad $\mathcal{T}_0$ centered at point T_0 describes the tower tip undeformed configuration, with $\boldsymbol{R}_{\mathcal{I}\to\mathcal{T}_0} = \boldsymbol{I}$ for a straight tower.

2. The deformed tower configuration is described by triad $\mathcal{T}$ centered at point T, where

$$\boldsymbol{r}^{\mathcal{I}}_{T_0T} = \sum_{i=1}^{N_t} \boldsymbol{\Phi}^{\mathcal{I}}_{t_i}(\xi_T)\hat{q}_{t_i}, \tag{5.21a}$$

$$\boldsymbol{R}^{\mathcal{I}}_{\mathcal{I}_0\to\mathcal{T}} = \boldsymbol{I} + \big(\sum_{i=1}^{N_t} \boldsymbol{\Theta}^{\mathcal{I}}_{t_i}(\xi_T)\hat{q}_{t_i}\big)_\times. \tag{5.21b}$$

3. The yawing nacelle-attached triad $\mathcal{Y} = \{\boldsymbol{y}_1, \boldsymbol{y}_2, \boldsymbol{y}_3\}$ is centered at $Y \equiv T$ and it is obtained from the $\mathcal{T}$ triad through a planar rotation of yaw angle θ about axis $\boldsymbol{t}_3$.

4. The shaft-parallel nacelle-fixed triad $\mathcal{S} = \{\boldsymbol{s}_1, \boldsymbol{s}_2, \boldsymbol{s}_3\}$ is obtained from the $\mathcal{Y}$ triad through a planar rotation of angle $-\gamma$ about the $\boldsymbol{y}_2$ axis, where γ is the rotor uptilt angle.

5. The hub-fixed rotating triad $\mathcal{H} = \{\boldsymbol{h}_1, \boldsymbol{h}_2, \boldsymbol{h}_3\}$ is obtained from the $\mathcal{S}$ one by a planar rotation of azimuthal angle ψ about the $\boldsymbol{s}_1$ axis, and centered at point H.

6. The blade-root-fixed triad $\mathcal{B} = \{\boldsymbol{b}_1, \boldsymbol{b}_2, \boldsymbol{b}_3\}$ is obtained from the $\mathcal{H}$ triad by a planar rotation of blade pitch angle β about the $\boldsymbol{h}_3$ axis, and centered at point $B \equiv H$.

7. The undeformed blade configuration is described in terms of a local body-attached triad $\mathcal{P}_0$ centered at point P_0. The rotation $\boldsymbol{R}_{\mathcal{B}\to\mathcal{P}_0}$ accounts for blade pre-cone, twist and sweep at that location along the blade span.

8. Finally, the deformed blade configuration is described by a body-attached triad $\mathcal{P}$ centered at point P. The blade deformation is modeled using N_b assumed mode shapes, whose components in the blade-root pitching triad $\mathcal{B}$ we assume to have been obtained by using some finite element software. The relative displacement and rotation components account-

ing for blade deformation are, respectively,

$$\boldsymbol{r}^{\mathcal{B}}_{P_0P} = \sum_{i=1}^{N_b} \boldsymbol{\Phi}^{\mathcal{B}}_{b_i}(\xi_P) q_{b_i}, \tag{5.22a}$$

$$\boldsymbol{R}^{\mathcal{B}}_{\mathcal{P}_0\to\mathcal{P}} = \boldsymbol{I} + \big(\sum_{i=1}^{N_b} \boldsymbol{\Theta}^{\mathcal{B}}_{b_i}(\xi_P) q_{b_i}\big)_\times, \tag{5.22b}$$

where $\boldsymbol{\Phi}^{\mathcal{B}}_{b_i}(\xi)$ and $\boldsymbol{\Theta}^{\mathcal{B}}_{b_i}(\xi)$ are the components in $\mathcal{B}$ of the i-th blade displacement and rotation mode shape, respectively, and q_{b_i} the associated unknown modal amplitude.

We assume that the nacelle yaw angle θ, rotor azimuth ψ and blade pitch β are known at each instant of time from onboard sensors, together with their times rate of change, possibly obtained by finite differences.

Similarly to the tower case, the components of the acceleration in the body-attached frame, $\boldsymbol{a}^{\mathcal{P}}_{P/\mathcal{I}}$, are sensed by the blade accelerometer which yields a reading $\boldsymbol{a}_{\mathrm{acc}\,P}$ affected by noise $\boldsymbol{m}_{\mathrm{acc}}$:

$$\boldsymbol{a}_{\mathrm{acc}\,P} = \boldsymbol{a}^{\mathcal{P}}_{P/\mathcal{I}} + \boldsymbol{m}_{\mathrm{acc}}. \tag{5.23}$$

Since the blade mode shapes are computed in the blade-pitching triad $\mathcal{B}$, it is convenient to express the acceleration in that same triad, which, given the cascading reference frame definitions above, can be written as

$$\boldsymbol{a}^{\mathcal{B}}_{P/\mathcal{I}} = \boldsymbol{a}^{\mathcal{B}}_{B/\mathcal{I}} + \boldsymbol{a}^{\mathcal{B}}_{P/\mathcal{B}} + 2\,\boldsymbol{\omega}^{\mathcal{B}}_{\mathcal{B}/\mathcal{I}} \times \boldsymbol{v}^{\mathcal{B}}_{P/\mathcal{B}} + \big(\dot{\boldsymbol{\omega}}^{\mathcal{B}}_{\mathcal{B}/\mathcal{I}\,\times} + \boldsymbol{\omega}^{\mathcal{B}}_{\mathcal{B}/\mathcal{I}\,\times}\boldsymbol{\omega}^{\mathcal{B}}_{\mathcal{B}/\mathcal{I}\,\times}\big)\boldsymbol{r}^{\mathcal{B}}_{BP}. \tag{5.24}$$

The term $\boldsymbol{a}^{\mathcal{B}}_{B/\mathcal{I}}$ can be readily expressed in terms of known tower quantities as

$$\boldsymbol{a}^{\mathcal{B}}_{B/\mathcal{I}} = \boldsymbol{R}^{T}_{\mathcal{I}\to\mathcal{B}}\Big(\sum_{i=1}^{N_t} \boldsymbol{\Phi}^{\mathcal{I}}_{t_i}(\xi_T)\dot{\hat{v}}_{t_i} + \big(\dot{\boldsymbol{\omega}}^{\mathcal{I}}_{\mathcal{Y}/\mathcal{I}\,\times} + \boldsymbol{\omega}^{\mathcal{I}}_{\mathcal{Y}/\mathcal{I}\,\times}\boldsymbol{\omega}^{\mathcal{I}}_{\mathcal{Y}/\mathcal{I}\,\times}\big)\boldsymbol{R}_{\mathcal{I}\to\mathcal{Y}}\boldsymbol{r}^{\mathcal{Y}}_{YH}\Big), \tag{5.25}$$

where

$$\boldsymbol{\omega}^{\mathcal{I}}_{\mathcal{Y}/\mathcal{I}} = \sum_{i=1}^{N_t} \boldsymbol{\Theta}^{\mathcal{I}}_{t_i}\hat{v}_{t_i} + \dot{\theta}\boldsymbol{R}_{\mathcal{I}\to\mathcal{Y}}\left\{\begin{array}{c} 0 \\ 0 \\ 1 \end{array}\right\}, \tag{5.26}$$

and the rotation tensor components are

$$\boldsymbol{R}_{\mathcal{I}\to\mathcal{Y}} = \Big(\boldsymbol{I} + \big(\sum_{i=1}^{N_t} \boldsymbol{\Theta}^{\mathcal{I}}_{t_i}(\xi_T)\hat{q}_{t_i}\big)_\times\Big)\boldsymbol{R}_{\mathcal{I}\to\mathcal{T}_0}\left[\begin{array}{ccc} \mathrm{c}\,\theta & -\mathrm{c}\,\theta & 0 \\ \mathrm{c}\,\theta & \mathrm{s}\,\theta & 0 \\ 0 & 0 & 1 \end{array}\right], \tag{5.27}$$

where s = sin and c = cos, and

$$\boldsymbol{R}_{\mathcal{I}\to\mathcal{B}} = \boldsymbol{R}_{\mathcal{I}\to\mathcal{Y}}\boldsymbol{R}_{\mathcal{Y}\to\mathcal{B}}, \tag{5.28}$$

with

$$\boldsymbol{R}_{\mathcal{Y}\to\mathcal{B}} = \begin{bmatrix} \mathrm{c}\,\gamma\,\mathrm{c}\,\beta - \mathrm{s}\,\gamma\,\mathrm{s}\,\psi\,\mathrm{s}\,\beta & -\mathrm{c}\,\gamma\,\mathrm{s}\,\beta - \mathrm{s}\,\gamma\,\mathrm{s}\,\psi\,\mathrm{c}\,\beta & -\mathrm{s}\,\gamma\,\mathrm{c}\,\psi \\ \mathrm{c}\,\psi\,\mathrm{s}\,\beta & \mathrm{c}\,\psi\,\mathrm{c}\,\beta & -\mathrm{s}\,\psi \\ \mathrm{s}\,\gamma\,\mathrm{c}\,\beta + \mathrm{c}\,\gamma\,\mathrm{s}\,\psi\,\mathrm{s}\,\beta & -\mathrm{s}\,\gamma\,\mathrm{s}\,\beta + \mathrm{c}\,\gamma\,\mathrm{s}\,\psi\,\mathrm{c}\,\beta & \mathrm{c}\,\gamma\,\mathrm{c}\,\psi \end{bmatrix}, \tag{5.29}$$

The terms $\boldsymbol{v}^{\mathcal{B}}_{P/\mathcal{B}}$ and $\boldsymbol{a}^{\mathcal{B}}_{P/\mathcal{B}}$ are simply

$$\boldsymbol{v}^{\mathcal{B}}_{P/\mathcal{B}} = \sum_{i=1}^{N_b} \boldsymbol{\Phi}^{\mathcal{B}}_{b_i}(\xi_P) v_{b_i}, \tag{5.30a}$$

$$\boldsymbol{a}^{\mathcal{B}}_{P/\mathcal{B}} = \sum_{i=1}^{N_b} \boldsymbol{\Phi}^{\mathcal{B}}_{b_i}(\xi_P) \dot{v}_{b_i}, \tag{5.30b}$$

whereas the angular velocity $\boldsymbol{\omega}^{\mathcal{B}}_{\mathcal{B}/\mathcal{I}}$ can be obtained as

$$\boldsymbol{\omega}^{\mathcal{B}}_{\mathcal{B}/\mathcal{I}} = \dot{\beta}\boldsymbol{h}^{\mathcal{B}}_3 + \Omega\boldsymbol{R}^T_{\mathcal{H}\to\mathcal{B}}\boldsymbol{h}^{\mathcal{H}}_1 + \dot{\theta}\boldsymbol{R}^T_{\mathcal{T}\to\mathcal{B}}\boldsymbol{t}^{\mathcal{T}}_3 + \boldsymbol{R}^T_{\mathcal{I}\to\mathcal{B}}\sum_{i=1}^{N_t}\boldsymbol{\Theta}^{\mathcal{I}}_{t_i}(\xi_T)\hat{v}_{t_i}, \tag{5.31a}$$

$$= \begin{Bmatrix} \Omega\,\mathrm{c}\,\beta + \dot{\theta}(\quad \mathrm{s}\,\gamma\,\mathrm{c}\,\beta + \mathrm{c}\,\gamma\,\mathrm{s}\,\psi\,\mathrm{s}\,\beta) \\ -\Omega\,\mathrm{s}\,\beta + \dot{\theta}(-\mathrm{s}\,\gamma\,\mathrm{s}\,\beta + \mathrm{c}\,\gamma\,\mathrm{s}\,\psi\,\mathrm{c}\,\beta) \\ \dot{\beta} + \dot{\theta}\,\mathrm{c}\,\gamma\,\mathrm{c}\,\psi \end{Bmatrix} + \boldsymbol{R}^T_{\mathcal{I}\to\mathcal{B}}\sum_{i=1}^{N_t}\boldsymbol{\Theta}^{\mathcal{I}}_{t_i}(\xi_T)\hat{v}_{t_i}. \tag{5.31b}$$

Inserting these expressions into (5.24), we find

$$\begin{aligned}\sum_{i=1}^{N_b}\boldsymbol{\Phi}^{\mathcal{B}}_{b_i}(\xi_P)\dot{v}_{b_i} = -2\,\boldsymbol{\omega}^{\mathcal{B}}_{\mathcal{B}/\mathcal{I}}\times\sum_{i=1}^{N_b}\boldsymbol{\Phi}^{\mathcal{B}}_{b_i}(\xi_P)v_{b_i} - \\ \big(\dot{\boldsymbol{\omega}}^{\mathcal{B}}_{\mathcal{B}/\mathcal{I}\times} + \boldsymbol{\omega}^{\mathcal{B}}_{\mathcal{B}/\mathcal{I}\times}\boldsymbol{\omega}^{\mathcal{B}}_{\mathcal{B}/\mathcal{I}\times}\big)\big(\boldsymbol{r}^{\mathcal{B}}_{BP_0} + \sum_{i=1}^{N_b}\boldsymbol{\Phi}^{\mathcal{B}}_{b_i}(\xi_P)q_{b_i}\big) + \\ \Big(\boldsymbol{I} + \big(\sum_{i=1}^{N_b}\boldsymbol{\Theta}^{\mathcal{B}}_{b_i}(\xi_P)q_{b_i}\big)_\times\Big)\boldsymbol{R}_{\mathcal{B}\to\mathcal{P}_0}(\boldsymbol{a}_{\mathrm{acc}\,P} - \boldsymbol{m}_{\mathrm{acc}}) - \\ \boldsymbol{R}^T_{\mathcal{I}\to\mathcal{B}}\Big(\sum_{i=1}^{N_t}\boldsymbol{\Phi}^{\mathcal{I}}_{t_i}(\xi_T)\dot{\hat{v}}_{t_i} + \big(\dot{\boldsymbol{\omega}}^{\mathcal{I}}_{\mathcal{Y}/\mathcal{I}\times} + \boldsymbol{\omega}^{\mathcal{I}}_{\mathcal{Y}/\mathcal{I}\times}\boldsymbol{\omega}^{\mathcal{I}}_{\mathcal{Y}/\mathcal{I}\times}\big)\boldsymbol{R}_{\mathcal{I}\to\mathcal{Y}}\boldsymbol{r}^{\mathcal{Y}}_{YH}\Big).\end{aligned} \tag{5.32}$$

Similarly to the tower case, consider now $N_{b_{\text{acc}}}$ accelerometers located in the set of points $S_{b_{\text{acc}}}$ on the blade, and define matrix

$$\boldsymbol{A}_b = [\boldsymbol{\Phi}^{\mathcal{B}}_{b_i}(\xi_P)], \quad P \in S_{b_{\text{acc}}}, \quad i = 1, \ldots, N_{b_{\text{acc}}}, \tag{5.33}$$

and vector $\boldsymbol{a}_b = \left\{ \ldots, \boldsymbol{a}^{\mathcal{B}^T}_{P/\mathcal{B}}, \ldots \right\}^T$ with $P \in S_{b\text{acc}}$, where the expression for $\boldsymbol{a}^{\mathcal{B}}_{P/\mathcal{B}}$ is given by the right hand side of (5.32). Defining the blade modal amplitude $\boldsymbol{q}_b = \{\ldots, q_{b_i}, \ldots\}^T$ and velocity $\boldsymbol{v}_b = \{\ldots, v_{b_i}, \ldots\}^T$ vectors, the modal equations of motion are obtained using least-squares on (5.32) as

$$\dot{\boldsymbol{q}}_b = \boldsymbol{v}_b, \tag{5.34a}$$

$$\dot{\boldsymbol{v}}_b = (\boldsymbol{A}_b^T \boldsymbol{A}_b)^{-1} \boldsymbol{A}_b \boldsymbol{a}_b. \tag{5.34b}$$

Consider now a strain gauge placed at a location identified by the abscissa ξ_Q along the blade axis. As for the tower case, we find here that the local body-attached curvature components are

$$\boldsymbol{c}^{\mathcal{Q}}_{\mathcal{Q}/\mathcal{Q}_0} = \boldsymbol{R}^T_{\mathcal{B}\to\mathcal{Q}_0} \Big(\boldsymbol{I} + \big(\sum_{i=1}^{N_b} \boldsymbol{\Theta}^{\mathcal{B}}_{b_i}(\xi_Q) q_{b_i} \big)_\times \Big)^{-1} \sum_{i=1}^{N_b} \boldsymbol{\Theta}'^{\mathcal{B}}_{b_i}(\xi_Q) q_{b_i}, \tag{5.35}$$

which are sensed by the strain gauge yielding a reading $\boldsymbol{c}_{\text{sg}\,Q}$ affected by noise $\boldsymbol{n}_{\text{sg}}$:

$$\boldsymbol{c}_{\text{sg}\,Q} = \boldsymbol{c}^{\mathcal{Q}}_{\mathcal{Q}/\mathcal{Q}_0} + \boldsymbol{n}_{\text{sg}}. \tag{5.36}$$

Considering $N_{b_{\text{sg}}}$ strain gauges located in the set of points $S_{b_{\text{sg}}}$ along the blade, we define the output vector

$$\boldsymbol{y}_b = \{\ldots, \boldsymbol{c}^{\mathcal{Q}^T}_{\mathcal{Q}/\mathcal{Q}_0}, \ldots\}^T, \quad Q \in S_{b_{\text{sg}}}, \tag{5.37}$$

where the expression for $\boldsymbol{c}^{\mathcal{Q}}_{\mathcal{Q}/\mathcal{Q}_0}$ is given in (5.35), and measurement vector

$$\boldsymbol{z}_b = \{\ldots, \boldsymbol{c}^T_{\text{sg}\,Q}, \ldots\}^T, \quad Q \in S_{b_{\text{sg}}}. \tag{5.38}$$

The equations of motion (5.34) together with the output and measurement definitions (5.37,5.38) represent a set of states-space equations for the blade observer, which can be written in the following compact form

$$\dot{\boldsymbol{x}}_b = \boldsymbol{f}_b(\boldsymbol{x}_b, \boldsymbol{u}_b, \boldsymbol{m}_b), \tag{5.39a}$$

$$\boldsymbol{y}_b = \boldsymbol{h}_b(\boldsymbol{x}_b), \tag{5.39b}$$

$$\boldsymbol{z}_b = \boldsymbol{y}_b + \boldsymbol{n}_b, \tag{5.39c}$$

where the state vector is

$$\boldsymbol{x}_b = \{\boldsymbol{q}_b^T, \boldsymbol{v}_b^T\}^T, \tag{5.40}$$

the input vector

$$\boldsymbol{u}_b = \{\ldots, \boldsymbol{a}_{\mathrm{acc}\,P}^T, \ldots, \hat{\boldsymbol{x}}_t^T\}^T \tag{5.41}$$

with $P \in S_{b_{\mathrm{acc}}}$ and $\hat{\boldsymbol{x}}_t$ the state estimates provided by the tower filter, the process noise vector $\boldsymbol{m}_b = \boldsymbol{m}_{\mathrm{acc}}$, and the measurement noise vector $\boldsymbol{n}_b = \boldsymbol{n}_{\mathrm{sg}}$.

Estimates of the blade states are obtained at each time step using an adaptive Kalman filter with zero-phase pre-filtering of the measurements, exactly as in the tower case. Notice that there is one observer per blade; the blade observers operate in parallel to one another and in series with the tower observer.

5.2.3 Observer of Wind States

A wind state observer is here formulated by taking advantage of the reconstructed wind turbine states, available from the previously described tower and blade flexible state observers, to obtain time-varying estimates of suitably chosen wind states using a wind turbine model. In fact, a dynamic model of a wind turbine can be expressed in terms of its governing equations as

$$\dot{\boldsymbol{x}}_{\mathrm{wt}} = \boldsymbol{f}_{\mathrm{wt}}(\boldsymbol{x}_{\mathrm{wt}}, \boldsymbol{u}_{\mathrm{wt}}, \boldsymbol{w}), \tag{5.42}$$

where $\boldsymbol{x}_{\mathrm{wt}}$ are wind turbine states, $\boldsymbol{u}_{\mathrm{wt}}$ is the wind turbine input vector, and $\boldsymbol{w} = \boldsymbol{w}(\boldsymbol{r}, t)$ the spatially and temporally varying wind vector. Consider now a wind turbine model such that its state vector $\boldsymbol{x}_{\mathrm{wt}}$ is

$$\boldsymbol{x}_{\mathrm{wt}} = \{\theta, \dot{\theta}, \psi, \dot{\psi}, \ldots, \beta_i, \dot{\beta}_i, \ldots, \boldsymbol{q}_t^T, \boldsymbol{v}_t^T, \ldots, \boldsymbol{q}_{b_i}^T, \boldsymbol{v}_{b_i}^T, \ldots, T_{el_e}\}^T, i = 1, \ldots, B, \tag{5.43}$$

where T_{el_e} is the generator torque and B the number of blades, whereas the input vector is

$$\boldsymbol{u}_{\mathrm{wt}} = \{\theta_c, \ldots, \beta_{i_c}, \ldots, T_{el_c}\}^T, i = 1, \ldots, B, \tag{5.44}$$

where θ_c is the commanded yaw angle, β_{i_c} the commanded blade pitch setting and T_{el_c} the commanded generator torque. At each instant of time the states are known, either from sensors or from the observers described above. Similarly, at each instant of time also the inputs are known from the onboard controllers.

Taking advantage of the fact that both states and inputs are known in (5.42), one can infer the wind $\boldsymbol{w}$ blowing on the rotor. To this end, it

is first necessary to introduce a spatial discretization of the wind. A possible solution is provided by the frequently used wind model given by

$$\boldsymbol{w}(\boldsymbol{r},t) = \Bigg(V_h(t)\Big(1+\frac{z-H}{H}\Big)^{V_\mathrm{s}(t)} + V_\mathrm{ls}(t)\frac{z-H}{2R} + H_\mathrm{ls}(t)\frac{y\cos\alpha(t) - x\sin\alpha(t)}{2R}\Bigg)\boldsymbol{i}_v(t) + V_z(t)\boldsymbol{i}_3, \quad (5.45)$$

where x, y and z are coordinates measured along the unit vectors $\boldsymbol{i}_1$, $\boldsymbol{i}_2$ and $\boldsymbol{i}_3$, respectively, of $\mathcal{I}$. V_h is the horizontal wind speed at the height $z = H$ of the rotor hub, V_s is the vertical-shear power law exponent, V_ls and H_ls are the vertical and horizontal, respectively, linear shear coefficients, R being the rotor radius. The instantaneous horizontal wind direction is given by unit vector $\boldsymbol{i}_v$, which forms an angle $\alpha = \mathrm{acos}(\boldsymbol{i}_1 \cdot \boldsymbol{i}_v)$ with unit vector $\boldsymbol{i}_1$ of the inertial triad $\mathcal{I}$, while V_z is the vertical wind component.

Selecting as unknown wind parameters the hub wind V_h, either the power law exponent V_s or the vertical shear coefficient V_ls, the horizontal wind shear coefficient H_ls, the relative wind direction α and the vertical wind component V_z, we can define the vector

$$\boldsymbol{x}_\mathrm{wind}(t) = \{V_h(t), V_\mathrm{s}(t) | V_\mathrm{ls}(t), H_\mathrm{ls}(t), \alpha(t), V_z(t)\}^T, \quad (5.46)$$

and write the wind parameterization as $\boldsymbol{w}(\boldsymbol{r},t) = \boldsymbol{w}(\boldsymbol{x}_\mathrm{wind}(t))$.

A graphical definition of the considered wind states is provided in Fig. 5.3.

Next, the unknown wind parameters $\boldsymbol{x}_\mathrm{wind}$ are promoted to the role of states, which transforms their estimation problem into a new state estimation one. The governing wind estimation equations in states-space form are written as

$$\dot{\boldsymbol{x}}_\mathrm{wind} = \boldsymbol{m}_\mathrm{wind}, \quad (5.47a)$$

$$\boldsymbol{y}_\mathrm{wind} = \boldsymbol{h}_\mathrm{wind}(\boldsymbol{x}_\mathrm{wind}, \boldsymbol{u}_\mathrm{wind}), \quad (5.47b)$$

$$\boldsymbol{z}_\mathrm{wind} = \boldsymbol{y}_\mathrm{wind} + \boldsymbol{n}_\mathrm{wind}. \quad (5.47c)$$

Equations (5.47a) represent the wind parameter dynamics evolution equations, where a process noise term $\boldsymbol{m}_\mathrm{wind}$ to the right hand side is responsible for exciting the temporal variations of the wind states. Equations (5.47b) are the output definition equations, representing the residuals of (5.42):

$$\boldsymbol{h}_\mathrm{wind}(\boldsymbol{x}_\mathrm{wind}, \boldsymbol{u}_\mathrm{wind}) = \big(\dot{\hat{\boldsymbol{x}}}_\mathrm{wt} - \boldsymbol{f}_\mathrm{wt}(\hat{\boldsymbol{x}}_\mathrm{wt}, \boldsymbol{u}_\mathrm{wt}, \boldsymbol{w}(\boldsymbol{x}_\mathrm{wind}))\big)_\mathrm{dyn\ eq}. \quad (5.48)$$

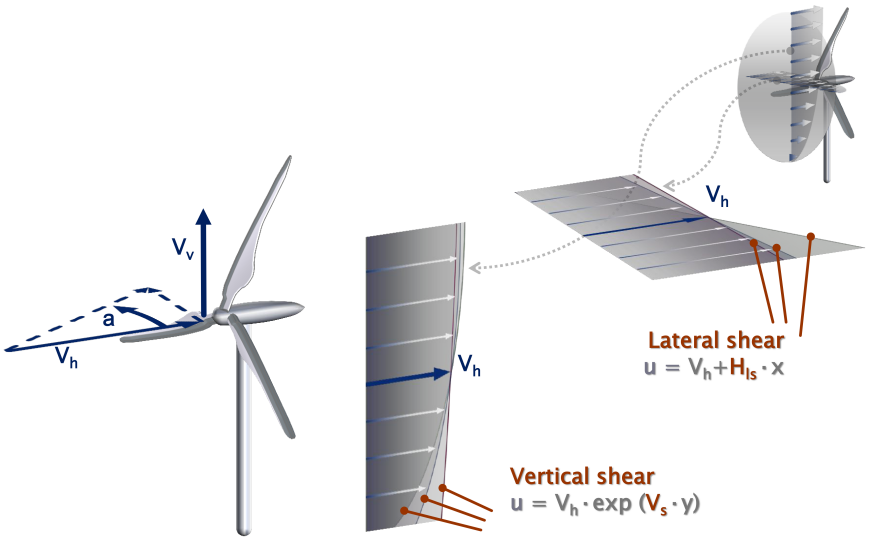

Figure 5.3: Graphical definition of the considered wind states.

Notice that the residuals are evaluated for the known wind turbine state $\hat{\boldsymbol{x}}_{\text{wt}}$ and known input $\boldsymbol{u}_{\text{wt}}$ vectors, which can therefore be considered as inputs to the wind states-space model, i.e. $\boldsymbol{u}_{\text{wind}} = \{\hat{\boldsymbol{x}}_{wt}^T, \boldsymbol{u}_{\text{wt}}^T\}^T$. Furthermore, of the complete set of governing equations (5.42) represented by dynamic equilibrium and kinematic equations, only the former set depends on the wind $\boldsymbol{w}$; therefore, in (5.48), only the dynamic equilibrium set of equations enters into the definition of the outputs. Finally, equations (5.47c) represent the measurement definition equations. For this special problem, the measurements at all time instants are simply

$$\boldsymbol{z}_{\text{wind}} = \boldsymbol{0}, \tag{5.49}$$

which means that we are trying to enforce a null error in the satisfaction of the dynamic equilibrium equations of the wind turbine model. In other words, we are trying to find those wind states which satisfy the dynamic equilibrium equations with the given measured and reconstructed quantities. Notice that a noise term $\boldsymbol{n}_{\text{wind}}$ appears in the measurement definitions; however, in this case this is not a proper measurement noise term but in reality a process noise one, since it appears as an additive term in the dynamic equilibrium equations.

The state estimation problem (5.47) is solved here again with an adaptive extended Kalman filter. The reconstructed wind states, together with the elastic tower and blade states, can now be used by advanced online control laws which this way can explicitly account for this information in their

formulation.

The overall architecture of the state estimators is shown in Fig. 5.4.

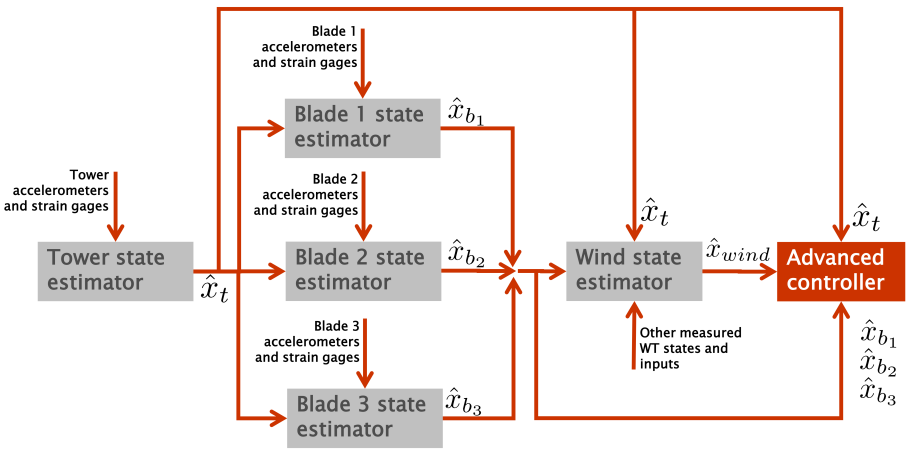

Figure 5.4: Overall architecture of the estimators of flexible tower and blade states, and of wind states.

5.3 Results

5.3.1 Observer of Structural Flexible States

To illustrate the performance of the proposed observer of structural flexible states, we consider here the response of the LTW62 wind turbine (see chapter 1). The tests are conducted within the `Cp-Lambda` simulation environment.

The tower has a strain gauge located at $\xi_Q = 25$ m ($L = 58.27$ m), and an accelerometer at its top in the nacelle. Each blade has a strain gauge at $\xi_Q = 25$ m ($R = 30.08$ m), and an accelerometer at $\xi_P = 5$ m. All sensors are affected by errors modeled as white noise with an amplitude not to exceed the 5% of the measured signal. Sensor signals are filtered with a 2 Hz passband low-pass filter. The adaptive Kalman filters use buffers of 15 past samples to reconstruct online the noise statistics by means of an adaptive Kalman algorithm.

At first, we consider the case of the extreme operating gust (EOG) at 15 m/sec [74]. Fig. 5.5 shows the time history of the wind, and the resulting rotor angular speed and collective blade pitch (respectively, from top to bottom).

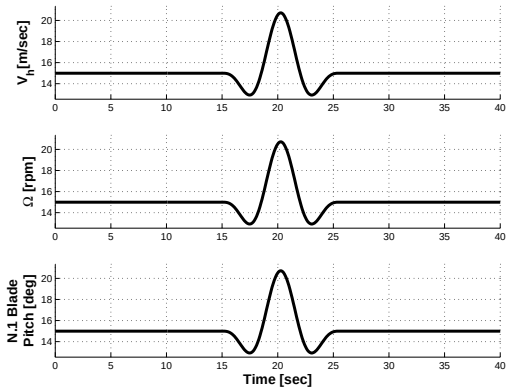

Figure 5.5: IEC extreme operating gust at 15 m/sec. From top to bottom, time history of wind, rotor angular speed and collective blade pitch.

Fig. 5.6 shows, at left, the time history of the blade deflection at the accelerometer location, and at right the time history of the tower tip deflection. The "true" plant response is reported using a solid line, while the observed response is shown using a dashed line. In both cases, it appears that there is an excellent correspondence between the reference and reconstructed states. The only observable inaccuracy is an offset in the peak response of the blade, corresponding to the maximum wind speed during the gust.

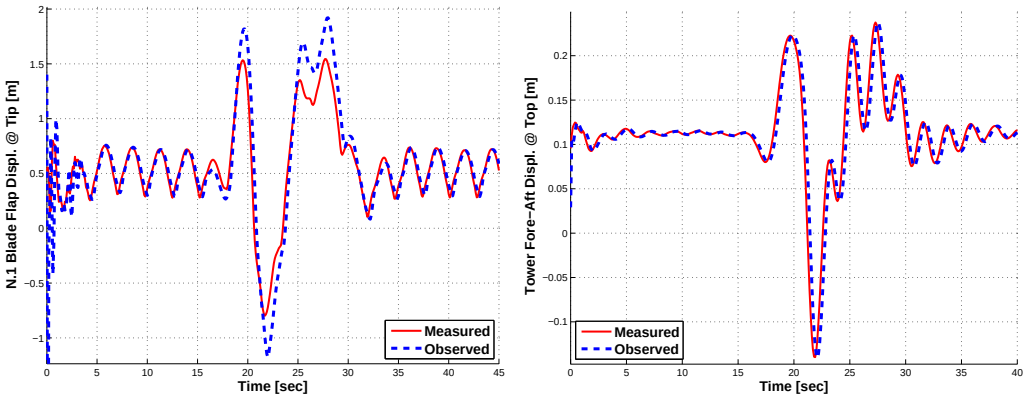

Figure 5.6: IEC extreme operating gust at 15 m/sec. Time history of blade (left) and tower (right) deflections. Real: solid line; observed: dashed line.

Next, we evaluate the performance of the observer in turbulent wind conditions. Transient simulations were conducted for a duration of 600 sec with constant mean hub-height wind speed and Category A turbulence [66, 74]. Fig. 5.7 shows the time history of the turbulent wind in the case of the

16 m/sec mean hub-height wind speed, and the resulting rotor angular speed and collective blade pitch (respectively, from top to bottom).

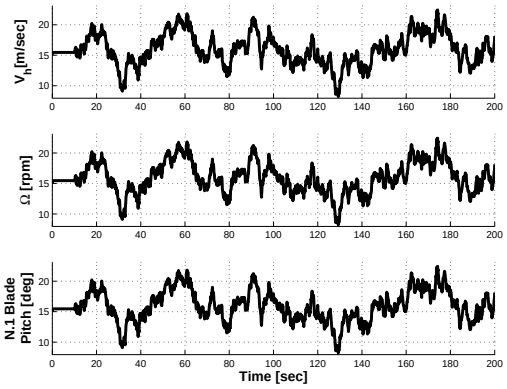

Figure 5.7: Turbulent wind with 16 m/sec mean hub-height wind speed and IEC category A turbulence. From top to bottom, time history of wind, rotor angular speed and collective blade pitch.

Fig. 5.8 reports at left the blade deflection time history, and at right the tower tip deflection time history. As in the previous plots, the plant response is reported using a solid line, while the observed response is shown using a dashed line. Here again, the observed deflections match very well the true ones throughout the entire simulation.

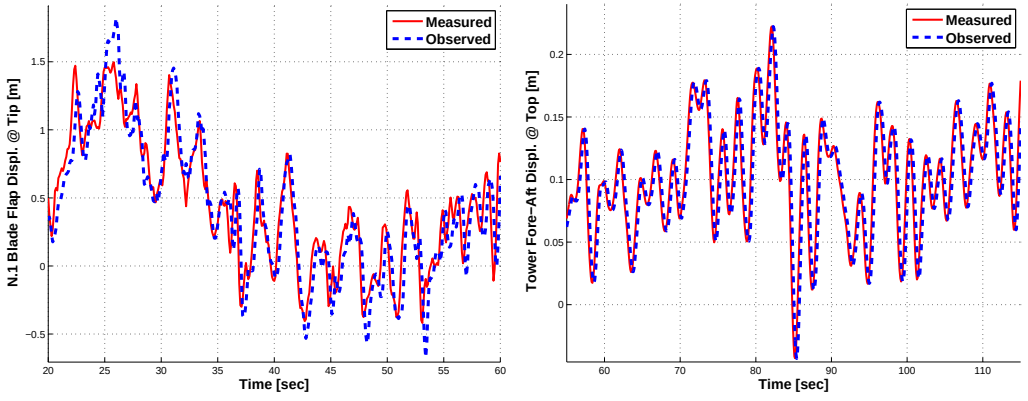

Figure 5.8: Turbulent wind with 16 m/sec mean hub-height wind speed and IEC category A turbulence. Time history of blade (left) and tower (right) deflections. Real: solid line; observed: dashed line.

5.3.2 Observer of Wind States

In the first examples, the reduced model is implemented with the `SymDyn` software [17], and the identified modal amplitudes of tower and blades are mapped into equivalent hinge rotations. Time histories of generalized wind states were generated and used for calculating the response of a `SymDyn` model of the LTW62 wind turbine. Horizontal, vertical and lateral wind components were generated using the Kaimal turbulence model, while the vertical shear power law exponent and horizontal wind shear coefficient were varied according to an assumed deterministic time history. Based on this response, estimates of the wind states were obtained using the Kalman observer. Notice that there is no mismatch between plant model and observer model in the results reported below. Consequently, discrepancies between the actual and reconstructed wind states are only due to the presence of noise in the procedure. These preliminary computations were conducted so as to determine the actual observability of the wind states and to verify the correct implementation of the software.

Fig. 5.9 shows a sketch of the simulation setup used to test the wind observer.

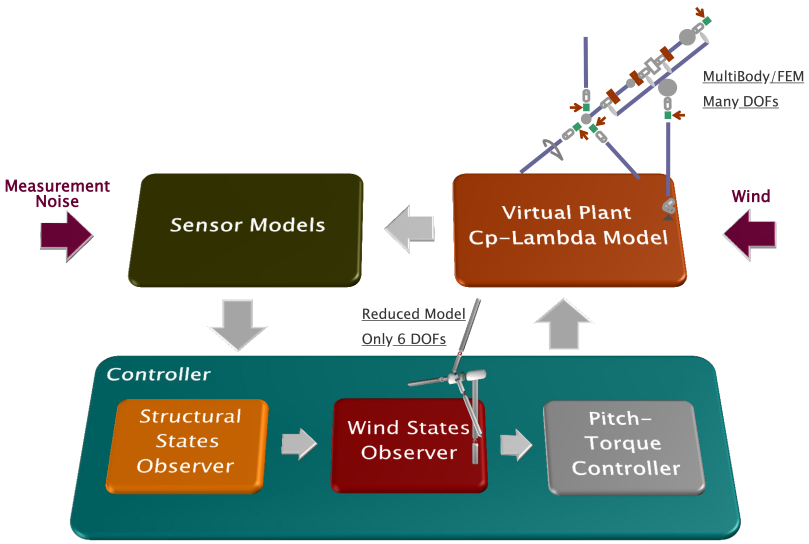

Figure 5.9: Sketch of the simulation setup used to test the wind state observer.

Fig. 5.10 shows at left the time history of the horizontal wind component of Eq. (5.46), i.e. the hub wind V_h, where the actual wind is reported with a solid line and the reconstructed one using a dashed line. Similarly, the right

part of the same figure shows the reconstruction of the linear vertical shear coefficient V_{ls}. In the third figure below it is shown the reconstruction of the linear horizontal shear coefficient H_{ls}. Even in this case, the time histories of these parameters are captured very well by the observer.

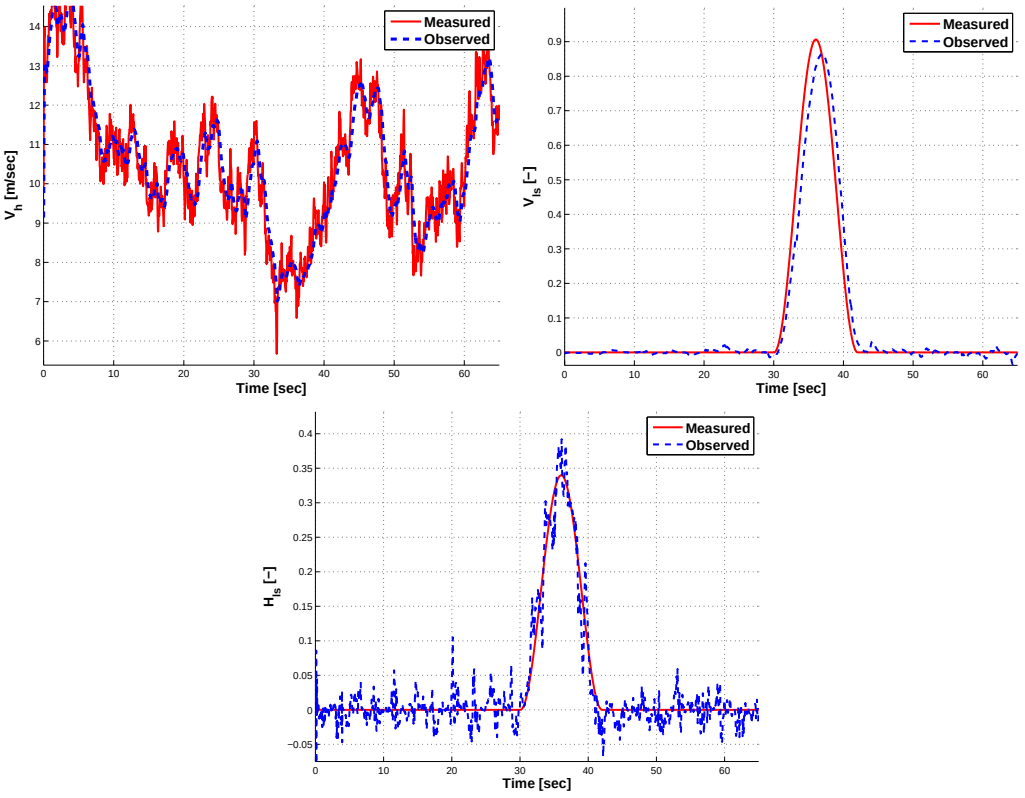

Figure 5.10: Estimation of generalized wind states. Hub wind V_h (left) and vertical linear shear exponent V_{ls} (right). Vertical linear shear exponent H_{ls} (bottom). Real: solid line; observed: dashed line.

From this first test phase it was possible to argue that some wind states are more easily observable than others; this is due to the lack of differences between the structural response of the plant under some different wind conditions, so that it is very difficult for the observer algorithm to distinguish the contributes given by different wind states. In particular the lateral shear H_{ls} and the yaw angle α, as well as the vertical shear $V_{\text{ls}}(t)$ tend to give the same change in the structural states when changed singularly. As a consequence, considering the observation of these wind states together can result in visible inaccuracies in the observation results [71]. An assessment of the observability of the system based on more trials and on the use of Fisher's

information matrix has basically confirmed the existence of an observability issue under test wind conditions where the aforementioned states are observed together [71]. This problem will be analyzed more thoroughly in the chapter devoted to the observation of the misalignment between the incoming flow and the turbine (6).

We focused on the most clearly observable wind states for more in depth testing on the wind observer. In the following examples the response is obtained using `Cp-Lambda`, the fine scale aero-servo-elastic model as plant. Tower fore-aft and side-side and blade flap signals are obtained from the implemented structural observers and used to feed the wind observer. This is based on the same `SymDyn` reduced model equations described above.

In the next example we consider two wind states as unknown, namely the horizontal speed V_h and the linear horizontal shear coefficient H_{ls} . The first is set to a constant value of 14 m/sec. Both states are interested by a gust at 15 sec after the beginning of the simulation. A gust on the horizontal shear coefficient may be used to model a temporary disturbance in the uniform horizontal wind spatial distribution along a horizontal diameter of the rotor disc. The results in Fig. 5.11 show a good accordance between the real and observed wind states values, even if the observed signals are here more noisy than in the previous observation examples. Good performances can be obtained through a careful selection of the covariances used for tuning the Kalman algorithm – even if the various Kalman filters have been implemented following an adaptive approach, a mild dependence of the observation results on the initial values of the covariances can be noticed in practice.

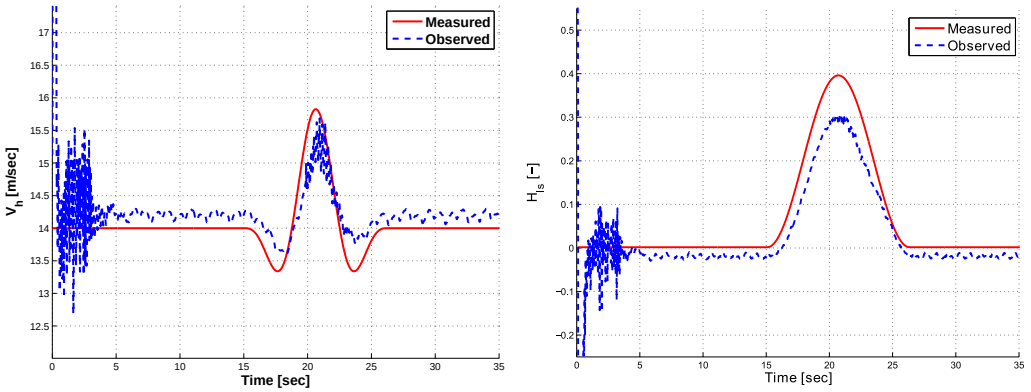

Figure 5.11: Estimation of generalized wind states with cascading structural and wind observers. Deterministic wind. Hub wind V_h (left) and horizontal linear exponent H_{ls} (right). Real: solid line; observed: dashed line.

The choice of the tuning parameters is more critical in turbulent wind

fields. In the following example (Fig. 5.12) the observer is used to reconstruct the horizontal component V_h of a turbulent wind of Category A intensity with a mean value of 21 m/sec. The observer performance is fairly good, even if the algorithm tuning does not allow the reproduction of fluctuations due to higher frequencies.

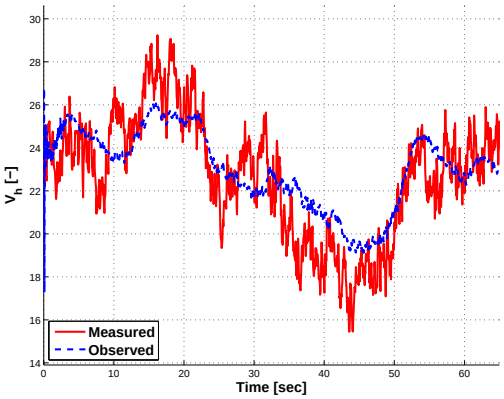

Figure 5.12: Estimation of generalized wind states with cascading structural and wind observers. Category A turbulence. Hub wind V_h. Real: solid line; observed: dashed line.

Generally speaking, it is possible to notice a growing difficulty in obtaining good observation results when trying to observe an increasing number of states. This is particularly apparent when turbulence is involved, for in this case a fine tuning of the parameters of the wind Kalman observer becomes of pivotal relevance. A certain difference between the fine aero-servo-elastic model and the reduced model causes troubles when trying to observe wind states used to model the wind component in the rotor plane. This can be solved only by moving to a different set of equations for the reduced model, that is, switching to a reduced model showing a structural response closer to that of the more sophisticated multi-body code [100].

Of course, limiting the number of observed parameters may be of great help in reducing the difficulty of the observation process. In the presented algorithm, this is equal to adopt a simpler description of the wind, where some of the wind states are assumed to be known (like the wind speed at the hub height V_h) or constant [71]. A more radical redesign of the whole observer, aimed at the estimation of the yaw misalignment only is presented in another chapter 6.

5.4 Conclusions

Structural Kalman observers for fore-aft and side-side motion of the tower tip, and for flap and lag motion of the blades have been formulated. Their implementation in a control algorithm has been used to observe these signal using sensors applied to a the `Cp-Lambda` model of the LTW62 multi-MW turbine.

Good results have been obtained from these observers both in deterministic and turbulent wind fields. A Kalman observer for wind states has been formulated, based on a commonly accepted six states model of the wind field.

This observer has been implemented using the equations of a reduced model, accounting for blade and tower deformability through springs applied to hinges connecting rigid bodies. This observer has been initially tested feeding it with structural signals generated from the same reduced model, showing good observation performances concerning the horizontal speed and the vertical and horizontal shear coefficients in particular.

Further testing have been carried out of the complete cascading observer series, where the structural observers for tower and blade motion have been used to feed the wind observer. In this testing phase some problems showed up, related to sensibility of the observation performances to the tuning parameter of the Kalman observer, even when working with a self-tuning algorithm. Moreover, some important differences in the response of the multi-body and the reduced model can prevent the cascading observer series from reconstruct some states. This latter issue can be probably solved selecting a more sophisticated reduced model, showing a structural response closer to that of the multi-body model.

In the next chapter an alternative way of observing a smaller set of wind states is presented, this time not based on a Kalman algorithm.

Chapter 6

Yaw Observer

In this chapter a research activity aimed at the development and verification of a yaw observer is illustrated. The proposed technology uses loads measured on the blades of the turbine to infer the direction of the wind. The yaw measurements are not affected by the usual limitations and disturbances affecting existing wind sensors. Furthermore, the new observer can be implemented on wind turbines equipped with blade load sensors without the need for modifications or additional on board devices, and hence at virtually no cost.

6.1 Introduction

On board wind turbines, yaw control is needed because operation at high yaw angles causes a number of negative effects. For instance, it reduces the power available in the wind incident over the rotor with the third power of the cosine of the yaw angle; for example, operating at 20 deg of yaw reduces the available power of about 17 %. It changes the angle of attack of the airfoils, which can further degrade aerodynamic performance in addition to the cosine effect mentioned above. It generates side-side loads that tend to excite low damped modes of the machine, thereby inducing loads and vibrations, which in turn increase fatigue damage to the machine components.

Although it would appear beneficial to operate at low yaw because of the above reasons, these effects need to be carefully weighed against the cost of frequent yaw actuation. In fact, yawing the nacelle and rotor of a modern large wind turbine requires moving a very massive structure (for example weighing in excess of 150 tons for a typical 3.0 MW machine), overcoming the static friction in the yaw bearing when initiating the maneuver and slowing down once the new alignment is reached, while limiting gyroscopic and

aerodynamic loads throughout the whole maneuver. Hence, to reduce cost, complexity, size and maintenance of the yaw actuation system, its duty-cycle must be carefully limited.

In practice, such trade-offs between operation in yawed flow and yaw actuation are translated into control policies that realign the machine only when the yaw error exceeds a sufficiently large predetermined threshold for a sufficiently long period of time. The fact that yawing is important for performance and loads, but must be done only when really necessary because of the reasons noted above, implies that one would like to have precise and reliable measurements of the yaw angle, so as to yaw only for the right reason, of the right amount and at the right time.

Unfortunately, high-quality measurements of yaw are difficult to obtain. In fact, onboard wind sensors for yaw, typically wind vanes, are affected by various sources of inaccuracy, including disturbances caused by the rotor wake and its turbulence, the presence of the nacelle, the periodic passing of the blades upstream of the instrument, etc. Although most sensors can be calibrated for compensating these effects, it is well known that the resulting wind measures are typically not very reliable nor accurate. Furthermore, existing sensors, even when well compensated for all sources of error, can only provide point information, usually at hub height. For the very large diameters of modern wind turbines this limitation can provide for an additional source of error, and a more global view of the wind direction over the rotor disk would be more appropriate.

Goal of the present research effort is the development and testing of a yaw observer that overcomes the limitations of currently available wind vanes, using only sensors already available on board existing modern wind turbines. This problem has not yet been successfully solved before. As for the more complex observer described in chapter 5, the approach proposed here uses the whole rotor, and more specifically the blade loads, to infer the yaw direction; hence, the whole wind turbine is used as a large sensor that, responding to the wind, provides the necessary information for estimating the wind direction relative to the rotor. This way all limitations of current wind direction sensors are removed, including the one regarding the localized information that they provide.

In the following, some theoretical aspects relevant to prove the feasibility of the proposed yaw observer will be shown first. Then a description of the actual methodology implemented to practically design the observer will follow. After that, some validation of the proposed design and some simulation results proving the capabilities of this novel approach will be presented.

6.2 Theoretical Aspects

The basic idea behind the proposed yaw observer is to postulate the existence of a measurable effect of a yaw angle between the incoming flow and the rotor axis on the amplitude and phase of some oscillatory components of the loads at the root of the blades. When the machine operates in trimmed conditions under the effect of an ideal constant wind, with standard shear and aligned to the rotor axis, the loads at the root of the blades oscillate basically at the frequencies multiple of rev, as a result of shear and gravity. In that case it is possible to evaluate some characteristic coefficients of the oscillating signals, namely amplitudes and phases, which will be constant in time. Suppose now to introduce a yaw angle so that the incoming wind field would not be aligned with the rotor axis. In the new resulting equilibrium some values of the characteristic coefficients of the oscillating loads will be different from before. So, if it is possible to find a connection between the changes in the value of the coefficients and the change in yaw, then it is also possible to exploit the knowledge of the coefficients to infer the intensity of the yaw misalignment. A theoretical proof of the existence of this connection is provided in the following section, based on a simplified model of the blade.

6.2.1 Equation of the Flapping Blade

To demonstrate the feasibility of the proposed yaw observer it is convenient to start from a simplified model of the flapping blade. The method used to synthesize the model is the similar to [101], with some simplifications. Even if the procedure to build up the model for the scope of this analysis is fully described here, refer to the reference if more details on the hypotheses or other aspects of the derivation process are needed.

Basically, the blade is described by a couple of rigid bodies connected by a hinge allowing only one rotational degree of freedom. To account for the elastic characteristics of the blade in the flapwise direction, a suitably tuned torsional spring is positioned at the hinge. The inner rigid body is rigidly connected to the rotor hub, and rotates around the rotor axis with rotational speed Ω. The outer rigid body can be positioned at a non-zero angle in the flapwise direction with respect to the inner one as in Fig. 6.1.

It is possible to define μ – the flapwise angle between the rigid bodies – as the flap angle. Notice that even if this is a kinematical quantity, after the completion of the current analysis it will be shown how it can be easily changed to a root bending load for the scope of this research work.

In the modeling process, starting from real data, the size of both rigid bodies and the stiffness of the torsional spring can be evaluated to match

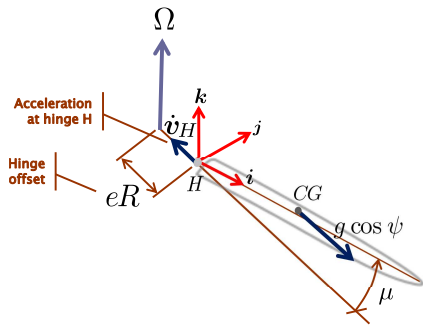

Figure 6.1: Simplified scheme of the flapping blade.

the flapwise deformation and frequency associated to the first flapwise mode of the blade. Given the undeformability of the rigid bodies, this match will be investigated in the least-squares sense: the lengths of the bodies and the stiffness of the torsional spring can be selected to minimize the square error between the deformed shape of the real blade and that of the model, the latter being made up of two linear parts each corresponding to one of the two rigid bodies. In this way, the equation of motion obtained from this model will be able to describe an approximation of the flapwise motion, namely a modal approximation truncated at the first mode.

To build up a differential model for the flap angle μ of the blade, the loads exerted on the blade due to gravity, inertia and aerodynamics will be taken into account. First, an expression for the resultant of the forces exerted on the blades not due to inertia, which are gravity, reaction forces due to deformability, and those due to aerodynamics, will be derived.

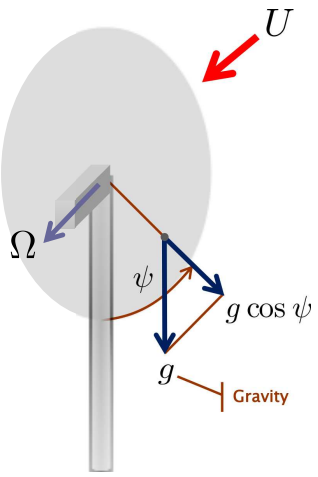

Figure 6.2: Definition of the azimuth angle ψ and gravity g.

Let ψ be the rotor azimuth angle and g the gravity acceleration, taken positive downwards as in Fig. 6.2. Consider a reference frame as in Fig. 6.1, with an origin in the hinge point H, bound to the inner rigid body and rotating rigidly with it. Let $\boldsymbol{r}_g$ be the position vector pointing from the frame origin H to the center of gravity CG of the outer rigid body, such that its components in the hinge reference can be written as

$$\boldsymbol{r}_g = \left\{ \begin{array}{c} x_g \\ 0 \\ 0 \end{array} \right\}. \tag{6.1}$$

Let k_μ be the stiffness of the torsional spring and M the mass of the outer rigid body. The total hinge moment $\boldsymbol{m}_H$ measured in H will be given by the vectorial expression

$$\boldsymbol{m}_H = \boldsymbol{m}_A + \boldsymbol{r}_g \times \left\{ \begin{array}{c} Mg\cos\psi\cos\mu \\ 0 \\ -Mg\cos\psi\sin\mu \end{array} \right\} + \left\{ \begin{array}{c} 0 \\ k_\mu\mu \\ 0 \end{array} \right\} \tag{6.2}$$

where the moment $\boldsymbol{m}_A$ is due to aerodynamics and will be characterized shortly, while the second and third terms on the right-hand side express the contributions of gravity and blade stiffness respectively. If the axes of the considered reference are principal axes, the tensor of the moments of inertia of the outer rigid body measured in H can be written in the diagonal form

$$\boldsymbol{J}_H = \left[\begin{array}{ccc} J_x & & \\ & J_y & \\ & & J_z \end{array} \right]. \tag{6.3}$$

Based on this inertial properties, the vectorial equation expressing the dynamic equilibrium of the flapping blade can be written as

$$\boldsymbol{J}_H\dot{\boldsymbol{\omega}} + \boldsymbol{\omega} \times \boldsymbol{J}_H\boldsymbol{\omega} = \boldsymbol{m}_H - M\boldsymbol{r}_g \times \dot{\boldsymbol{v}}_H, \tag{6.4}$$

where $\dot{\boldsymbol{v}}_H$ is the linear centripetal acceleration, as shown in Fig. 6.1.

Now consider only the scalar equation in the direction of the unitary vector $\boldsymbol{j}$. By rearranging it in terms of the unknown μ and of its time derivatives $\dot{\mu}$ and $\ddot{\mu}$, and dividing all terms by the scalar J_y it is possible to get the form

$$\ddot{\mu} + ((1 + \frac{Mx_geR}{J_y})\Omega^2 + \frac{k_\mu}{J_y} + \frac{Mgx_g}{J_y}\cos\psi)\mu + \frac{m_{A_y}}{J_y} = 0. \tag{6.5}$$

The stiffness term of this second-order equation is bound to three terms, from left to right a centrifugal stiffness term, a structural stiffness term and

a final term due to the stiffening effect of gravity, which acts at the 1P frequency. The forcing effect is due to aerodynamics, and still needs to be written explicitly. To simplify the notation, let the quantities ϵ, $\omega_{\mu NR}$ and G be defined as follows:

$$\epsilon = \frac{Mx_g eR}{J_y}, \omega_{\mu NR} = \frac{k_\mu}{J_y}, G = \frac{Mgx_g}{J_y}. \tag{6.6}$$

Based on these definitions, the equation of the flapping blade can be simplified into

$$\ddot{\mu} + ((1+\epsilon)\Omega^2 + \omega_{\mu NR}^2 + G\cos\psi)\mu + \frac{m_{A_y}}{J_y} = 0. \tag{6.7}$$

It is now possible to turn to the modeling of the aerodynamic loads. Consider a blade element of infinitesimal span, with an aerodynamic cross section as in Fig. 6.3. Let the angle ϕ be defined between the total wind speed U_R seen by the profile and the plane of the rotor disc, or equivalently between the rotor axis and the direction of the lift component exerted by the flow on the considered profile. The speed U_R is given by the composition of the tangential wind speed U_T, the component in the rotor plane, and the axial wind speed U_P, normal to the rotor plane and aligned with the axis of the rotor. Let the angle β be the blade pitch angle, and the angle α be the incidence angle, linearly proportional to the lifting force, and such that $\alpha = \phi - \beta$.

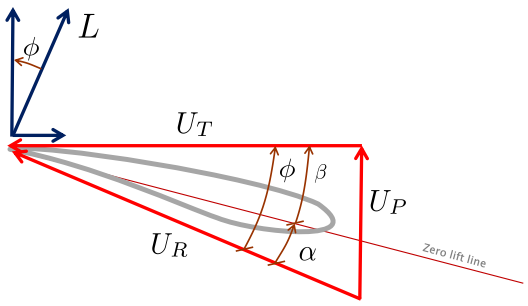

Figure 6.3: Blade element profile.

The lifting force exerted on the considered profile can be expressed as a function of the total speed U_R, the local chord c, the local aerodynamic coefficient $C_{L/\alpha}\alpha$ and the air density ρ as

$$L = \frac{1}{2}\rho U_R^2 c C_{L_\alpha}\alpha. \tag{6.8}$$

If it is assumed that the angle ϕ be small, then the definition of the incidence α can be given as

$$\alpha = \phi - \beta = \tan^{-1}\frac{U_P}{U_T} - \beta \approx \frac{U_P}{U_T} - \beta. \tag{6.9}$$

Moreover, under the latter hypothesis it is possible to assume that

$$U_R^2 = U_P^2 + U_T^2 \approx U_T^2. \tag{6.10}$$

Following these approximations, the definition of the local lifting force can be written as

$$L = \frac{1}{2}\rho c C_{L_\alpha}(U_P U_T - \beta U_T^2). \tag{6.11}$$

Notice that the hypothesis of small ϕ by the geometrical definition of that angle (Fig. 6.3) implies a hypothesis on the incidence α and pitch β, which must be small too. As α is usually not very high for reasons bound to aerodynamic stall, this constraint is basically imposed to the pitch angle β. Moreover, a small value of ϕ implies that the flap motion of the blade can be confused with the out-of-plane motion. Speaking of steady state conditions, this hypothesis can be verified in practice in partial load region II, when the pitch angle in equilibrium is actually small (recall chapter 2). However, this assumption is far from reality when the machine operates in region III, as in that case the pitch angle β can be much higher than zero. So, it is already possible to forecast a loss of fidelity of this model when working on trim points at wind speeds above rated.

It is now necessary to specify expressions for U_T and U_P as functions of the states defining the spatial distribution of the wind over the rotor disc. The wind field can be not uniform because of vertical wind shear, local inflow effects and of course because of a lateral wind component (cross flow) V_0. The latter is very important in the current analysis, as it may be considered as a lateral wind component given by a misalignment of the incoming flow with respect to the rotor axis, and thus strictly related to yaw. In Fig. 6.4 left the adopted model for the wind shear is graphically described: it is linear with $\frac{r}{R}cos(\psi)$ and modulated by the shear intensity K. In Fig. 6.4 right the effect of the lateral wind V_0, the inflow (notice the inflow coefficient a) and the vertical shear are illustrated. Notice that a damping effect $\dot{\mu}r$ arises in presence of a flap oscillation. The inflow effect, which in real environment is given by the interaction between the incoming flow and the rotor, is modeled by means of the coefficient $a \leq 1$ applied to the value of the upstream axial wind speed U.

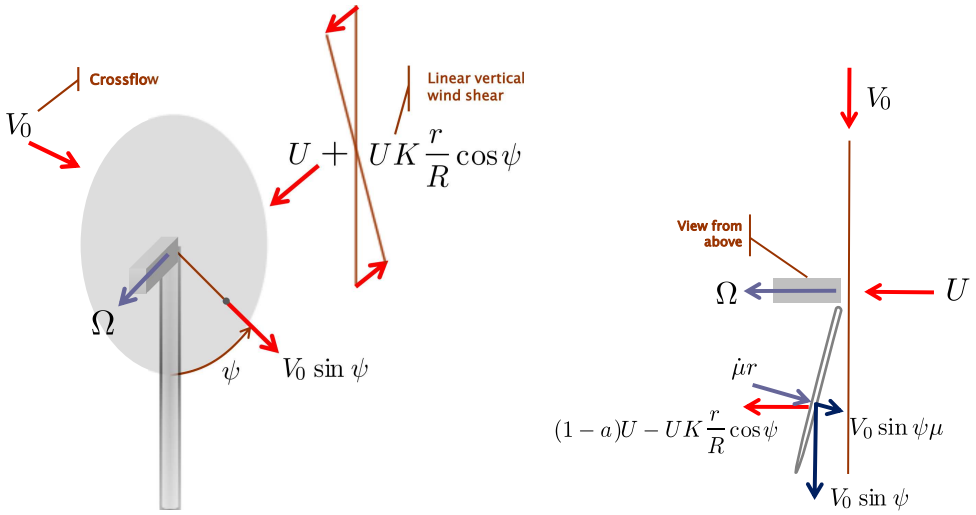

Figure 6.4: Definition of crossflow, inflow and shear effects.

With the provided description of the local wind seen by the generic profile along the blade span, it is possible to get an expression for U_T and U_P as follows:

$$U_T = \Omega r - V_0 \cos\psi, \tag{6.12}$$

$$U_P = (1-a)U - \dot{\mu}r - V_0 \sin\psi\mu - UK\frac{r}{R}\cos\psi. \tag{6.13}$$

From Eq. (6.12) the wind speed component U_T laying in the rotor plane depends on the speed of the rotating blade and on the cross flow V_0. From equation (6.13) the wind component U_P normal to the rotor plane depends on the axial wind component U, weighed by the inflow effect modeled by a, on the speed of the blade in the flapwise direction due to the flapping rate $\dot{\mu}$, on the cross flow V_0 and on the effect of the wind shear.

From definitions (6.12) and (6.13), and from Eq. (6.11) it is possible to provide an analytical expression for the component m_y of the aerodynamic moment $\boldsymbol{m_A}$ in the flapwise direction (i.e. out-of-plane direction, for this can be confused with flapwise direction thanks to the hypothesis of low ϕ), measured at the hinge point H:

$$\begin{aligned} m_y &= -\int_0^R L\cos\phi\cos\mu r\mathrm{d}r \approx -\int_0^R Lr\mathrm{d}r = \\ &= -\int_0^R \frac{1}{2}\rho c C_{L_\alpha}(U_P U_T - \beta U_T^2) r\mathrm{d}r. \end{aligned} \tag{6.14}$$

If the geometric and aerodynamic characteristics of the rotor (in terms of c and C_{L_α} for any position in the spanwise direction) are known, it is possible to solve the integral (6.14), and, by substituting the result in (6.7), to complete the description of the dynamics of the flapping blade.

The resulting equation can be rewritten in terms of the azimuthal coordinate ψ following the hypothesis of constant Ω: in that case it is possible to pass from the time derivative $\dot{\mu}$ to the azimuthal derivative μ' by the definition

$$\dot{\mu} = \dot{\psi}\frac{d\mu}{d\psi} = \Omega\mu'. \tag{6.15}$$

By substituting this definition in Eq. (6.7), rearranging and dividing by the mass coefficient multiplying μ'', it is possible to get the equation of the dynamics of the flapping blade in terms of the azimuthal derivatives:

$$\begin{aligned}
&\mu'' + \gamma\left(\frac{1}{8} - \frac{\bar{V}_0\cos\psi}{6}\right)\mu' + \\
&+ \left(1 + \epsilon + \left(\frac{\omega_{\mu NR}}{\Omega}\right)^2 + \frac{G}{\Omega^2}\cos\psi + \frac{\gamma\bar{V}_0\sin\psi}{6}\right)\mu \\
&= \frac{\gamma}{2}\left(\frac{\Lambda}{3} - \frac{\beta}{4}\right) - \cos\psi\frac{\gamma}{2}\bar{V}_0\left(\frac{\Lambda}{2} + \frac{2\beta}{3}\right) + \frac{\gamma K}{8}\cos\psi U,
\end{aligned} \tag{6.16}$$

where $\gamma = \frac{\rho C_{l_\alpha} c R^4}{J_y}$ is the Locke number, $\bar{V}_0 = \frac{V_0}{\Omega R}$ and $\Lambda = \frac{U}{\Omega R}$ is the inverse of the tip speed ratio.

Now, Eq. (6.16) can be solved hypothesizing that the solution be oscillating at the 1P frequency. Following the hypothesis of constant Ω driving to this equation and supposing operation in constant wind with the description of the incoming wind field provided above, this hypothesis on the solution is not that heavy, even if it explicitly limits the frequency spectrum of the resulting flap signal. It yields

$$\mu = \mu_0 + \mu_{1s}\sin\psi + \mu_{1c}\cos\psi. \tag{6.17}$$

By substituting this hypothesis into Eq. (6.16) and collecting the terms to match the harmonic coefficients of the solution μ_0, μ_{1s}, μ_{1c}, dropping higher harmonic terms in the process – that is, any products of sine and cosine functions by themselves or mixed –, it is possible to get the solving system

$$\begin{bmatrix} F & B & 0 \\ 2B & F-1 & \gamma/8 \\ \gamma\bar{V}_0/6 & -\gamma/8 & F-1 \end{bmatrix} \begin{Bmatrix} \mu_0 \\ \mu_{1c} \\ \mu_{1s} \end{Bmatrix} = \begin{Bmatrix} \gamma A/2 \\ -\frac{\gamma}{2}\left(\bar{V}_0 A_3 + \frac{K\bar{U}}{4}\right) \\ 0 \end{Bmatrix} \tag{6.18}$$

where for convenience some terms previously presented have been grouped as follows:

$$\begin{aligned} F &= 1 + \epsilon + \left(\frac{\omega_{\mu NR}}{\Omega}\right)^2, \\ A &= \frac{\Lambda}{3} - \frac{\beta}{4}, \\ A_3 &= \frac{\Lambda}{2} - \frac{2\beta}{3}, \\ B &= \frac{G}{2\Omega^2}. \end{aligned} \tag{6.19}$$

Here F represents the natural frequency corrected by the stiffening effect of the centrifugal force, A and A_3 represent the effect of an horizontal asymmetric flow, B represents gravity.

Notice the presence in the system above of the two wind states used to describe a nonuniform incoming wind field, namely $\bar{V}_0$ and K. It is possible to rearrange the solving system promoting the wind states $\bar{V}_0$ and K to the role of unknowns in the scalar equations where they appear. By this process it is possible to get to the following solving system:

$$\begin{bmatrix} -\frac{\gamma}{2}A_3 & -\frac{\gamma}{2}\frac{U}{4} \\ \frac{\gamma}{6}\mu_0 & 0 \end{bmatrix} \begin{Bmatrix} \bar{V}_0 \\ K \end{Bmatrix} = \begin{Bmatrix} 2B\mu_0 + (F-1)\mu_{1c} + \frac{\gamma}{8}\mu_{1s} \\ \frac{\gamma}{8}\mu_{1c} - (F-1)\mu_{1s} \end{Bmatrix}. \tag{6.20}$$

Eq. (6.20) is of primary relevance. It states that if it is possible to measure the harmonic coefficients of the solution μ then it is also possible to solve the system determining $\bar{V}_0$ and K, provided the system matrix is not singular. About this latter issue, the equation written for this model assures that the model matrix is nonsingular in any real operating wind condition, that is when the three coefficients that are not identically null are not equal to zero. So, this equation not only shows that there is a straightforward relationship between the flap motion and the wind states $\bar{V}_0$ and K, but also that the effects due to changes in $\bar{V}_0$ and K on the flap motion of the blade are different from one another, because the two lines of the system matrix are linearly independent by constitution.

Based on this equation, it is possible to state that the two wind states have distinguishable effects on the flap motion of the blade. Put in an easier way, a change in yaw will generate on the measured flap signal at the 1P an effect which can be distinguished from the effect of a change in shear. This is crucial, as without this notion the feasibility of a yaw observer could not be postulated: if the effects of the two wind states were not different, then a measured flap motion could not be mathematically related to the presence

of a cross flow instead of a shear layer of given intensity. This issue has been remarked through practical results and highlighted in chapter 5.

As a final consideration, taking only the second line of Eq. (6.20), which is not dependant on the shear coefficient K, an even simpler expression for the cross flow $\bar{V}_0$ can be found:

$$\bar{V}_0 = \begin{bmatrix} \frac{3}{4} & (1-F) \end{bmatrix} \begin{Bmatrix} \frac{\mu_{1c}}{\mu_0} \\ \frac{\mu_{1s}}{\mu_0} \end{Bmatrix}. \tag{6.21}$$

From the latter equation it is possible to get some further indications about the feasibility of a yaw observer: it can be seen that the relationship between the coefficients of the flap solution and the cross flow $\bar{V}_0$ comes in the form

$$\bar{V}_0 = \boldsymbol{T}(\Omega) \begin{Bmatrix} \frac{\mu_{1c}}{\mu_0} \\ \frac{\mu_{1s}}{\mu_0} \end{Bmatrix} \tag{6.22}$$

where a mild dependence of the coefficients of the model $\boldsymbol{T}(\Omega)$ from Ω can be expected, as the first coefficient is constant, while the second depends on F, the flap frequency modified due to the stiffening effect of the centrifugal force: the intensity of this effect usually varies only slightly with the rotational speed of the rotor, and so will the coefficients of $\boldsymbol{T}(\Omega)$. Moreover, the wind state $\bar{V}_0$ does not depend directly on the coefficients of the solution μ, but on the ratios $\frac{\mu_{1s}}{\mu_0}$ and $\frac{\mu_{1c}}{\mu_0}$. This suggests that $\bar{V}_0$ is not bound to the absolute amplitude of the flap angle, but to both simultaneous values of the normalized coefficients of the 1P solution, and so arguably to the phase of the measured flap signal.

For the sake of clarity, notice that even if the yaw angle is not explicitly present in the equation of the flapping blade, the quantity $\bar{V}_0$ is representative of the lateral wind V_0. Thus it is representative of the angle between the actual wind field and the rotor axis – what it is here intended as "yaw".

Now, as previously mentioned, the assumptions made to proceed to the synthesis of the simplified model described above are sometimes rather stringent. As will be apparent from the next two paragraph, the quality of the linear model $\boldsymbol{T}(\Omega)$ deteriorates quickly as the wind speed is increased above rated. The reason for that is that in real environment at the higher pitch values typical of trim points corresponding to higher wind speeds the incoming wind tends to have more and more effect on the edgewise motion, while the effect on flap angle tends to be less intense. As it will be clearly shown in the next paragraphs, it is possible to improve the quality of the model at higher wind speeds by augmenting the array of measurements with measures of blade lag.

6.2.2 Equation of the Lagging Blade

The equation for the lagging blade can be derived following the same approach described above for the flapping blade. The simplified model is graphically presented in Fig. 6.5. The modeling process follows the same procedure presented for the model of the flapping blade (two rigid bodies connected by a hinge, stiffness modeled by means of a torsional spring of prescribed stiffness, etc.).

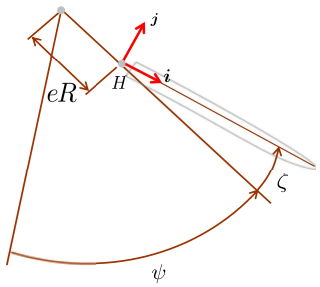

Figure 6.5: Simplified scheme of the lagging blade. Hinge frame.

Let ζ be the lag angle. With qualitatively the same passages presented above, the governing equation for lag, expressed in the azimuthal variable (i.e. as a function of ψ) in a condition with constant Ω, yields

$$\begin{aligned}
&\zeta'' + \left(\epsilon_2 + \frac{G}{\Omega^2}\cos\psi + \left(\frac{\omega_{\zeta NR}}{\Omega}\right)^2\right)\zeta \\
&= \left(2\mu - \gamma\left(\frac{\Lambda}{3} + \frac{\beta}{8}\right) + \frac{\gamma K}{4}\bar{U}\cos\psi + \frac{\gamma}{2}\left(\frac{\beta}{2}\cos\psi + \frac{2\mu}{3}\sin\psi\right)\bar{V}_0\right)\mu' \\
&+ \frac{G\sin\psi}{\Omega^2} + \frac{\gamma}{2}\left(\frac{\Lambda^2}{2} + \frac{\Lambda\beta}{3}\right) \\
&- \frac{\gamma}{2}\left(\mu\left(\Lambda + \frac{\beta}{3}\right)\sin\psi + \frac{\beta\Lambda}{2}\cos\psi\right)\bar{V}_0 - \frac{\gamma K}{2}\left(\frac{2\Lambda}{3} + \frac{\beta}{4}\right)\bar{U}\cos\psi,
\end{aligned} \tag{6.23}$$

where on the left hand side the quantities ϵ_2 and $\omega_{\zeta NR}$ are defined like their counterparts in the flap equation, and on the right hand side a flap-lag coupling term involving the azimuthal derivative μ' can be found, besides a gravity term, a term depending on the Locke number γ, namely a steady lag term (not depending on azimuth angle ψ), a cross flow term depending basically on the wind state $\bar{V}_0$, and finally a term proportional to the vertical shear coefficient K.

By hypothesizing a solution oscillating at the 1P, as previously done for the flap equation, so that

$$\zeta = \zeta_0 + \zeta_{1s}\sin\psi + \zeta_{1c}\cos\psi, \tag{6.24}$$

by substitution, dropping the higher harmonics and the flap-lag coupling effects, it is possible to get the solving equation

$$\zeta'' + \left(\epsilon_2 + \frac{G}{\Omega^2}\cos\psi + \left(\frac{\omega_{\zeta NR}}{\Omega}\right)^2\right)\zeta = \\ \frac{G\sin\psi}{\Omega^2} + \frac{\gamma}{2}\left(\frac{\Lambda^2}{2} + \frac{\Lambda\beta}{3}\right) - \frac{\gamma}{2}\frac{\beta\Lambda}{2}\bar{V}_0\cos\psi - \frac{\gamma K}{2}\left(\frac{2\Lambda}{3} + \frac{\beta}{4}\right)\bar{U}\cos\psi. \tag{6.25}$$

As previously done for the equation of the flapping blade, Eq. (6.25) can be rearranged into a solving system in the unknowns ζ_0, ζ_{1s} and ζ_{1c}. Selecting the scalar equation where the coefficients $\bar{V}_0$ and K appear, it is possible to find a new equation to augment the system (6.20), which becomes

$$\begin{bmatrix} -\frac{\gamma}{2}A_3 & -\frac{\gamma}{2}\frac{U}{4} \\ \frac{\gamma}{6}\mu_0 & 0 \\ \frac{\gamma}{4}\beta\lambda & \frac{\gamma}{2}UA_4 \end{bmatrix} \begin{Bmatrix} \bar{V}_0 \\ K \end{Bmatrix} = \begin{Bmatrix} 2B\mu_0 + (F-1)\mu_{1c} + \frac{\gamma}{8}\mu_{1s} \\ \frac{\gamma}{8}\mu_{1c} - (F-1)\mu_{1s} \\ 2B\zeta_0 + (F_\zeta - 1)\zeta_{1c} \end{Bmatrix}, \tag{6.26}$$

where the term $A_4 = \frac{2\Lambda}{3} + \frac{\beta}{4}$ is bound to the asymmetry of the flow, and $F_\zeta = \epsilon_2 + \left(\frac{\omega_{\zeta NR}}{\Omega}\right)^2$ represents the lag frequency, accounting for the effect of centrifugal forces.

The solving system (6.26) comes in the linear parametric form

$$\bar{V}_0 = \boldsymbol{T}(\Omega)\begin{Bmatrix} \frac{\mu_{1c}}{\mu_0} \\ \frac{\mu_{1s}}{\mu_0} \\ \frac{\zeta_{1c}}{\zeta_0} \\ \frac{\zeta_{1s}}{\zeta_0} \end{Bmatrix}, \tag{6.27}$$

formally identical to Eq. (6.22), but with an augmented array of measurements accounting also for the normalized lag oscillations at the 1P.

In the next paragraphs it will be shown how using the augmented measurement array, accounting also for lag measurements instead of only accounting for flap measurements, it is possible to identify a model $\boldsymbol{T}(\Omega)$ of improved quality, working well also at higher pitch values.

6.3 Observer Synthesis: Approach by Linear Model Identification

In the previous paragraph a theoretical support for the proposed yaw observer has been provided. Moreover, the solving systems (6.20) and (6.26) gave indications about the shape that the model $\boldsymbol{T}$ should take, and what dependencies of the coefficients on the flow and on the machine characteristics should be expected.

This proof is of great importance, but on the other hand, the analytical model previously described is rather simplified and limited, being based on some hypotheses on the structure of the blade – basically modeled by two rigid bodies – which are not verified on the slender and flexible blades typically found on larger wind turbines. Moreover, the hypotheses made on the solutions μ and ζ – which are said to oscillate at 1P – are restrictive and acceptable only when the turbine works with constant Ω.

So, if on one side the described model allows to make some useful considerations, trying to base the yaw observer directly on the analytical expressions of the coefficients presented above may be not a smart way to proceed, because the analytical model is not enough close to reality.

However, based on the informations provided by Eq. (6.20) and (6.26) it is possible to envisage a procedure to get the coefficients of a model between a given set of measurements relative to the blade and the wind states $\bar{V}_0$ and K. From $\bar{V}_0$ it is easy to obtain the measurement of the yaw angle – the misalignment of the instantaneous wind speed averaged over the rotor with respect to the rotor axis.

To find the actual coefficients of the linear model, a model identification approach has been selected. Put in the simplest way possible, a problem of model identification is that of getting a function connecting an array of measurements to an array of inputs, when the inputs are fed to a generic system whose output are the considered measurements. If the model is linear, then the problem is that of finding out the values of the coefficients of the model matrix $\boldsymbol{T}$ defining the linear relationship between the two arrays. The model described previously shows that there exists a linear relationship between $\bar{V}_0$ and K and the coefficients of the flap motion, at least for low values of pitch β.

Before describing the actual identification process it is necessary to show some basic choices operated on the array of measurements, on the model parametrization and also on the wind states.

Because one of the aims of the proposed yaw observer is that of using only those sensors which are commonly present on larger wind turbines,

which include strain gauges but not always accelerometers on the blades – accelerometers may be needed for the observation of kinematic quantities as shown in chapter 5 –, the strain measurements coming from strain gauges at the blade root are considered instead of the flap and lag angles. Moreover, the measures that are actually used are those of the bending moments at the blade roots, which in a simulation environment can be measured directly, while in reality they can be obtained from measures of strain through a tuning process. It should also be noted that this choice of measurements makes sense on a real turbine, where the blade gets deformed in a rather complex way and the definition of a flap (or lag) angle is not so simple as for the schematic structural model presented above. On a real blade, the loads at root can be seen as a synthetic way to get an idea of the average effect of the wind blowing on the blade itself.

As stated above, it is important to remark that the developed model holds only for constant Ω. Given a certain trim condition, it is possible to characterize it by means of the sole axial wind speed averaged over the rotor, U, provided there is a trimming control system able to keep the machine at the value of Ω^* prescribed for that wind speed, by means of suitable pitch and torque inputs. In other words, the hypothesis of constant Ω can be turned into an hypothesis of constant U if the machine is regulated by an appropriate control system keeping it at the prescribed rotational speed for that U. In this fashion, it is possible to identify a linear model parametrized as a function of the rotor averaged axial wind speed, $\boldsymbol{T}(U)$. Scheduling the model with respect to U is useful for a better characterization of the behavior in region III, where Ω is usually the same for any wind speed (see chapter 2). Of course, on the real machine both measurements are always available, making this choice not critical for operations in real environment.

In the theoretical model the incoming wind field is described by means of the axial wind speed, of the crossflow V_0 and of the linear shear coefficient K. Instead of using the linear shear model it is possible to hypothesize a more usual power law model. Like the linear model, it is fully characterized by means of a single coefficient, the exponent of the power law, defined here as K_{pl}. This change does not bring in significant alterations to the considerations supported by the model described previously.

The identification procedure implemented to obtain the coefficients of the model $\boldsymbol{T}(U)$ is based on a few steps. First, it is necessary to run a group of constant wind simulations, where the rotor-averaged wind value U, the yaw angle and the shear coefficient are kept constant. For any U of interest several simulations are performed: a set with a given yaw angle and standard shear coefficient (0.2 as usual), another set with no yaw misalignment and non-standard values for the shear coefficient. In these simulations a trim-

ming control system is operative, and keeps the rotational speed Ω at the prescribed value for the considered axial wind speed. Given the values of U, Ω and that of the yaw angle, it is easy to evaluate for each simulation the real value of $\bar{V}_0$. Moreover, during each simulation the values of the bending moments at the root of the blades are recorded. Because the machine is kept trimmed in a constant wind condition, the time histories of the considered loads will show an evident periodicity. After having completed the simulation set for the identification, it is possible to post-process the time histories of the loads, demodulating them at the 1P frequency in order to get the amplitude of the oscillation at the 1P frequency, and in a formally identical way, demodulating at the 0P to find the constant. The demodulation process is carried out independently on the three blades, based on the integral method

$$\begin{aligned} M_{1s} &= \frac{1}{k\pi}\int_{\psi}^{\psi-2k\pi} M(t)sin(\psi)d\psi, \\ M_{1c} &= \frac{1}{k\pi}\int_{\psi}^{\psi-2k\pi} M(t)cos(\psi)d\psi, \end{aligned} \tag{6.28}$$

which can be applied on one period of oscillation of the load signal (that is with $k = 1$), or on a larger number of revolutions ($k > 1$) to obtain a better filtering effect. In the same fashion, the constant component of the signal $M(t)$ over the selected demodulation window can be computed as

$$M_0 = \frac{1}{2k\pi}\int_{\psi}^{\psi-2k\pi} M(t)d\psi. \tag{6.29}$$

Subsequently, an average of the resulting 1P and 0P amplitudes over the three blades is calculated, to filter any difference that may arise even in constant wind conditions due to small oscillations of Ω, which is kept under control by a realistic control system and thus may not be perfectly constant in time.

After the completion of all the simulations, for any given U it is formally possible to formulate the following relationship, where the coefficients of the matrix $\boldsymbol{T}(U)$ are still unknown:

$$\boldsymbol{W} = \boldsymbol{T}(U)\boldsymbol{M}, \tag{6.30}$$

where

$$\boldsymbol{W} = \left\{ \begin{array}{c} \bar{\boldsymbol{V}}_0 \\ \boldsymbol{K}_{pl} \end{array} \right\} = \left[\begin{array}{cccc} \bar{V}_0^1 & \bar{V}_0^1 & \dots & \bar{V}_0^N \\ K_{pl}^1 & K_{pl}^2 & \dots & K_{pl}^N \end{array} \right], \tag{6.31}$$

$$\boldsymbol{M} = \left[\begin{array}{ccc} \frac{M_{1c}^1}{M_0^1} & \frac{M_{1c}^2}{M_0^2} & \dots \quad \frac{M_{1c}^N}{M_0^N} \\ \frac{M_{1s}^1}{M_0^1} & \frac{M_{1s}^2}{M_0^2} & \dots \quad \frac{M_{1s}^N}{M_0^N} \end{array} \right], \tag{6.32}$$

and the number N is the total number of simulations performed at the same rotor averaged wind speed U and at different values of $\bar{V}_0$ or shear coefficient K_{pl}. Matrix $\boldsymbol{M}$ will be two rows – as in the previous formula – if only the flap loads will be accounted for, or four rows if both flap and lag will be. As will be shown shortly, the number of yaw angle values considered for the identification process should be large enough to cover a suitable range of possible misalignment conditions met in real environment. As a result, the matrix $\boldsymbol{W}$ will not be square. Once all the aforementioned matrices have been prepared, it is possible to evaluate the coefficients of the model matrix $\boldsymbol{T}(U)$, by computing the pseudo-inverse of $\boldsymbol{M}$, as

$$\boldsymbol{T}(U) = \boldsymbol{W}\boldsymbol{M}(\boldsymbol{M}\boldsymbol{M}^T)^{-1}. \tag{6.33}$$

From the latter equation it is clearly visible that the model can only be identified if there exists the pseudo-inverse of matrix $\boldsymbol{M}$, that is true when the columns of $\boldsymbol{M}$ corresponding to different values of $\bar{V}_0$ and K_{pl} are not linearly dependant. This is equal to say that only if the two considered wind states have an effect on the considered measurement array then it is possible to find a relationship between this measurement array and the wind states $\bar{V}_0$ and K. As shown in the previous paragraph, this is one of the key problems addressed on a theoretical level by the use of a simplified blade model.

It is important to notice that even if the only state of interest is yaw (or cross flow $\bar{V}_0$), both the cross flow and the shear coefficient are considered in the identification process. The reason for that is the necessity to identify a model able to distinguish between the effects of a non-null yaw and a non-standard shear. While the quality of the observation of shear will not be investigated, as the main focus is here on the measurement of a signal allowing yaw control, in the results it will be shown how following this identification procedure the quality of the observation of yaw is not touched by the presence of a non-standard shear.

6.4 Results

In the following subparagraphs the results of the identification process and some applications of the observer in simulation environment are shown. All the experiments in simulation environment have been carried out on the `Cp-Lambda` model of the 3.0 MW turbine (see chapter 1), equipped with sensors for the flap and lag components of the bending moment at the root of each of the three blades.

6.4.1 Identification Process

In order to identify the coefficients of $\boldsymbol{T}(U)$ the procedure presented in the previous paragraph has been used. For any given value of rotor averaged mean speed U between 3 and 25 m/sec and every 2 m/sec, fifteen 100 sec simulations with different misalignment angles, ranging from -48 deg to +48 deg every 8 deg, and shear power law exponent 0.2 have been performed. Besides them, four more 100 sec simulations for every constant wind U have been completed with 0 deg yaw and shear exponent 0.4, 0.3, 0.1 and 0.0 respectively. The trimming control system is the baseline full-state feedback LQR, with knowledge of the tower top fore-aft motion and of the integral of Ω, presented in chapter 2.

In a first trial made to verify the reliability of the information coming from the theoretical model, an array of measurements $\boldsymbol{M}$ based only on the normalized 1P amplitude of the bending moments in the flapwise direction has been used. What can be expected, based on the considerations presented in the previous paragraphs, is a good general identifiability of the model for a broad range of wind speeds from the minimum (cut-in) up to lower region III, while some loss of quality in the model can be expected as pitch is increased for trim points at higher wind speeds towards the cut-out value. The results presented on Fig. 6.6 show a comparison, for U of 7 m/sec, 15 m/sec and 25 m/sec, between the values of $\bar{V}_0$ imposed during the simulations performed to identify the model (reported on the horizontal axis) and the values $\bar{V}_0^*$ obtained from the identified model, that is, from the multiplication of the array of the normalized 1P amplitudes M obtained from the simulation and the model matrix $\boldsymbol{T}(U)$. If the identified model was perfect, the values of the imposed (real) $\bar{V}_0$ should be equal to those of the observed $\bar{V}_0^*$: the resulting theoretical line is reported in red on the following graphs (solid line). The actual reconstructed values $\bar{V}_0^*$ are reported as blue squares for each imposed value $\bar{V}_0$.

Fig. 6.6 clearly matches predictions, as for lower wind speeds U, that is in region II and in lower region III, the observer works fine. On the other hand, for increasing wind speeds the quality of the model shows a negative trend, ending up in a total failure at the highest considered wind speed. This means that the effect of the yaw angle is decreasingly visible on the normalized 1P amplitude of the flap moment signal as U increases.

Based once more on the considerations presented above, a new identification trial is performed based on an augmented array of measurements, where the sine and cosine amplitudes at the 1P of the lag moment at blade root, normalized by its constant component, are added to the normalized amplitudes of the flap moment. Fig. 6.7 shows how the quality of the latter

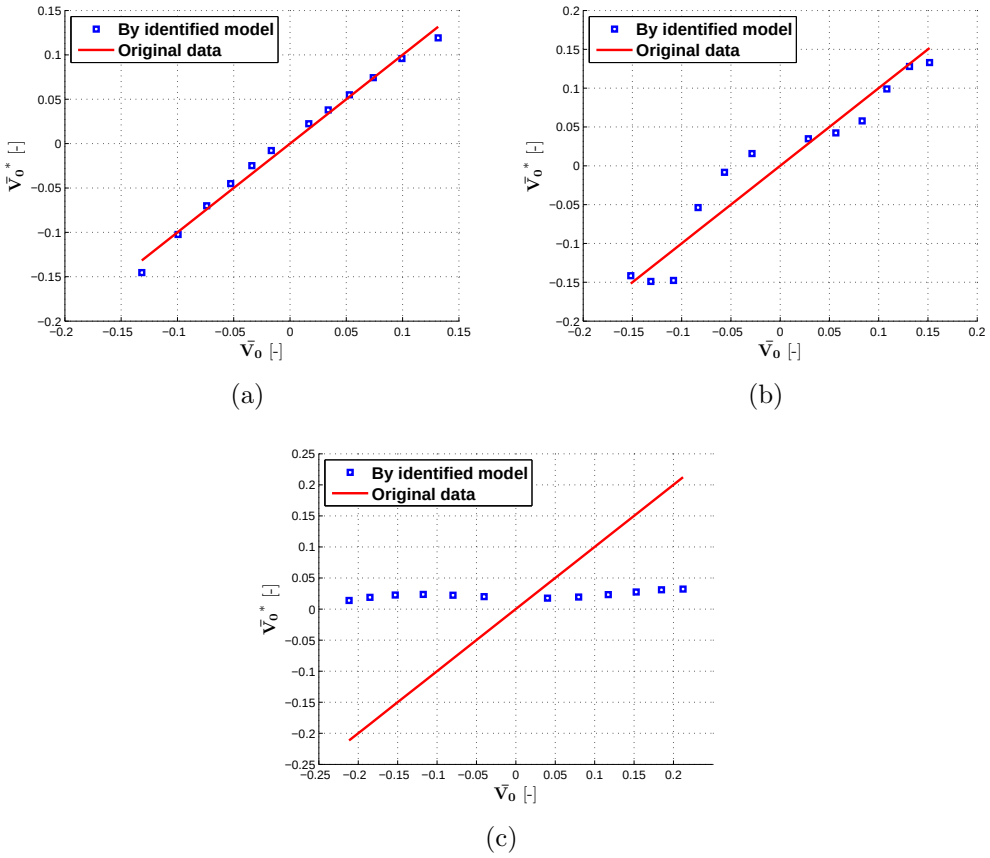

Figure 6.6: Test of the identified model based on normalized 1P amplitudes of blade flap moments. (a) 7 m/sec. (b) 15 m/sec. (c) 25 m/sec.

model is better even at higher wind speeds.

6.4.2 Observation Results

The model matrices, stored as functions of U, can now be used to provide a measurement of the yaw angle between the incoming wind and the rotor axis in operating conditions. To test the quality of the reconstruction, a set of increasingly demanding simulations has been carried out. In all of them a time history for the yaw angle is imposed. From that, and from the instantaneous values of the wind speed U, measured by the anemometer, and Ω, it is possible to evaluate the real $\bar{V}_0$, which can be compared to the observed $\bar{V}_0^*$. The results presented in the following paragraphs were obtained from an observer based on the measurement of both flap and lag loads at blade root.

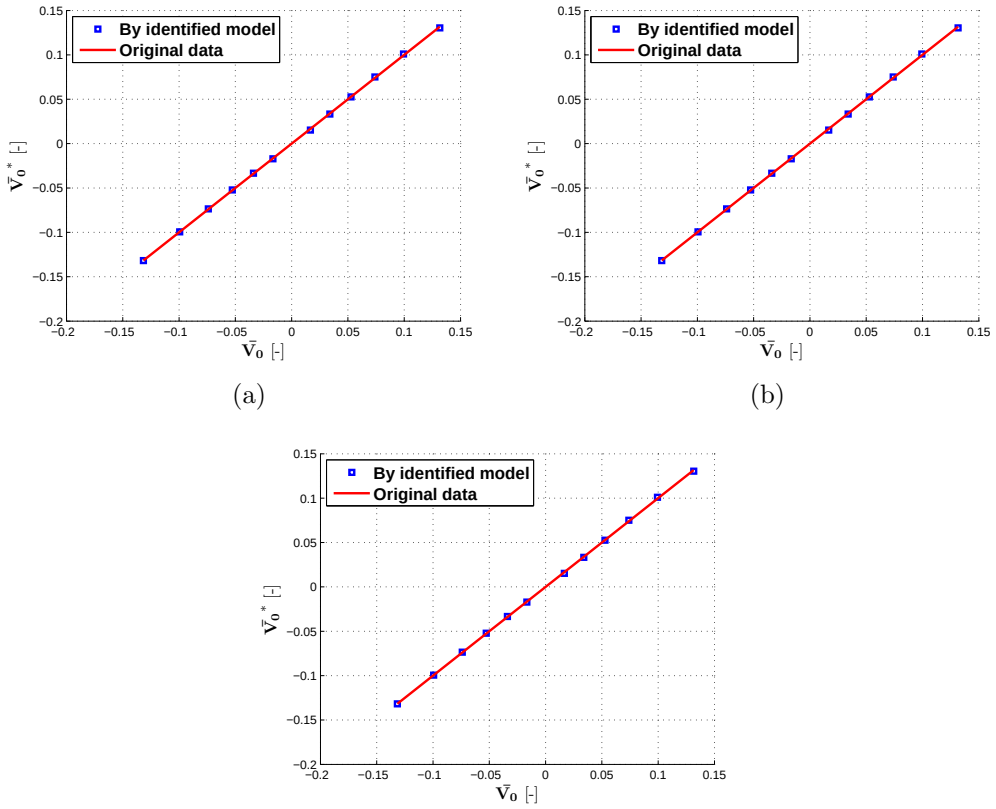

Figure 6.7: Test of the identified model based on normalized 1P amplitudes of blade flap and lag moments. (a) 7 m/sec. (b) 15 m/sec. (c) 25 m/sec.

Constant Wind Speed, Variable Angle

A first set of simulations was performed with constant wind speed from 3 to 25 m/sec every 2 m/sec, with a yaw angle kept at different constant values for time spans of 40 sec, connected by ramps of 10 sec. In a first phase only yaw is changed. To make sure that there is not any interference of the shear value on the yaw reading, in a second phase yaw is kept constant at a not null value, while shear is changed according to a time history made up of constant values connected by ramps. In Fig. 6.8 the result for a simulation at 15 m/sec is reported. It clearly shows that the reconstruction based on the model previously identified allows to follow the movements of yaw with virtually no delay. Moreover, after 550 sec, in presence of a variable shear coefficient, the estimation of yaw is still rather good.

On the load plot (bottom quadrant) of Fig. 6.8, it is possible to see the

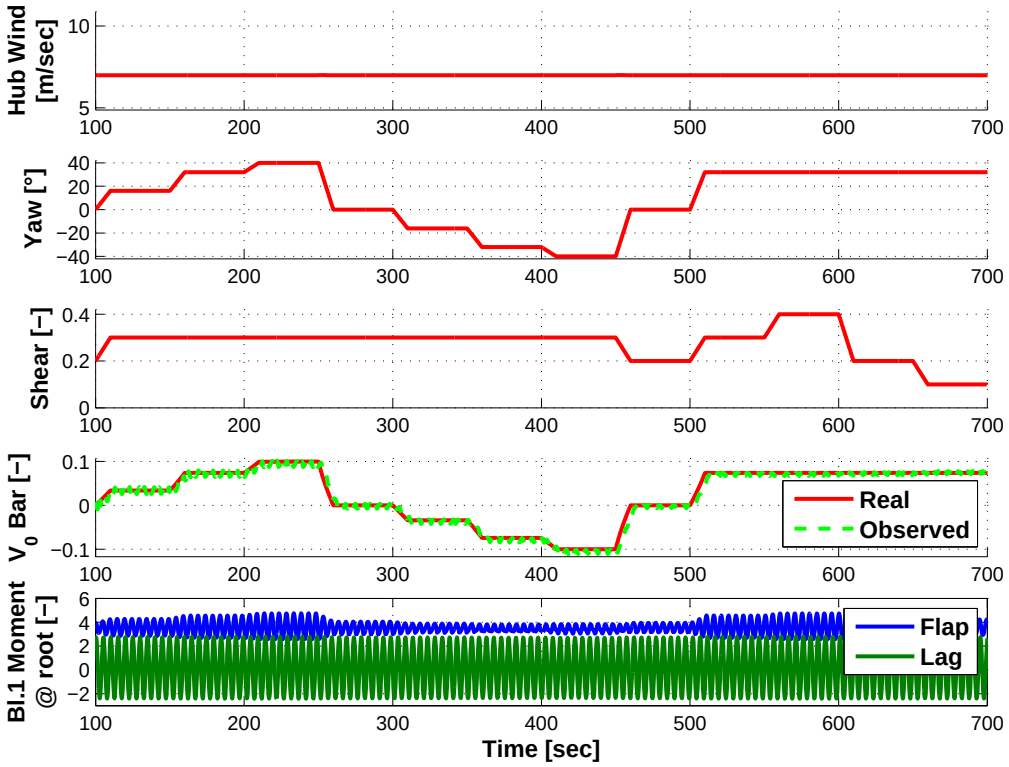

Figure 6.8: Observation results with constant U and variable yaw angle and shear. Time histories of U, shear coefficient K_{pl}, yaw angle, $\bar{V}_0$ real and observed, Nr. 1 non-dimensional blade flap and lag moments at root.

large contribution of the 1P oscillatory component to the time history of the loads. This can be confirmed by a spectral analysis, as shown in Fig. 6.9, where a portion of the time histories of the loads at the root of Nr. 1 blade, presented in Fig. 6.8, has been used. Here the peak at the 1P is larger than those corresponding to higher frequencies by about two orders of magnitude. Recall that the observer is based on a model identified considering only the 1P frequency in the blade loads. The frequency separation between the oscillatory components at the 1P and those at higher frequencies is of help to get high-quality observation results in this condition. Nonetheless, as witnessed by good observation results in turbulent conditions (see the following paragraphs), where the load spectra are obviously more disturbed, a reduced difference between the peak at 1P and the following peaks, as well as a less marked frequency separation between oscillatory components of blade loads, do not hamper the performance of the observer. The choice of the demodulation process based on the integral method and making use of

the azimuth variable ψ instead of the rotational speed proves very useful in catching the desired 1P component of the load also in conditions of variable Ω (see Eq. 6.28), while suitable filtering techniques are able to limit the pollution of the observation results due in particular to a diminished frequency separation between peaks at frequencies close to each other. For now, i.e. in deterministic and piecewise constant wind conditions, the use of filtering techniques is not required.

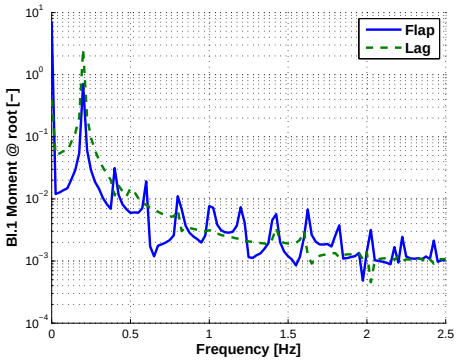

Figure 6.9: Normalized frequency spectra of non-dimensional Nr. 1 blade flap and lag moments at root, under the wind conditions described in Fig. 6.8, between 110 and 150 sec.

Piecewise Constant Wind Speed, Variable Angle

To understand the effect of model switching on the performance of the observer, the same time history for yaw selected for the previous trial can be superimposed to a changing value of wind speed U. The change in U is managed by the observer like done by the LQR controller with respect to the control gains [23]. The matrices $\boldsymbol{T}(U)$ are stored offline for some values of U_k, ranging from 3 m/sec to 25 m/sec every 2 m/sec. A linear interpolation is performed based on the real wind U and on the two closest values U_k and U_{k+1} such that $U_k < U < U_{k+1}$. Fig. 6.10 shows the results for a starting hub wind speed of 7 m/sec, which is then increased or decreased by +/-2 m/sec. Even if the effects of transients are noticeable, the behavior of the observer is still rather satisfying.

Constant Averaged Wind Speed, Variable Angle

After having positively tested the observer with totally deterministic wind fields, it is necessary to assess the quality of the results obtained in presence

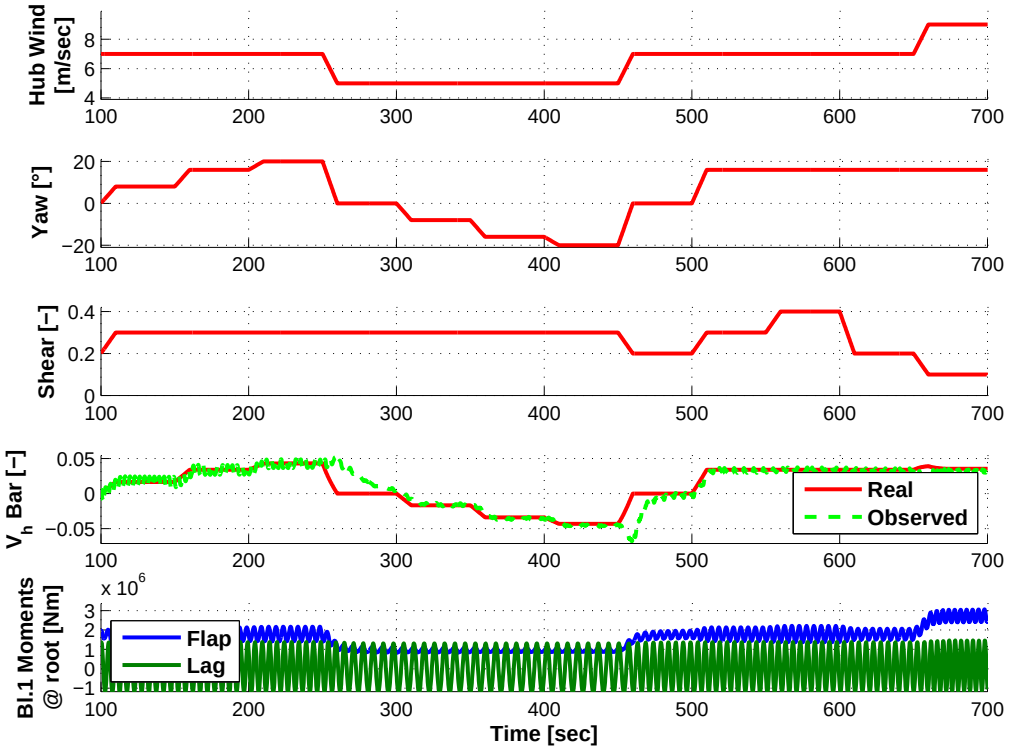

Figure 6.10: Observation results with piecewise constant ramp-connected U and variable yaw angle and shear. Time histories of U, shear coefficient K_{pl}, yaw angle, $\bar{V}_0$ real and observed, Nr. 1 non-dimensional blade flap and lag moments at root.

of a stochastic disturbance. A first trial has been performed based on time histories of wind where the wind speed is composed of a constant value to which a random disturbance, of intensity up to 15% of the mean speed, is superimposed. The yaw angle is then changed according to a piecewise constant ramp-connected fully deterministic time history as in the previous trials.

A set of simulations with increasing average wind speeds from 3 m/sec up to 25 m/sec every 2 m/sec have been completed. An example of the results for U=15 m/sec is shown in Fig. 6.11. The effect of the wind disturbance is clearly visible.

As previously mentioned, the load spectra are rather more disturbed than in a fully deterministic wind condition. In Fig. 6.12 the spectra of a portion of the time histories of the flap and lag moments measured at the root of blade Nr. 1 are reported for the considered turbulent wind condition. With respect to Fig. 6.9, the peak at 1P is less marked if compared to other peaks, yet

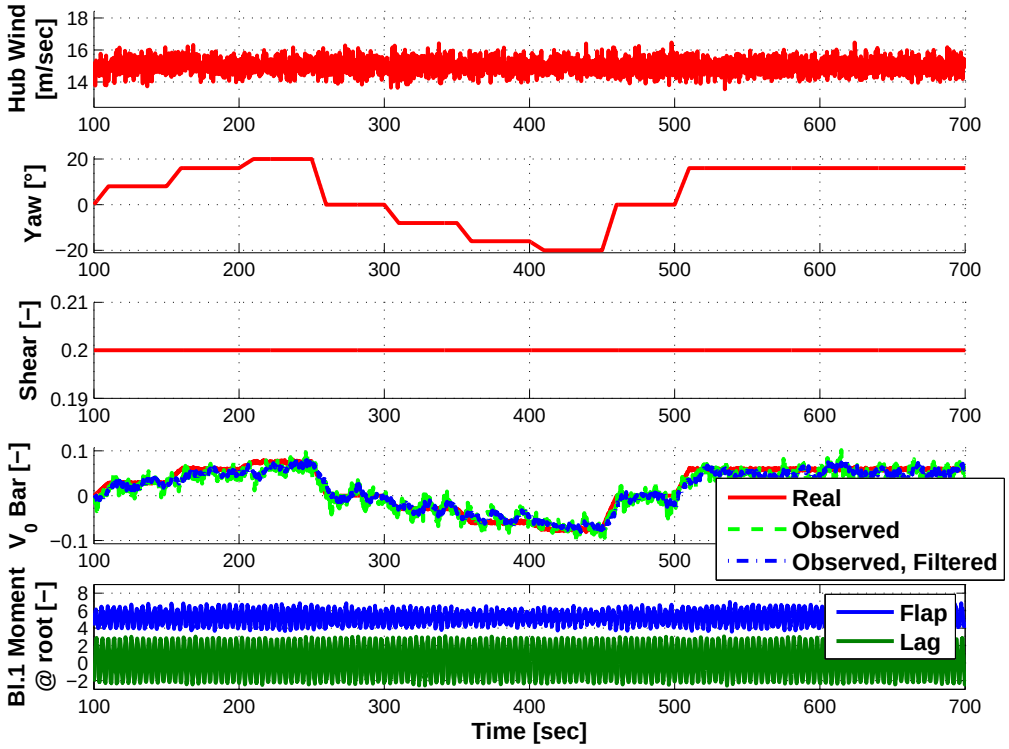

Figure 6.11: Observation results with constant average U, disturbance (15% of instantaneous U) and deterministically varying yaw angle. Time histories of U, shear coefficient K_{pl}, yaw angle, $\bar{V}_0$ real and observed, Nr. 1 non-dimensional blade flap and lag moments at root.

remaining higher than these by about one order of magnitude. The spectra are also more disturbed, and the separation between frequencies less marked.

Notice that a relevant disturbance effect on the observation is also given by a high frequency change in the selection of model coefficients, which causes at every instant a transient effect similar to that observed in Fig. 6.10.

To damp the resulting oscillations it is possible to introduce some elegant filtering techniques, to apply to both the mean wind speed and in the demodulation process. First, it is possible to filter the signal U by means of a moving average filter. Second, the demodulation procedure can be applied to an azimuth window lasting more than a rotor revolution. Considering Eq. (6.28), the latter technique is equal to choose a coefficient $k > 1$. Moreover, it is possible to apply a zero phase filtering technique on the buffer of data collected between the two extreme azimuths appearing as the integral extremes in the same equation, thus denoising the signal before actually run-

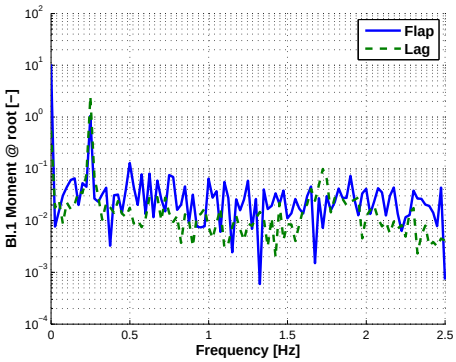

Figure 6.12: Normalized frequency spectra of non-dimensional Nr. 1 blade flap and lag moments at root, under the wind conditions described in Fig. 6.11, between 110 and 150 sec.

ning the demodulation. A period of T=5 sec has been selected for the moving average on U, the demodulation has been carried out on a window of 2 revolutions, applying a zero-phase filter based on a fourth-order Butterworth low-pass with T_{filter}=1 sec. The blue curve on the quadrant of Fig. 6.11 referring to the observation performance is the result of the filtering process. Notice that all this filtering processes have been implemented online (they are not just post-processing), and they can be applied also in real environment. The comparison between the standard and the filtered observations shows the expected improvement in the stability of the observed signal.

The filtering techniques mentioned above and the selected demodulation method (see Eq. (6.28)) allow to get satisfying observation results also in this wind condition and in those analyzed next, featuring a wind intensity continuously changing in time.

Notice that, even if reference yaw is basically a piecewise constant in time, $\bar{V}_0^*$ is not totally so, because of two effects: of course, as neither the average of the wind nor the rotational speed are perfectly constant, then by definition $\bar{V}_0^*$ will change in time; moreover, to account for the fact that only the effect of the wind vectors acting instantaneously on the blades is visible by the observer, an average of $\bar{V}_0^*$ is calculated instantaneously from the local values assumed by V_0^* over the length of the three blades in the considered instant: especially in presence of turbulence, and hence of a non-uniform over-the-rotor V_0^* field, this measurement of effective yaw may be different from that given by a simple average of V_0^* evaluated over the rotor disc, and will typically vary in time a little more than the latter. This measurement has been used for comparisons also in the next paragraphs, in order to lower

the risk of errors in the evaluation of the observation performance.

Variable Mean Wind Speed with Disturbances, Variable Angle

In the next example the disturbance of 15% on U is maintained, but the average U is changed following a sinusoidal law with a period of 50 sec. Based on the same filtering techniques just presented, the resulting observer performance is reported in Fig. 6.13. The same filtering as in the previous paragraph has been implemented, resulting in a moderate disturbance of the observed $\bar{V}_0$ value.

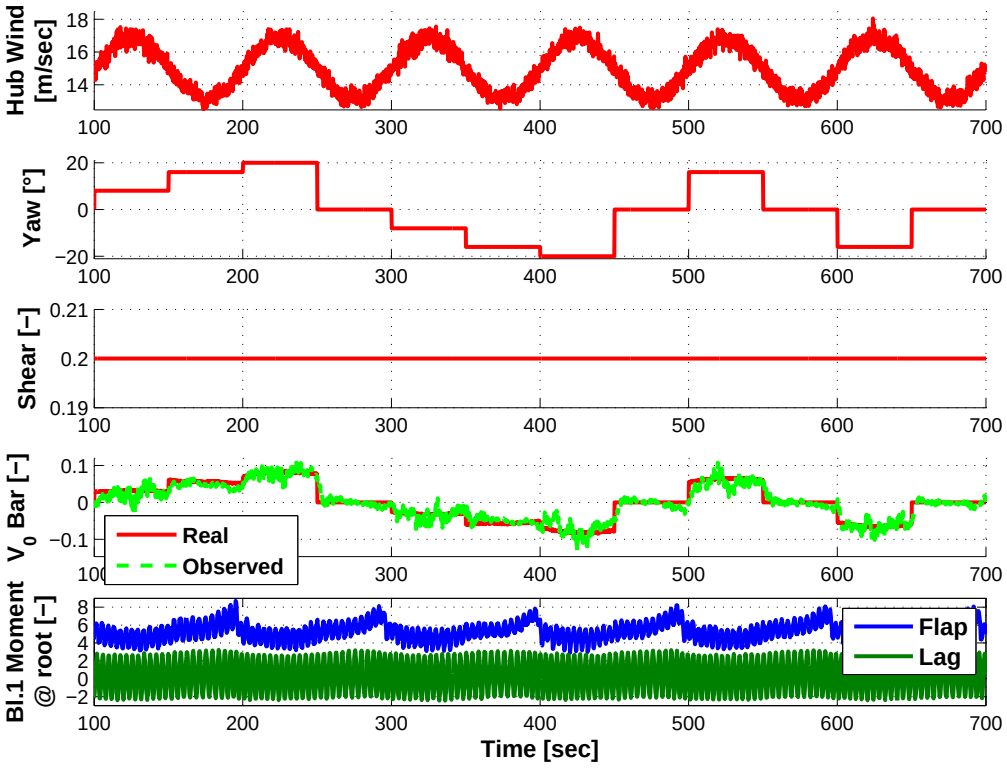

Figure 6.13: Observation results with periodically varying average U, disturbance (15% of instantaneous U) and deterministically varying yaw angle. Time histories of U, shear coefficient K_{pl}, yaw angle, $\bar{V}_0$ real and observed, Nr. 1 non-dimensional blade flap and lag moments at root.

IEC Turbulent Field with Assigned Misalignment Angle

Up to now, the results of the observation process show a rather good performance in almost any analyzed condition. The final check comes from sim-

ulations in which the machine is subject to a turbulent wind flow prepared on a realistic turbulence model. A set of simulations has been performed with different mean wind speeds, with the wind blowing from a given yaw angle with respect to the rotor axis, whose average has been kept constant along all the simulation. Realistic wind fields, produced by a sophisticated turbulence model as prescribed by IEC [66, 74], were used for these trials. Differently from previous test cases, the presence of turbulence in the flow is not modeled by adding a purely random disturbance to a deterministic wind field. Therefore, these simulations are closer to the real operating condition of the turbine in presence of yaw misalignment.

As both the average and local values of the wind speed are continuously changing, also here it is necessary to deploy the filtering techniques presented above. Here the demodulation is performed over 5 rotor revolutions, and the wind speed for the selection of the model coefficients is averaged by a 5 sec moving average.

The aim of the observer in these wind conditions is not that of accurately reproducing the instantaneous value of the yaw angle, but to provide a reliable reading of the mean yaw evaluated on a given time span. Actually, as previously stated, a high frequency actuation of the yaw actuators is not conceivable, making the instantaneous correctness of the observation a non-critical problem. On the other hand, a reliable measurement of the average over a reasonable span is of greater importance for such a control problem.

Several simulations have been performed with turbulent wind speed from 7 m/sec to 23 m/sec every 4 m/sec, with mean yaw angles spanning from -32 deg to +32 deg every 8 deg, with turbulent flows of intensity 10% based on the Kaimal model. The results of the observation process are synthetically presented in Fig. 6.14 for simulations with mean wind speeds of 11, 15 and 19 m/sec. Every point on these plots corresponds to a 600 sec simulation in turbulent wind, with a given misalignment with respect to the rotor axis. The mean values of the real (imposed) yaw, of the observed yaw and of a 50 sec moving average of the observed yaw are shown. Notice that, unlike on previous plots, the yaw misalignment is used here instead of the variable $\bar{V}_0$: of course, the observed value of this yaw angle was obtained at every time step by definition from the values of the observed $\bar{V}_0^*$, and from Ω and the wind speed U, and averaged in time.

At lower wind speeds the observer is able to catch the correct value of the mean with only minor errors for a wide span of misalignment values. For increased wind speeds the performance shows a negative trend, as the error brought in by the observer on the average of yaw is clearly larger. However, the observer provides a slightly better estimation of the misalignment if an average over a suitable time span is considered.

Further information can be obtained from the behavior of the ratios given by the mean error and the mean of the signal, and that of the standard deviation of the error with respect to the mean of the signal (Fig. 6.15, for the same wind speeds considered for Fig. 6.14). The first of these parameters is basically a measure of how large is the average of the local (instantaneous) error, compared to the imposed yaw. From the upper quadrants on Fig. 6.15 it is clear that this error tends to increase for lower yaw angles: this is due to the low value of the imposed yaw, which is the dividing term in the considered ratio, and drives it up. The moving average technique provides a modest aid in reducing this effect. Nonetheless, at least for lower wind speeds, the error is not large with respect to the real mean, and remains acceptable for more likely operating conditions, i.e. for lower yaw values. However, this results show that the error that can be committed using the instantaneous value of the observed signal may be significant. Therefore, as previously stated, the use of the mean value obtained from an average over a suitably long time span should be preferred.

The performance parameter presented on the lower quadrants on Fig. 6.15 is bound to the amplitude of the oscillation of the observation error, divided by the imposed yaw. A rather intense oscillation of the signal with respect to the mean can be noticed for lower yaw angles, while this negative effect is more limited at higher angles. This tells once more that the observed signal should not be used instantaneously, as the local error can be quite high. Vice versa, on longer time spans the value obtained is very reliable. This in turn assures that the observer can be successfully used for low frequency yaw control.

6.5 Conclusions

The proposed yaw observer, based on the use of a scheduled linear model between the 1P amplitudes and the constant components of flap and lag bending moment and the lateral wind, has been implemented and tested thoroughly.

Some preliminary testing has been completed on the identified linear model, highlighting the necessity for lag measurements to mantain identifiability at higher wind speeds and pitches.

Tested in deterministic wind conditions, the observer shows very good instantaneous accuracy.

Tested in more requiring turbulent wind conditions, the observer proves satisfactory in providing reliable time-averaged observations of the yaw angle. The use of some filtering techniques, involving also the use of demodulation

procedures accounting for time windows corresponding to more than one rotor revolution, has been investigated.

All results were obtained from simulations performed on a `Cp-Lambda` model of a three-bladed 3.0 MW horizontal axis wind turbine.

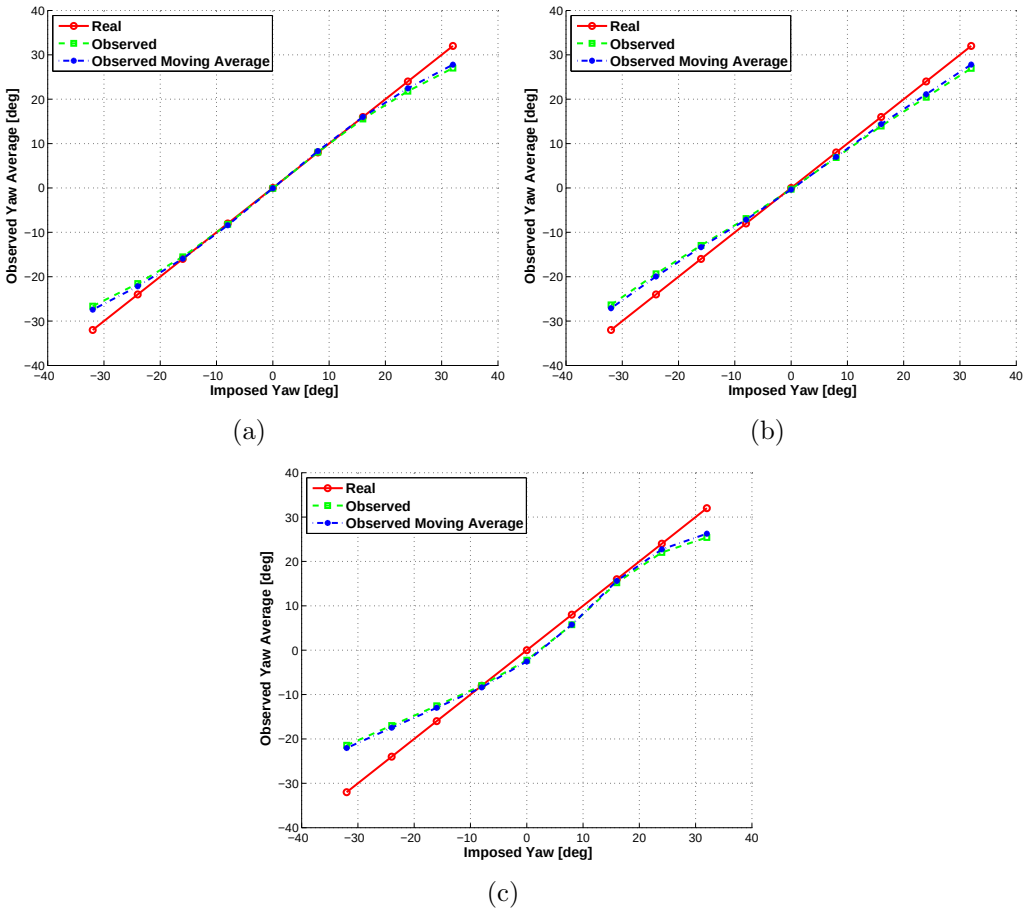

Figure 6.14: Comparison between the means of the real and observed signals, from 600 sec simulations in turbulent wind conditions. Red plain line: real (imposed) value; green dashed line: observed, no moving average; blue dash-dotted line: observed and averaged with 50 sec moving average. (a) 11 m/sec. (b) 15 m/sec. (c) 19 m/sec.

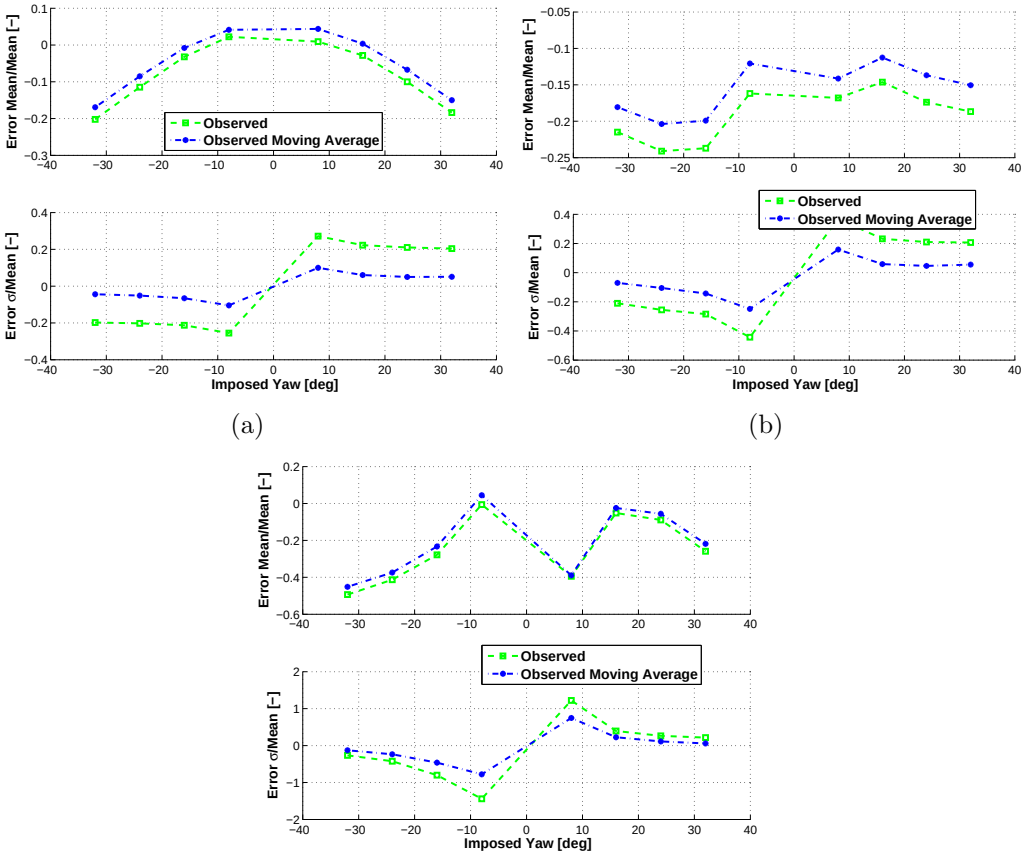

(a) (b)

(c)

Figure 6.15: Average of the observation error normalized by the imposed yaw (upper quadrant), and of the standard deviation of the observation error normalized by the imposed yaw (lower quadrant), from 600 sec simulations in turbulent wind conditions. Green dashed line: observation without moving average; blue dash-dotted line: observation averaged with 50 sec moving average. (a) 11 m/sec. (b) 15 m/sec. (c) 19 m/sec.

Chapter 7

Conclusions

7.1 Contributions and Final Remarks

In this paragraph the conclusions presented at the end of the previous chapters will be briefly recalled.

In chapter 2 a comparison between an industrial PI trimming control system and some proposed controllers based on a common LQR base was carried out using the `Cp-Lambda` model of a 3.0 MW turbine. The goal of the comparison was to prove the reliability of the LQR controller, and to quantify the advantages or disadvantages given by the proposed MIMO architecture with respect to that of a PI-based, SISO industrial controller. Both controllers used collective pitch and electrical torque as control inputs.

In deterministic IEC gust conditions it was discovered that there exists a potential problem with the LQR based on the fore-aft motion, on the rotational speed and on the states of the actuators in keeping the correct trim, mainly because of the model mismatch between the real plant (represented by the detailed `Cp-Lambda` model) and the reduced model considered for the design of the controller. The reduced model has been formulated analytically and completed with data obtained in simulation environment from the multi-body code through *ad hoc* simulations. The use of an array of states augmented by means of an integral state on the rotational speed has solved the problem, the resulting LQR controller being able to target the steady-state differences between actual and reference states.

The control systems were verified also in category A turbulent wind conditions. To deal with an ever changing wind, multiple controllers were designed at different reference wind speeds, and the resulting gains and references were interpolated online on the basis of the value of a filtered, slowly varying measure of the wind. No stability problems were observed anywhere over the

real span of operating wind speeds. Moreover, it was realized that, besides a similar performance obtained from the various systems in terms of power quality, the LQR trimmer without integral state fails in keeping the correct average rotational speed, while the LQR with augmented state is able to solve the problem, and to keep the oscillations of the rotational speed to a level similar to that obtained from the PI.

As the reduced design model of the LQR accounts also for the fore-aft motion of the tower, better results were obtained with the considered LQRs than with the PI on the fore-aft bending moment in turbulent wind conditions.

In chapter 3 a comparison between the performance obtained from a non-predictive LQR with integral state (designed in chapter 2) and two different predictive controllers making use of the anticipate knowledge of the wind as provided by a LiDAR sensor was completed on the `Cp-Lambda` model of a 3.0 MW turbine.

As suggested by the existing literature and by previous negative experiences with less accurate tools, a sufficiently accurate LiDAR simulator was set up, able to process the wind data complying with the IEC specifications and used for all `Cp-Lambda` simulations (and for simulations performed with other tools as well), and to extract from them the information that a LiDAR sensor would provide. The simulator is based on a realistic 3–D motion of the focus of the sensor, and produces an intrinsically filtered signal as the real LiDAR would do, thus reducing the noise in the measured wind without dramatically altering the phase. A realistic delay in the update of the measurement was taken into account, to reproduce the characteristic time taken by the sensor to complete a scan and to produce an updated reading of the wind signal.

The predictive controllers considered and implemented here were a receding horizon control (RHC) and a non-homogeneous LQR control. They are based on a very similar cost function, which for the case of the first controller is optimized numerically over a finite window, while for the other case is optimized analytically over an infinite window. An implementation of the RHC controller was given based on external optimization routines. The implementation of the non-homogeneous LQR could be completed with modifications to the offline gain design phase. It was shown how to treat in an elegant way the theoretical constraints on the non-homogeneous LQR, by considering a piecewise constant disturbance to model the wind, which copes very well with the information coming from the LiDAR simulator.

The performance of the controllers was analyzed first in IEC deterministic gusts. It was shown how the use of the predicted wind can improve the performance of the baseline LQR rather substantially in terms of peak-to-

peak variations of the fore-aft bending load and of the rotational speed. The positive contribution of the predictive component in these wind conditions was verified over all the operative regions, but was found to be more prominent in region III. The comparison between the two predictive controllers showed how the RHC can reach the best performance on both considered performance indices, but at the same time the results obtained from that controller compare well with what was obtained from the non-homogeneous LQR. Moreover, in region II the two predictive controllers give the same results in terms of fore-aft bending load.

The test phase in deterministic wind conditions was used to tune some of the parameters, in particular the length of the prediction window of the controller. It was found that a prediction window shorter than the update time of the LiDAR, and so looking in the future for only very few seconds, gives optimal results.

The tuning has been verified in category A turbulent wind conditions. As done for the feedback LQR trimmers in chapter 2, also here for the non-homogeneous LQR a gain scheduling is implemented based on a filtered measurement of the actual wind. For the RHC the LiDAR measurements over the prediction window are used to interpolate between stored values of the coefficients of the linearized system, available at various reference values of the wind speed. The same scheduling and interpolation strategy is used on the weight matrices and reference arrays with the RHC.

It was shown that the performance of the predictive controllers in terms of power quality is generally good but not very relevant with respect to that of the baseline LQR. Also some problems can be noticed when operating with the RHC in region $\mathrm{II}\frac{1}{2}$, resulting in a worsening effect with respect to the baseline non-predictive controller. On the other hand, the results obtained on the tower bending load are better, and clearly show the ability of the proposed predictive control laws to lower this index. In region II and high region III the results of the two predictive controllers are very close to each other, while in the central region III the RHC behaves clearly better than the non-homogeneous LQR, as it could be expected given its greater complexity.

A comparison of the execution times of the core routines of the two predictive controllers showed a substantial difference, largely in favor of the non-homogenous controller. The fairly simple implementation and definitely lower computational cost of the latter, together with a performance which compares well with that of the RHC, make this control law a possible alternative to the receding horizon control.

In chapter 4 a multi-layer control approach was presented. Besides the ability to trim the machine states inherited by the implemented core trimmer, an industrial PI, for the middle and external layers a centralized implemen-

tation aimed at the reduction of the shaft bending loads was presented first, based on the use of a cyclic pitch input. The middle layer, targeting deterministic loads, was implemented based on an HHC law, itself based on the preliminary identification of a suitable linear wind-scheduled model between the amplitudes of some characteristic oscillatory components of the input and output.

It was shown how such a high fidelity model can be identified by using an appropriate input time history. Moreover, the use of an individual pitch controller based on the Coleman's transformation was implemented in the external layer.

A complete test-campaign was carried out on the `Cp-Lambda` model of the 2.5 MW machine. For the centralized case, it was shown how the proposed controller could add to the performance of a more straightforward controller aimed at the same goal, like the Coleman-based IPC, both in constant wind and category A turbulent wind. The good performance on the selected target loads does not bring side effects in terms of power output or of increased loads on other parts of the turbine, meaning that the application of the HHC control and of the Coleman-based individual pitch control can be correctly tuned to avoid any drift from the normal operating condition, which is satisfactorily maintained by the inner trimming layer. The gain in terms of shaft loads can be expected to be greater in region III, where as usual the pitch input is really actuated without the intervention of constraints due to physical limits.

More results were obtained testing an alternative decentralized control configuration, where besides the collective pitch input component imposed by the trimmer, an individual control input is given to each blade in order to target the bending moment at its root. The middle layer was set up based on an HHC law, while the external layer, aimed at the reduction of the fastly oscillating load components, was implemented in the form of a decentralized PID control. From the results obtained in category A turbulent wind it can be seen that, except for very low wind speeds, this controller is able to provide significant results with respect to the trimmer operating alone, or compared to the little beneficial effect given on the blades by the centralized implementation. On the other hand, it was realized that the side effect on the shaft can be not so good as the effect of the centralized implementation. Moreover, to avoid potential significant drifts from the trimmed conditions, which may derive from a non-null average of the three pitch inputs, it is necessary to limit the intensity of the individual pitch commands by using suitably tuned weights and relaxation factor. As a result, the load-targeting loops of the controller cannot be very aggressive.

In chapter 5 a series of Kalman filters to observe the displacements of the

tower and blades was described first. To that aim, a model-based approach was used to formulate in an exact way the kinematics of the parts of interest. An example of the observation results obtained on the `Cp-Lambda` model of a multi-MW turbine in turbulent conditions demonstrated the feasibility of the proposed structural observer.

The so-obtained observers have been used to feed a wind estimator, formulated to be able to observe an array of wind states, providing a schematic description of the wind blowing on the turbine. In order to make this observer work, it was necessary to integrate a reduced model able to correctly reconstruct the effects of the wind states on the structural states. The selected model was `SymDyn`. Several observation trials were performed in a first phase to check the validity of the concept, using the `SymDyn` model as a simulator, thus avoiding any potential error due to model mismatch. The proposed results show that there is a good accordance between the real and reconstructed signals for some of the considered wind states. Besides these results, it was practically verified that there exists a potential problem of observability, as some different wind states cause equal changes in the structural states, making the interpretation of the deformation difficult. In particular, the vertical shear, the yaw angle and the horizontal shear, all have basically a similar effect on the deformation of the blades.

When performing trials in presence of a model mismatch, i.e. working with measurements coming from `Cp-Lambda`, the observer is still able to reconstruct some of the wind states both in deterministic and turbulent wind conditions, but with some local inaccuracies.

In chapter 6 an observer for the yaw misalignment between the incoming flow and the rotor axis was presented, based on a significant theoretical basis. It was implemented and tested on the `Cp-Lambda` model of the 3.0 MW turbine. The aim was that of obtaining a reliable observation for low frequency yaw control.

As suggested by theory, a model was identified able to put into a relationship some relevant signal components of the blade loads and the intensity of the desired wind state. The linear model, scheduled in wind, was used to test the observation capabilities even in category A turbulent wind, obtaining very good observation performance on the average of the misalignment on prolonged time windows. Moreover, it was shown how the presence of variations on the shear coefficients had not any detrimental effect on the reconstruction of the state of interest, as made immediately clear by theory.

As stated in the introduction, the aim of the present work was not only that of investigating some active control and observation issues, but also to provide realistic results and tools which could be readily applied in real environment. As a consequence, all the control and observation routines were

implemented in a tree of dinamically linked libraries, which communicate with the simulator using the standard interface used by `Bladed`, which in turn can be used also for real-time control, both on scaled wind tunnel models and on real plants.

The use of a sophisticated aero-servo-elastic simulation tool was also a key-feature of the presented research efforts. It should be noted that some of the control issues would not even show up in a simplified testing environment. For instance, the model mismatch between the reduced model used for control design and the simulation model gives an effect only in presence of a significant difference between the reduced model and the simulator, where the latter should behave almost like the real turbine. Moreover, given the filtering action of the modal-based models of the flexible parts of the turbine, on lower-order simulators the proposed multi-layer approach would behave differently, as the load signal obtained would be far less noisy, thus making the external layer less relevant.

7.2 Future Work

Apart from further investigation in new control and observation issues, some work may be done to improve the methodologies and the results obtained till now. Some possible such research objectives are presented in this paragraph.

Much effort is typically devoted to the trial-and-error process of the tuning of the weights for all the considered controllers. This is particularly true with the RHC, the non-homogeneous LQR and the multi-layer controller. To avoid spending too much time on this phase especially when dealing with a new turbine, an automatic optimization procedure based on the use of `Cp-Lambda` coupled with some optimization software may be of great use. Of course, to avoid an overwhelming optimization time, a smart selection of the optimization parameters should be carried out in a first stage, typically limiting the number of the weights which need to be optimized. Moreover, a good initial guess may come from some usual hand-tuning.

As shown in the introduction chapter 1, much work has been devoted in recent times to the investigation of linear parameter varying controllers (LPV) for application in the field of wind turbines. The most basic use of this form of control can be for trimming purposes. A further comparison between the proposed LQR and an LPV would be interesting, in order to quantify the advantages or disadvantages of the latter with respect to a simpler controllers like those proposed in chapter 2. To this aim, an implementation of an LPV may be attempted.

The architecture based on multiple Kalman observers for the observation

of the wind states can be based on a more high-fidelity reduced model. Trials made using `FAST` instead of `SymDyn` have provided encouraging results, but the difficult process of integration of that code in the existing control code, a necessary implementation step, may be not worth the effort. A procedure to get a reduced model directly from `Cp-Lambda`, based on some form of identification, may be more interesting and would provide also a powerful tool for control design.

The observer for the yaw misalignment has been deemed very promising, and was recently validated by the author on the `FAST` model of the CART machine of the NREL. However, testing on the real thing will constitute the final proof of the applicability in real environment. To this end some research work is under way, based on real data collected on the CART plant, where both the wind components and the loads can be measured. Moreover, as the observation of the yaw misalignment is strictly related to the observation of vertical shear, further testing may allow an assessment of the performance of an observer able to provide a reading of both wind states, leading to a better characterization of the wind. This may be used to implement suitable control laws able to account for this information, based also on the use of multiple flap actuators to account for the non-uniformity of the incoming wind field.

It should be mentioned that thanks to the followed programming approach, it will be soon possible to apply all the control and observation algorithms presented in this work to a fully aero-elastic wind tunnel model of a three-bladed turbine, sponsored by Vestas [102], in a final stage of characterization and validation at the Department of Aerospace Engineering of the Politecnico di Milano. Actually, the migration of the code from a PC to an industrial real-time hardware is already well under way. Immediate activities on that model will involve further validation and applicability studies on the observers of the wind states.

As pointed out in chapter 2, the LQR control approach bends itself to an integrated use in more comprehensive partially automated design optimization tools, specifically prepared for wind turbines. Actually, as the array of available control systems, both designed for trimming or load dampening purposes, is able to provide a remarkable standard performance, the sizing of the turbine can be carried out taking advantage of the load abatement guaranteed by the controllers. A similar integrated design approach, also involving a structural optimization part, has been proposed in [75], where a mostly automatic gain synthesis procedure, easily feasible when using an LQR, is exploited.

Moreover, recent advances in the development of manufacturing technologies typically applied to the assembly of the blades (the so-called "smart blade" design) have made possible load reductions of the same entity of those

provided by control systems specifically aimed at the reduction of the same loads [103]. By performing a suitable tuning of the gains of an individual pitch controller like the IPC, it is possible to get further substantial load reductions. As a result, the same actuator duty-cycle commonly used to get a satisfying load abatement from an IPC controller can be used to get a largely better result in association with some blade design and manufacturing technologies. This and similar issues show how the design of the turbine could be improved by accounting for the envisaged design of the control system during the design phase. In the same fashion, the control system could be tuned differently from usual when working on a structure designed in a smart way, thus saving some actuator duty-cycle.

Given the strict limits in particular on the actuation bandwidth of pitch actuators, which is bound to the large size and inertia of the blades of modern turbines, and the resulting standardization of the advantage given by the existing control systems, it is possible to forecast that distributed controls, both active and passive, will receive an increasing attention in the near future, as a mean to improve controllability. They can be based on the addition of one or more flaps positioned at the trailing edge of the blades. In the case of actively actuated flaps, it may be possible to try new applications of the control design techniques presented in this work, like the multi-layer HHC-based control, which may be applied after a suitable model will have been identified between the harmonics in the various inputs and the harmonics of the target load. Of course, the increase in the number of controls may make the design of more complex model-based predictive controllers more difficult. In that case the use of a non-homogeneous LQR may be preferred to that of the more computationally heavy RHC, which may impose an unbearable computational-time toll because of the increased size of the system.

Anyway, these new control inputs may allow to make better use of a detailed description of the incoming wind to target blade loads and their combined effect on the fixed part of the system. Concerning these issues, an activity aimed at the assessment of the advantages and disadvantages of flap-based passive and active control is already under way, involving once more the use of the code `Cp-Lambda`.

Generally speaking, all the aforementioned control and aerodynamic-structural (aero-elastic) design techniques can be deployed together in order to prolongate the life of the turbine, by lowering the loads and stresses on its key-parts, and to optimize the use of the materials, thus reducing also the initial cost of the plant. By an integrated design of the plant and its controller and monitoring systems, these goals can be pursued more easily than by applying only a good controller to an existing turbine. So, it can be said that the technologies available today can be fully exploited by con-

sidering the design of the wind turbine as a single multi-disciplinary design problem [75]. In particular, the design of the controller should not be considered as a separate problem with respect to the aero-elastic design of the turbine, but as an aspect of the overall design, i.e. as a step in an integrated aero-servo-elastic design process.

Appendix A

Individual Pitch Control with the Coleman's Transformation

To better assess the potential of the new proposed control schemes (chapter 4), aimed at the reduction of the loads on some components of the turbine, it is useful to provide a brief insight of a widespread controller, often simply termed as individual pitch control (IPC), in the form presented by Bossanyi in [35, 86], whose performance results can be used as a basis for comparisons. This controller is basically aimed at the reduction of the 1P oscillations of the blade loads by means of an appropriate cyclic contribution to the collective control input used to trim the machine. Actually, it can be shown how the control action required to lower the 1P component of the out-of-plane moments at the blade root be the same required to target the constant values of the bending moments measured on the shaft at the height of the hub, and defined around the nodding and yawing axes.

A.1 Coleman's Transformation at 1P and Bossanyi's IPC

The analytic relationship between the 1P amplitudes of the out-of-plane moments at the root of the blades and the shaft moments at the hub is expressed by the Coleman's transformation, which to the purpose of explaining the controller presented by Bossanyi can be seen as a particular kinematic transformation, which for for three-bladed rotors allows to switch from a collection of three blade-specific measurements, each expressed in terms of components with respect to a blade root frame rotating with the rotor, to two equivalent measurements in a fixed system.

Consider a three-bladed turbine under the action of a constant wind and

kept trimmed by a suitable trimmer. Let M_{OoP_b} be the 1P amplitudes of the out-of-plane moments at the root of each of the three b-th blades, with $b = 1, 2, 3$. Let M_n and M_y be the constant values (0P amplitudes) of the bending moments measured at the hub height on the shaft around the nodding and yawing axes respectively. By defining the azimuth angle of the blade for which $b = 1$ as ψ, the equation of the Coleman's transformation can be written as

$$\left\{ \begin{array}{c} M_n \\ M_y \end{array} \right\} = \frac{2}{3} \left[\begin{array}{ccc} cos(\psi) & cos(\psi + \frac{2\pi}{3}) & cos(\psi + \frac{4\pi}{3}) \\ sin(\psi) & sin(\psi + \frac{2\pi}{3}) & sin(\psi + \frac{4\pi}{3}) \end{array} \right] \left\{ \begin{array}{c} M_{OoP_1} \\ M_{OoP_2} \\ M_{OoP_3} \end{array} \right\}. \quad \text{(A.1)}$$

From Bossanyi's work [35–37, 86], it is possible to close a control loop between the two scalar signals on the left of Eq. (A.1) and an array of two controls, which can be transformed by the inverse of the Coleman's transformation back into an array of three elements, and fed to the pitch actuators. In Bossanyi's work on the topic it is shown that there is very low coupling between the two shaft loads and the two equivalent pitch controls in the fixed frame, so that the control laws can be designed independently as for two decoupled SISO systems, where the moment M_n is controlled by β_n and the same happens for M_y and β_y. As a result, even a simple PID control law can be implemented and tuned to provide the desired amount of control authority and promptness for each of the two independent loops. In analytical terms, the two independent control laws can be written as

$$\begin{aligned} \beta_n &= k_{P_n} M_n + k_{I_n} \int_t^{t+T} M_n \mathrm{d}t + k_{D_n} \frac{\mathrm{d}M_n}{\mathrm{d}t}, \\ \beta_y &= k_{P_y} M_y + k_{I_y} \int_t^{t+T} M_y \mathrm{d}t + k_{D_y} \frac{\mathrm{d}M_y}{\mathrm{d}t}, \end{aligned} \quad \text{(A.2)}$$

where the values of the six PID gains k_{P_n}, k_{I_n}, k_{D_n}, k_{P_y}, k_{I_y}, k_{D_y}, can be appropriately tuned to get the desired level of control authority and performance on loads. Once the two pitch controls β_n and β_y in the fixed frame are known, they can be turned into three pitch inputs by the inverse transformation

$$\left\{ \begin{array}{c} \beta_1 \\ \beta_2 \\ \beta_3 \end{array} \right\} = \left[\begin{array}{cc} cos(\psi) & sin(\psi) \\ cos(\psi + \frac{2\pi}{3}) & sin(\psi + \frac{2\pi}{3}) \\ cos(\psi + \frac{4\pi}{3}) & sin(\psi + \frac{4\pi}{3}) \end{array} \right] \left\{ \begin{array}{c} \beta_n \\ \beta_y \end{array} \right\}, \quad \text{(A.3)}$$

and the resulting three pitch inputs can be fed to the pitch actuators. A schematic plot of the controller resulting from the superimposition of a trimmer and the IPC proposed by Bossanyi is presented in Fig. A.1.

It should be noted at this level that Eq. (A.1) holds only under two hypotheses. First, as the nodding and yawing moments measured on the shaft are put into a relationship only with the moments measured at the blade root, the moment measured on the shaft due to the shear forces at the blade root must be enough lower than the pure bending moments on the blades, in order to make possible to forget about the contribution of shear forces to the bending moment measured on the rotor axis. Second, to allow accounting only for the out-of-plane moments in the definition of the bending moments on the shaft, it is necessary to implicitly hypothesize a null effect of the in-plane moments on the latter. That hypothesis holds when there is no cone angle on the rotor ($\chi = 0$ deg). If this is not the case, a more complete Coleman's transformation can be written, accounting for both the out-of-plane and in-plane moments:

$$\begin{Bmatrix} M_n \\ M_y \end{Bmatrix} = \begin{bmatrix} cos(\psi) & cos(\psi + \frac{2\pi}{3}) & cos(\psi + \frac{4\pi}{3}) \\ sin(\psi) & sin(\psi + \frac{2\pi}{3}) & sin(\psi + \frac{4\pi}{3}) \end{bmatrix} \begin{Bmatrix} M_{OoP_1} \\ M_{OoP_2} \\ M_{OoP_3} \end{Bmatrix} + \begin{bmatrix} sin(\psi) & sin(\psi + \frac{2\pi}{3}) & sin(\psi + \frac{4\pi}{3}) \\ -cos(\psi) & -cos(\psi + \frac{2\pi}{3}) & -cos(\psi + \frac{4\pi}{3}) \end{bmatrix} sin(\chi) \begin{Bmatrix} M_{InP_1} \\ M_{InP_2} \\ M_{InP_3} \end{Bmatrix}, \tag{A.4}$$

where obviously $M_{InP_b}, b = 1, 2, 3$ are the in plane moments at the root of the blades, and the aforementioned cone angle χ is positive if the blades are bent upwind. Actually, if only the contribution to the shaft moments due to the out-of-plane was considered, then only that contribution could be targeted by the proposed controller, thus obtaining only a partial reduction of the target load.

The use of the decoupled PID controllers proposed by Bossanyi gives good results in terms of damping of the oscillations of the 1P components of the out-of-plane loads on the blade and of the constant components of the nodding and yawing moments measured on the shaft, if compared to what is obtained from a simple trimmer. For this reason, this architecture has been chosen and tested extensively in this work to compare to the proposed multi-layer controller, where the middle loop is based on HHC (chapter 4).

A.2 Coleman's Transformation at Multiple Frequencies

A different analysis of the effects of the Coleman's transformation especially in terms of the frequency content of both the blade-specific and transformed

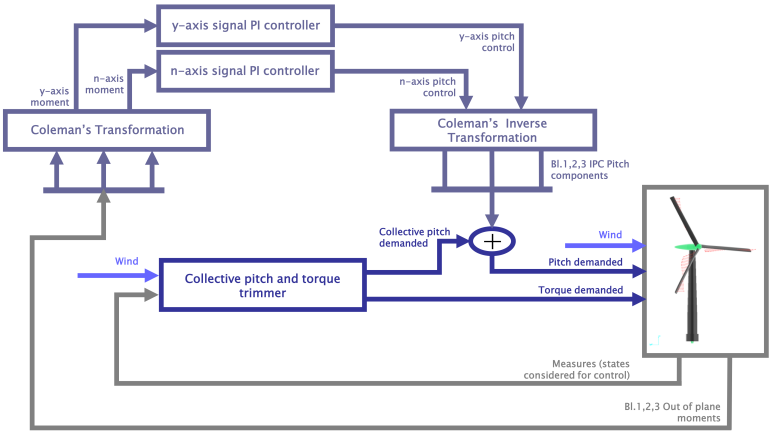

Figure A.1: Individual pitch control (IPC) as proposed by Bossanyi.

equivalent loads will be presented now, integrating the work of van Engelen [87].

To this aim, consider a generic definition of the moment m_b at the root of the b-th blade of a generic turbine with N_b blades. An analytical expression for this moment can be formulated, hypothesizing that it was composed by a part due to pitch β_b, a part bound to a disturbance effect u due to deterministic and non-deterministic aerodynamic loads, and a constant part m_0 not depending on pitch or aerodynamics:

$$m_b = m_{0,b} + \gamma\beta_b + \alpha u_b, \tag{A.5}$$

where the characteristic coefficients γ and α depend on the aero-elastic response of the blade. By defining the array

$$\boldsymbol{m} = \left\{ \begin{array}{c} m_1 \\ m_2 \\ m_3 \\ \dots \\ m_{N_b} \end{array} \right\}, \tag{A.6}$$

and similarly $\boldsymbol{m}_0$, $\boldsymbol{\beta}$ and $\boldsymbol{u}$ as $N_b \times 1$ arrays, it is possible to rewrite the latter equation in vectorial form as

$$\boldsymbol{m} = \boldsymbol{m}_0 + \gamma\boldsymbol{\beta} + \alpha\boldsymbol{u}. \tag{A.7}$$

Notice that the coefficients γ and α remain unaltered in the vectorial form (A.7) if all blades have the same aero-elastic properties.

Starting from the definition of the Coleman's transformation (A.1), which is based on the value of the azimuth ψ, it is possible to define a more generic transformation matrix $\boldsymbol{C}_K$, based on the angle $K\psi$. For a three-bladed rotor ($N_b = 3$), the definition can be written explicitly as

$$\boldsymbol{C}_K = \frac{2}{3}\begin{bmatrix} cos(K\psi_1) & cos(K\psi_2) & cos(K\psi_3) \\ sin(K\psi_1) & sin(K\psi_2) & sin(K\psi_3) \end{bmatrix}, K = 1, 2, \ldots \tag{A.8}$$

where ψ_1,ψ_2 and ψ_3 are the azimuth angles of the three blades. Its inverse is

$$\tilde{\boldsymbol{C}}_K = \frac{3}{2}\begin{bmatrix} cos(K\psi_1) & sin(K\psi_1) \\ cos(K\psi_2) & sin(K\psi_2) \\ cos(K\psi_3) & sin(K\psi_3) \end{bmatrix}, K = 1, 2, \ldots . \tag{A.9}$$

The transformation, which can now be formalized as

$$\boldsymbol{m}_K = \boldsymbol{C}_K \boldsymbol{m}, \tag{A.10}$$

where

$$\boldsymbol{m}_K = \begin{Bmatrix} m_{dK} \\ m_{qK} \end{Bmatrix}, \tag{A.11}$$

for $K = 1$ turns the blade-specific signals defined in the blade root frame into two equivalent fixed frame signals, indexed in the previous section as n and y standing for "nodding" and "yawing" respectively, and now defined for generality as d and q and forming the $(d-q)_1$ frame.

For $K = 2$, the transformation turns the blade-specific signals into two equivalent signals in a frame $(d-q)_2$, rotating with angular speed $-\frac{\mathrm{d}\psi}{\mathrm{d}t}$ with respect to the fixed frame $(n-y)$ around the axis of the rotor, i.e. rotating opposite to the rotor with the same absoulte rotational speed. For $K = 3$ the transformation is into a frame $(d-q)_3$, rotating at $-2\frac{\mathrm{d}\psi}{\mathrm{d}t}$, i.e. opposite to the rotor at twice its absolute rotational speed, and so on for larger values of K.

For every transformation $\boldsymbol{C}_K$ the corresponding inverse transform $\tilde{\boldsymbol{C}}_K$ changes the two signals in frame $(d-q)_K$ into signals in the rotor frame.

Consider now the array

$$\boldsymbol{\beta}_K = \begin{Bmatrix} \beta_{dK} \\ \beta_{qK} \end{Bmatrix} \tag{A.12}$$

of the pitch inputs in the $(d-q)_K$ frame, obtained for instance from a suitable control law from the equivalent loads defined with respect to the

same frame (like the law proposed by Bossanyi considering only $K = 1$). This array can be transformed into one of blade-specific pitch input signals

$$\boldsymbol{\beta}_{b_K} = \left\{ \begin{array}{c} \beta_{1_K} \\ \beta_{2_K} \\ \beta_{3_K} \end{array} \right\} \tag{A.13}$$

following the inverse transformation

$$\boldsymbol{\beta}_{b_K} = \tilde{\boldsymbol{C}}_K \boldsymbol{\beta}_K. \tag{A.14}$$

To better understand the effect of the generic K-th transformation defined by $\boldsymbol{C}_K$, consider the blade load model defined in Eq. (A.7). It is possible to apply the Coleman's K-th transformation to both sides of the equation, yielding

$$\boldsymbol{m}_K = \boldsymbol{C}_K \boldsymbol{m} = \boldsymbol{C}_K \boldsymbol{m}_0 + \gamma \boldsymbol{C}_K \boldsymbol{\beta} + \alpha \boldsymbol{C}_K \boldsymbol{u}, \tag{A.15}$$

where by definition the cosntant term $\boldsymbol{C}_K \boldsymbol{m}_0 = \boldsymbol{0}$ for any K. The term $\alpha \boldsymbol{C}_K \boldsymbol{u}$ is made up of a constant and a cyclic component. For any transformation K, for a three-bladed rotor this term can be written as

$$\boldsymbol{C}_K \boldsymbol{u} = \boldsymbol{u}_K + \sum_{m=1}^{\infty} \delta \boldsymbol{u}_K(3mP), \tag{A.16}$$

where $\boldsymbol{u}_K$ is a constant term obtained from the load component oscillating at the K-th frequency in the blade-specific signal, while $\delta \boldsymbol{u}_K(3mP), m = 1, 2, \ldots$ is due to all other blade-specific load components, oscillating at mP frequencies, $m = 1, 2, \ldots$. The latter disturbance term, representing a residual oscillating load component on the $(d-q)_K$ frame, features a frequency content bound to the number of blades on the considered rotor. For a three-bladed rotor the loads not oscillating at the K-th rotor frequency generate load components modulated by m-th multiples of the 3P.

About the remaining term in Eq. (A.15), by hypothesizing to have $\boldsymbol{\beta} = \boldsymbol{\beta}_{b_K}$, which is the case for instance when the pitch input comes from a control system like Bossanyi's, it is possible to write

$$\boldsymbol{C}_K \boldsymbol{\beta}_{b_K} = \boldsymbol{C}_K \tilde{\boldsymbol{C}}_K \boldsymbol{\beta}_K = \boldsymbol{\beta}_K, \tag{A.17}$$

where the identity $\boldsymbol{C}_K \tilde{\boldsymbol{C}}_K = \boldsymbol{I}$ has been used.

The latter identity is mathematically exact for values of K which are not multiples of three when $N_b = 3$, meaning that for three-bladed rotors the transformation $\boldsymbol{C}_K$ is not such that $\boldsymbol{C}_K \tilde{\boldsymbol{C}}_K = \boldsymbol{I}$ if the frequency on which it is based is a triple multiple of the revolution frequency. Take for instance

the transformation for $K = 3$. Calculating the product $\boldsymbol{C}_3\tilde{\boldsymbol{C}}_3$ it is possible to notice that the result is not only the identity $\boldsymbol{I}$, but instead it is

$$\boldsymbol{C}_3\tilde{\boldsymbol{C}}_3 = \boldsymbol{I} + \boldsymbol{\Delta}_6, \tag{A.18}$$

where

$$\boldsymbol{\Delta}_6 = \begin{bmatrix} -cos(6\psi_1) & sin(6\psi_1) \\ sin(6\psi_1) & cos(6\psi_1) \end{bmatrix}. \tag{A.19}$$

So, the term $\boldsymbol{C}_K\boldsymbol{\beta}_{b_K}$ in Eq. (A.17) will be interested by a disturbance for $K = 3$, such that

$$\boldsymbol{C}_3\boldsymbol{\beta}_{b3} = \boldsymbol{\beta}_3 + \boldsymbol{\Delta}_6\boldsymbol{\beta}_3. \tag{A.20}$$

Similar results can be obtained for $K = 6, 9, \ldots$ for three-bladed rotors. It is important to notice that the disturbance acts at a frequency that is higher than that used to define the K-th transform (in this example with $K = 3$ the disturbance acts at the 6P).

Based on the results (A.16) and (A.17), Eq. (A.15) can be rewritten for values of K not multiples of three as

$$\boldsymbol{m}_K = \gamma\boldsymbol{\beta}_K + \alpha(\boldsymbol{u}_K + \sum_{m=1}^{\infty} \boldsymbol{u}_K(3mP)), \tag{A.21}$$

while for K multiples of three the same expression takes the shape

$$\boldsymbol{m}_K = \gamma(\boldsymbol{\beta}_K + \boldsymbol{\Delta}_{2K}\boldsymbol{\beta}_K) + \alpha(\boldsymbol{u}_K + \sum_{m=1}^{\infty} \boldsymbol{u}_K(3mP)). \tag{A.22}$$

Suppose now to filter out the oscillating components from the transformed signal $\boldsymbol{m}_K$. The result would be in any case

$$\boldsymbol{m}_K = \gamma\boldsymbol{\beta}_K + \alpha\boldsymbol{u}_K. \tag{A.23}$$

Eq. (A.23) shows how the equivalent loads in frame $(d-q)_K$ are bound to the constants $\boldsymbol{\beta}_K$ and $\boldsymbol{u}_K$. These constants are by definition the amplitudes of the oscillatory signals of pitch and aerodynamic load at the KP frequency. So, the effect of the K-th Coleman's transformation is that of promoting the amplitudes of the KP oscillatory component in the blade-specific signals, weighed by the model coefficients γ and α, to the role of constants in the $(d-q)_K$ frame. The constant equivalent load can be successfully targeted by means of two decoupled integral controls, as proposed by Bossanyi for the $K = 1$ case. The control law can be written for the K-th transformation as

$$\boldsymbol{\beta}_K(t) = -k_I \int_{t-T}^{t} \boldsymbol{m}_K(t)\mathrm{d}t, \tag{A.24}$$

and the resulting equation of the controlled system can be obtained by substitution in Eq. A.23. It yields

$$\boldsymbol{m}_K = -\gamma k_I \int_{t-T}^{t} \boldsymbol{m}_K(t)\mathrm{d}t + \alpha \boldsymbol{u}_K. \tag{A.25}$$

Notice that the control law is based only on one scalar gain value, k_I, so that even if multiple controllers are used simultaneously to target the blade loads at different frequencies, it is not necessary to tune each controller differently from the other. This is all the more true considering that for every considered frequency of the transformation (i.e. for every K) the dynamic equation of the system is based on the same coefficients γ and α, making any gain tuning unnecessary.

As usual, to improve the promptness of the control in real environment, it is also possible to put proportional and derivative gains besides the integral one, even if not required from the viewpoint of theory. Based on the same considerations just presented for the integral gain, also for potential further proportional or derivative gains a multiple definition for the different considered frequencies would not be necessary.

A.3 Results

In practical terms, the control proposed by Bossanyi in [86] based on measures of blade loads can be implemented following three steps: first, a transformation of the blade loads by means of a Coleman's transformation with $K = 1$ should be implemented; second, a filtering technique should be used to filter out any oscillatory components from the transformed load signals: the result would be an array of two constant loads, which could be targeted by two decoupled integral controllers; finally, the resulting control inputs in the $(d-q)_1$ system should be transformed back into blade-specific pitch inputs, using the inverse Coleman's transformation.

Achieving a multifrequency control involves the simultaneous application of multiple pitch control components, each obtained from basically the same procedure just presented. For each K of interest the blade-specific loads can be transformed by the corresponding Coleman's transformation. Filtering the resulting loads and keeping only the constant (using the same low-pass filter for every K) will make possible the application of the integral control law, obtaining two control inputs which can be changed into additional pitch inputs by means of an inverse Coleman's transformation.

Some results obtained in constant wind with constant standard shear are presented below (Fig. A.2) for the `Cp-Lambda` model of the 2.5 MW turbine

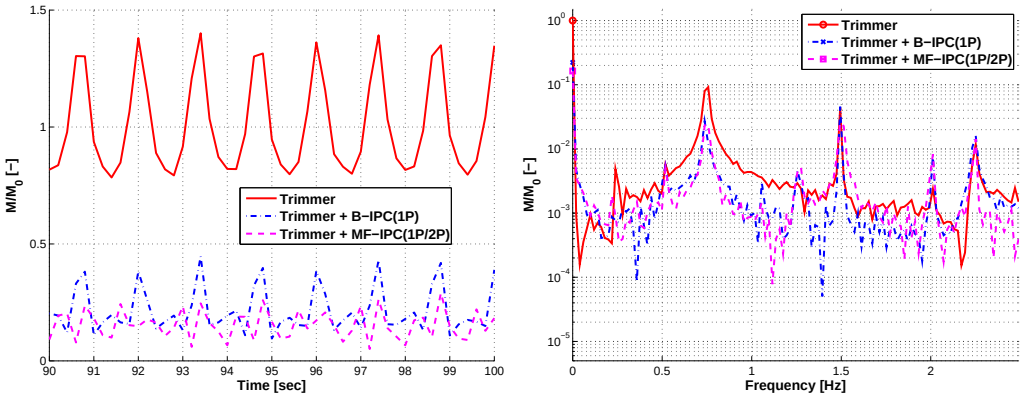

(a) (b)

Figure A.2: Normalized time histories (left) and spectra (right) of shaft bending moment resultant in deterministic wind at 15 m/sec with power law shear coefficient 0.2. Comparison between the PID trimmer operating alone, the trimmer working together with an individual pitch controller based on the usual Coleman's transformation, and the trimmer working with an individual pitch controller based on the Coleman's transformation at the 1P and 2P. Both time histories and spectra are normalized to the zero-frequency peak value obtained with the sole collective trimmer.

(see chapter 1). The trimmer is based on a PID industrial control law. The comparison is between the basic trimmer, the same trimmer operating with the Bossanyi IPC (which is the limit case of the proposed multifrequency controller, with only $K = 1$), and the trimmer with a multifrequency controller as described above, with $K = 1$ and $K = 2$, i.e. based on the 1P and 2P of the blade-specific loads. Here a Butterworth fourth-order low-pass is used to filter out the oscillating components on the loads in the $(d - q)_K$ reference. A purely integral control is used to target the resulting loads.

From Fig. A.2 a modest improvement on the oscillations at the 2P is noticeable on both time histories and spectra of loads. This is normal, as the amplitude of the 2P oscillation in blade-specific loads is smaller than that of the 1P, an so the reduction of the component of the shaft target load due to the 2P component of the blade load is less important than the reduction of the effect of the 1P. On the other hand, if a more intense reduction effect on the contribution given by a precise frequency in the blade-specific load is required, then different control gains can also be used for each considered K.

It should be pointed out that of course the use of this control, based on the Coleman's transformation, has beneficial effects also on those blade-specific loads which are used to derive the equivalent loads directly targeted by the

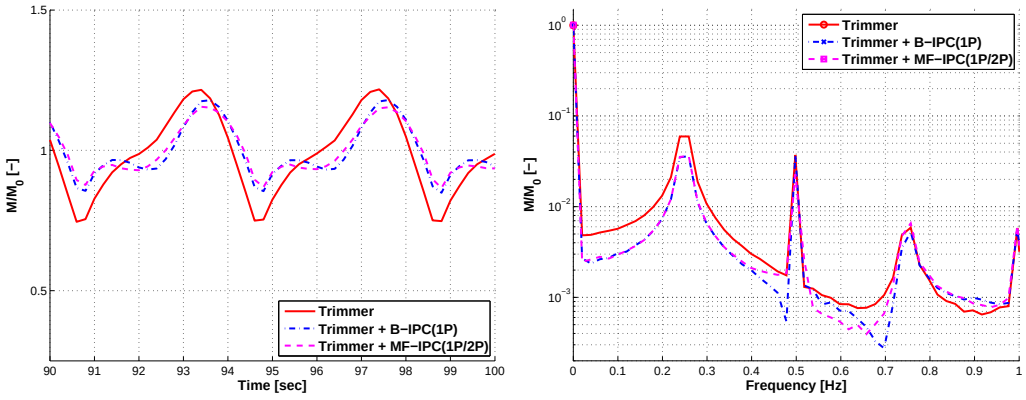

(a) (b)

Figure A.3: Normalized time histories (left) and spectra (right) of bending moment resultant at blade root (blade Nr.1) in deterministic wind at 15 m/sec with power law shear coefficient 0.2. Comparison between the PID trimmer operating alone, the trimmer working together with an individual pitch controller based on the usual Coleman's transformation, and the trimmer working with an individual pitch controller based on the Coleman's transformation at the 1P and 2P. Both time histories and spectra are normalized to the zero-frequency peak value obtained with the sole collective trimmer.

controller. For the same simulation conditions used to produce the results plotted in Fig. A.2, the next Fig. A.3 reports the time history and spectra of the out-of-plane loads on the blades.

Also here a minor advantage on the load component at the 2P is noticeable when the multifrequency controller is used with respect to the IPC based on the 1P only.

Appendix B

Output-Feedback LQR Formulation

The synthesis of the LQR gain matrix for the output-feedback control case can be carried out following several different algorithms. In this work a convenient algorithm has been implemented and described in the following. The presented algorithm is almost directly transcribed from [73].

B.1 Implementation of the Algorithm by Moerder and Calise

The implementation can be divided into an initialization and an iterative core. Let $\boldsymbol{A}$,$\boldsymbol{B}$,$\boldsymbol{C}$ be the matrices of the state and measurement equations, while $\boldsymbol{Q}$ and $\boldsymbol{R}$ are the usual weight matrices.

Initialization

- Let the counter $k = 0$;
- a first-guess stabilizing gain $\boldsymbol{G}_0$ is evaluated as the full-state feedback gain on the system with matrices $\boldsymbol{A}$ and $\boldsymbol{B}$. Actually, as in the output-feedback problem the matrix $\boldsymbol{C}$ is rectangular, the gain $\boldsymbol{G}_0$ will be trimmed in order to keep only the columns related to the states which will be available in the output-feedback problem.

k-th Iteration

- Let $\boldsymbol{A}_k = \boldsymbol{A} - \boldsymbol{B}\boldsymbol{G}_k\boldsymbol{C}$;

- the Lyapunov equation

$$\mathbf{0} = \boldsymbol{A}_k^T \boldsymbol{P}_k + \boldsymbol{P}_k \boldsymbol{A}_k + \boldsymbol{C}^T \boldsymbol{G}_k^T \boldsymbol{R} \boldsymbol{G}_k \boldsymbol{C} + \boldsymbol{Q} \tag{B.1}$$

  is solved in terms of the unknown $\boldsymbol{P}_k$;

- the Lyapunov equation

$$\mathbf{0} = \boldsymbol{A}_k \boldsymbol{S}_k + \boldsymbol{S}_k \boldsymbol{A}_k^T + \boldsymbol{X} \tag{B.2}$$

  is solved in terms of the unknown $\boldsymbol{S}_k$;

- the cost function $J_k = \frac{1}{2}\mathrm{Tr}(\boldsymbol{P}_k \boldsymbol{X})$ is evaluated;

- the change in the value of the gain matrix $\boldsymbol{G}$ for the current iteration is evaluated as

$$\Delta \boldsymbol{G}_k = \boldsymbol{R}^{-1} \boldsymbol{B}^T \boldsymbol{P}_k \boldsymbol{S}_k \boldsymbol{C}^T (\boldsymbol{C} \boldsymbol{S}_k \boldsymbol{C}^T)^{-1} - \boldsymbol{G}_k; \tag{B.3}$$

- the updated value of the gain matrix, $\boldsymbol{G}_{k+1}$, is computed as

$$\boldsymbol{G}_{k+1} = \boldsymbol{G}_k + \alpha \Delta \boldsymbol{G}_k, \tag{B.4}$$

  where α is chosen in order to keep the controlled system $\boldsymbol{A} - \boldsymbol{B}\boldsymbol{G}_{k+1}\boldsymbol{C}$ stable.

The check at the end of the k-th iteration is the evaluation of the new cost function $J_{k+1} = \frac{1}{2}\mathrm{Tr}(\boldsymbol{P}_{k+1}\boldsymbol{X})$, which is compared to the previous J_k. If their difference is less than a user-specified tolerance, then the method is stopped, and the last $\boldsymbol{G}_k$ is given as output. Otherwise a new iteration is inaugurated.

Notice that, besides a user-dependent choice of the tolerance, the method allows the user to specify the weight $\boldsymbol{X}$ in the cost function. The final gain resulting from the iterative method is not heavily dependant on the choice of $\boldsymbol{X}$, which in practice may be defined as $\boldsymbol{X} = \boldsymbol{I}$. The value can be altered in order to improve convergence in the initial stage of the iterative procedure [31].

Bibliography

[1] R.E. Wilson and P. Lissaman. Applied aerodynamics of wind power machines. Technical report, Oregon State University, Corvallis, OR, 1974.

[2] E. Hau. *Wind Turbines: Fundamentals, Technologies, Application, Economics*. Berlin: Springer, 3rd edition, 2006.

[3] E. Bossanyi. The design of closed loop controllers for wind turbines. *Wind Energy*, 3(3):149–163, 2000.

[4] S. De La Salle, D. Reardon, W. Leithead, and M. Grimble. Review of wind turbine control. *International Journal of Control*, 52(6):1295–1310, 1990.

[5] J.M. Kos. On line control of a large horizontal-axis energy conversion system and its performance in a turbulent wind environment. *Proceedings of the 13th Intersociety Energy Conversion Engineering Conference, USA*, 3:2064–2073, 1978.

[6] E.N. Hinrichsen. Control for variable pitch wind turbine generators. *IEEE Transactions on Power Apparatus and Systems*, 103(4):886–892, 1984.

[7] E.N. Hinrichsen and P.J. Nolan. Dynamics and stability of wind turbine generators. *IEEE Transactions on Power Apparatus and Systems*, 101(8):2640–2648, 1984.

[8] D. Leith and W. Leithead. Application of nonlinear control to hawt. In *Proceedings of the Third IEEE Conference on Control Applications, Glasgow, UK, 24–26 August*, volume 1, pages 245–250, 1994.

[9] D. Leith and W. Leithead. Implementation of wind turbine controllers. *International Journal of Control*, 66:349–380, 1997.

[10] W. Leithead and B. Connor. Control of variable speed wind turbines: design task. *Inernational Journal of Control*, 73(13):1189–1212, 2000.

[11] P. Bongers. Robust control using coprime factorizations, application to flexible wind turbine. In *Proccedings of the 31st IEEE Conference on Decision and Control, vol.2, Tucson, AZ*, pages 2436–2441, 1992.

[12] W.E. Holley, S.M. Rock, and K. Chaney. Control of variable speed wind turbines below rated wind speed. In *Proceedings of the 3rd ASME-JSME Joint Fluids Engineering Conference, San Francisco, CA, July 18–23*, 1999.

[13] W. Leithead and S. Dominguez. Controller design for the cancellation of the tower fore-aft mode in a wind turbine. In *Proceedings of the 44th Conference on Decision and Control, Seville, Spain*, pages 1276–1281, 2005.

[14] W. Leithead and S. Dominguez. Coordinated control design for wind turbine control systems. In *Proceedings of the European Wind Energy Conference (EWEC 2006), Athens, Greece*, 2006.

[15] E. Bossanyi. *Bladed for Windows theory manual*. Garrad Hassan, Bristol, UK, 1999.

[16] B. Jonkman and M. Buhl. *FAST User's Guide*. National Renewable Energy Laboratory (NREL), Golden, CO, August 2005.

[17] K. Stol and G. Bir. *SymDyn User's Guide*. National Renewable Energy Laboratory (NREL), Golden, CO, 2003.

[18] C.L. Bottasso, A. Croce, B. Savini, W. Sirchi, and L. Trainelli. Aero-servo-elastic modeling and control of wind turbines using finite element multibody procedures. *Multibody System Dynamics*, 16(3):291–308, 2006.

[19] O.A. Bauchau, C.L. Bottasso, and Y.G. Nikishkov. Modeling rotorcraft dynamics with finite element multibody procedures. *Mathematics and Computer Modeling*, 33:1113–1137, 2001.

[20] T. Ekelund. Dynamics and control of structural loads of wind turbines. In *Proceedings of the American Control Conference, vol.3, Philadelphia, PA*, pages 1720–1724, 1998.

[21] M. Lima, J. Silvino, and P. deResende. h_∞ control for a variable-speed adjustable-pitch wind energy conversion system. In *Proceedings of the IEEE International Symposium on Industrial Electronics, vol.2, Bled, Slovenia*, pages 556–561, 1999.

[22] T. Ekelund. Yaw control for reduction of structural dynamic loads in wind turbines. *Journal of Wind Engineering & Industrial Aerodynamics*, 85(3):241–262, 2000.

[23] C.L. Bottasso and A. Croce. Advanced control laws for variable-speed wind turbines and supporting enabling technologies. Scientific Report DIA-SR 09-01, Dipartimento di Ingegneria Aerospaziale, Politecnico di Milano, January 2009.

[24] Jr. A. Eggers, W. Holley, K. Chaney, and C. Jennings. Some effects of actuator lag, error sensing and non-uniform turbulence on a blade pitch control of fluctuating aerodynamic loads on hawts. In *Proceedings of 37th AIAA Aerospace Sciences Meeting and Exhibit, Reno, NV*, pages 104–113, 1999.

[25] P.J. Moriarty, Jr. A. Eggers, K. Chaney, and W.E. Holley. Scale and lag effects on control of aerodynamic power and loads on a hawt rotor. In *Proceedings of the 2001 ASME Wind Energy Symposium, Reno, NV*, pages 306–314, 2001.

[26] K. Stol. *Dynamics modeling and periodic control of horizonal axis wind turbines*. PhD thesis, University of Colorado, 2001.

[27] A. Wright and M. Balas. Design of state-space-based control algorithms for wind turbine speed regulation. In *Proceedings of the 21st American Society of Mechanical Engineers (ASME) Wind Energy Simposium, Reno, NV*, 2002.

[28] A. Wright and M. Balas. Design and controls to attenuate loads in the controls advanced research turbine. *Journal of Solar Energy Engineering*, 126(4):1083–1091, 2004.

[29] K. Stol, W. Zhao, and A. Wright. Individual blade pitch control for the controls advanced research turbine (cart). *Journal of Solar Energy Engineering*, 128(4):498–505, 2006.

[30] M. Geyler and P. Caselitz. Robust multivariable pitch control design for load reduction on large wind turbines. *Journal of Solar Energy Engineering*, 130(3):031014/1–031014/12, 2008.

[31] C.E.D. Riboldi. Controllo ciclico di aerogeneratori e tecnologie di supporto. Master's thesis, Dipartimento di Ingegneria Aerospaziale, Politecnico di Milano, Milano, Italy, 2008.

[32] A. Wright, K. Stol, and L.J. Fingersh. Progress in implementing and testing state-space controls for the controls advanced research turbine. In *Proceedings of the 43rd AIAA Aerospace Science Meeting and Exhibit, Reno, NV*, pages 10–13, 2005.

[33] A. Wright, L.J. Fingersh, and M. Balas. Testing state-space controls for the controls advanced research turbine. In *Proceedings of the 25th American Society of Mechanical Engineers Wind Energy Symposium, Reno, NV*, 2006.

[34] K. Stol and M.J. Balas. Full-state feedback control of a variable speed turbine: a comparison of periodic and constant gains. *Journal of Solar Energy Engineering*, 123(4):319–326, 2001.

[35] E. Bossanyi. Wind turbine control for load reduction. *Wind Energy*, 6(3):229–244, 2003.

[36] E. Bossanyi. Developments in individual blade pitch control. In *Proceedings of The Science of Making Torque from Wind Conference, Delft, The Netherlands, 19–21 April*, 2004.

[37] E. Bossanyi. Further load reductions with individual pitch control. *Wind Energy*, 8(4):481–485, 2005.

[38] K. Selvam, K. van Wingerden, T. van Engelen, and M. Verhaegen. Feedback-feedforward individual pitch control for wind turbine load reduction. *International Journal of Robust and Nonlinear Control*, 19(1):72–91, 2008.

[39] N. Bao and Z. Ye. Active pitch control in larger scale fixed speed horizontal axis wind turbine systems part ii: Non-linear controller design. *Wind Engineering*, 26(1):27–38, 2002.

[40] K. Ostergaard, P. Brath, and J. Stoutstrup. Estimation of effective wind speed. *Journal of Physics: Conference Series*, 75:012082, 2007.

[41] C.L. Bottasso and A. Croce. Power curve tracking with tip speed constraint using lqr regulators. Scientific Report DIA-SR 09-04, Dipartimento di Ingegneria Aerospaziale, Politecnico di Milano, March 2009.

[42] D. Leith and W. Leithead. Performance enhancement of wind turbine power regulation by switched linear control. *International Journal of Control*, 65(2):555–572, 1996.

[43] I. Kraan. Control design for a flexible wind turbine. Technical Report TUD-WBMR-A-613, Delft University of Technology, Delft, The Netherlands, 1992.

[44] F. Bianchi, R. Mantz, and C. Christiansen. Control of variable-speed wind turbines by lpv gain scheduling. *Wind Energy*, 7(1):1–8, 2004.

[45] K. Ostergaard. *Robust, gain-scheduled control of wind turbines*. PhD thesis, Aalborg University, 2008.

[46] F. Lescher, J. Zhao, A. Martinez, and L. deLille. Multiobjective h_2/h_∞ control of a pitch regulated wind turbine for mechanical load reduction. In *Proceedings of the International Conference on Renewable Energies and Power Quality, Palma de Mallorca, Spain*, 2006.

[47] M. Simoes, B. Bose, and R. Spiegel. Design and performance evaluation of a fuzzy-logic-based variable-speed wind generation system. *IEEE Transactions on Industry Applications*, 33(4):956–965, 1997.

[48] M. Mayosky and G. Cancelo. Adaptive control of wind energy conversion systems using radial basis networks. In *Proceedings of the IEEE International Joint Conference on Neural Networks Proceedings, IEEE World Congress on Computational Intelligence, vol.2*, pages 996–1001, 1998.

[49] R. Chedid, F. Mrad, and M. Basma. Intelligent control of a class of wind energy conversion systems. *IEEE Transactions on Energy Conversion*, 14(4):1597–1604, 1999.

[50] X. Ma. *Adaptive extremum control and wind turbine control*. PhD thesis, Technical University of Denmark, 1997.

[51] T. Larsen, H. Madsen, and K. Thomsen. Active load reduction using individual pitch, based on local blade flow measurements. *Wind Energy*, 8(1):67–80, 2005.

[52] A. Ozdemir, P. Seiler, and G. Balas. Performance of disturbance augmented control design in turbulent wind conditions. *Mechatronics*, 21(4):634–644, 2011.

[53] K. Stol and M.J. Balas. Periodic disturbance accomodating control for speed regulation of wind turbines. In *Proceedings of the 2002 ASME Wind Energy Symposium, Reno, NV*, pages 310–320, 2002.

[54] K.A. Stol. Disturbance tracking control and blade load mitigation for variable-speed wind turbines. *ASME Journal of Solar Energy Engineering*, 125(4):396–401, 2003.

[55] M. Harris, M. Hand, and A. Wright. Lidar for turbine control. Technical Report NREL/TP-500-39154, National Renewable Energy Laboratory (NREL), 2006.

[56] D. Schlipf, J.J. Trujillo, V. Basterra, and M. Kühn. Development of a wind turbine lidar simulator. In *Proceedings of the European Wind Energy Conference (EWEC 2009), Marseille, France*, 2009.

[57] D. Schlipf, T. Fischer, C.E. Carcangiu, M. Rossetti, and E. Bossanyi. Load analysis of look-ahead colective pitch control using lidar. In *Proceedings of the German Wind Energy Conference (DEWEK 2010), Bremen, Germany*, 2010.

[58] D. Schlipf, D. Trabucchi, O. Bischoff, M. Hofsäß, J. Mann, T. Mikkelsen, A. Rettenmeier, J.J. Trujillo, and M. Kühn. Testing of frozen turbulence hypothesis for wind turbine applications with a scanning lidar system. In *Proceedings of the International Symposium on Advancement of boundary layer Remote Sensing (ISARS), Saint Quentin-en-Yvelines, France*, 2010.

[59] J. Laks, F. Dunne, and L. Pao. Feasibility studies on disturbance feedforward techniques to improve load mitigation performance. Technical Report NREL/SR-5000-48598, National Renewable Energy Laboratory (NREL), 2010.

[60] J. Laks, A. Wright, L. Pao, N. Kelley, and B. Jonkman. The use of preview wind measurements for blade pitch control. *Mechatronics*, 21(4):668–681, 2011.

[61] D. Biondani. Implementazione di un controllore predittivo-adattivo in tempo reale per il controllo di passo e coppia di un aerogeneratore. Master's thesis, Dipartimento di Ingegneria Aerospaziale, Politecnico di Milano, Milano, Italy, 2007. pp. 16–19.

[62] D. Devecchi. Tecniche di controllo aeroelastico con passo individuale delle pale per aerogeneratori. Master's thesis, Dipartimento di Ingegneria Aerospaziale, Politecnico di Milano, Milano, Italy, 2008.

[63] A. Korber and R. King. Model predictive control for wind turbines. In *Proceedings of the European Wind Energy Conference (EWEC 2010), Warsaw, Poland*, 2010.

[64] M. Soltani, R. Wisniewski, P. Brath, and S. Boyd. Load reduction of wind turbines using receding horizon control. Technical report, Department of Electronics Systems, Aalborg University, Aalborg, Denmark and Vestas Technology R&D, Aarhus, Denmark and Department of Electrical Engineering, Stanford University, Palo Alto, CA, 2010.

[65] A. Kumar and K. Stol. Scheduled model predictive control of a wind turbine. In *Proceedings of the European Wind Energy Conference (EWEC 2010), Warsaw, Poland*, 2010.

[66] B.J. Jonkman and M.L. Buhl. *TurbSim's User Guide*. National Renewable Energy Laboratory (NREL), Golden, CO, 2007.

[67] Kangwon National University. 1 Kangwondaehak-gil, Chuncheon-si, Gangwon-do, 200-701 Republic of Korea.

[68] LEITWIND S.p.A. Via Brennero 34, 39049 Vipiteno (BZ), Italia.

[69] Clipper Windpower LLC. 6305 Carpinteria Avenue, Suite 300, Carpinteria, CA 93013.

[70] C.L. Bottasso, A. Croce, C.E.D. Riboldi, and Y. Nam. Power curve tracking in the presence of a tip speed constraint. *Renewable Energy*, –:–, 2012. To appear April 2012, in press.

[71] V. Ronchi. Osservatori del vento per il controllo di aerogeneratori. Master's thesis, Dipartimento di Ingegneria Aerospaziale, Politecnico di Milano, Milano, Italy, 2009.

[72] D.W. Gu, P.H. Petkov, and M.M. Konstantinov. *Robust Control Design with Matlab*. Springer-Verlag London Limited, 2005.

[73] D.D. Moerder and A.J. Calise. Convergence of a numerical algorithm for calculating optimal output feedback gains. *IEEE Trasactions on Automatic Control*, 30(9):900–903, 1985.

[74] *Wind Turbines — Part 1: Desing Requirements, Ed. 3.0*, 2005. International Standard IEC 61400-1.

[75] C.L. Bottasso, F. Campagnolo, and A. Croce. Multi-disciplinary constrained optimization of wind turbines. *Multibody System Dynamics*, –:–, 2012. To appear 2012, in press.

[76] R.D. Hampton, C.R. Knospe, and M.A. Townsend. A practical solution to the deterministic nonhomogenous lqr problem. *Journal of Dynamic Systems, Measurements and Control*, 118(2):354–359, 1996.

[77] M. Sjöholm, T. Mikkelsen, L. Kristensen, J. Mann, P. Kirkegaard, S. Kapp, D. Schlipf, and J.J. Trujillo. Spectral analysis of wind turbulence measured by a doppler lidar for velocity fine structure and coherence studies. In *Proceedings of the International Symposium on Advancement of boundary layer Remote Sensing (ISARS), Saint Quentin-en-Yvelines, France*, 2010.

[78] F. Dunne, L. Pao, A.D. Wright, B. Jonkman, N. Kelley, and E. Simley. Adding feedforward blade pitch control for load mitigation in wind turbines: non-causal series expansion, preview control, and optimized fir filter methods. In *Proceedings of the AIAA 2011 - 819, Orlando, FL, USA, January*, 2011.

[79] F. Dunne, L. Pao, A. Wright, B. Jonkman, and N. Kelley. Adding feedforward blade pitch control to standard feedback controllers for load mitigation in wind turbines. *Mechatronics*, 21(4):682–690, 2011.

[80] A. Rettenmeier, O. Bischoff, M. Hofsäß, D. Schlipf, J.J. Trujillo, and M. Kühn. Wind field analyses using a nacelle-based lidar system. In *Proceedings of the European Wind Energy Conference (EWEC 2010), Warsaw, Poland*, 2010.

[81] V.A. Banakh and I.N. Smalikho. Estimation of the turbulence energy dissipation rate from the pulsed doppler lidar data. *Atmospheric and Oceanic Optics*, 10:957–965, 1997.

[82] P. Lindelöw. *Fiber-based coherent LiDARs for remote wind sensing.* PhD thesis, Technical University of Denmark, 2008.

[83] J.P. Cariou. Pulsed coherent lidars for remote wind sensing. In *Proceedings of the Ph.D. Remote Sensing Summer School at Ris-DTU, Roskilde, Denmark*, 2011.

[84] G. Giansiracusa. Tecniche di controllo predittivo per aerogeneratori con ausilio di strumentazione lidar. Master's thesis, Dipartimento di Ingegneria Aerospaziale, Politecnico di Milano, Milano, Italy, 2011.

[85] J. Mattingley and B. Stephen. Cvxgen: A code generator for embedded convex optimization. Technical report, Electrical Engineering Department, Stanford University, Palo Alto, CA, 2010.

[86] E. Bossanyi. Individual blade pitch control for load reduction. *Wind Energy*, 6(2):119–128, 2003.

[87] T.G. van Engelen. Design model and load reduction assessment for multi-rotational mode individual pitch control (higher harmonics control). In *Proceedings of the European Wind Energy Conference (EWEC 2006), Athens, Greece, February 27–March 2*, 2006.

[88] T.van Engelen and S. Kanev. Exploring the limits in individual pitch control. In *Proceedings of the European Wind Energy Conference (EWEC 2009), Marseille, France, 16–19 March*, 2009.

[89] M. Geyler and P. Caselitz. Individual blade pitch control design for load reduction on large wind turbines. In *Proceedings of the European Wind Energy Conference (EWEC 2007), Milano, Italy, 7–10 May*, 2007.

[90] W.E. Leithead, V. Neilson, and S. Dominguez. Alleviation of unbalanced rotor loads by single blade controllers. In *Proceedings of the European Wind Energy Conference (EWEC 2009), Marseille, France, 16–19 March*, 2009.

[91] W. Johnson. *Helicopter Theory*. Princeton University Press, Princeton, NJ, 1981.

[92] W. Johnson. Self-tuning regulators for multicyclic control of helicopter vibration. Nasa technical paper, Ames Research Center, Moffett Field, CA, USA, 1996.

[93] K. Nguyen, M. Betzina, and C. Kitaplioglu. Full-scale demonstration of higher harmonic control for noise and vibration reduction on the xv-15 rotor. Technical report, Army/NASA Rotorcraft Division, NASA Ames Research Center, Moffett Field, CA, USA, 2000.

[94] D. Patt, L. Liu, J. Chandrasekar, D.S. Bernstein, and P.P. Friedmann. Higher-harmonic-control algorithm for helicopter vibration reduction revisited. *Journal of Guidance, Control and Dynamics*, 28(5):918–930, 2005.

[95] M. Lovera, P. Colaneri, C. Malpica, and R. Celi. Discrete-time, closed-loop aeromechanical stability analysis of helicopters with higher harmonic control. *Journal of Guidance, Control and Dynamics*, 30(5):1249–1260, 2007.

[96] D. Simon. *Optimal State Estimation: Kalman, H_∞, and Nonlinear Approaches*. John Wiley & Sons, Inc., 2006.

[97] K. Reif and R. Unbehauen. The extended kalman filter as an exponential observer for nonlinear systems. *IEEE Transactions on Signal Processing*, 47(8):2324–2328, 1999.

[98] K.A. Myers and B.D. Tapley. Adaptive sequential estimation with unknown noise statistics. *IEEE Transactions on Automatic Control*, 21(4):520–523, 1976.

[99] R.W. Schafer and A.V. Oppenheim. *Discrete-Time Signal Processing*. Prentice-Hall, 1989.

[100] M. Gutierrez and A. Perez-Sanchez. Set-up and performance assessment of a reduced model for the online observation of the states of the wind field over the rotor of a wind turbine. Master's thesis, Dipartimento di Ingegneria Aerospaziale, Politecnico di Milano, Milano, Italy, 2010.

[101] D.M. Eggleston and F.S. Stoddard. *Wind Turbine Engineering Design*. Van Nostrand Reinhold Company, New York, 1987.

[102] Vestas Wind Systems A/S. Hedeager 44, 8200 Aarhus N, Denmark.

[103] C. Tibaldi. Ottimizzazione aeroelastica per il controllo passivo dei carichi su pale di aerogeneratori ed integrazione con tecniche di controllo attivo. Master's thesis, Dipartimento di Ingegneria Aerospaziale, Politecnico di Milano, Milano, Italy, 2011.